UNIWERSYTET WARSZAWSKI

Université Paris Cité

Uniwersytet Warszawski

Wydział Fizyki

&

Université Paris Cité

Laboratoire Matière et Systèmes Complexes

Morphodynamic systems: from initial instability to network formation

Stanisław Żukowski

Under the supervision of **Piotr Szymczak** and **Stéphane Douady**

A dissertation submitted in fulfillment of the requirements
for the degree of Doctor of Philosophy

Warsaw/Paris, 2026

to Natalia and Emma

Morphodynamic systems: from initial instability to network formation

Abstract:

Natural shapes are often viewed as the result of an optimization process, or as being predetermined, for instance by a genetic program. This overlooks the problem of *how* shapes appear in the first place. To understand this, we must examine the underlying growth dynamics. We study the relationship between final shapes and growth processes to address the inverse problem: Given a shape, how can we determine the details of its growth process or, more broadly, identify the fundamental mechanism behind its emergence? Answering such a question could help us reconstruct environmental information from geological forms or understand how to arrest pathological processes in biological systems.

In this thesis, we focus on forms that initiate as an instability at a moving front. The small protrusions later develop into finger-like shapes that interact with each other and can form a network structure. The analyzed systems range from solution pipes in limestone to river networks to the canal network of *Aurelia* jellyfish. In the first two cases, growth models can be established and solved, for instance, by assuming that the studied shape is invariant. We demonstrate how to use these growth models to extract details of the governing growth laws or conditions during the emergence of a structure just by examining its final geometry. This is particularly important for geological forms that evolve over timescales beyond human measurement capabilities. We show that a single snapshot of geometry is sufficient to reconstruct historical flow rates in an emerging solution pipe or to identify the growth laws of a river network.

Next, we investigate loops in physical networks. Looping networks have been shown to be more resilient to damage and to be selected in biological evolution. However, their dynamic formation remains elusive. How do branches in a growing network attract each other and reconnect to form a loop? Classical models of networks growing in response to the gradient of an external field explain the competition, screening, and repulsion between branches. Yet, in remarkably diverse processes, ranging from unstable fluid flows to the canal system of jellyfish, loops suddenly form near breakthrough, when the longest branch reaches the boundary of the system. We study this process and demonstrate that when growth is governed by diffusive fluxes, screening and repulsion shift to attraction near the breakthrough event. Finally, we investigate the morphogenesis of a specific looping network: the gastrovascular canal network of *Aurelia* jellyfish. Our experimental observations suggest that canals emerge in a self-organized manner. We relate this process to the mechanics of jellyfish and hypothesize that canals are guided by a stress or diffusive field in the tissue. We build a numerical model of canal network development and show

that both processes can reproduce the patterns observed in the experiments equally well.

Keywords: morphodynamics, pattern formation, moving-boundary problem, unstable growth processes, Laplacian growth, physical networks

Układy morfodynamiczne: od początkowej niestabilności po wzrost sieci

Streszczenie:

Naturalne kształty są często postrzegane jako wynik procesu optymalizacji lub jako struktury z góry określone, na przykład przez program genetyczny. Pomija to jednak problem, *w jaki sposób* takie kształty powstają. Aby to zrozumieć, musimy zbadać dynamikę ich wzrostu. W tej pracy badamy związek między kształtami a procesami wzrostu, aby zmierzyć się z problemem odwrotnym: znając dany kształt, w jaki sposób możemy określić szczegóły procesu jego wzrostu lub, bardziej ogólnie, zidentyfikować podstawowe mechanizmy leżące u podstaw jego powstania? Odpowiedź na to pytanie mogłaby pomóc nam w odtworzeniu informacji środowiskowych na podstawie form geologicznych lub zrozumieniu, w jaki sposób zatrzymać procesy patologiczne w układach biologicznych.

W niniejszej pracy skupiamy się na formach, które początkowo powstają wskutek niestabilności na ruchomym froncie. Małe wypukłości przekształcają się później w wyciągnięte kształty przypominające palce, które oddziałują ze sobą i mogą tworzyć strukturę sieci. Analizowane układy obejmują świece krasowe, sieci rzeczne oraz sieć kanałów meduzy *Aurelia*. W pierwszych dwóch przypadkach można określić model wzrostu i rozwiązać go, na przykład zakładając, że badany kształt jest niezmienniczy. W pracy pokazujemy, jak wykorzystać znajomość takiego modelu wzrostu do wydobycia szczegółów dotyczących praw wzrostu lub warunków podczas powstawania struktury, badając wyłącznie jej ostateczną geometrię. Jest to szczególnie ważne w przypadku form geologicznych, które ewoluują w skali czasowej przekraczającej możliwości pomiarowe człowieka. Pokazujemy, że pojedyncza migawka geometrii wystarcza do odtworzenia historycznych natężeń przepływu w powstającej świecy krasowej lub do zidentyfikowania praw wzrostu sieci rzecznej.

Następnie skupiamy się na pętlach w sieciach fizycznych. Sieci z pętlami zostały zidentyfikowane jako bardziej odporne na uszkodzenia i są preferowane w ewolucji biologicznej. Jednak dynamika ich wzrostu pozostaje niejasna. W jaki sposób gałęzie w rosnącej sieci przyciągają się nawzajem i ponownie łączą, tworząc pętlę? Klasyczne modele sieci rosnących w odpowiedzi na gradient pola zewnętrznego wyjaśniają konkurencję, ekranowanie i odpychanie między gałęziami. Jednak w różnych procesach, od niestabilnych przepływów płynów po system kanałów meduz, pętle powstają nagle, gdy najdłuższa gałąź sięga do granicy układu i następuje przebicie. Badamy ten proces i wykazujemy, że gdy wzrost jest regulowany przez strumienie dyfuzyjne, ekranowanie i odpychanie zmieniają się w przyciąganie w momencie przebicia. Na koniec badamy morfogenezę konkretnej sieci z pętlami: sieci kanałów w układzie gastrowaskularnym meduzy Aurelia. Nasze obserwacje eksperymentalne sugerują, że kanały wyłaniają się w procesie samoorganizacji. Łączymy

ten proces z mechaniką meduz i stawiamy hipotezę, że kanały są kierowane przez pole naprężeń lub strumienie dyfuzyjne w tkance. Tworzymy model numeryczny rozwoju sieci kanałów i pokazujemy, że oba procesy mogą równie dobrze odtworzyć wzorce zaobserwowane w eksperymentach.

Słowa kluczowe: morfodynamika, formowanie wzorów, zagadnienie z ruchomą granicą, niestabilne procesy wzrostu, wzrost Laplace'a, sieci fizyczne

Systèmes morphodynamiques : des instabilités à la formation de réseaux

Résumé :

Les formes naturelles sont souvent considérées comme le résultat d'un processus d'optimisation ou comme étant prédéterminées, par exemple par un programme génétique. Cela néglige la question de savoir comment les formes apparaissent en premier lieu. Pour comprendre cela, nous devons examiner la dynamique de croissance sous-jacente. Nous étudions la relation entre les formes finales et les processus de croissance afin d'aborder le problème inverse : étant donné une forme, comment pouvons-nous déterminer les détails de son processus de croissance ou, plus largement, identifier le mécanisme fondamental à l'origine de son apparition ? Répondre à une telle question pourrait nous aider à reconstituer les informations environnementales à partir des formes géologiques ou à comprendre comment arrêter les processus pathologiques dans les systèmes biologiques.

Dans cette thèse, nous nous intéressons aux formes qui apparaissent sous forme d'instabilité à un front mobile. Les petites protubérances se développent ensuite en formes semblables à des doigts qui interagissent entre elles et peuvent former une structure en réseau. Les systèmes analysés vont des conduites de solution dans le calcaire aux réseaux fluviaux en passant par le réseau de canaux de la méduse Aurelia. Dans les deux premiers cas, des modèles de croissance peuvent être établis et résolus, par exemple en supposant que la forme étudiée est invariante. Nous montrons comment utiliser ces modèles de croissance pour extraire des détails sur les lois ou les conditions de croissance qui régissent l'émergence d'une structure, simplement en examinant sa géométrie finale. Cela est particulièrement important pour les formes géologiques qui évoluent à des échelles de temps dépassant les capacités de mesure humaines. Nous montrons qu'un seul instantané de la géométrie suffit pour reconstruire les débits historiques dans un conduit de solution émergent ou pour identifier les lois de croissance d'un réseau fluvial.

Ensuite, nous étudions les boucles dans les réseaux physiques. Il a été démontré que les réseaux en boucle sont plus résistants aux dommages et sont sélectionnés dans l'évolution biologique. Cependant, leur formation dynamique reste difficile à cerner. Comment les branches d'un réseau en croissance s'attirent-elles les unes les autres et se reconnectent-elles pour former une boucle ? Les modèles classiques de réseaux se développant en réponse au gradient d'un champ externe expliquent la compétition, le filtrage et la répulsion entre les branches. Pourtant, dans des processus remarquablement divers, allant des écoulements fluides instables au système de canaux des méduses, des boucles se forment soudainement près du point de rupture, lorsque la branche la plus longue atteint la limite du système. Nous étudions ce processus et démontrons que lorsque la croissance est régie par des flux

diffusifs, le filtrage et la répulsion se transforment en attraction près du point de rupture. Enfin, nous étudions la morphogenèse d'un réseau en boucle spécifique : le réseau de canaux gastrovasculaires de la méduse Aurelia. Nos observations expérimentales suggèrent que les canaux émergent de manière auto-organisée. Nous relions ce processus à la mécanique des méduses et émettons l'hypothèse que les canaux sont guidés par un champ de contrainte ou de diffusion dans les tissus. Nous construisons un modèle numérique du développement du réseau de canaux et montrons que les deux processus peuvent reproduire aussi bien les modèles observés dans les expériences.

Mots-clés : morphodynamique, formation de motifs, problème de frontière mobile, processus de croissance instables, croissance laplacienne, réseaux physiques

Acknowledgments

First of all, I would like to thank my wife, Natalia. Without you, none of this would have been possible. Thank you for your flexibility and patience while we jumped back and forth between Warsaw and Paris. Thank you for your companionship and constant support. Finally, thank you for being the best mother I could have imagined and for taking care of Emma, especially during those last intense days of my writing.

Piotr, thank you for being my supervisor for almost ten years. What started as a student-professor relationship evolved into an equal partnership and, I believe, a friendship. I will always be grateful for that. Thank you for sharing with me your way of treating natural systems as fascinating puzzles and your rigorous scientific approach to solve those. I owe much of my scientific development to your guidance.

Annemiek, you may not be my supervisor on paper, but you certainly provided essential guidance during this work. Thank you for inviting me to your lab, introducing me to the beautiful world of jellyfish, and showing how to work with living organisms, both practically and conceptually. Thank you for your enthusiasm and leadership in fostering collaborations - withouth your support, neither this cotutelle nor the "looping community" would exist.

Stéphane, thank you for your broad perspective and willingness to discuss any subject I brought to you. Your extensive knowledge and creative ideas were invaluable when it came to investigating topics for my thesis. Thank you also for your kind, relaxed spirit, and always positive attitude. You and Annemiek made me feel like part of the family in Paris.

I also express my sincere gratitude to all my "soft matter" colleagues at the Faculty of Physics UW: Maciej Lisicki, Rishabh Sharma, Tomek Szawełło, Antek Wrzos, Dawid Woś, Michał Dzikowski, Agnieszka Budek, Yiwei Cai, Jordan Orchard, Akash Unnikrishnan, Stanisław Rakowski, Radost Waszkiewicz, Rafał Błaszkiewicz, and Michał Czerepaniak. You have created an inspiring and vibrant community that I truly enjoyed being a part of.

The Laboratoire Matière et Systèmes Complexes was a similarly inspiring environment for me. The abundance of intriguing soft matter, biophysical, and pattern formation topics I encountered there will not cease to impress me. Special thanks go to Camille Le Scao, Sélène Jeammet, Martin Chaigne, Laureline Julien, Giulio Facchini, Thierry Savy, and Saatvik Potluri for making the time in the lab so enjoyable. I also thank Léna Zig for her tireless care of the jellyfish.

Throughout the thesis I also enjoyed many inspiring and fruitful discussions with various people, including Olivier Devauchelle, Predrag Popović, Tony Ladd, John Shaw, Hans Hermann, and Eleni Katifori. I am grateful to all of you for your time and for the insights you shared.

I am also grateful to all my colleagues from my Bachelor's and Master's studies with whom I shared my path during these past ten years at the University of Warsaw. Special thanks go to Stanisław Kurdziałek and Krzysztof Mękała. I would also like to thank the whole academic staff at the Faculty of Physics UW for providing an inspiring environment that challenged me to grow. Finally, I would like to thank the students with whom I had the pleasure of working, especially Błażej Rozwoda and Maciej Pawlus.

I would also like to thank all the people involved in the "looping community" – a project that started as a way of keeping contact between the Polish and French groups, but is still ongoing, with nearly 80 seminars and two conferences held to date. I especially thank the other coordinators of this project: Annemiek Cornelissen, John Shaw, Stéphane Douady, and Piotr Szymczak.

I would like to thank Michael Berhanu and Lucas Leclère for serving on my thesis advisory committee. Our annual meetings were instrumental in assessing my progress and determining the future direction of the project.

My fascination with physics began early in my school years. I would like to thank my physics teachers, Alicja Szymańska and Ewa Drozdowska, for inspiring me and investing extra time in my education. I thank my parents, Basia and Jarek, for their constant support and for giving me the freedom to develop my passions without any limits.

My gratitude extends to everyone who has supported me along the way and I apologize to anyone I unintentionally left out.

Publications comprising the Thesis

- S. Żukowski, S. Magni, F. Osselin, F. Dutka, M. Cooper, A. J. C. Ladd, and P. Szymczak, "Invariant Forms of Dissolution Fingers", Physical Review Letters, vol. 134, no. 9, p. 094101, Mar. 2025, doi: 10.1103/PhysRevLett.134.094101.
- S. Żukowski, P. Morawiecki, H. J. Seybold, and P. Szymczak, "Through history to growth dynamics: deciphering the evolution of spatial networks", Scientific Reports, vol. 12, no. 1, Art. no. 1, p. 20407, Nov. 2022, doi: 10.1038/s41598-022-24656-x.
- S. Żukowski, A. J. M. Cornelissen, F. Osselin, S. Douady, and P. Szymczak, "Breakthrough-induced loop formation in evolving transport networks", Proceedings of the National Academy of Sciences, vol. 121, no. 29, p. e2401200121, Jul. 2024, doi: 10.1073/pnas.2401200121.
- S. Song, S. Żukowski, C. Gambini, P. Dantan, B. Mauroy, S. Douady, A. J. M. Cornelissen, "Morphogenesis of the gastrovascular canal network in Aurelia jellyfish: Variability and possible mechanisms", Frontiers in Physics, vol. 10, p. 966327, 2023, doi: 10.3389/fphy.2022.966327.

The research was supported by the National Science Center (Poland) under research grant 2023/49/N/ST3/03502; by Labex Who Am I?, ANR-11-LABX-0071, the Université Paris Cité, Idex ANR-18-IDEX-0001 funded by the French Government through its Investments for the Future program; and by the Foundation for Polish Science under the START programme.

Contents

Chapter 1

Introduction

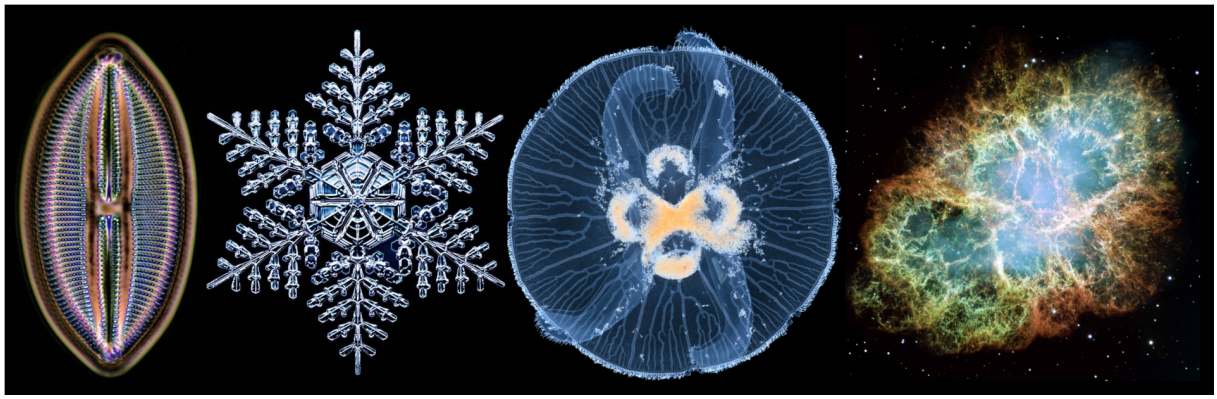

Figure 1.1 Patterns of nature. From left to right: the diatom *Lyrella hennedyi* [1], a snowflake [2], the jellyfish *Aurelia*, the Crab Nebula [3]

Nature strikes us with a plethora of patterns, shapes, forms, morphologies and geometries. They span across all scales – from micrometer diatoms to milimeter snowflakes to centimeter jellyfish to light years nebulas (Fig. 1.1). The beauty of them have inspired people to ponder for centuries. Where does the variety of forms come from? Despite the sheer diversity of systems, the forms also share certain similarities (Fig. 1.2). How is it possible that root systems are so similar to lightnings? Why are mineral dendrites similar to bacterial colonies? Why are we still unsure whether certain forms are purely geological or if living organisms played a role in their creation? This kind of questions have long motivated curiosity-driven science, and continue to do so today.

Natural shapes are often viewed as the result of an optimization process, or as being predetermined, for instance by a genetic program. This overlooks the problem of *how* shapes appear in the first place. To understand this, we must examine the underlying growth mechanism. *Morphodynamics* of natural systems – the link between their shape and growth dynamics – remain largely unexplored, but can provide valuable insights. For instance, understanding how geological forms such as river networks or solution pipes in

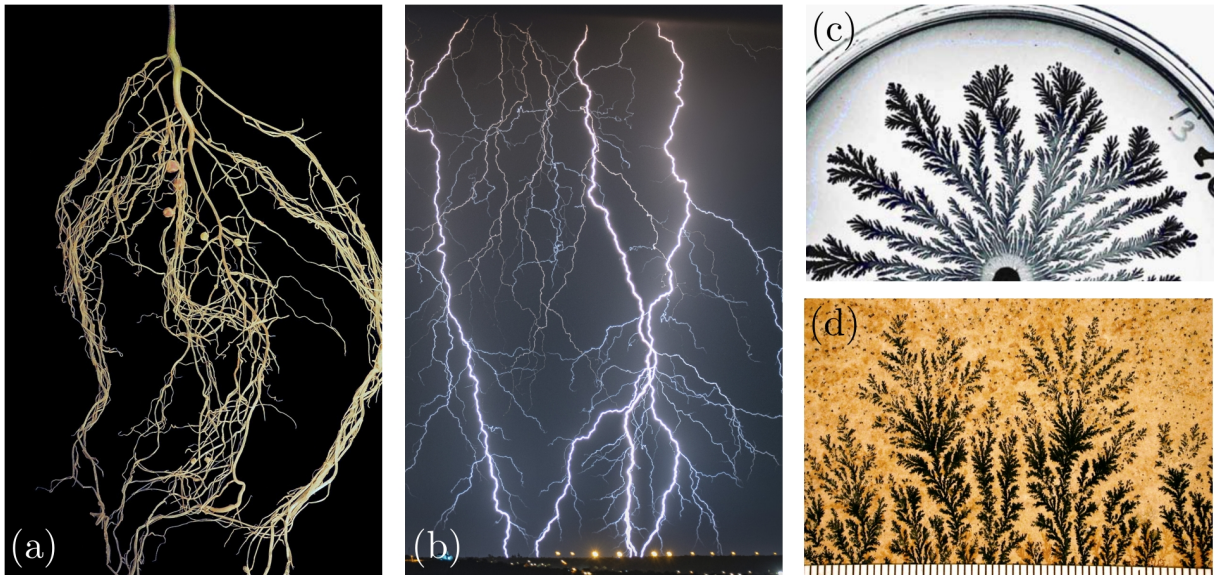

Figure 1.2 The resemblance of biological and physical patterns. (a) The root system of a black locust [4] (b) Lightnings [5] (c) A bacteria colony on a Petri dish [6] (d) The manganese oxide dendrites on a limestone bedding plane from Solnhofen, Germany [7]

limestone emerged provides a unique window into history. This knowledge can help us decipher the conditions under which these forms evolved and inform us about paleoclimate. On the other hand, studying patterns in living organisms, such as jellyfish, and understanding the development of biological structures, fine-tuned by millions of years of evolution, can help us engineer efficient structures on our own and have possible medical applications.

1.1 What is a morphodynamic system?

The word 'morphodynamic' comes from Greek roots: *morphē*, meaning 'form' or 'shape' and *dynamikos*, meaning 'powerful' or pertaining to power and force. Consequently, the term literally translates to the study of changing forms driven by powers or forces. In the scientific context, a morphodynamic system is one that dynamically adapts its morphology through response to a driving force. The term morphodynamics is used frequently in the field of geomorphology [8, 9], but terms like pattern formation or self-organization in physics [10–17] or morphogenesis in biology [13, 18–20] are similar in their attempt to explain emergent self-organized phenomena from local interactions which are relatively simple.

Morphodynamics require three components, sometimes referred to as the *morphodynamic trinity* [21, 22] (Fig. 1.3a). The first component is the *evolving geometry*: a full spatial and physical specification of the object of interest. The second component is the

driving field that can be computed at a given time based on system geometry and additional internal/external boundary conditions. In many cases, the system evolution is driven by physical fields such as flow, stress, or growth-factor concentration in the system. However, the driving force/field can be treated more abstractly. For instance, it could be a group of termites working together to build a mound. The final component is the *response* of the system to the driving field. This can be a mechanical response to shear stresses acting on the walls of an object due to fluid flow or a biological response translating incoming growth-factor gradients to local growth rate. The morphodynamic system evolves then in the following manner (Fig. 1.3a): (i) the geometry at a given time allows one to specify the driving field in the whole system; (ii) the system locally responds to the driving field; (iii) the geometry is updated which completes a feedback loop.

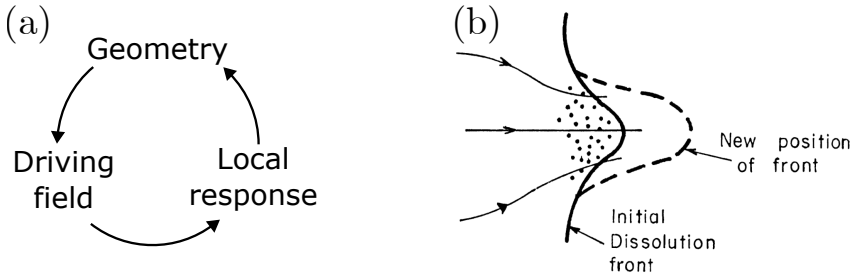

Figure 1.3 (a) Schematic of the morphodynamic trinity. (b) An example of unstable growth process – the reactive-infiltration instability [23]. The front between dissolved and undissolved parts of the system (solid vs dashed lines) grows rapidly due to a positive feedback loop that acts on the flow and concentration field (arrows). For details see text.

Morphodynamic processes are often unstable – due to a positive feedback loop small perturbations in the initial geometry tend to grow rapidly. A good example of unstable growth is the dissolution process induced by a flow of reactive fluid in a soluble medium, referred to in the literature as the *reactive-infiltration instability* (Fig. 1.3b). The reactant advected by flow is consumed as it dissolves the matrix and dissolution is usually concentrated at the interface between the dissolved and undissolved parts of the system. Even if the dissolution front is initially almost planar, flow naturally focuses on any small bumps. This brings more reactant there and locally increases dissolution. The bump is amplified, causing more flow focusing. Soon, finger-like structures emerge.

In this thesis, we focus on forms that initiate as an instability at a moving front. The small protrusions later develop into finger-like shapes that interact with each other and can form a network structure. The analyzed systems range from solution pipes in limestone to river networks to the canal network of *Aurelia* jellyfish. We study the relationship between final shapes and growth processes to address the inverse problem: Given a shape, how can we determine the details of its growth process or, more broadly, identify the fundamental mechanism behind its emergence?

1.2 Instabilities

In the following section, we provide a historical context for concepts used throughout the thesis, such as moving-boundary and Stefan problems, Darcy's law, the Hele-Shaw cell and viscous fingering. We also briefly summarize the study of well-known instabilities such as the Saffman-Taylor, the Rayleigh-Taylor, and the Mullins-Sekerka instabilities; the reactive inflitration instability; the reaction-diffusion model and the Turing instability.

We discuss invariant forms in nature – a concept used in Chapter 2 to link conditions during the emergence of solution pipes with their shape. Next, we derive a paradigm model for unstable growth processes – Laplacian growth. As most of the systems studied in the thesis – including dissolution and viscous fingers in a Hele-Shaw cell, river networks, and possibly jellyfish canals – are governed by diffusive fluxes it provides useful intuitions when studying these problems.

1.2.1 An overview

Although natural patterns have drawn attention and inspired people for ages, a quantitative, mathematically rigorous studies of them only began in the 19th and 20th centuries. A well studied branch of morphodynamic systems in physics are moving, or free, boundary problems. The history of moving-boundary problems began with the study of phase change. In 1831, Gabriel Lamé and Émile Clapeyron first mathematically tackled a free boundary problem by analyzing the solidification of a cooling sphere, introducing a problem where the domain itself evolves [24]. This was formalized by Jožef Stefan in 1889 in his study of freezing ice [25,26], and to this day, the canonical moving-boundary phase-change model is known as the *Stefan problem*.

At the same time, in 1883, the study of hydrodynamic instabilities began with Lord Rayleigh (John William Strutt), who used linear stability analysis to predict the unstable growth of disturbances at the interface of a heavier fluid on top of a lighter fluid in a gravitational field [27] (Fig. 1.5a). Geoffrey Ingram Taylor in 1950 generalized the analysis to arbitrary accelerations [28], establishing what is now known as the *Rayleigh-Taylor instability*.

In 1898, Henry Selby Hele-Shaw worked with a viscous fluid flowing between two closely-spaced parallel plates. Even though the flow between two plates was dominated by viscous forces, he showed that the in-plane, depth-averaged streamline patterns coincide with those of two-dimensional potential flow [29] (Fig. 1.4). Soon after, George Gabriel Stokes proved that the harmonic potential in this case is in fact pressure in the system [30].

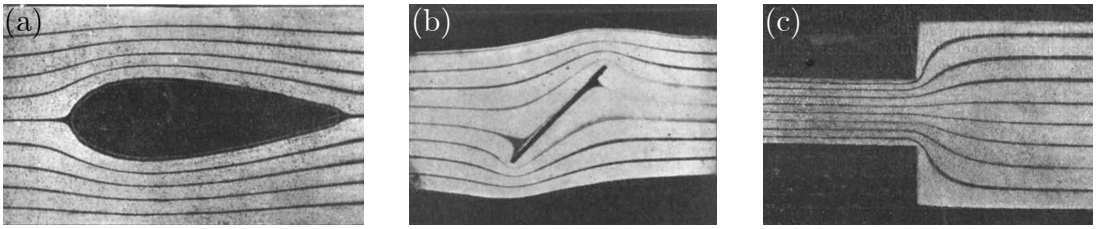

Figure 1.4 Streamlines of flow in a Hele-Shaw cell [29]. (a) "Round a section of the twin screw strut of one of Her Majesty's cruisers" (b) Past a plate inclined at 45° (c) In a channel with a variable width.

In parallel, the understanding of flow in porous media was developed. In 1856, Henry Darcy was tasked with designing and improving the water supply and filtration systems for the city of Dijon in France. He conducted numerous experiments on the flow of water through columns packed with sand, and described a linear relationship between volumetric flow rate with the hydraulic gradient [31]. Today, this relationship is known as *Darcy's law*. The concept was later generalized by Morris Muskat in the context of petroleum reservoir engineering. He explicitly separated the fluid properties from the rock properties in the linear relationship and developed the governing equations for porous media flow. He also studied a problem of evolution of the interface between two fluids [32]. Later in 1952, Hill experimentally studied the displacement of sugar liquors by water from columns of granular bone charcoal in the process of refining raw sugar [33]. He was the first to systematically study and quantify the highly ramified, finger-like invasion patterns, when a less viscous fluid is injected in a more viscous fluid (Fig. 1.5b). At the time he called it channeling, but nowadays it is rather known as *viscous fingering*.

Real interest in viscous fingering did not arise until 1958, when Philip Saffman and Geoffrey Ingram Taylor systematically studied this instability [35] (Fig. 1.5c). They demonstrated the analogy between Hele-Shaw flow and flow through two-dimensional porous media, analyzed the instability using linear stability analysis, and derived the shape of a viscous finger in a channel. The results of their works were so fundamental that nowadays this phenomenon is known as the *Saffman–Taylor instability*. An analogous linear stability framework for diffusion/heat-flow controlled moving boundaries was developed for solidification by William Wilson Mullins and Robert Floyd Sekerka in 1963-1964. They showed that a solid–liquid interface governed by diffusive heat and/or solute transport can become morphologically unstable, leading to the formation of complex patterns like dendrites in what is now known as the *Mullins–Sekerka instability* [39, 40] (Fig. 1.5d).

The discovery of viscous fingering helped the petroleum industry understand why oil recovery by waterflooding – injecting water to push oil out – was often far lower than predicted and how to improve it by damping the instability. To increase near-

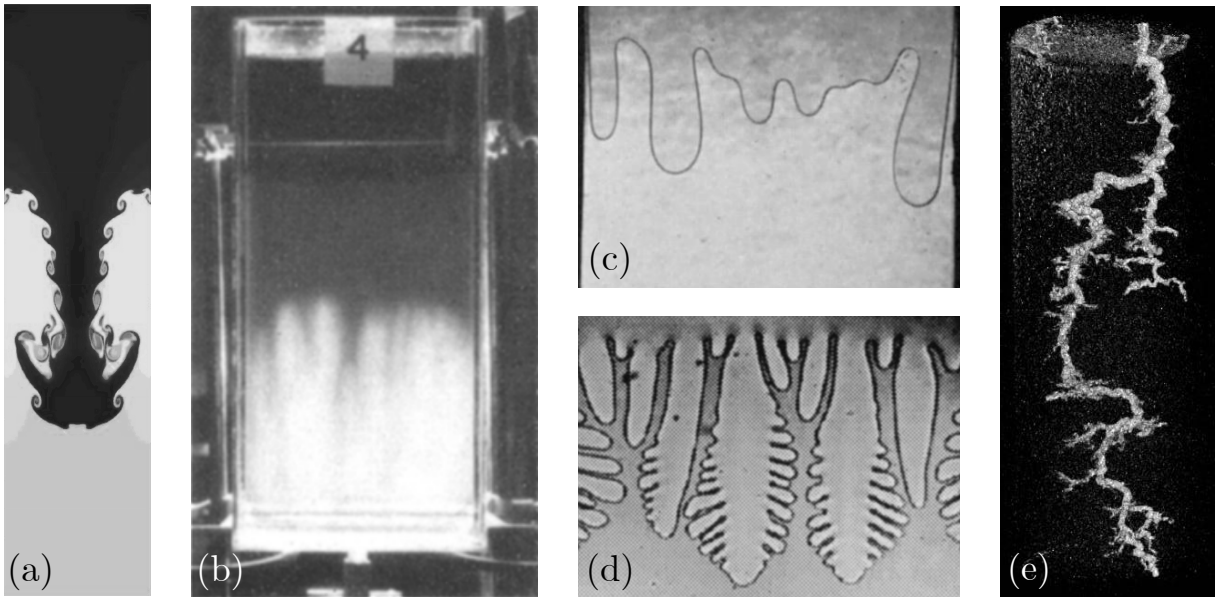

Figure 1.5 **Instabilities.** (a) The Rayleigh-Taylor instability simulation (adapted from [34]). Note the Kelvin-Helmholtz instability at the sides of the finger, where two fluids are in shear. (b) Channeling observed by Hill in his experiment of flow in columns packedwith granular material [33]. (c) The Saffman-Taylor instability (air injected into glycerin in a Hele-Shaw cell [35]). (d) The Mullins-Sekerka instability appearing in alloy solidification [36]. (d) A wormhole resulting from HCl injection into a limestone core [37, 38].

wellbore permeability, engineers also developed matrix acidizing, in which acid is injected to dissolve reactive minerals and open flow pathways. In 1959, Rowan reported that the permeability gain depends non-monotonically on the acid injection rate around a wellbore [41]. The optimal flow rate producing the largest increase in permeability for a given amount of acid corresponds to the spontaneous development of highly localized flow paths called *wormholes* (Fig. 1.5e). More detailed studies of the *reactive-infiltration instability* followed in the '80s [23, 42–44]. The same instability occurs when rainwater acidified by dissolved carbon dioxide infiltrates limestone. Dissolution focuses flow into channels, forming cave conduits and solution pipes [45, 46].

The idea that complex patterns can emerge from systems governed solely by physical laws has gradually made its way into the field of biology in 20th century. In 1917, D'Arcy Thompson argued in his work "On Growth and Form" that biological morphology is not only programmed by genes as an effect of natural selection, but is also largely dictated by physical and mechanical constraints [13]. He provided mathematical descriptions of biological forms and compared them to physical systems. A major turning point came in 1952 with Alan Turing's paper "The Chemical Basis of Morphogenesis" [18]. He introduced a mathematical model of diffusing and reacting substances, morphogens. He showed that, when their diffusion rates are sufficiently different, a uniform state can become unstable to

spatial perturbations, generating stationary patterns. Turing demonstrated that periodic patterns in biology can spontaneously emerge from instabilities (Fig. 1.6 and Fig. 1.7). These patterns are highly sensitive to initial conditions and variable. Thus, variability in the pattern can be interpreted as a trace of instability. Turing's reaction-diffusion model was popularized in 1972, when Alfred Gierer and Hans Meinhardt introduced biologically relevant non-linear form of kinetic functions (rate of chemical reactions) [47]. The work established the principle of *local activation, long-range inhibition* as the key concept in the study of biological pattern formation.

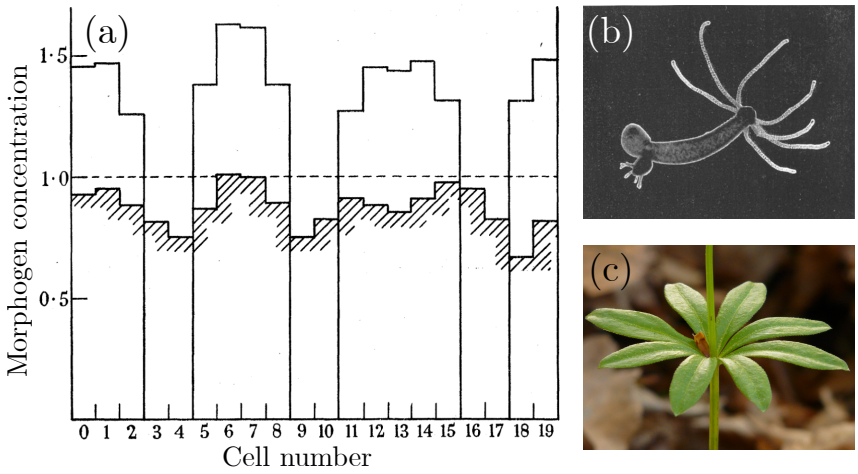

Figure 1.6 The Turing instability. (a) Results of Alan Turing showing that an almost homogeneous initial distribution of morphogens (horizontal dashed line) may develop a signal of specified wavelength (hashed line – incipient, solid line – final pattern) [18]. Turing considered reacting and diffusing chemicals on a ring of cells and hypothesized that the maxima of morphogen could determine positioning of: (b) *Hydra* tentacles [48] or (c) woodruff leaves [49].

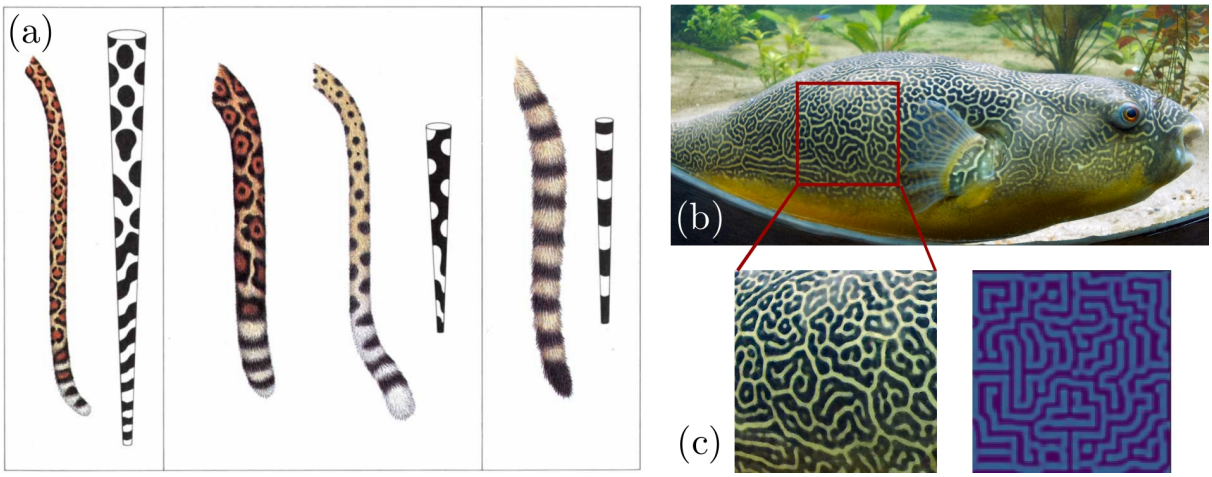

Figure 1.7 The reaction-diffusion patterns in biology. (a) Tails of a leopard, jaguar, cheetah and genet, followingly, along with the patterns from a reaction-diffusion model solved in the geometry of a narrowing cylinder [50]. (b) Giant Freshwater Puffer fish with elaborate skin patterns [51]. (c) A zoom in along with the result of a computer simulation of a reaction-diffusion model (the Gray-Scott model [52]).

Invariant forms

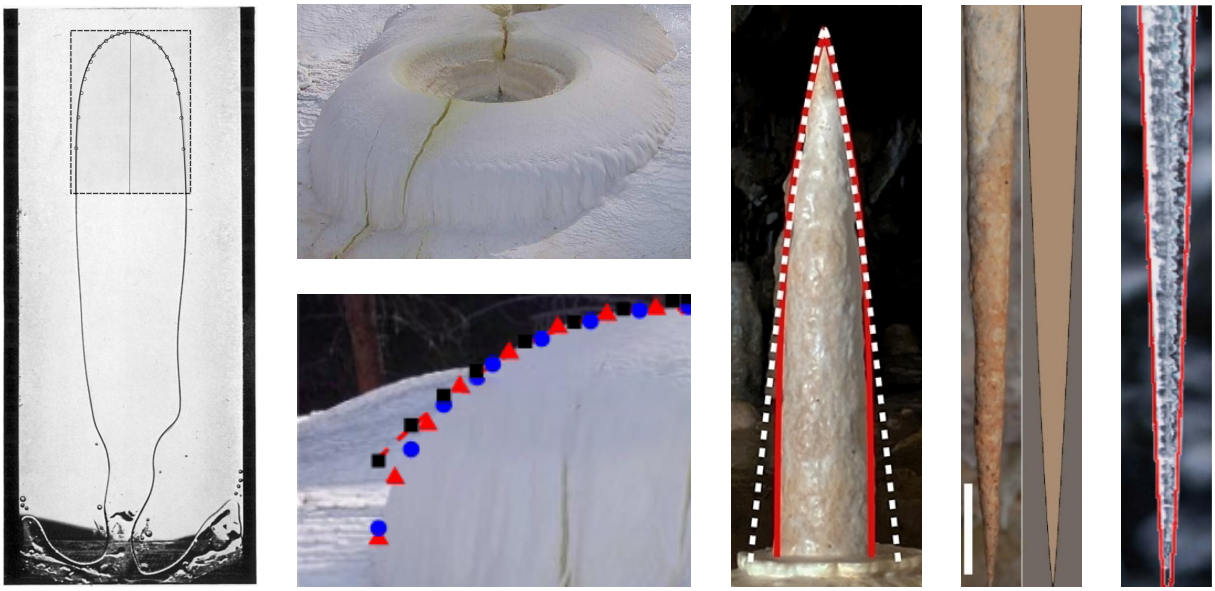

Figure 1.8 **Invariant forms in lab experiments and nature.** (a) The Saffman-Taylor finger in a channel (air advancing into glycerine). Inset (marked with a dashed rectangle) shows a tip with overlayed points indicating theoretical shape [35]. (b)) *top*: A travertine dome, *bottom*: A side-view with theoretical prediction marked with blue dots. Adapted from Ref. [53]. (c) A stalagmite, red line indicates theoretical shape developed in Ref. [54]. (d) *left*: A stalactite from Kartchner Caverns (Benson, AZ), *right*: theoretical prediction [55]. (e) An icicle, red line indicates theoretical prediction of the shape [56].

After the initial chaotic phase, the instabilities in many cases simplify in the long-time limit. Invariant growth forms appear and advance into the system without changing shape. One example is already mentioned Saffman-Taylor finger (Fig. 1.8a), which emerges as an asymptotic solution in viscous fingering [35] or the corresponding solution in solidification – the Ivantsov paraboloid [57]. Other examples include the regular shapes of flames [58] or crystals growing in a capillary [59]. The concept of invariant shapes can be also found in natural systems and was used to describe karst pinnacles [60] and travertine cones [53] (Fig. 1.8b), stalagmites [54] (Fig. 1.8c) and stalactites [55] (Fig. 1.8d), and icicles [56, 61] (Fig. 1.8e). In Chapter 2, we apply the concept of invariant growth to derive a formula for the ideal form of dissolution finger. This formula can be used to reconstruct historical flow rates in an emerging solution pipe.

1.2.2 Laplacian growth

The unstable growth processes are usually modeled as an invasion of one phase into another. In a classical Stefan problem, the boundary – the interface between two phases – moves due to the external forcing, such as the pressure gradient between the inlet and outlet of the system. Important parameters in such models are the mobilities of the two phases, e.g. hydraulic permeabilities for pressure-driven growth. Whenever the mobility of the invading phase (λ_1) is larger than the mobility of the displaced phase (λ_2) the flux concentrates on small protrusions of the interface. Without a regularization mechanism any initial geometry leads to the generation of finite-time cusps [62, 63]. The infinite growth of short wavelengths at the boundary is sometimes referred to as the *ultraviolet catastrophe*, in reference to the classical black-body problem, in which the energy emitted by the body diverges for the shortest wavelengths. However, in physical cases of boundary growth, the instability is regularized by effects such as surface tension. In such a case, linear stability analysis can be used to obtain a dispersion relation and determine the most unstable wavelength. This determines the characteristic spacing and size of the fingers in the system [35, 39, 64]. Additional effects, such as tip splitting, can give rise to a highly ramified, hierarchical tree-like structure.

A paradigm for such growth processes is *Laplacian growth* (Fig. 1.9), in which evolution is driven by a harmonic field, ϕ, obeying the Laplace equation. Essentially, the Laplace equation may be derived from Fick's law, which states that the flux is proportional to the gradient of the field:

$$\boldsymbol{J} = -\lambda \boldsymbol{\nabla} \phi \,, \tag{1.1}$$

and the continuity equation:

$$\boldsymbol{\nabla} \cdot \boldsymbol{J} = -\frac{\partial \phi}{\partial t} \,. \tag{1.2}$$

The combination of the two results in a diffusion equation:

$$\lambda \Delta \phi = \frac{\partial \phi}{\partial t} \,. \tag{1.3}$$

The boundary between two phases moves with a velocity proportional to the flux of the field: $\boldsymbol{v} \sim -\lambda \boldsymbol{\nabla} \phi$. Assuming that the timescales of the boundary evolution are much smaller than the timescales of field relaxation, the time derivative in the diffusion equation can be neglected.

The above results in the Laplace equation both in the invading ($\mathcal{D}_1$) and the displaced phase ($\mathcal{D}_2$):

$$\Delta \phi_1(\boldsymbol{x}) = 0 \quad \boldsymbol{x} \in \mathcal{D}_1 \qquad \text{and} \qquad \Delta \phi_2(\boldsymbol{x}) = 0 \quad \boldsymbol{x} \in \mathcal{D}_2 \,. \tag{1.4}$$

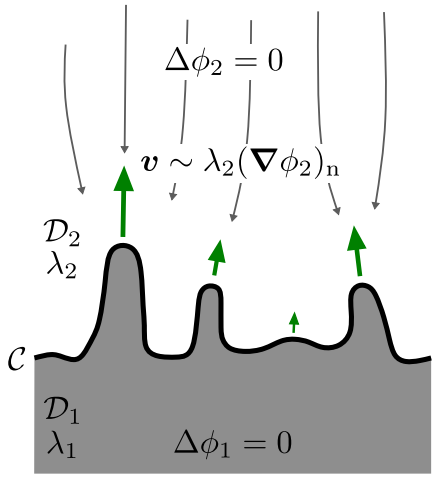

Figure 1.9 Schematic of Laplacian growth. There are two phases: the invading phase ($\mathcal{D}_1$) of mobility λ_1 and the displaced phase ($\mathcal{D}_2$) of mobility λ_2. The interface between them, $\mathcal{C}$, moves with velocity $\boldsymbol{v}$ (green arrows) proportional to the incoming flux of the field $\nabla\phi$ (thin gray arrows). The field obeys the Laplace equation, $\Delta\phi = 0$, in both phases.

These equations are supplemented with the continuity condition for the field and its flux at the interface ($\mathcal{C}$):

$$\begin{aligned} \phi_1(\boldsymbol{x}) &= \phi_2(\boldsymbol{x}) \qquad && \boldsymbol{x} \in \mathcal{C}\,, \\ \lambda_1(\boldsymbol{\nabla}\phi_1(\boldsymbol{x}))_\mathrm{n} &= \lambda_2(\boldsymbol{\nabla}\phi_2(\boldsymbol{x}))_\mathrm{n} \qquad && \boldsymbol{x} \in \mathcal{C}\,, \end{aligned} \tag{1.5}$$

where n denotes the normal to the interface. Additional boundary conditions are imposed on the boundaries of the system, depending on the problem at hand.

Both the continuity equation and Fick's law are ubiquitous in the study of transport phenomena, which makes the Laplacian growth model relevant across many settings. Although the Laplace equation is linear, time-dependent boundary conditions introduce nonlinearity to the Laplacian growth problem. This yields a rich spectrum of complex phenomena and morphologies. Growth dynamics of a similar type underlies a wide range of different processes, including formation of the lungs [65–67], bacterial colony growth [68], cave formation [45, 69], metallic dendrite formation in electrochemical deposition [70, 71], dielectric breakdown [72], discharge trees [73], combustion fingers [74], tributary and distributary channel formation in river networks [75–77], dendritic patterns in superconducting films [78], leaf venation [79], or sprouting angiogenesis [80–82].

1.3 Network formation

In the following section, we summarize different approaches to study network geometries and their formation. We focus on physical networks embedded in space and describe the processes responsible for their morphodynamics: remodeling and tip-growth. We focus on Laplacian networks that extend at the tips with velocity proportional to the gradient of harmonic field. In Chapter 3, we use thic concept to model river networks and decipher their growth laws.

We describe how common assumptions lead to branch screening and repulsion in Laplacian networks, making loop formation elusive. In the thesis, we try to fill this gap and identify the fundamental mechanism behind the dynamical emergence of loops in tip-growing networks. In Chapter 4, we demonstrate the transition from repulsion to attraction between fingers when the longest finger reaches the boundary of the system. In Chapter 6, we simulate the growth of the jellyfish canal network in response to diffusive fluxes, but also stress field induced by swimming contractions.

1.3.1 An overview

The modern boom in network science came after the work of Duncan J. Watts and Steven Strogatz on small-world networks and Albert-László Barabási and Réka Albert on scale-free networks, such as the World Wide Web or network of scientific articles connected by citations [83, 84]. Models such as the *Watts–Strogatz model* or the *Barabási–Albert model* explained emergent properties of network graphs. Treating networks as a set of vertices connected by links became also useful in the context of engineered networks, such as power grids, where networks indeed develop by attaching new vertices to the network [85]. However, most natural, *physical* networks that are embeded in space show very different properties. This might derive from their morphodynamics, as they emerge in the process of *tip growth* or *adaptation* (remodeling).

Remodeling vs tip growth

A good illustration of the tip growth and the adaptation processes is the development of the vascular networks, where they both take place. During vasculogenesis, precursor cells assemble to form an initial network of capillaries known as the primitive capillary plexus [86], which is then remodeled by blood flow (Fig. 1.10a). This results in the emergence of a hierarchical structure of arteries and veins. In contrast, in sprouting angiogenesis, new vessels branch out from the pre-existing ones [86]. These new vessels

grow, guided by tip cells (Fig. 1.10b) that respond to the gradients of vascular endothelial growth factor (VEGF), among others.

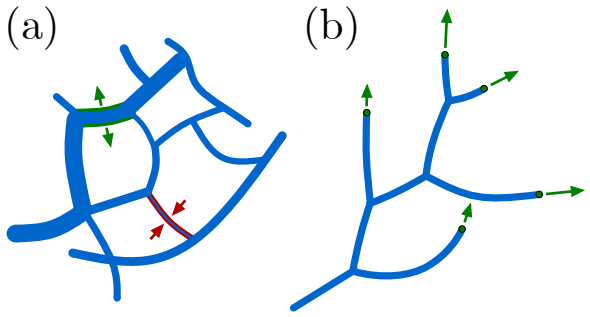

Figure 1.10 Schematic of two key morphodynamic processes responsible for network morphogenesis. (a) Remodeling – network branches shrink (red arrows) or widen (green arrows). (b) Tip growth – network branches extend at the tips (green arrows). The two processes can change the topology of the network: remodeling can break loops, while tip growth can create loops.

The class of adaptive networks also includes physical systems such as the pore space evolving during reactive infiltration of rocks [87], channel networks in river deltas [88] or network of *Physarum polycephalum* [89]. These networks are modeled by adapting the links between the nodes of the initial network, reinforcing some of them and trimming others. Adapting the links can follow from some local rules, but it can be also treated as optimization of a global property of the network (i.e., transport through it or energy dissipation) [85, 88, 90–94].

In the case of tip growth, network development involves a dynamic system of branches that extend at the tips and sometimes bifurcate into new branches or reconnect to already existing parts of the network (Fig. 1.10b). One way to describe such a process is to coarsen the microscopic features responsible for branch extension and bifurcation, and adopt a simple set of rules governing tip evolution. A convenient minimal description treats tips as stochastic walkers that can branch and annihilate upon encounter, leading to models in the branching annihilating random walk (BARW) class, introduced by Maury Bramson and Lawrence Gray in 1985 [95] and later adapted to the context of spatial network evolution by Edouard Hannezo et al. [96]. Additionally, elements such as global guidance or local self-avoidance of neighboring branch segments can be included. These models have been proven to successfully reproduce the statistical properties of branched networks in many real-world examples [96–99].

Yet, in many cases in nature the network is not only guided by some external forcing/field, but also impacts it exactly like a lightning rod impacts the electric field around it. The field and the network co-evolve in time, since as the network grows, it continuously

modifies the boundary conditions that determine the field. Growing parts of the structure compete for the available flux of the field, effectively interacting with each other. This description is derived from a relatively well-studied branch of physics – unstable growth processes (Section 1.2.2).

In this approach, a more detailed picture of the evolving network emerges: tips move with different velocities depending on the flux of the field reaching them; bifurcations can occur based on some deterministic criteria; after splitting, branches often maintain characteristic angles, because the tips follow the gradient at each moment of the evolution. Such an approach has been applied to model growth of river networks [75, 100–103], river deltas [76], viscous fingers [104], discharge trees [73] or coral growth [105], leading to network geometries qualitatively and quantitatively similar to those observed in nature. For instance, the mean branching angle in the case of river networks is equal to 72° and matches the analytical predictions [75].

Branching and looping networks

An important characteristic of a network is its topology – networks can take the form of either branched, tree-like structure (Fig. 1.11a) or looping pattern (Fig. 1.11b). The latter are more robust against damage [93, 106], hence are thought to be favored by biological evolution. Paleobiological records show that the leaf venation in ancestral plants is branched, but highly reticulated in more evolutionary recent ones [107–109].

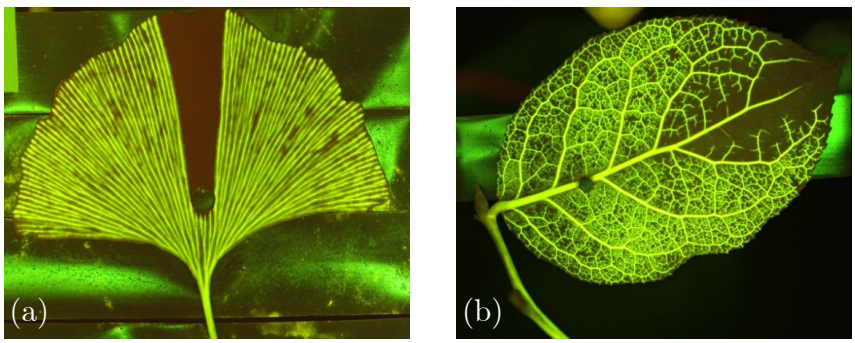

Figure 1.11 Fluorescent dye visualization of transport in damaged leaves [93]. (a) In the ginkgo branching network, damage cuts off an entire section of the leaf from nutrients and water supply. (b) The lemon looping network continues to supply to almost entire leaf even after damage.

The question of why looping networks might have been selected by evolution and what quantity, if any, they optimize, has been extensively studied in the domain of adaptive networks [85, 88, 90–94]. In the case of tip-growing networks a natural candidate for an underlying driving field leading to reconnections and loop creation is a tensorial stress

field [110, 111]. However, it is less clear how branches in the network driven by a scalar field interact to form a looping network. As we describe in the following section, classical models of networks growing in response to the gradient of an external field explain rather the competition, screening, and repulsion between branches.

1.3.2 Laplacian networks

In moving-boundary problems, initial instabilities at the front grow and develop into finger-like shapes that interact and can form a network. Eventually, the widths of the fingers become much smaller than the distances between them. The flux of the field focuses at the tips, rendering them the most intense growth zones. Consequently, instead of solving a full moving-boundary problem, it is convenient to assume that an evolving network consists of branches that can only extend at the tips. By analogy with Laplacian growth in moving-boundary problems, the framework of *Laplacian networks* can be defined with similar evolution rules. The growth velocity is related to the flux of the field at the tips. A common extension of the linear model assumes a power-law relation between the flux into the tip and the growth velocity, $v \sim |\boldsymbol{\nabla}\phi|^{\eta}$ [72, 112] (studied in detail in Chapter 3). Following the *principle of local symmetry*, applicable in Laplacian networks [101], but also in stress driven problems [113, 114], the branches extend in the direction from which most flux of the field is coming.

There are two main processes responsible for pattern formation in these systems: (i) *tip splitting*, when the branch bifurcates, giving rise to a pair of daughter branches, and (ii) *competition* between the nearby branches mediated by the harmonic field, which results in an increase in the growth rate of the longer branches and suppression of the growth of the shorter ones. The interplay of these two processes leads to the appearance of a highly ramified hierarchical network structure.

In the full moving-boundary problem tip splitting is a result of the inherent instability at the tip, such as in Fig. 1.2c-d. When modeling extension of the branches only, bifurcation is no more an intrinsic part of the dynamics [115] and needs to be re-introduced by hand, based on certain criteria. Different splitting rules can be found in the literature: the velocity criterion [35, 104] or the bimodality criterion [100, 105], among others. The first comes from a close study of tip splitting events in the full moving-boundary problem. The instability wavelength decreases as the front propagation velocity increases [14, 35] and at a critical velocity it becomes so small that it fits within the tip width, resulting in a bifurcation. The second criterion is linked to the appearance of two maxima of the flux in the neighborhood of the tip. Other works consider also stochastic growth and

bifurcations [112].

The strong competition between the branches in Laplacian networks is a result of a widely used simplification – the field drop inside the invading phase is neglected, and the Laplace equation is solved only in the displaced phase with a constant value of the field directly on the branches of the network. The Dirichlet boundary condition on the fingers results in: (i) two neighboring fingers growing away from each other (Fig. 1.12a); (ii) the long fingers screening the shorter ones and hindering their growth (Fig. 1.12b). Consequently, reconnections and loop creation is usually not obtained in this model [14, 17, 116].

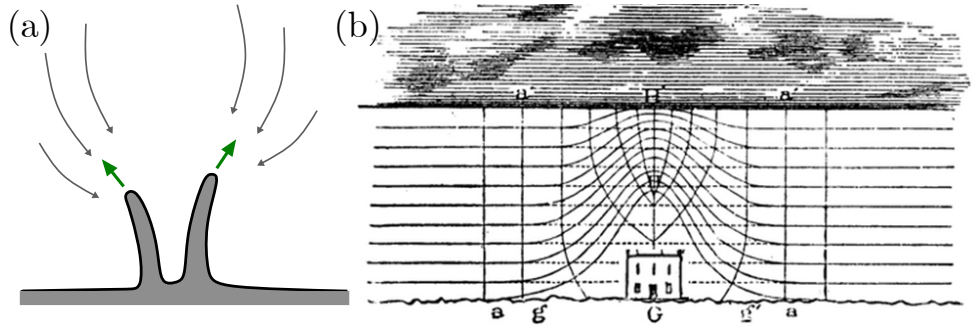

Figure 1.12 The repulsion and screening mediated by harmonic field. (a) Two adjacent fingers receive more flux from outside and effectively repel each other. (b) A lightning rod effect [117] – a long finger screens (shadows) its neighborhood and hinders growth of shorter fingers.

The effective repulsion between the fingers arises from the fact that they grow in the direction from which most flux of the field is coming. Each finger absorbs the flux of the field, and influences the field in the neighborhood. When placed close together, the fingers receive more flux from outside and they start to effectively repel each other. It has been shown that two diverging fingers stabilize at an opening angle of $\pi/5 = 36°$ in a half-plane or $2\pi/5 = 72°$ if they stem from a single mother branch and create a bifurcation [75, 100, 103, 118, 119]. Interestingly, following optimal local rules might not lead to a globally optimal structure. Although the tips individually maximize the incoming flux at each moment, the resulting 72° angle is not the most optimal. The bifurcation angle that, as a structure, maximizes the flux into the tips is slightly wider, around 78.5° [103].

A single long branch in the system acts as a lightning rod, wrapping the isolines of the field around it (Fig. 1.13b). For an absorbing needle of length L, protruding from the X-axis in a two-dimensional system with $(\boldsymbol{\nabla}\phi)_y = -1$ at infinity, the solution to the Laplace equation in the real plane can be obtained with complex analysis and is related to the imaginary part of the complex potential $\Phi(z) = \sqrt{z^2 + L^2}$: $\phi(x, y) = \Im(\Phi(z =$

$x + iy$)). Far from the finger, it introduces a dipole correction to the unperturbed field: $\phi_{\text{corr}} \sim L^2/2r$, and a $1/r^2$ correction to the gradient, where $r = \sqrt{x^2 + y^2}$. Technically the $1/r^2$ term is long-range and never vanishes completely. However, it plays a major role within distances comparable to the size of the finger. This suggests that a typical distance over which fingers can interact in an unbounded domain is of the same order as their size.

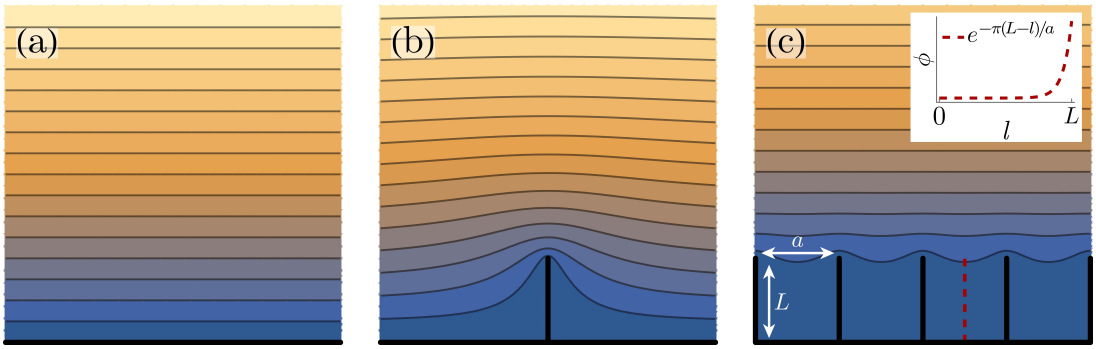

Figure 1.13 Solutions of the Laplace equation in a half-plane. (a) Unperturbed field: $\Phi(z) = z$ (b) Field around a needle: $\Phi(z) = \sqrt{z^2 + L^2}$ (c) The solution around a periodic array of needles of lengths L and a separation of a. The inset shows exponential screening near the tip of a shorter finger (length l), placed between two longer fingers (along the red dashed line).

The situation is different in a bounded domain, such as a channel, or when studying a shorter finger of length l, between two longer fingers of length L at a distance a. In this case, the field (and the gradient) near the tip of the shorter finger obeys: $\phi \sim e^{-\pi(L-l)/a}$ [120–122]. The finger is exponentially screened. Whenever it loses the competition, even slightly, it quickly slows down and falls behind the other, still-growing tips. Soon, the screened finger stops growing entirely and 'dies'.

Treating the moving boundary as an isoline of the field is equivalent to taking the limit of the mobility ratio to infinity ($M = \lambda_1/\lambda_2 \to \infty$). In the case of a lightning rod, the mobilities correspond to the conductivity of the rod and the surrounding air. A lightning rod with high conductivity can be safely assumed to hold ground potential along its entire length (Fig. 1.14a). However, a rod with lower conductivity would experience a potential drop along its length and have less impact on the surrounding field. Therefore, taking into account a finite mobility ratio reduces screening and effective repulsion in the system (Fig. 1.14b). The field gradients resulting from the potential drop along the fingers greatly impact the evolution of the system. The shorter fingers can still grow, but also receive some flux of the field from the longer fingers. This can be seen in the asymmetry of the isolines around the shorter finger tip, which are more concentrated on the side closer to the longer finger (Fig. 1.14b), indicating an effective attraction. This can lead to reconnections and loop creation within specific ranges of mobility and finger

length ratios [73, 123].

Yet, loop formation in general cases, for instance for high mobility ratio, remains elusive. In Chapter 4, we address this issue and demonstrate the transition from repulsion to attraction between fingers when the longest finger reaches the boundary of the system. In Chapters 5 and 6, we study a specific looping network – the gastrovascular canal network of *Aurelia* jellyfish – and attempt to determine the mechanisms responsible for its morphogenesis, and formation of loops in particular.

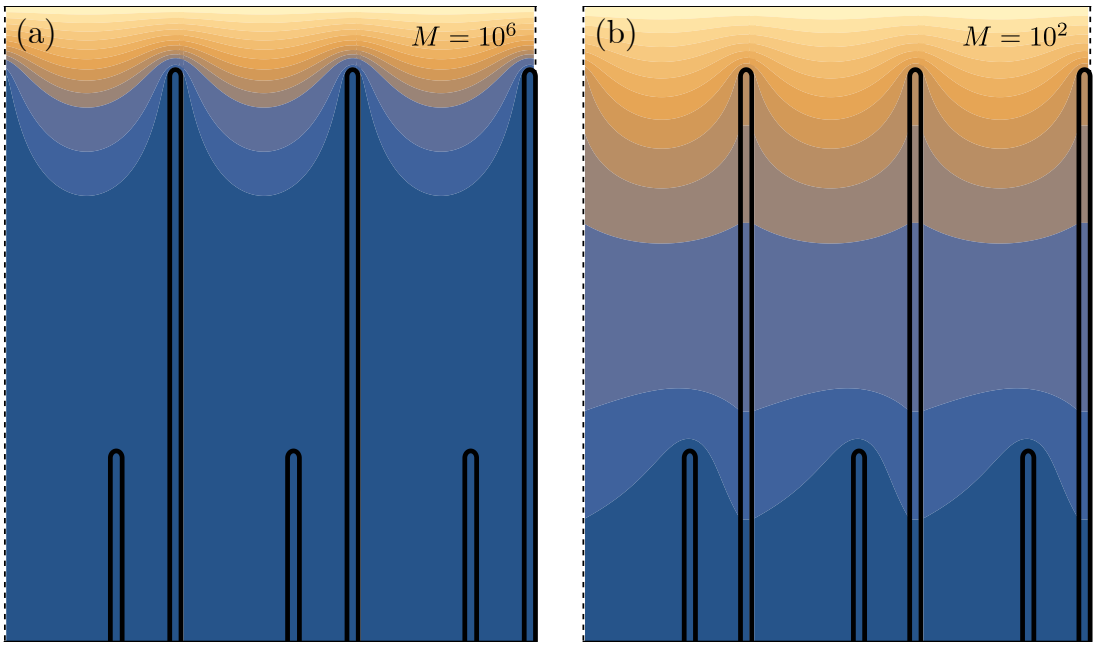

Figure 1.14 Numerical solutions of the Laplace equation around fingers with finite mobility ratio, $M = \lambda_1/\lambda_2$**.** The short and long fingers (black contours) are placed periodically in a strip with $\phi = 0$ at the bottom and $\phi = 1$ at the top. The mobility inside the fingers is higher than the mobility outside. (a) For high mobility ratio ($M = 10^6$), we recover the results for the needles with Dirichlet boundary condition (constant field) on them. The longer fingers act as lightning rods and exponentially screen the shorter ones. (b) For low mobility ratio ($M = 10^2$), the isolines penetrate the fingers. The shorter fingers receive some flux and can be attracted to the longer ones.

1.4 Theoretical and experimental approaches

In the following section, we provide an overview of the methods and systems considered in this thesis. First, we describe a numerical approach to network growth problem. In Chapter 3, we use this approach to simulate the evolution of river networks and extract their growth laws. In Chapter 4, we simulate loop formation near breakthrough and in Chapter 6, we adapt this model to simulate the jellyfish canal network growing in response to diffusive fluxes or a stress field.

Next, we describe the classical Hele-Shaw cell and its modified version with a soluble bottom. The former is used in Chapter 4 to study loop formation near breakthrough in viscous fingering. The latter is used in Chapter 2 to study invariant forms of dissolution fingers and in Chapter 4 to demonstrate loop formation in the case of low mobility ratio.

Lastly, we focus on a specific biological looping network: the gastrovascular canal network in jellyfish. First, we thoroughly describe this fascinating organism and explain its importance from evolutionary and developmental point of view. Next, we analyze canal networks in the Discomedusae and describe their similarities with patterns produced by physical growth processes. Finally, we turn our attention to the *Aurelia* jellyfish and its canal network – the subject of the thesis, whose morphogenesis we try to understand.

1.4.1 Network growth simulations

The growth of Laplacian networks can be studied using the *thin finger model*. This model approximates the branches of a network growing in a plane as thin, one-dimensional lines extending in length only [119, 120, 124]. Considering two-dimensional systems and thin needles simplifies the problem and allows the use of complex analysis and conformal mappings to study it. As noted by Peterson [124], studying only branch extension eliminates the problem of short wavelengths growing infinitely without introducing a regularization mechanism. This model has been used for the analysis of finger growth in 2D systems in both the Laplacian [119, 120, 125, 126] and Poissonian fields [77, 127, 128]. The latter appears if the continuity equation, Eq. (1.2), includes a source term on the right hand side.

For an absorbing finger, the field gradient at the tip becomes singular, diverging like $r^{-1/2}$ in the vicinity of the tip. Hence, the growth rules have to be carefuly defined. In polar coordinates (where the direction of the tangent to the finger at the tip sets $\theta = 0$)

the field near the tip can be expanded [129, 130]:

$$\phi(r,\theta) = a_1 r^{1/2}\cos\frac{\theta}{2} + a_2 r\sin\theta + a_3 r^{3/2}\cos\frac{3\theta}{2} + \mathcal{O}\left(r^2\right), \tag{1.6}$$

where the coefficients a_i depend on the boundary conditions far from the finger tip. In the simulations of network growth, we solve the Laplace (or Poisson) equation for the field with the finite element method, and then integrate the field over a circular contour of radius r_0 around the tips to obtain the a_i coefficients:

$$a_1 = \frac{1}{\pi r_0^{1/2}}\int_{-\pi}^{\pi}\phi(r_0,\theta)\cos\frac{\theta}{2}\mathrm{d}\theta\,, \tag{1.7}$$

$$a_2 = \frac{1}{\pi r_0}\int_{-\pi}^{\pi}\phi(r_0,\theta)\sin\theta\mathrm{d}\theta\,, \tag{1.8}$$

$$a_3 = \frac{1}{\pi r_0^{3/2}}\int_{-\pi}^{\pi}\phi(r_0,\theta)\cos\frac{3\theta}{2}\mathrm{d}\theta\,. \tag{1.9}$$

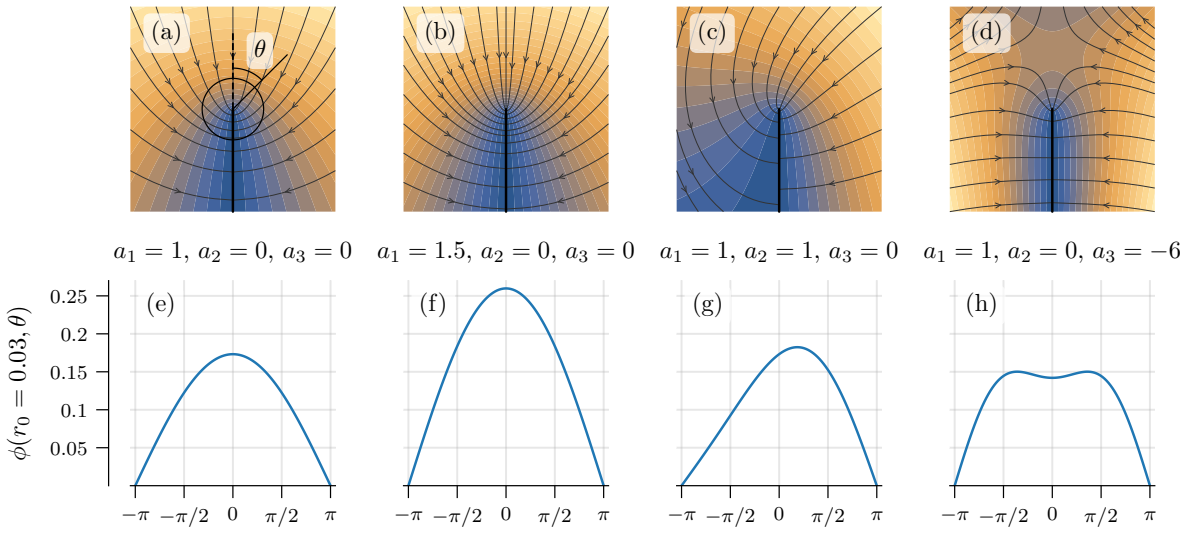

Figure 1.15 Impact of the a_1, a_2, a_3 coefficients on the field around the finger (after Ref. [77, 101]). (a-d) Field around the finger tip (indicated by a black line). Gray arrows follow the field lines. (e-h) Profiles of the field along a small circle around the tip (black circle in (a)).

Each of the leading coefficients a_i has a clear physical interpretation: a_1 is linked to the total flux over a small circular contour around the tip (Fig. 1.15a-b, e-f); a_2 is related to the field asymmetry with respect to the finger axis (Fig. 1.15c, g); a_3 is related to the bimodality of the driving field in the neighborhood of the tip (Fig. 1.15d, h). Consequently, the velocity of the tip is proportional to a_1. The trajectory of the finger in the neighborhood of the tip, which follows from growth in the gradient direction [103], can be determined with a_1 and a_2.

The simulation of network growth proceeds as follows [100]. A geometry of the system is constructed with appropriate boundary conditions on the walls and the initial branches are placed in the system. In each iteration of the growth algorithm, the Laplace (or Poisson) equation is solved with the finite element method (for instance, with the FreeFem++ solver [131]). Next, the field around the tip is integrated to obtain the coefficients of expansion of the field in the vicinity of the tips. Finally, the velocity of the tips and their growth direction is determined based on the expansion coefficients and the branches are extended (or split if a bifurcation condition is met). The process is repeated iteratively, and in each timestep the network extends and colonizes the available domain.

In Chapter 3, using this approach we develop a numerical package to simulate network growth dynamics. We apply it to simulate the evolution of river networks and extract their growth laws. In Chapter 4, we extend the method to incorporate the finite mobility ratio. We then use it to simulate loop formation near breakthrough. In Chapter 6, we adapt this model to simulate the jellyfish canal network growing in response to diffusive fluxes, and a stress field.

1.4.2 The Hele-Shaw cell

Flow

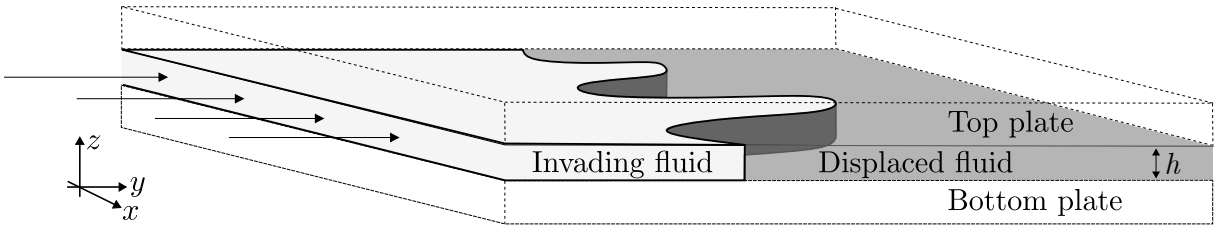

Figure 1.16 The Hele-Shaw cell. Two fixed plates at a distance h. The invading fluid is injected on the left.

A Hele-Shaw cell consists of two parallel plates separated by a narrow gap of thickness h (Fig. 1.16). In most general terms, the motion of the fluid between the plates is described by the Navier-Stokes equation:

$$\frac{\partial \boldsymbol{u}}{\partial t} + (\boldsymbol{u} \cdot \boldsymbol{\nabla})\boldsymbol{u} = -\frac{1}{\rho}\boldsymbol{\nabla} p + \frac{\mu}{\rho}\boldsymbol{\nabla}^2 \boldsymbol{u} + \boldsymbol{f}\,, \tag{1.10}$$

where $\boldsymbol{u}(x, y, z)$ is velocity vector field, ρ fluid density, μ viscosity, p pressure and $\boldsymbol{f}$ external body forces acting on the fluid.

In the present case, there are no external forces ($\boldsymbol{f} = 0$) and the fluid is assumed to be incompressible:

$$\boldsymbol{\nabla} \cdot \boldsymbol{u} = 0\,. \tag{1.11}$$

The plates are sufficiently close together, so that the nonlinear and time dependent terms in Eq. (1.10) can be neglected leading to Stokes flow:

$$\boldsymbol{\nabla} p = \mu \boldsymbol{\nabla}^2 \boldsymbol{u}\,. \tag{1.12}$$

The lubrication approximation is then used. The pressure is independent of z ($\frac{\partial p}{\partial z} \approx 0$), so $p = p(x, y)$. The velocity component in the z-direction is negligible ($u_z \approx 0$) and the derivatives of velocity in the x and y directions are much smaller than the derivative in the z direction ($\frac{\partial^2}{\partial x^2}, \frac{\partial^2}{\partial y^2} \ll \frac{\partial^2}{\partial z^2}$). The parallel flow ($\boldsymbol{u}_{xy} = (u_x, u_y)$) remains dependent on the z variable:

$$\boldsymbol{\nabla} p = \mu \frac{\partial^2 \boldsymbol{u}_{xy}}{\partial z^2}\,. \tag{1.13}$$

Assuming a no-slip boundary condition at the top and bottom plates, Poiseuille (parabolic) flow is obtained:

$$\boldsymbol{u}_{xy}(x, y, z) = \frac{1}{2\mu} z(z - h) \boldsymbol{\nabla} p(x, y)\,. \tag{1.14}$$

Note that in the above and from now on the gradient is two-dimensional.

The z-coordinate can be removed from consideration entirely by defining the gap averaged velocity:

$$\boldsymbol{v}(x,y) = \frac{1}{h}\int_0^h \boldsymbol{u}_{xy}(x,y,z)\mathrm{d}z = -\frac{h^2}{12\mu}\boldsymbol{\nabla}p(x,y)\,, \tag{1.15}$$

The linear relationship between velocity and pressure gradient is known as Darcy's law, and the proportionality constant, $M = \frac{h^2}{12\mu}$, as mobility. An analogous formula describes flow in porous media. In this case, the mobility is $M = \frac{k}{\mu}$, where k is permeability of the medium.

Recalling the incompressibility condition, Eq. (1.11) and assuming that h is constant, the Laplace equation for the pressure is obtained:

$$\Delta p = 0\,. \tag{1.16}$$

The velocity of the interface between two fluids is thus proportional to the gradient of a harmonic field and is an example of Laplacian growth.

Viscous fingers

In the classical Saffman-Taylor experiment, a fluid with viscosity μ_1 is injected into the cell. It displaces a fluid with viscosity μ_2 that initially fills the space between two plates. According to the Young-Laplace law, the pressure is discontinuous at the interface of the two fluids due to surface tension effects:

$$p_1 - p_2 = \gamma(2/h + 1/R)\,, \tag{1.17}$$

where γ is the surface tension, $2/h$ is the curvature of the meniscus in the transverse plane of the Hele-Shaw cell, and $1/R$ is the in-plane curvature of the front.

Two common setups are usually considered: a radial and a rectangular one. The Hele-Shaw cell is initially filled with a high viscous fluid. In the first case, less viscous fluid is injected at the center of a Hele-Shaw cell and it initially creates a growing circle. In the second case, fluid is injected uniformly along an entire edge of the system, initially forming a planar interface. The initial stage of instability can be studied with linear stability analysis. Let us consider the rectangular case and two fluids moving with velocity $v_x = V$. In the co-moving reference frame the interface lies at $y = 0$. Suppose the interface

is deformed slightly into a wave-like corrugation:

$$y(x) = \epsilon e^{\sigma t} \sin(kx)\,, \tag{1.18}$$

where $e^{\sigma t}$ is the amplitude of the perturbation, k is the wave vector, and $\lambda = 2\pi/k$ is the wavelength. For positive σ the amplitude increases at an exponential rate and the interface is unstable to small disturbances. Conversely, for negative σ, the deviation is damped and the motion is stable.

By substituting the perturbation into the governing Laplace equation, Darcy's law, and the Young-Laplace law, and applying the appropriate far-field constraints, one obtains the dispersion relation [35] (Fig. 1.17a):

$$\sigma(k) = \frac{\mu_2 - \mu_1}{\mu_2 + \mu_1} V k - \gamma \frac{h^2}{12(\mu_2 + \mu_1)} k^3\,, \tag{1.19}$$

or in terms of wavelength (Fig. 1.17b):

$$\sigma(\lambda) = \frac{\mu_2 - \mu_1}{\mu_2 + \mu_1} V \frac{2\pi}{\lambda} - \gamma \frac{h^2}{12(\mu_2 + \mu_1)} \left(\frac{2\pi}{\lambda}\right)^3\,. \tag{1.20}$$

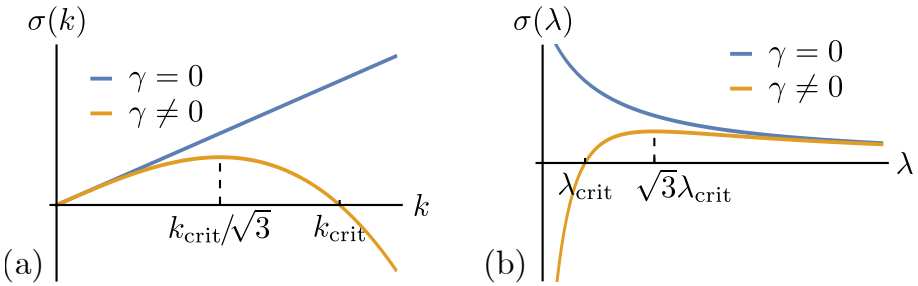

Figure 1.17 The dispersion relation resulting from the linear stability analysis of the Saffman-Taylor problem.

Several insights can be drawn from Eq. (1.20). First, a positive value of σ is only possible if $\mu_1 < \mu_2$. This shows that instability can only occur when a less viscous fluid is injected into a more viscous fluid. Second, when surface tension is absent ($\gamma = 0$) the growth rate diverges as the wavelength decreases, leading to an ultraviolet catastrophe. Third, including surface tension ($\gamma \neq 0$) regularizes the problem and introduces a critical wavelength below which σ becomes negative:

$$\lambda_{\text{crit}} = 2\pi h \sqrt{\frac{\gamma}{12(\mu_2 - \mu_1)V}}\,. \tag{1.21}$$

Finally, the non-monotonic dispersion relation has a well-defined maximum at $\sqrt{3}\lambda_{\text{crit}}$.

This defines the most amplified wavelength that should be observed in experiments.

Hence, the instability originates as a regular sinusoidal perturbation with a wavelength of $\sqrt{3}\lambda_{\text{crit}}$. The pattern quickly enters the nonlinear regime, in which the fingers compete for available flux and screen each other. After this transient period, the pattern simplifies again into an invariant shape that advances into the system without changing. Saffman and Taylor already proved the equation for the invariant shape in their original work in 1958 [35]. For fluid injected along x direction into a channel of width W the shape can be described with the formula:

$$x = \frac{W(1-\lambda)}{2\pi} \ln\left[\frac{1}{2}\left(1 + \cos\frac{2\pi y}{\lambda W}\right)\right], \tag{1.22}$$

where, far upstream at $x \to -\infty$, $\lambda = w/W$ relates the width of the finger, w, with the channel width. From the mathematical point of view, when surface tension is neglected, λ can be any number between 0 and 1. In physical experiments, the finger width fraction approaches the universal limit of $\lambda = 0.5$ as the fluid velocity increases or the relative influence of surface tension decreases [132].

In Chapter 4 we perform the Saffman-Taylor experiment in a radial Hele-Shaw cell. We show that loops suddenly form when one of the viscous fingers reaches the outlet of the system. This occurs even in a high mobility ratio case, which was previously thought to be impossible.

Dissolution fingers

An instability in a Hele-Shaw cell appears when a high-mobility phase displaces a low-mobility phase. In the previous section, the mobility contrast was introduced by using two fluids with different viscosities. According to the mobility formula, $M = \frac{h^3}{12\mu}$, the same can be achieved if the two phases have different apertures, h. This is the case in systems where the aperture can change under flow – for instance, when the bottom plate is replaced with a soluble material, such as gypsum (Fig. 1.18). Such an experimental setup is a direct analog of fracture dissolution observed in nature. It also mathematically maps to the reactive-infiltration problem in porous media [133].

In the experiment, distilled water is injected on one side of the cell, and flows over the gypsum, gradually dissolving it (Fig. 1.18a). Starting from the inlet side, a dissolved area appears with an aperture h_{max} (black in Fig. 1.18b). As water quickly becomes saturated with calcium ions, the regions behind the reaction front maintain the initial aperture, h_0 (white in Fig. 1.18b).

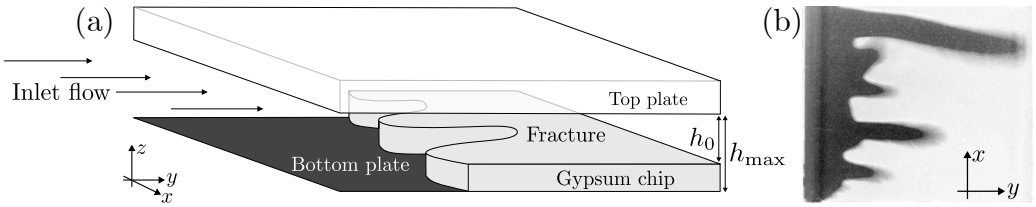

Figure 1.18 The Hele-Shaw cell with a soluble bottom. (a) Part of the bottom plate is replaced with a gypsum chip that dissolves under water flow. Different apertures in the undissolved and dissolved areas result in mobility contrast and lead to instability. (b) Top view on the experiment. The black part is the dissolved area, white – undissolved. The elongated fingers are a result of the reactive-infiltration instability.

The change in aperture of the system is caused by a dissolution reaction. The kinetics for gypsum dissolution is approximately linear with respect to calcium ion undersaturation: $c_{3\mathrm{d}} = c_{\mathrm{sat}} - [\mathrm{Ca}^{2+}]$. Similarly to gap-averaged flow, $\boldsymbol{v}$, we can define a two-dimensional concentration field, c, by integrating the third dimension:

$$c(x,y) = \frac{1}{|\boldsymbol{v}|h}\int_0^h |\boldsymbol{u}| c_{3\mathrm{d}}(x,y,z)\mathrm{d}z\,. \tag{1.23}$$

The concentration field obeys then the two-dimensional convection–diffusion–reaction equation:

$$\boldsymbol{\nabla}\cdot(\boldsymbol{v}hc) = \boldsymbol{\nabla}\cdot(Dh\boldsymbol{\nabla}c) - \theta(h_{\max}-h)kc\,, \tag{1.24}$$

where D is the diffusion coefficient of the calcium ions, k is the reaction rate constant, and θ is a step function: $\theta(x) = 1$ if $x > 0$ and zero otherwise. The aperture change is given by:

$$\frac{\partial h}{\partial t} = \theta(h_{\max}-h)\alpha kc\,, \tag{1.25}$$

where $\alpha = \nu_{\mathrm{m}}/(1-\varphi)$ is the volume (per mole) occupied by the solid phase. It is determined by the molar volume (ν_{m}) and the porosity (φ) of the soluble material [133]. The characteristic dissolution time is much larger than the relaxation timescale of the concentration field, which justifies dropping the time dependence in Eq. (1.24).

Writing Eq. (1.24) in a non-dimensional form introduces two dimensionless numbers that control system behavior. The Damköhler number compares the reaction and diffusion rates:

$$\mathrm{Da} = \frac{kW^2}{Dh_{\max}}\,, \tag{1.26}$$

and the Péclet number is the ratio of the advection to diffusion rates:

$$\mathrm{Pe} = \frac{v_0 W}{D} = \frac{Q_{\mathrm{tot}}}{Dh_{\max}}. \tag{1.27}$$

Above, W is the width of the system, v_0 is the average velocity: $v_0 = Q_{\text{tot}}/(W h_{\max})$, and Q_{tot} is the total flux in the system.

Although the aperture, $h(x, y)$, varies continuously, under certain conditions, the problem can be reduced to a moving boundary (Stefan) problem with a sharp interface between the dissolved and undissolved regions. When the dissolution reaction is much faster than ion diffusion across the finger (large Da), the solution saturates essentially instantaneously as it crosses the reaction front. This corresponds to a Dirichlet condition, $c = 0$, and a sharp transition in the aperture field from $h_{\max}$ to h_0 at the boundary of the finger. The boundary evolution is then determined by the diffusive flux of ions:

$$v_n(t) = -\alpha D \frac{h_{\max}}{h_{\max} - h_0} \left(\boldsymbol{\nabla} c\right)_n \,, \tag{1.28}$$

where n is the outward normal to the moving boundary. Note that this approximation breaks down near the tip of the finger because focused flow advects the undersaturated fluid deeper into the undissolved region.

In one dimension, Eqs. (1.24)–(1.25) have a simple solution involving a uniform reactive front propagating from inlet to outlet. The advected reactant is consumed quickly as it reaches the undissolved matrix and dissolves it; hence, it cannot penetrate deep into the system. This has long puzzled researchers studying cave formation in limestone, a process in which fracture dissolution is recognized as the primary origin. The short penetration length of an undersaturated solution made it seem impossible for long conduits to develop. Treating the system as a two-dimensional moving-boundary problem revealed that the front is unstable to transverse perturbations. The wavelength of this reactive-infiltration instability calculated from linear stability analysis [45, 64] agrees well with the initial dissolution patterns observed experimentally [133]. After the initial period, the instability enters a nonlinear regime with many interacting fingers, as visible in Fig. 1.18b. As in the Saffman-Taylor case, in the long time limit the pattern simplifies and a single invariant dissolution finger emerges.

This experimental system is used to study the invariant form of a dissolution finger in Chapter 2. Additionally, in Chapter 4, we show that fingers can attract each other and create loops when the mobility ratio is low.

1.4.3 The jellyfish gastrovascular canal network

Jellyfish are free-swimming marine animals widespread in oceans around the world. They belong to the subphylum Medusozoa, which along with corals, hydras or sea anemones is part of the phylum Cnidaria. Many aspects of jellyfish have brought attention of researchers. Neuroscientists focus on their decentralized nervous system [134–136]. The way they swim has been found to be one of the most efficient locomotion on the planet [137]. There are attempts to use them as a low-cost biohybrid robots for ocean exploration by enhancing their swimming speed and controlling it with microelectronics embedded in the living jellyfish body [138, 139]. They exhibit remarkable regenerative capacity. The 'immortal jellyfish', *Turritopsis dohrnii*, has gained worldwide fame for its ability to theoretically live forever. Under stress, it transdifferentiates reverting its specialized adult cells back into a stem-cell-like state [140]. Other studies on jellyfish show rapid regeneration and restoration of injured organs [141] or mechanical reorganization of the body to regain symmetry and functionality [142].

The phylum Cnidaria is an interesting reference point from the evolutionary perspective [143, 144]. It is the 'sister group' of Bilateria – a clade including most of extant animals. The two groups diverged on the phylogenetic tree around 700 million years ago, before the appearance of the mesoderm or circulatory systems [143]. However, jellyfish do display an internal delivery network – one of the earliest evolutionary attempts to overcome the limitations of short-distance diffusive transport of nutrients and oxygen. The gastrovascular canal network of jellyfish is a phylogenetic precursor of vascular architectures in higher animals. Fossils from the Middle Cambrian period (around 505 million years ago) suggest that the fundamental body plans of jellyfish have endured for over half a billion years [145]. While the gastrovascular canal system is not preserved in the fossil record, the substantial size of these specimens suggests that specialized transport networks were already a functional necessity. Thus, jellyfish provide a unique window into the history of transport networks in animals.

The key differences between the Bilaterians and Cnidarians appear at the early stage of development – the gastrulation. During Bilaterian gastrulation, the blastula – a hollow sphere of cells – folds inward and reorganizes. The basic body axes are established, and the cells undergo specification into primary germ layers: ectoderm, endoderm and mesoderm. These germ layers later develop into different tissues and organs: the ectoderm gives rise to organs of protection and sensing, such as the skin (epidermis) and nervous system; the endoderm produces the lining of the digestive and respiratory system; the mesoderm forms the circulatory system, connective tissues, and bones.

The Bilaterians develop three body axes: Anterior-Posterior (head-to-tail), Dorsal-

Ventral (back-to-belly) and Left-Right. They are triploblastic, meaning that all three germ layers appear in their development. They usually have a through-gut with a separate mouth and anus, and a circulatory system deriving from the mesoderm. Contrarily, jellyfish have a single axis – Oral-Aboral (the line from the mouth to the top of the bell) and radial symmetry. Their organism is a 'blind sac' with an opening used both to ingest and egest. They are usually considered diploblastic, so with only two germ layers: the ectoderm and endoderm. Unlike more complex animals that integrate the germ layers to form internal organs, the layers in jellyfish remain distinct. The ectoderm forms the outer layer (epidermis), while the endoderm forms the layer lining the gastrovascular system (gastrodermis). The two layers are separated by the mesoglea – an extracellular matrix composed mainly of water, some collagen and polysaccharides.

The gastrovascular canal network of Discomedusae

The jellyfish gastrovascular system includes a central cavity from which a network of canals extend to the periphery of the body. Although evolutionarily ancient, the delivery network exhibits a remarkably complex and variable form. This is similar to the domain of unstable growth processes – a simple system exhibiting complex patterns with high variability. Interestingly, patterns in different jellyfish across the class Scyphozoa (true jellyfish), subclass Discomedusae resemble patterns in physical experiments (Fig. 1.19). *Cyanea* has a purely branching network [146,147], resembling viscous fingers, particularly those obtained in a lifting Hele-Shaw cell [148]. *Rhizostoma* exhibits a dense, highly reticulated network with many reconnections and loops [146, 149], similar to cracking patterns in drying mud [150]. Finally, *Aurelia* jellyfish, the main object of study in the thesis, has a sparse reticulated network, sharing similarities with patterns observed in both diffusion-driven and stress-driven growth [146,151,152] (Fig. 1.20).

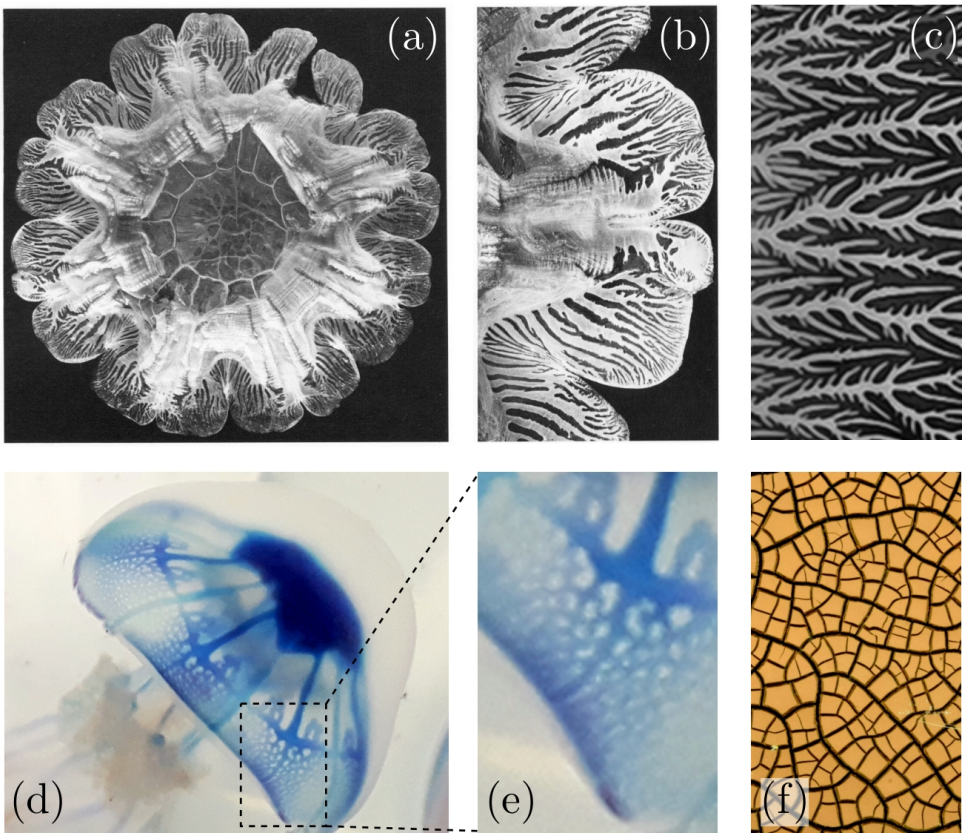

Figure 1.19 **The gastrovascular canal networks of Discomedusae.** (a) *Cyanea capillata* sub-umbrella and (b) a zoom in on the branching canals (white color) [146]. (c) Viscous fingers in a lifted Hele-Shaw cell. Instead of pushing air into silicon oil with a pump, the top plate is lifted and the air (black) invades the system to fill the space that appears. Photo adapted from [148]. (d) *Rhizostoma pulmo* with stomachs and canal network stained in blue [149]. (e) A zoom in on the reticulated canal network that resembles (f) cracks on mud [150].

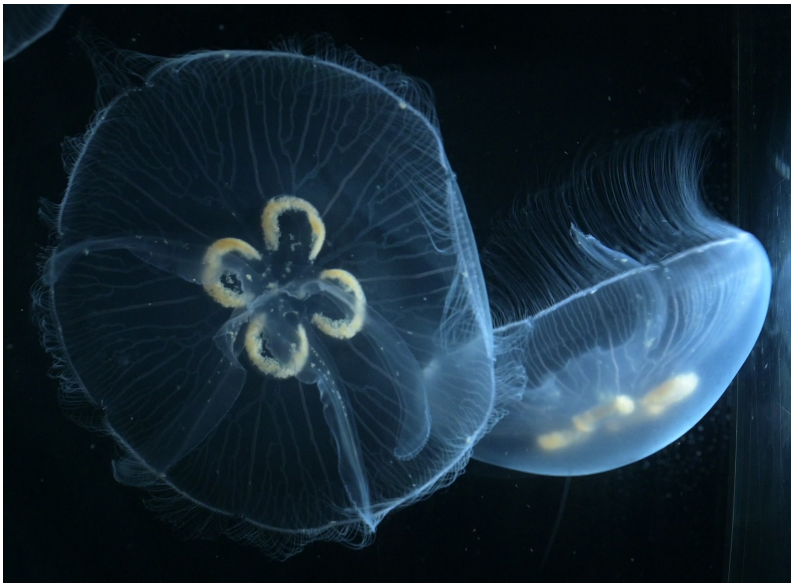

Figure 1.20 **Two adult *Aurelia* jellyfish swimming in an aquarium in Dr. Cornelissen's lab at the Laboratoire Matière et Systèmes Complexes.**

The *Aurelia* jellyfish

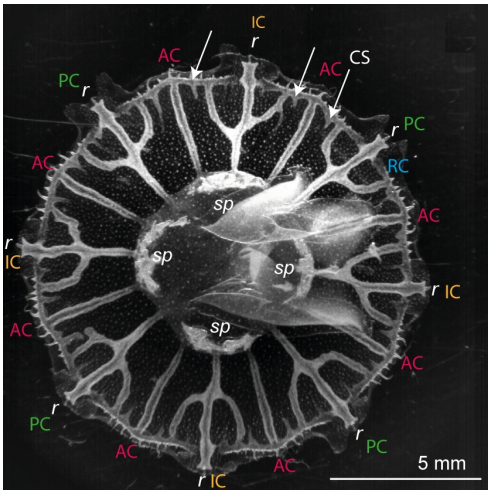

Figure 1.21 The *Aurelia* jellyfish anatomy. The view on the sub-umbrella showing a stereotypical primary network in a juvenile jellyfish [152]. There are typically four stomach pouches (*sp*) and eight sensory organs – rhopalium (*r*). At the periphery of the jellyfish there is a ring canal (RC in blue). Eight straight adradial canals (AC in red) connect the ring canal and stomach pouches. Between the adradial canals there is either the perradial canal (PC in green) or the interradial canal (IC in orange), connecting the rhopalia with the stomach pouch or the junction between two stomach pouches, accordingly. New canal sprouts (CS) sprout from the ring canal (arrows).

The *Aurelia* jellyfish has a bell shaped body (Fig. 1.20). The top surface of the bell is called the ex-umbrella, and the bottom – the sub-umbrella (Fig. 1.21). Along the margin tentacles are found. The mouth and the oral arms of the jellyfish are located in the central part of the sub-umbrella. Above the mouth there is a gastric cavity surrounded by four stomach pouches. From each pouch two adradial canals go directly to the ring canal at the periphery of the jellyfish. The adradial canals define eight sections called octants. In the middle of each octant there is either an interradial canal, going from the ring canal to the gastric pouch or a perradial canal connected directly to the central cavity and the oral arms. Additional canals can extend from the ring canal toward the center, sometimes reconnecting to the inter- or perradial canals, but rarely to the adradial ones. Each eighth of the jellyfish, bordered by two adradial canals, is very similar, regardless of whether it has an inter- or perradial canal in the middle. Hence, the jellyfish canal system is often considered to have tetra-radial symmetry.

The *Aurelia* jellyfish is a predator that eats small crustaceans or larval fish. The food is collected on the whole surface of the animal and then moved by cilia to the marginal groove. From there, the cilia push the food toward the rhopalium, where the oral arms pick it up and the food is transported to the mouth located centrally on the sub-umbrella. It is then predigested by the four gastric pouches. Food particles are then distributed by a

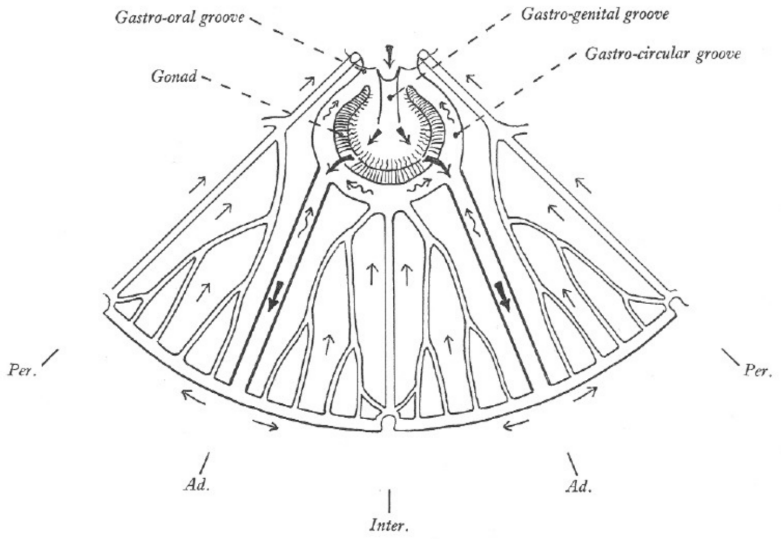

Figure 1.22 Ciliary flows in the *Aurelia* jellyfish after Ref. [153]. Arrows indicate flow direction.

network of canals above the muscle layer on the sub-umbrella (Fig. 1.22). First, it goes by the adradial canals toward the margin and then comes back by the smaller and the inter- or perradial canals. The flow is driven by the activity of cilia and the peristalsis induced by the contractions of the whole body during swimming movements. Interestingly, flow in the canals can be bi-directional, as indicated by wavy arrows in Fig. 1.22.

From a practical standpoint, *Aurelia* jellyfish is a convenient model organism for biophysical research. They are relatively easy to grow and observe *in vivo*. Their transparency allows for noninvasive observation of the gastrovascular canal system day by day using methods such as transillumination. This allows to capture the development of a transport network over time and acquire a time-lapse of its growth, which is rarely possible with living organisms. Their specific life cycle, which includes a stage of asexual reproduction from a polyp, results in dozens of clone jellyfish available for the experiments. Although genetically identical, each jellyfish has a unique gastrovascular canal pattern. This allows to study how physical processes, independently of detailed genetic instructions, play a role in developing the network pattern.

The medusa form originates from the polyp stage through strobilation (Fig. 1.23a) – a process of transverse fission of multiple jellyfish larva, called ephyra (Fig. 1.23b). They have a few mm in diameter and eight arms that already contain the straight canals that will become inter- and perradial canals. In the first two weeks of its life, the ephyra becomes a juvenile jellyfish (Fig. 1.23c). The space between the arms is filled and the body becomes circular. The adradial canals extend and a trident form of the inter-/perradial canals emerge. The ring canal is formed as all canals fuse at the rim. This stage of growth is rather stereotypical and results in a regular, symmetric primary network (Fig. 1.21).

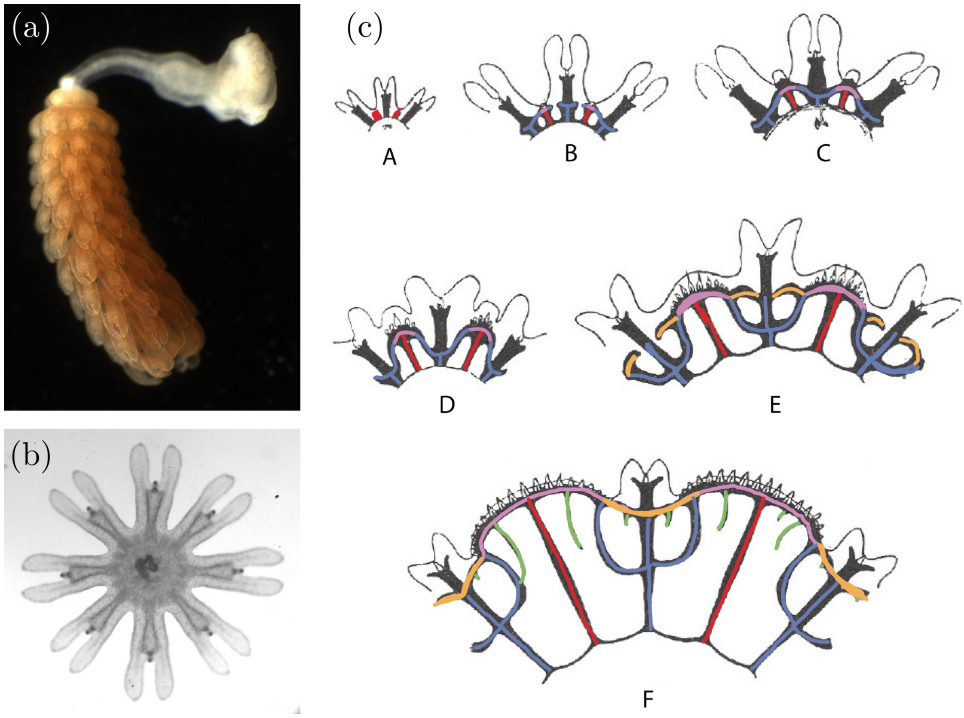

Figure 1.23 Initial stages of the *Aurelia* jellyfish development. (a) A strobilating polyp. (b) An ephyra just after detaching from the polyp. (c) The development of the primary network from star shape ephyra to juvenile jellyfish (A-F). Red indicates adradial canals, blue – initial tri-fork structure, green – sprouts, yellow and purple – closing marginal canal. Adapted from Ref. [146].

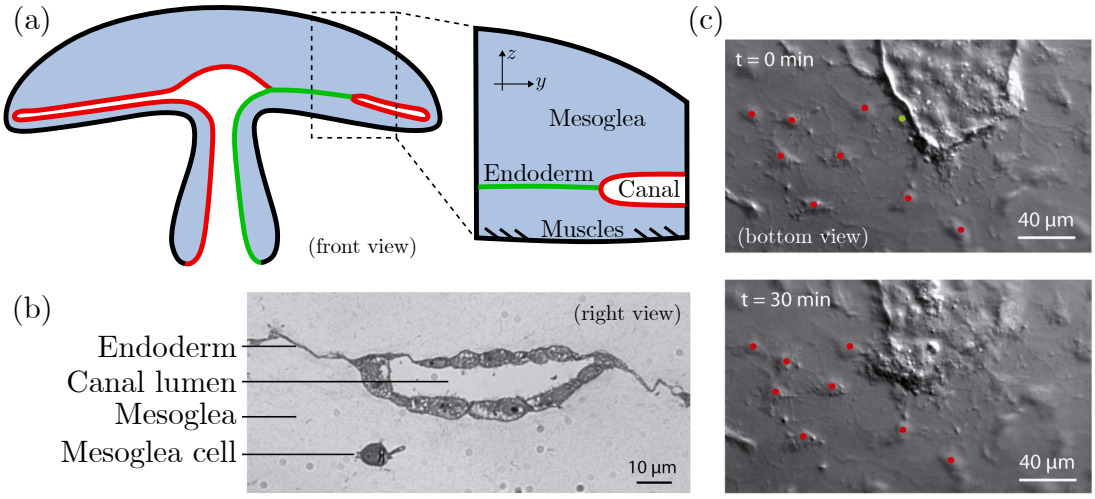

Figure 1.24 The gastrodermis in the *Aurelia* jellyfish (after [151]). (a) The canals grow in a unicellular endodermal layer, just above the lower epidermis with muscles (subumbrella). (b) An optical view of a histological cross section of a canal.(c) The extension of a canal at its tip. Red dots indicate the nucleus of the endodermal cells. The cell closest to the tip (green dot) is integrated into the canal after 30 min.

The subsequent stage, from juvenile to adult jellyfish, is more variable. New canals sprout at the ring canal and grow in the direction of the stomachs [151, 152, 154]. The canals grow directly in the monolayer of endoderm (Fig. 1.24), making the developing network quasi-two-dimensional. The sprouts extend at their tips, by integrating the preceding endodermal cells into the canal and proliferating the canal cells [151, 152] (Fig. 1.24c). Some of the sprouts go directly to the stomachs, but most of them reconnect to other canals. The sprouts tend to reconnect to the youngest canal in their neighborhood. A natural question is what determines their growth direction and what leads to the preferential reconnections to the younger canals.

The endodermal sheet behaves mechanically as an elastic sheet embedded in gelatinous mesoglea. The muscle contractions responsible for swimming movements exert tension on the endodermal sheet. The variability of the patterns and the mechanical forces apparent in the system suggest that physical fields like stress or pressure can be responsible for determining the direction of canal growth [151, 152].

In Chapter 5, we analyze more closely the variability of the *Aurelia* jellyfish gastrovascular canal pattern. We show that the breakthrough-induced reconnections, similar to those observed in viscous fingering or fracture dissolution, also occur in this biological system. In Chapter 6, we describe the tracking of the jellyfish canal network in time and and how we model its evolution numerically.

1.5 Summary of the thesis

Natural shapes are often viewed as the result of an optimization process, or as being predetermined, for instance by a genetic program. This overlooks the problem of *how* shapes appear in the first place. To understand this, we must examine the underlying growth dynamics. We study the relationship between final shapes and growth processes to address the inverse problem: Given a shape, how can we determine the details of its growth process or, more broadly, identify the fundamental mechanism behind its emergence? The answer to this question is useful in many contexts, for instance, to reconstruct environmental information from geological forms or to understand how to arrest pathological processes in biological systems.

We focus on forms that initiate as an instability at a moving front. The small protrusions later develop into finger-like shapes that interact with each other and can form a network structure. The examples range from solution pipes to river networks to the canal network of *Aurelia* jellyfish.

First, we analyze the systems in which the growth mechanism has been previously identified or can be derived theoretically. We demonstrate how to extract details of the governing growth laws or conditions during the emergence of a structure just by examining its final geometry. This is particularly important for geological forms that evolve over timescales beyond human measurement capabilities. We show that a single snapshot of geometry is sufficient to reconstruct historical flow rates in an emerging solution pipe or to identify the growth laws of a river network.

In the long-time limit, some natural forms attain an ideal shape, independent of the initial conditions and characterized by a small number of parameters. This provides a unique insight into the physical conditions under which the structure emerged. In Chapter 2, we study the ideal forms of dissolution fingers. These structures result from the reactive-infiltration instability – positive feedback between fluid flow and reactant transport that occurs during the dissolution of fractured or porous media. We examine the formation of these finger-like channels using a microfluidic Hele-Shaw cell with a soluble bottom.

We observe a strong competition between the fingers in this system. The longest finger, which offers the path of least resistance, captures an increasing amount of the flow at the expense of the shorter fingers. Consequently, the shorter fingers slow down and widen. Interestingly, the longest finger neither accelerates nor changes shape. Superimposing the snapshots of the longest finger throughout its evolution reveals that it has been tracing the same shape since the beginning. Over time, the invariant part of the finger simply

shifts in the flow direction, and an increasingly longer invariant finger emerges.

To study the emergence of the invariant shape in more detail, we performed single-finger experiments in a narrow microfluidic cell. The fingers are regular in shape, with a constant slope at the walls far from the tip and parabolic tips. They are more elongated at higher flow rates. Using a combination of reactive-transport theory and conformal mapping techniques, the shape of the ideal finger can be derived that matches the shapes observed in experiments.

The analysis can be extended to three dimensions and used to interpret natural forms, such as solution pipes – vertical channels formed by acidic rainwater infiltrating limestone. The critical parameter controlling the ideal shape is the Péclet number, $\mathrm{Pe} = Q/Da$, where Q is the flow rate in the system, D is the diffusion constant, and a is the channel radius. By measuring the pipe diameter and its slope at the sides, we can reconstruct the historical flow rate in an emerging solution pipe. This may provide information about the environmental conditions under which they developed.

Even if a structure does not attain an ideal shape, its geometry conceals a wealth of information about the laws of its growth and the environment in which it was formed. In Chapter 3, we describe a framework for reconstructing this information from a single snapshot of a morphodynamic network. We consider tip-growing networks with branches that extend and bifurcate in response to an external field. The field and the network co-evolve in time, as the growing network changes the boundary conditions for the field. Network dynamics are defined by growth laws – a set of rules that link the extension and bifurcation processes to the characteristics of the driving field, such as its gradient in the vicinity of the tip. Once the growth laws are known, we can predict the shape of the network in the future, but also in the past.

To decipher the growth laws, we developed the Backward Evolution Algorithm. First, the growth laws are parametrized, and an initial set of parameters is selected. Using these specific growth rules, the network is evolved backward in time over a small interval, dt, and subsequently evolved forward over the same time step. If the selected growth law is incorrect, time reversibility of the problem is broken, and we do not return to the original state. Conversely, with a correct growth law we replicate the initial geometry after the backward-forward step.

The forward step is then neglected, and the procedure repeated, backtracking the evolution of the network completely down to its seeds. By measuring deviations from the original state and other metrics after each backward step, such as the symmetry of the field around each tip, we can estimate the fitness of the selected growth rule. We repeat the same procedure for different sets of parameters and select the most optimal one.

We validate this approach using synthetic data from simulations of networks grown in a diffusive field. The growth rules of the branches and the conditions under which branch splitting occurs are successfully determined. We then apply this approach to analyze the growth of a real river network in Vermont, USA. Our results show that the forming tributaries of this network competed strongly for groundwater flow. We also argue that branch splitting events were triggered by an increase in tip growth velocity. This tool opens new perspectives for the analysis of spatial networks in nature. A comprehensive analysis of river networks on Earth could correlate growth laws with local climate conditions, such as rainfall intensity. This could be used to reconstruct past conditions on other planets with ancient river networks. A similar analysis based solely on bifurcation angles has yielded promising results regarding the once-prevailing climate on Mars.

Next, we investigate loops in physical networks. Looping networks have been shown to be more resilient to damage and to be selected in biological evolution. However, little is known about their development, particularly in a process called tip-growth, in which networks extend at branch tips in response to the gradient of an external field. Classical models of this process explain the competition, screening, and repulsion between branches and produce purely branching networks, such as the ones presented in Chapter 3. The question remains: How do branches attract each other and reconnect to form loops?

In Chapter 4, we identify sudden loop formation near the breakthrough event. When the longest finger reaches the boundary of the system, the shorter fingers revive and are attracted to it. Breakthrough reconnections appear in remarkably diverse processes, including electric discharges, conduits in karst caves, dissolution and viscous fingers in a Hele-Shaw cell, canals in the gastrovascular system of the *Aurelia* jellyfish. The growth of these structures is governed by diffusive fluxes. An important parameter here is the mobility ratio, M – the ratio of mobility inside the growing fingers to mobility outside. Previous studies have shown that a finite mobility ratio reduces screening and effective repulsion in the system. This can lead to loop formation within specific ranges of mobility and finger length ratios. However, breakthrough reconnections are not limited to these specific scenarios. Near breakthrough, the branches reconnect even for a high mobility ratio, which was previously thought impossible due to screening effects.

To provide a physical explanation of the breakthrough reconnections, we first consider a one-dimensional model of Laplacian fingers. We note that the field within a short finger far from the outlet of the system is almost constant. This suggests that treating the fingers as isolines of the field, as in Chapter 3, is justified in this case. However, the field decreases along longer fingers closer to the outlet. The transition from isoline fingers to fingers exhibiting a field gradient occurs at a distance from the outlet that is inversely

proportional to the mobility ratio. If a short finger and a long finger were placed next to each other, there would be a potential difference between the short finger tip and the long finger. Consequently, the short finger would be attracted to the longer one.

In the one-dimensional model, each finger is treated independently. In reality, however, the fingers interact; the longer finger screens the shorter one. To investigate this effect, we conduct numerical simulations of a two-dimensional system. For low mobility ratio, the shorter finger is weakly screened and receives some flux, even when the longer finger is far from the outlet. The higher the mobility ratio, the stronger the screening effect. In this case, when the gap – the distance from the longest finger to the outlet – is large the total flux in the shorter finger is close to zero. As the gap decreases, the field in the longest finger begins to drop and the shorter finger receives more flux.

The shorter finger not only revives and starts to grow again, but its growth direction also changes near the breakthrough event. When the gap is large, more flux comes from outside, and the shorter finger grows away from the longer one. For a smaller gap, more flux comes from the longer finger. This results in an effective attraction toward the longer finger.

Finally, we adapt the model from Chapter 3 to include finite mobility ratio. Instead of thin fingers treated as isolines of the field, we consider fingers of finite width with the field decreasing along them. We perform simulations of the temporal evolution of the fingers to demonstrate how revival and attraction to the longest finger lead to dynamic loop formation. For two fingers with slightly different initial lengths, we observe all of the previously described interactions between them: competition and repulsion, screening, revival, and attraction.

We then conduct experiments in a Hele-Shaw cell: fracture dissolution (as described in Chapter 2) with low mobility ratio and viscous fingering with high mobility ratio. We compare the simulations to the experiments and find that the dynamics of the shorter finger are accurately reproduced. In both the experiments and simulations, we observe that, for low mobility ratio, the shorter finger is not screened and is attracted towards the longer one from the beginning. Conversely, for high mobility ratio, the shorter finger is initially screened. It then revives and suddenly reconnects to the longer finger. Our results demonstrate that reconnection is a prevalent phenomenon in systems driven by diffusive fluxes. It occurs both when the mobility inside the growing structure is similar to the mobility outside and near the breakthrough.

In the last part of the thesis, we focus on a specific biological looping network: the gastrovascular canal system of the Aurelia jellyfish. The jellyfish is a valuable model for studying the development of biological delivery networks due to its position on the

phylogenetic tree, simple anatomy, and ease of in vivo imaging. The gastrovascular system has four stomach pouches in the center of the jellyfish. At the end of the ephyra stage, sixteen straight canals extend from the jellyfish center to the marginal ring canal. Eight adradial canals border eight sections, called octants, with an inter- or perradial straight canal in the middle of each. Typically, two shorter canals are connected to the middle canal, forming a trident-like fork. As the jellyfish grow, new canals sprout from the marginal ring canal and grow toward the center. Some sprouts reconnect to other canals, while others go directly to the stomachs.

In Chapter 5, we describe the structure of the canal network and its variability. We focus on the stage from juvenile to adult jellyfish. The ideal geometric construction of the canal pattern can be described as follows: In each octant, the fork structure would split the marginal canal into four equal segments. A new sprout would appear in the middle of each segment. These sprouts would grow and connect to the youngest canal in the neighborhood (from the last previous generation), so to the side canals of the fork structure. Now, the marginal canal would have eight segments where the next generation of sprouts would appear. These sprouts would again grow and connect left or right, to the youngest canal in the neighborhood. This would lead to the distinctive fractal tree shape of the canal network.

If the canal structure were predetermined, the geometric construction would be precisely followed and the sprouts would always connect to the last previous generation. We quantify the deviation from this rule and count the number of the 'false' connections in jellyfish bred in our laboratory. Although sprouts preferentially connect to the youngest canal in the neighborhood, it is not a strict rule. Analyzing the canal patterns of jellyfish grown under different conditions further illustrates high variability in the system. This can be interpreted as a trace of instability arising from noise, suggesting that the pattern emerges in a self-organized manner.

We relate this self-organized process to the mechanics of jellyfish. The jellyfish swimming contractions induce considerable mechanical deformations on its body. This exerts mechanical stress on the unicellular endodermal sheet on which the canals grow and increases pressure inside them. To demonstrate that stress concentrates at the tips of the growing sprouts, we solve the Cauchy momentum equation numerically to determine the stress distribution in the jellyfish tissue. We consider a plane stress problem for a portion of an octant close to the ring canal. We assume that the endoderm is a flat, rigid, and nearly incompressible elastic sheet. The area normally occupied by the canals with lumens is approximated as a compressible elastic membrane of Young's modulus lower than that of the endoderm. The chosen Poisson's ratio of 0.3 translates the vertical expansion

of the canals into compression in the plane.

We analyze a small sprout growing between younger and older canals. Based on experimental observations, we assign a higher stiffness to the younger canal. We observe that stress accumulates at the sprout tip. The older, softer canal releases tension; therefore, close to the growing tip maximum stress is found on the side of the younger, stiffer canal. We hypothesize that high stress guides the sprout, explaining its preferential attachment to younger canals. We also identify the breakthrough-induced loop formation, described in detail in Chapter 4, in the canal network development. This suggests that the diffusive fluxes may also play a role in the morphogenesis of this system.

In Chapter 6, we investigate the dynamics of jellyfish canal network formation in order to validate the two hypotheses. We first approach the problem experimentally. We collect jellyfish images over a period of several dozen days, as they grow from ~5 mm to ~5 cm. The jellyfish radius grows linearly at a rate of 0.6 to 2 millimeters per day, depending on the growth conditions, such as food regime, flow rate, and aquarium size. We analyze images to detect the canals in the network and plot their azimuthally averaged density and spacing profiles as a function of relative radial position. These profiles do not depend on the growth rate, but change with the size of the jellyfish. In particular, we demonstrate that the typical canal spacing at the rim increases when the jellyfish grows. Interestingly, the spacing between the canals, adjusted for their changing width, remains nearly constant over time. This may be related to the characteristic reaction-diffusion length in the system – the effective range of nutrient delivery from a canal.

Finally, we adapt the numerical model from Chapters 3 and 4 to simulate the growing jellyfish canal network. We initiate the simulations with the stereotypical geometry of an octant – one-eighth of an annulus between the marginal canal and the stomachs. We impose linear growth on the jellyfish radius at the mean growth rate measured in the experiments. New sprouts are inserted at the rim with a probability that depends on the separation between neighboring canals, reproducing the typical spacing observed in the experiments. In each timestep of the simulation, we solve the elastic or diffusive problem. The sprouts grow with a velocity proportional to the von Mises stress or pressure gradient value at the tip and in the maximum stress or gradient direction. We run the simulations for different ratios of mechanical properties (Young's modulus or viscosity) of the endoderm to that of the canals. For low ratio, the canals do not interact and grow straight. For higher ratio, the canals attract each other strongly, leading to reconnections almost instantly after sprouting from the rim. Moderate ratio reproduces the patterns observed in experiments and the measured canal spatial frequency profiles. We discuss the limitations of the model and outline future research directions.

Chapter 2

Paper I: "Invariant Forms of Dissolution Fingers"

Author contributions

In this study, the author: conducted part of the microfluidic experiments on fracture dissolution, studied the influence of flow rate on the shape of invariant finger in experiments, performed image analysis, analyzed and interpreted data, compared theoretical and experimental results, prepared figures, and co-wrote the paper.

Invariant Forms of Dissolution Fingers

Stanisław Żukowski,[1,2] Silvana Magni,[1] Florian Osselin,[3] Filip Dutka,[1] Max Cooper,[1] Anthony J. C. Ladd,[4] and Piotr Szymczak[1]

[1]*Institute of Theoretical Physics, Faculty of Physics, University of Warsaw, Pasteura 5, 02-093 Warsaw, Poland*

[2]*Laboratoire Matière et Systèmes Complexes (MSC), UMR 7057, CNRS & Université Paris Cité, 10 rue Alice Domon et Léonie Duquet, 75013 Paris, France*

[3]*Institut des Sciences de la Terre, Orleans, France*

[4]*Chemical Engineering Department, University of Florida, Gainesville, Florida 32611, USA*

(Received 3 April 2024; accepted 29 January 2025; published 4 March 2025)

Dissolution of fractured and porous media introduces a positive feedback between fluid flow and reactant transport, leading to the emergence of pronounced, fingerlike channels. We investigate the formation of these structures using a microfluidic Hele-Shaw cell with a soluble bottom. Our experiments show that the shape of dissolution fingers is invariant and reveals itself over time as the fingers extend into the system. By combining reactive-transport theory and conformal mapping techniques we derive these invariant forms. We relate these results to natural dissolution fingers in karst landscapes, and illustrate how to determine the groundwater flow rate responsible for their formation based on the finger shape.

DOI: 10.1103/PhysRevLett.134.094101

Climatic conditions can leave a permanent mark on the landscape in the shapes and forms left behind by geological processes. Geochemical transformations are an unusual class of pattern-forming systems, in that the pattern does not decay once the driving force is removed [1–3]. While mechanical erosion shapes river valleys and mountain ridges [4–7], chemical erosion shapes caves and karst towers, as well as smaller surface forms, such as grooves, rills, or solution pans [8–12]. An intriguing example of spontaneously forming dissolution structures are solution pipes [Fig. 1(a)]. These fingerlike channels are caused by the infiltration of limestone formations by rainwater, which has become acidic through the absorption of carbon dioxide from the atmosphere and soil [13,14]. Such pipes are abundant in nature and often have regular forms, suggesting that they might represent invariant asymptotic forms of reactive-transport processes. In this Letter, we report theoretical and experimental evidence of an underlying time-invariant form for dissolution fingers, which reveals itself during the growth process.

The existence of invariant solutions is a compelling characteristic of many unstable growth processes, particularly since the early stages are often characterized by a chaotic sea of fingerlike structures [15,16]. And yet, in the longtime limit, the pattern often simplifies, with the appearance of invariant growth forms which advance into the system without changing their shape. A well-known example is the Saffman-Taylor finger, which emerges as an asymptotic solution in viscous fingering [17], or the Ivantsov paraboloid [18], which is the corresponding solution in solidification. Other examples include the regular shapes of flames [19] or crystals growing in a capillary [20]. In natural systems, a similar concept was used to describe stalactites [21], icicles [22,23], karst pinnacles [24] and travertine cones [25].

The importance of these invariant solutions lies in their independence from the initial conditions; the ideal shapes attained in the longtime limit are characterized by a small number of parameters, which record the physical conditions under which the growth occurred. For example, the width of a Saffman-Taylor finger is linked to the capillary number (involving viscosity, flow rate, and surface tension) [17], whereas the invariant shape of a crystal growing in a capillary is a function of solution supersaturation [20]. Our aim is to find a similar connection for dissolution fingers, which should enable us to obtain paleoenvironmental or even paleoclimatic data from the period in which they were formed.

Arguably, the simplest system in which to study dissolution instabilities is a Hele-Shaw cell with a soluble

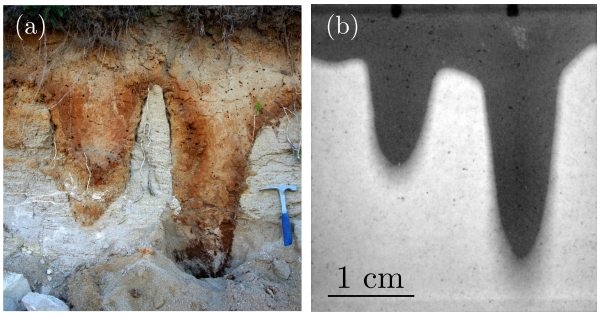

FIG. 1. (a) Solution pipes in limestone bedrock (Smerdyna, Poland). (b) Dissolution fingers formed in a microfluidic system.

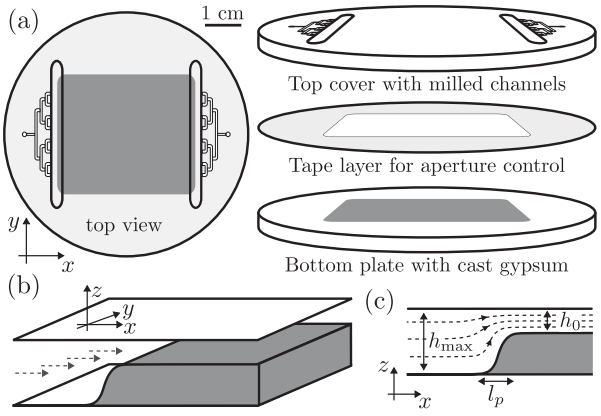

FIG. 2. The experimental setup. (a) The chip is a three-layer sandwich. The top polycarbonate plate has two networks of microfluidic channels: the inlet, delivering a uniform flow of fresh water into the system, and the outlet, draining fully saturated water. The bottom plate is flat, except for a shallow rectangular (3.3×3.8 cm) indentation filled with gypsum. The two plates are glued together by a double-coated tape, which at the same time introduces an aperture of thickness h_0. (b),(c) Fresh water flowing into the system (dashed arrows) gradually dissolves the gypsum, effectively introducing two phases: dissolved (with aperture h_{max}) and undissolved (h_0). The two phases are separated by a transition region with a characteristic length scale l_p.

bottom. A classical Hele-Shaw cell consists of two closely spaced flat plates with a small gap between them [Fig. 2(a)]. The average velocity in a thin film of liquid within the cell is linked with the pressure gradient through the Darcy's law, $\boldsymbol{v} = -M\nabla p$, where the mobility $M = h^2/12\mu$, h is the gap between the upper and lower surface [Fig. 2(b)], and μ represents the fluid viscosity. The mobility can thus be changed in two different ways: either by changing the viscosity of the fluid (as in the classical Saffman-Taylor experiment) or by modifying the depth of the Hele-Shaw cell.

A variable depth can be achieved by replacing part of the bottom plate with a soluble gypsum chip, as illustrated in Fig. 2(a). Fresh water, injected by a syringe pump, dissolves the gypsum layer from the left, becoming saturated with calcium ions in the process. Gradually, the dissolved region (with aperture h_{max}) appears at the inlet side, while the rest of the system maintains its initial aperture (h_0), as illustrated in Figs. 2(b) and 2(c). The boundary between these two regions, initially planar, becomes unstable due to a reactive-infiltration instability [26,27]: if small perturbations appear in the dissolution front, the flow will increase locally due to the higher mobility. This increased flow carries an undersaturated solution deeper inside the system. As a result, small inhomogeneities tend to grow and transform into highly permeable, fingerlike flow channels, as depicted in Fig. 1(b), similar in shape to the natural solution pipes in Fig. 1(a).

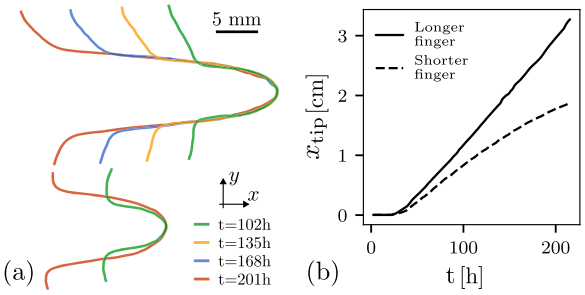

FIG. 3. (a) Outlines of the fingers, $x_f(y,t)$, from the experiment depicted in Fig. 1(b), captured at different moments of time and superposed at the tips. The body of the longer finger retains its shape once it has emerged. The experiment was conducted at a volumetric flow rate $Q_{tot} = 0.5$ ml/h, $h_0 = 210$ μm, and $h_{max} = 710$ μm. (b) The position of the tip versus time, $x_{tip}(t)$.

To investigate the shape of such fingers, we performed microfluidic experiments, introducing small cuts in the gypsum layer near the inlet, to trigger the formation of fingers in those locations [Fig. 1(b)]. We conducted both two-finger and single-finger experiments: the former to quantify the interaction between the fingers, and the latter to capture the invariant shapes of individual fingers.

In the two-finger system (Fig. 3), the individual fingers compete strongly: the longer finger, offering the path of least resistance, captures an ever-increasing portion of the flow at the expense of the shorter one. Interestingly, even though the shorter finger begins to move more slowly as it loses flow, the longer finger does not accelerate [Fig. 3(b)], unaffected by the fact that it is focusing an increasing fraction of the flow injected into the system. This is fundamentally different from most models of fingered growth [28–30] which predict a speedup in the longer finger.

Equally striking is an analysis of the finger shapes. If we trace the boundaries of the fingers at different moments in time and superimpose them in such a way that their tips overlap, we observe that they have been tracing the same invariant shape from the outset [Fig. 3(a)]. Over time, an invariant part of the finger simply shifts in the flow direction, and an increasingly longer invariant finger emerges. Parametrizing the shape of the finger as $x_f(y,t)$ the invariance condition becomes

$$x_f(y,t_1) - x_{tip}(t_1) = x_f(y,t_2) - x_{tip}(t_2), \qquad (1)$$

where $x_{tip}(t)$ is the x position of the tip at time t. Intriguingly, this behavior is observed only in the longer finger. By contrast, the shorter finger does not maintain its shape; a close examination of Fig. 3(a) reveals that it becomes progressively wider as it slows down.

The emergence of invariant shapes can be studied in more detail in single-finger experiments, using a larger aspect ratio microfluidic cell (5 cm × 1 cm). The growing

fingers have a regular shape, becoming more elongated at higher flow rates (Fig. 5). To find the invariant shape theoretically, we start with the equations describing flow and reactant transport in a Hele-Shaw cell. The average velocity $\boldsymbol{v}(x, y)$, comes from a lubrication (narrow aperture) approximation to the Stokes equations:

$$\boldsymbol{v} = -\frac{h^2}{12\mu}\nabla p, \qquad \nabla \cdot (h\boldsymbol{v}) = 0, \tag{2}$$

where ∇ is a two-dimensional gradient operator. The transport of calcium ions in the aqueous phase is described in terms of their undersaturation c, which is the difference between the saturation concentration c_{sat} and the average Ca^{2+} concentration in the fluid film. The vertically averaged concentration field in the fully dissolved finger body is described by the two-dimensional transport equation

$$\nabla \cdot (h_{\max}\boldsymbol{v}c - Dh_{\max}\nabla c) = 0, \tag{3}$$

where D is the diffusion coefficient of the calcium ions. A more detailed derivation can be found in Supplemental Material (SM), Sec. I [31].

Since the widths of the fingers are large, the dissolution process is transport limited. The relevant parameter here is the Damköhler number $\mathrm{Da} = kW^2/Dh_{\max}$ [see Eq. (8) in the SM [31]], where k is the reaction rate constant, and W is the width of the system. In our experiments Da is of the order of 1000; it can be even larger in natural systems such as solution pipes, where the diameter can be of the order of 1 m. Large values of Da indicate that the dissolution reaction is very fast compared to ion diffusion across the finger, implying that the solution saturates essentially instantaneously as it crosses the reaction front separating dissolved and undissolved material. This corresponds to a Dirichlet condition $c = 0$ at the boundary of the finger, and allows us to approximate the finger evolution as a moving boundary (Stefan) problem; a schematic is shown in Fig. 4. The local growth rate of the finger is determined by the diffusive flux of ions at the boundary (see SM, Sec. III [31])

$$u_n(t) = -\alpha D\frac{h_{\max}}{h_{\max} - h_0}(\boldsymbol{n} \cdot \boldsymbol{\nabla} c)_\Gamma, \tag{4}$$

where $\boldsymbol{n}$ is the outward normal to the finger boundary Γ. The coefficient $\alpha = \nu_{\mathrm{m}}/(1-\varphi)$ converts the flux of ions into a dissolved volume; it is determined by the molar volume (ν_{m}) and the porosity (φ) of the soluble material.

Solutions of Eq. (3) are characterized by the dimensionless Péclet number, which is a measure of the relative importance of advective and diffusive transport, $\mathrm{Pe} = Q_{\mathrm{tot}}/(Dh_{\max})$, where Q_{tot} is the total volumetric flow rate entering the system [see Eq. (9) in the SM]; in our experiments, Péclet numbers are in the range 50–500. For large Péclet numbers the fingers are strongly elongated, with a small aspect ratio, $w'(x) = \mathrm{d}w/\mathrm{d}x \ll 1$. One can

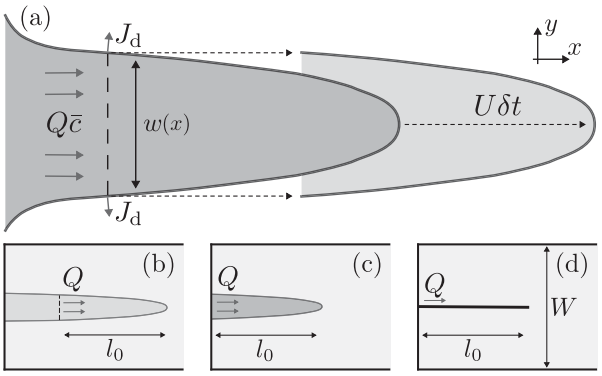

FIG. 4. (a) Schematic view of a single dissolution finger with a width profile $w(x)$, diffusive flux J_{d}, volumetric flow rate Q through the finger cross section, and total concentration flux $Q\bar{c}$ through the cross section. (b)–(d) Because of the invariance of the tip, the flow through a cross section located at distance l_0 from the tip of any finger (b), should be the same as the flow through the base of a finger of length l_0 (c). The total flow through the finger base is estimated analytically by approximating a finger with a thin line of the same length (d).

then assume that the flow rate and concentration profiles are locally analogous to those between the two parallel absorbing walls separated by distance $w(x)$. The flow is then simply a plug flow

$$\boldsymbol{v}(x, y) = \frac{Q(x)}{w(x)h_{\max}}\boldsymbol{e}_x + \mathcal{O}(w'(x))\boldsymbol{e}_y, \tag{5}$$

where $Q(x)$ is the total flow through the finger cross section at x. The problem of finding the concentration profile between two parallel absorbing walls is known as the Graetz problem [38], and for plug flow (5) the slowest spatially decaying mode is of the form [39]

$$c(x, y) = \frac{\pi\bar{c}(x)}{2}\cos\frac{\pi y}{w(x)}, \tag{6}$$

where axial diffusion has been neglected. In Eq. (6), $\bar{c}(x)$ is the average undersaturation in a cross section of the finger perpendicular to the direction of flow.

The flux of calcium ions within a cross section of the finger contains contributions from ion advection $Q\bar{c}$ and the diffusive fluxes, which are absorbed at the finger boundary, $J_{\mathrm{d}}(x) = -Dh_{\max}\boldsymbol{n} \cdot \boldsymbol{\nabla} c$ [Fig. 4(a)]. The latter can be approximated as $J_{\mathrm{d}}(x) = -Dh_{\max}\partial_y c$ by neglecting terms $\mathcal{O}(w'(x))$, as in Eq. (5). For steady state transport these fluxes balance:

$$(Q\bar{c})' = -Dh_{\max}\bar{c}\frac{\pi^2}{w}. \tag{7}$$

Next, we make use of the observation that the emerging body of the finger keeps its shape and translates only [Eq. (1)]. Points along the boundary move with the same x

velocity U, which is linked with the normal growth rate (4) by $u_n = Un_x$. In particular, this means that downstream of any cross section, the total volume of gypsum dissolved over time δt is $U(h_{\max} - h_0)w(x)\delta t$. This must be proportional to the incoming number of ions $Q\bar{c}(x)\delta t$ with proportionality constant α (Fig. 4):

$$U(h_{\max} - h_0)w = \alpha Q\bar{c}. \tag{8}$$

The volumetric flux inside a finger of length l, $Q(x, l)$, is constrained by the observation that the shape of the finger, starting from its tip ($x_{\text{tip}} = l$), remains the same during its evolution. This identity in shape implies that the flow field should also remain unchanged (SM, Sec. III [31]); thus $Q(x, l)$ should be a function of the distance from the tip only $Q(x, l) = Q(x_{\text{tip}}(t) - x)$. In particular, as shown in Figs. 4(b) and 4(c), the total flow through the base ($x = 0$) of the finger of length l_0, $Q(0, l_0) \equiv Q_0(l_0)$, should be the same as the flow at the cross section $x = x_{\text{tip}} - l_0$ of the same finger, captured at the later time

$$Q(x_{\text{tip}}(t) - l_0) = Q_0(l_0). \tag{9}$$

To calculate $Q_0(l_0)$, we approximate the finger by an infinitely thin line confined to a channel of width W [Fig. 4(d)], and use conformal mapping to derive the corresponding pressure field analytically. Even though the thin-finger approximation will not be an entirely faithful representation of the flow field near the finger, global quantities, such as the total flow focused in the finger, should be represented with good accuracy, as they primarily depend on the length of the finger.

The volumetric flux entering the finger base can be expressed as $Q_0(l_0) = Q_{\text{tot}} f(l_0/W)$ where W is the width of the Hele-Shaw cell. The function $f(\xi)$ can be determined from the pressure field derived in [40], by integrating the leakage flux around the exterior of the finger:

$$f(\xi) = 1 - \frac{2}{\pi}\arctan[\operatorname{csch}(\pi\xi)]. \tag{10}$$

Combining (7), (8) and (10) we get the slope of the finger

$$\frac{\mathrm{d}w}{\mathrm{d}\tilde{x}} = \frac{Dh_{\max}\pi^2}{Q_0(\tilde{x})} = \frac{\pi^2}{\mathrm{Pe}} f(\tilde{x}/W)^{-1}, \tag{11}$$

where $\tilde{x} = x_{\text{tip}} - x$ is the distance from the tip. The shape is then obtained as an integral of (11):

$$w(\tilde{x}) - w_0 = \frac{\pi^2}{\mathrm{Pe}} \int_{x_0}^{\tilde{x}} f(\zeta/W)^{-1}\mathrm{d}\zeta. \tag{12}$$

Since Eq. (11) defines only the slope of the finger, Eq. (12) includes an additional degree of freedom, corresponding to a translation of the entire shape by w_0.

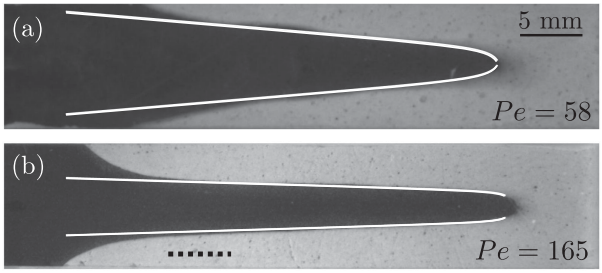

FIG. 5. Experimentally generated dissolution fingers with the theoretically predicted shapes (white) based on Eq. (12). The experimental parameters are (a) $Q_{\text{tot}} = 0.12$ ml/h, $h_0 = 70$ μm and $h_{\max} = 570$ μm, and (b) $Q_{\text{tot}} = 0.16$ ml/h, $h_0 = 70$ μm and $h_{\max} = 270$ μm. The black dashed line indicates the region in which the total flow in the finger can be estimated from the slope.

Additionally, the location of x_{tip} should be adjusted to account for the transition from a finite size finger to the needle shape used in the conformal mapping.

Equation (12) describes the body of the finger, apart from the tip. A comparison of the predicted shape with experimental observations is indicated by the white lines in Fig. 5. However, the same approach cannot be applied in the tip region for two reasons. First, the assumption of a large aspect ratio, $w'(x) \ll 1$, no longer holds near the tip. Second, the separation between reactive and diffusive timescales (and corresponding length scales) no longer holds. Near the tip, the flow becomes focused by the converging boundaries of the finger. The penetration length l_p (Fig. 2) increases due to the higher fluid velocity, and becomes comparable to the radius of curvature of the tip. Hence, a two-phase approximation with a sharp interface is not applicable in this region. Existing models of dissolution finger tips [41,42] assume a sharp interface and therefore depend only on the Péclet number. A proper theory of the tip shape should involve both Péclet and Damköhler numbers and would require resolving the partially dissolved region between the two phases. Such a solution could then be matched with the solution for the body at x_0.

Still, a number of conclusions can be drawn based on Eq. (12) alone. In particular, sufficiently far from the tip, the flow saturates to Q_{tot} with the corresponding slope $w' = \pi^2/\mathrm{Pe}$. This suggests the possibility of deducing the flow rate in the finger from its shape. Such measurements should be taken as far from the tip as possible but not too close to the base, where concave inlet structures connecting the finger to the system edges become noticeable. A suitable location is indicated by the black dashed line in Fig. 5(b).

The model can also be employed to understand the dynamics of interacting fingers. The key lies in Eq. (9), which shows that to maintain the invariance of the finger, the flow through any cross section comoving with the tip must be kept constant. When a finger wins the competition, and the flow through its base (Q_0) increases, it is easy to

meet the invariant flow condition by redirecting part of the excess flow to the sides of the finger. As for the shorter finger, since it is losing the competition, the flow entering its base decreases, making it impossible to maintain the same flow rates in its body. Lower flows result in higher slopes of the finger sides [cf. Eq. (11)], causing the finger to become more bulky with time.

To interpret natural forms, such as the solution pipes shown in Fig. 1, we must consider three spatial dimensions. Here, the invariance condition gives an equation for the radius of the pipe $a(x)$ as a function of volumetric flow rate through the cross section (see SM, Sec. IV [31]):

$$\frac{\mathrm{d}a}{\mathrm{d}x} = -\frac{\pi a D}{2Q}(j_{0,1})^2, \tag{13}$$

where $j_{0,1}$ is the first zero of the Bessel function J_0. From this equation, we can estimate the flow in natural fingers, as described earlier.

Taking as an example the solution pipe in Fig. 1(a), the slope of the sides, $\mathrm{d}a/\mathrm{d}x$ is about $1/10$, which gives the characteristic Péclet number, $\mathrm{Pe} = Q/Da \approx 100$. Taking the diffusion constant of calcium ions as $D = 10^{-5}$ cm^2/s and the pipe radius $a \approx 30$ cm gives an average velocity of about 10^{-5} cm/s, which is a reasonable value [43], given the high porosity and permeability of the underlying rocks [44].

In practice we rarely encounter fingers in isolation or in pairs; instead, we observe an entire group, as depicted in SM, Fig. S1 (microfluidic experiment) or Fig. S3 (natural forms). For the finger to keep its shape, we need only to ensure that the volumetric flow to the base of a given finger does not decrease over time. This can be easily achieved if the finger locally outcompetes its neighbors. Therefore, we can identify the fingers that are locally the longest (e.g., in Fig. S1C, there are five such fingers), measure their slopes, and average the results over the group.

In this Letter, we have summarized experimental results showing that an individual dissolution finger emerges with a shape that is invariant from its inception. This is different from the classical Saffman-Taylor finger, which only obtains its invariant shape at long times. We presented an analysis, based on reactive-transport theory, that allowed us to describe this invariant shape. Field measurements of the slope of the solution pipe allow us to estimate the flow in natural fingers during their formation. This may provide information about the environmental conditions under which they developed.

Acknowledgments—This work was supported by the National Science Centre (NCN; Poland) under CEUS-UNISONO Grant No. 2020/02/Y/ST3/00121. The work of A. L. was supported by the U.S. Department of Energy, Office of Science, Office of Basic Energy Sciences, Geosciences program under Award No. DE-SC0018676. We thank C. Josserand, M. Lipar, K. Mizerski, J. Piasecki, and Y. Pomeau for helpful discussions. We gratefully acknowledge the help of Prof. Piotr Garstecki group (Institute of Physical Chemistry, Polish Academy of Sciences) in setting up the microfluidic experiments.

[1] P. J. Ortoleva, *Geochemical Self-Organization* (Oxford University Press, New York, 1994).
[2] B. Jamtveit and P. Meakin, *Growth, Dissolution and Pattern Formation in Geosystems* (Springer, New York, 1999).
[3] B. Jamtveit and O. Hammer, Sculpting of rocks by reactive fluids, Geochem. Perspect. **1**, 341 (2012).
[4] A. P. Petroff, O. Devauchelle, D. M. Abrams, A. E. Lobkovsky, A. Kudrolli, and D. H. Rothman, Geometry of valley growth, J. Fluid Mech. **673**, 245 (2011).
[5] L. Ristroph, M. N. Moore, S. Childress, M. J. Shelley, and J. Zhang, Sculpting of an erodible body by flowing water, Proc. Natl. Acad. Sci. U.S.A. **109**, 19606 (2012).
[6] B. D. Quaife and M. N. J. Moore, A boundary-integral framework to simulate viscous erosion of a porous medium, J. Comput. Phys. **375**, 1 (2018).
[7] D. J. Jerolmack and K. E. Daniels, Viewing Earth's surface as a soft-matter landscape, Nat. Rev. Phys. **1**, 716 (2019).
[8] W. Dreybrodt, The role of dissolution kinetics in the development of karst aquifers in limestone: A model simulation of karst evolution, J. Geol. **98**, 639 (1990).
[9] A. Ginés, M. Knez, T. Slabe, and W. Dreybrodt, *Karst Rock Features. Karren Sculpturing: Karren Sculpturing* (Založba ZRC, 2009), Vol. 9.
[10] P. Szymczak and A. J. C. Ladd, The initial stages of cave formation: Beyond the one-dimensional paradigm, Earth Planet. Sci. Lett. **301**, 424 (2011).
[11] A. Guérin, J. Derr, S. Courrech Du Pont, and M. Berhanu, Streamwise dissolution patterns created by a flowing water film, Phys. Rev. Lett. **125**, 194502 (2020).
[12] J. M. Huang, J. Tong, M. Shelley, and L. Ristroph, Ultra-sharp pinnacles sculpted by natural convective dissolution, Proc. Natl. Acad. Sci. U.S.A. **117**, 23339 (2020).
[13] J. De Waele, S.-E. Lauritzen, and M. Parise, On the formation of dissolution pipes in quaternary coastal calcareous arenites in mediterranean settings, Earth Surf. Processes Landforms **36**, 143 (2011).
[14] M. Lipar, P. Szymczak, S. Q. White, and J. A. Webb, Solution pipes and focused vertical water flow: Geomorphology and modelling, Earth-Sci. Rev. **218**, 103635 (2021).
[15] P. Meakin, *Fractals, Scaling and Growth Far From Equilibrium* (Cambridge University Press, Cambridge, England, 1998).
[16] P. Pelcé, *New Visions on Form and Growth: Fingered Growth, Dendrites, and Flames* (Oxford University Press, New York, 2004).
[17] P. G. Saffman and G. Taylor, The penetration of a fluid into a porous medium or Hele-Shaw cell containing a more viscous liquid, Proc. R. Soc. A **245**, 312 (1958).
[18] G. Ivantsov, The temperature field around a spherical, cylindrical, or pointed crystal growing in a cooling solution, Dokl. Akad. Nauk SSSR **58**, 567 (1947).

[19] Y. B. Zeldovich, A. G. Istrtov, N. I. Kidin, and V. B. Librovich, Flame propagation in tubes: Hydrodynamics and stability, J. Cryst. Growth **24**, 1 (1980).
[20] P. Pelce and A. Pumir, Cell shape in directional solidification in the small Péclet number limit, J. Cryst. Growth **73**, 337 (1985).
[21] M. B. Short, J. C. Baygents, J. W. Beck, D. A. Stone, R. S. Toomey III, and R. E. Goldstein, Stalactite growth as a free-boundary problem: A geometric law and its platonic ideal, Phys. Rev. Lett. **94**, 018501 (2005).
[22] M. B. Short, J. C. Baygents, and R. E. Goldstein, A free-boundary theory for the shape of the ideal dripping icicle, Phys. Fluids **18**, 083101 (2006).
[23] A. S.-H. Chen and S. W. Morris, Experiments on the morphology of icicles, Phys. Rev. E **83**, 026307 (2011).
[24] J. Mac Huang and N. J. Moore, Morphological attractors in natural convective dissolution, Phys. Rev. Lett. **128**, 024501 (2022).
[25] N. Goldenfeld, P. Y. Chan, and J. Veysey, Dynamics of precipitation pattern formation at geothermal hot springs, Phys. Rev. Lett. **96**, 254501 (2006).
[26] D. Chadam, P. Ortoleva, and A. Sen, A weakly nonlinear stability analysis of the reactive infiltration interface, SIAM J. Appl. Math. **48**, 1362 (1988).
[27] P. Szymczak and A. J. C. Ladd, Reactive-infiltration instabilities in rocks. Fracture dissolution, J. Fluid Mech. **702**, 239 (2012).
[28] J. Krug, K. Kessner, P. Meakin, and F. Family, Laplacian needle growth, Europhys. Lett. **24**, 527 (1993).
[29] J. Krug, Origin of scale invariance in growth processes, Adv. Phys. **46**, 139 (1997).
[30] Y. Cabeza, J. J. Hidalgo, and J. Carrera, Competition is the underlying mechanism controlling viscous fingering and wormhole growth, Geophys. Res. Lett. **47**, e2019GL08479 (2020).
[31] See Supplemental Material at http://link.aps.org/supplemental/10.1103/PhysRevLett.134.094101 for derivations, which includes Refs. [32–37].
[32] F. Osselin, A. Budek, O. Cybulski, P. Kondratiuk, G. P., and P. Szymczak, Microfluidic observation of the onset of reactive in infiltration instability in an analog fracture, Geophys. Res. Lett. **43**, 6907 (2016).
[33] J. Colombani, Measurement of the pure dissolution rate constant of a mineral in water, Geochim. Cosmochim. Acta **72**, 5634 (2008).
[34] L. N. Plummer, T. L. M. Wigley, and D. L. Parkhurst, The kinetics of calcite dissolution in CO_2-water systems at 5°C to 60°C and 0.0 to 1.0 atm of CO_2, Am. J. Sci. **278**, 179 (1978).
[35] F. Dutka, V. Starchenko, F. Osselin, S. Magni, P. Szymczak, and A. J. C. Ladd, Time-dependent shapes of a dissolving mineral grain: Comparisons of simulations with microfluidic experiments, Chem. Geol. **540**, 119459 (2020).
[36] A. J. C. Ladd and P. Szymczak, Use and misuse of large-density asymptotics in the reaction-infiltration instability, Water Resour. Res. **53**, 2419 (2017).
[37] V. Balakotaiah, Hyperbolic averaged models for describing dispersion effects in chromatographs and reactors, Korean J. Chem. Eng. **21**, 318 (2004).
[38] R. Bird, W. Stewart, and E. Lightfoot, *Transport Phenomena* (John Wiley, New York, 2002).
[39] Y. Muzychka, E. Walsh, and P. Walsh, Simple models for laminar thermally developing slug flow in noncircular ducts and channels, J. Heat Transfer **132**, 111702 (2010).
[40] T. Gubiec and P. Szymczak, Fingered growth in channel geometry: A Loewner-equation approach, Phys. Rev. E **77**, 041602 (2008).
[41] R. H. Nilson and S. K. Griffiths, Wormhole growth in soluble porous materials, Phys. Rev. Lett. **65**, 1583 (1990).
[42] P. Kondratiuk and P. Szymczak, Steadily translating parabolic dissolution fingers, SIAM J. Appl. Math. **75**, 2193 (2015).
[43] S. Earle, *Physical Geology* (BCcampus, 2019).
[44] R. P. Sharma, M. Białecki, M. P. Cooper, A. P. Radliński, and P. Szymczak, Pore merging and flow focusing: Comparative study of undissolved and karstified limestone based on microtomography, Chem. Geol. **627**, 121397 (2023).

Supplemental material for *Invariant forms of dissolution fingers*

Stanisław Żukowski,[1,2] Silvana Magni,[1] Florian Osselin,[3] Filip Dutka,[1] Max Cooper,[1] Anthony J. C. Ladd,[4] and Piotr Szymczak[1]

[1] *Institute of Theoretical Physics, Faculty of Physics, University of Warsaw, Pasteura 5, 02-093 Warsaw, Poland*
[2] *Laboratoire Matière et Systèmes Complexes (MSC), UMR 7057, CNRS & Université Paris Cité, 10 rue Alice Domon et Léonie Duquet, 75013 Paris, France*
[3] *Institut des Sciences de la Terre, Orleans, France*
[4] *Chemical Engineering Department, University of Florida, Gainesville FL 32611, USA*

Here we derive equations describing the invariant propagation of a dissolution finger in a Hele-Shaw cell with a soluble base. A sketch of the experimental cell [1] is shown in the paper (Fig. 2). Fluid is injected in the narrow gap between the inert (polycarbonate) top layer and the soluble (gypsum) bottom layer (Figs. 2 b-c). The gypsum layer near the inlet dissolved rapidly (Fig. 2b), on a timescale of about 10 hours, to create a step profile extending over a distance of the order of 1 mm (Fig. 2c). The profile is uniform in the transverse (y) direction and at first propagates slowly downstream, on timescales up to a few days [1]. However, over longer times perturbations appear in the front (Fig. S1a), which eventually develop into well formed fingers (Fig. S1 b-c) that slowly coarsen over time. Results from those experiments are shown in Figs. 1b, 3, and 5. This document is largely a compendium of published results, which we have assembled for the convenience of readers desiring a more in depth description of the physics outlined in the main paper.

I. GOVERNING EQUATIONS

Gypsum dissolution,

$$\mathrm{CaSO_4(s)} \rightarrow \mathrm{Ca^{2+}} + \mathrm{{SO_4}^{2-}}, \tag{1}$$

has a particularly simple kinetics [2], which to a good approximation is linear in the undersaturation of calcium ions, $c = c_{\mathrm{sat}} - [\mathrm{Ca^{2+}}]$. The dissolution rate (the number of dissolved molecules per unit area and unit time) is then

$$R(c) = kc, \tag{2}$$

where k is the reaction rate constant, which can include corrections for the diffusional hindrance across the concentration boundary layer. A similar, product-controlled reaction kinetics is also appropriate for other minerals, such as halite (dissolved by water) or limestone dissolved by groundwater [3]. The rate constant for gypsum dissolution by distilled water is $k = 4.5 \times 10^{-4}$ cm/s [2, 4].

The dissolution reaction on the gypsum surface gives rise to an increase in aperture,

$$\partial_t h = \alpha k c \theta(h_{\max} - h), \tag{3}$$

where $\alpha = \nu_{\mathrm{m}}/(1-\varphi)$ is the volume (per mole) occupied by the solid phase; it is determined by the molar volume (ν_{m}) and the porosity (φ) of the soluble material [1]. The function θ is a step function; $\theta(x) = 1$ if $x > 0$ and zero otherwise. The large volume of solution needed to dissolve a given volume of mineral establishes a time scale separation between changes in aperture and the evolution of the flow and concentration fields, which can therefore be treated as stationary [5].

The thin film (or lubrication) approximation is used to describe flow and reactant transport in the Hele-Shaw cell. The average velocity $\boldsymbol{v}$ and concentration c are related to integrals over the aperture:

$$\boldsymbol{v}h = \int_0^h \boldsymbol{u}\mathrm{d}z, \quad \boldsymbol{v}hc = \int_0^h \boldsymbol{u}c\mathrm{d}z, \tag{4}$$

where $\boldsymbol{u}(x,y,z)$ is the three-dimensional flow field. After integrating over the fracture aperture (z-direction):

$$\boldsymbol{v} = -\frac{h^2}{12\eta}\boldsymbol{\nabla} p, \tag{5}$$

$$\boldsymbol{\nabla}\cdot(\boldsymbol{v}hc) = \boldsymbol{\nabla}\cdot(Dh\boldsymbol{\nabla}c) - kc\,\theta(h_{\max}-h), \tag{6}$$

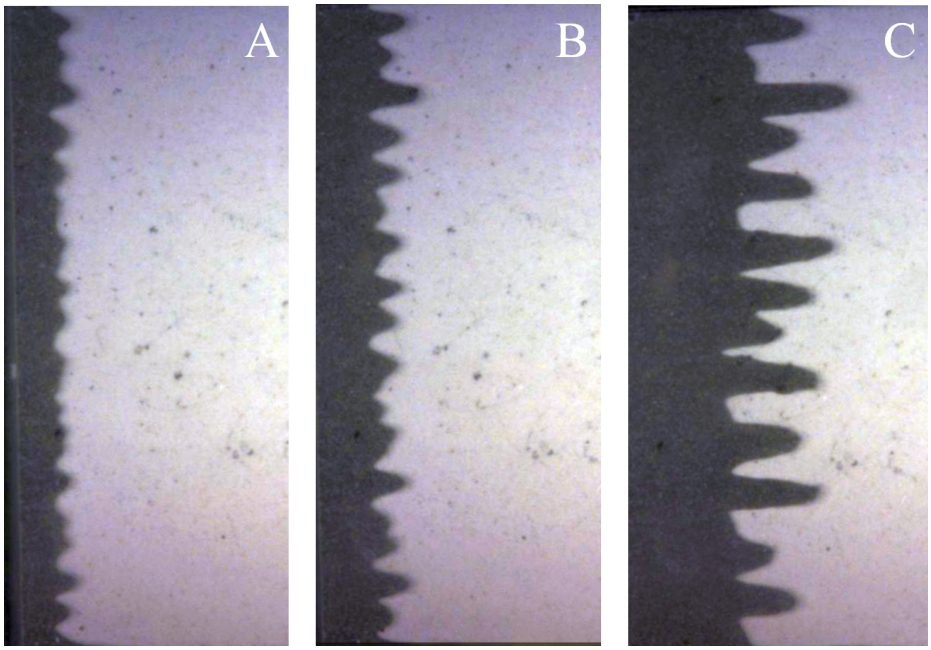

Figure S1. Evolution of the dissolution patterns in the microfluidic experiments. The flow enters from the left and progressively dissolves the gypsum block. The front between the dissolved area (black) and the undissolved area (white) becomes unstable, causing the dissolution to focus into fingers.

where $\boldsymbol{\nabla}$ is the two-dimensional (xy) gradient operator. We ignore the numerically small distinction between the velocity averaged concentration, which appears in the convective flux, and the average concentration in the diffusive flux [6].

Although equations (3)–(6) have a simple solution, with a uniform reactive front $h(x,t)$ propagating from inlet to outlet, they are linearly unstable to transverse perturbations in the aperture field [7]. Over time the front breaks down into interacting fingers (Fig. S1) with a wavelength controlled by the flow and reaction rate. The wavelength calculated from linear stability analysis [8] is in good agreement with the initial dissolution patterns observed experimentally [1]. In the later stages of evolution, the fingers begin to interact with each other. Two processes take place: one is the competition of the fingers for the flow, causing the longer ones to advance ahead of the shorter ones. The other is the merging of the fingers, reducing their total number. As a result, as shown in Fig. S1, the pattern coarsens. In the long-time limit, a single finger would emerge. However, observing the entire dynamics – from the formation of the initial instabilities to the emergence of one or two fingers – would require experiments in a very long system, which is technically unfeasible. Therefore, to analyze the interaction between two fingers or the growth of a single finger, we initialize growth in specific (y) locations by making small cuts in the gypsum at the inlet. The cuts are placed symmetrically, either a single one at the centerline of the system (for one-finger systems) or two at equal distances from the centerline (for two-finger systems).

Equation (6) can be written in dimensionless form by scaling coordinates with the width of the channel W, velocity by its average value $v_0 = Q_{\rm tot}/(Wh_{\rm max})$, aperture by $h_{\rm max}$, and concentration by $c_{\rm sat}$. Denoting the scaled variables with a hat, the dimensionless Eq. (6) is:

$$\mathrm{Pe}\,\hat{\nabla}\cdot(\hat{\boldsymbol{v}}\hat{h}\hat{\boldsymbol{\nabla}}\hat{c}) = \hat{\boldsymbol{\nabla}}\cdot\hat{h}\hat{\boldsymbol{\nabla}}\hat{c} - \mathrm{Da}\,\hat{c}, \tag{7}$$

where

$$\mathrm{Da} = \frac{kW^2}{Dh_{\rm max}}, \tag{8}$$

and

$$\mathrm{Pe} = \frac{v_0 W}{D} = \frac{Q_{\rm tot}}{Dh_{\rm max}}. \tag{9}$$

II. INVARIANT FINGERS

Equations (3)-(6) allow for invariant solutions for the aperture field in the coordinate system comoving with the finger tip:

$$\tilde{x} = x - x_{\mathrm{tip}}(t). \tag{10}$$

The aperture evolution, Eq. (3), in this coordinate system is

$$-U(t)\partial_{\tilde{x}} h = \alpha k c \theta(h_{\max} - h), \tag{11}$$

where $U(t) = \mathrm{d}x_{\mathrm{tip}}/\mathrm{d}t$. If h is to be invariant in the comoving frame, then $\partial_{\tilde{x}} h$ is time independent, which implies that the concentration field depends on time only through $U(t)$. Since in the comoving frame c can be written as a product of time and space dependent functions, and h is time independent, it follows from Eq. (6) that the flow field $\boldsymbol{v}$ must also be time-independent in the comoving frame. Thus the shape of the finger can remain invariant, even when the propagation velocity $U(t)$ is changing in time.

III. THIN-FRONT LIMIT

Away from the tip, the thickness of the interface between dissolved and undissolved material is controlled by the balance between diffusion of reactant from the fully dissolved finger body, which is of the order of $Dh_{\max}\partial_y^2 c$, and the rate of consumption as the reactant encounters the undissolved solid, kc. The reactant is consumed over a length scale $\sqrt{Dh_{\max}/k} \approx 0.05$ cm, which is much smaller than the width of the finger body (≈ 1 cm). Hence, we can replace the aperture field by a boundary separating fully dissolved ($h = h_{\max}$) and entirely undissolved ($h = h_0$) material. Within the finger there is no reaction, and Eq. (6) from the SM reduces to Eq. (3) in the paper. Outside the boundary, the water is fully saturated ($c = 0$). The state of the system is then specified by the position of the boundary, $x_{\mathrm{f}}(y,t)$, and the invariance condition reduces to Eq. (1) in the paper.

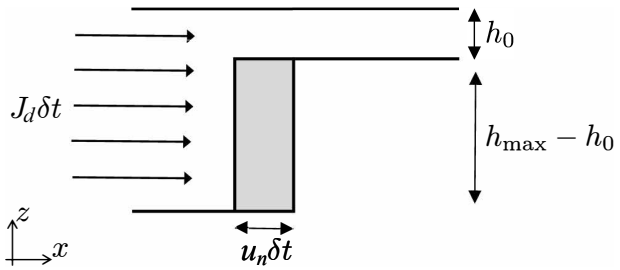

Figure S2. Cross section of the system in xz plane in the thin-front limit. Over the time interval δt, $J_d\delta t$ molecules of the reactant (per unit length in the y direction) dissolve the volume of $\nu_{\mathrm{m}} J_d \delta t$ of the mineral (marked in gray), which can also be expressed as $(1-\varphi)(h_{\max} - h_0)u_n\delta t$. The comparison of both expression for the dissolved volume leads to Eq. (12).

In the thin-front limit, the advancement of the boundary between the phases is linked to the flux of reactant at a given point $\boldsymbol{r}_{\mathrm{f}} = (x_{\mathrm{f}}(y), y)$

$$u_n = \boldsymbol{n} \cdot \frac{\mathrm{d}\boldsymbol{r}_{\mathrm{f}}}{\mathrm{d}t} = -\frac{\alpha}{(h_{\max} - h_0)} D h_{\max} \left(\nabla c\right)_n , \tag{12}$$

where the subscript n indicates the component normal to the interface. Only the (depth-integrated) diffusive flux $J_{\mathrm{d}} = -Dh_{\max}\nabla c$ is present in Eq. (12). Since the concentration at the front vanishes, so does the convective contribution to the flux. The front velocity (12) is then obtained from the flux by observing that the total volume dissolved by the reactant crossing the reaction front over a time δt, can be expressed, on one hand, as $\nu_{\mathrm{m}} J_{\mathrm{d}} \delta t$, and, on the other, as $(1-\varphi)(h_{\max} - h_0)u_n\delta t$ (see Fig. S2).

IV. INVARIANT FINGERS IN THREE DIMENSIONS

For the interpretation of natural forms, such as the solution pipes shown in Fig. 1 or Fig. S3, we must consider three spatial dimensions. Here, the invariance condition becomes

$$U\pi a^2 = \alpha Q \bar{c}, \tag{13}$$

while the transport equation is now

$$\frac{\partial(v_x c)}{\partial x} = D\frac{1}{r}\frac{\partial}{\partial r}r\left(\frac{\partial c}{\partial r}\right), \tag{14}$$

where x is the axial direction of the pipe, r is the radial coordinate and $a(x)$ is the radius of the pipe. If the pipe is treated as locally uniform, Eq. (14) can again be solved by separation of variables. For the slowest decaying mode

$$c(r,x) = \frac{\bar{c}(x) j_{0,1}}{2J_1(j_{0,1})} J_0\left(j_{0,1}\frac{r}{a}\right), \tag{15}$$

where J_n denotes a Bessel function of the first kind, and $j_{0,1}$ is the first zero of J_0. Similarly to the two-dimensional case, we will use this solution also for a nonuniform radius, $a(x)$, assuming that $\mathrm{d}a/\mathrm{d}x \ll 1$.

Combining an integration over r of Eq. (14),

$$(Q\bar{c})' = -D\pi\bar{c}(j_{0,1})^2, \tag{16}$$

with the invariance condition (13) gives the shape equation:

$$\frac{\mathrm{d}a}{\mathrm{d}x} = -\frac{\pi a D}{2Q}(j_{0,1})^2. \tag{17}$$

Figure S3. Group of soil-filled solution pipes in Canunda National Park, Australia. The photo is courtesy of Ken Grimes.

[1] F. Osselin, A. Budek, O. Cybulski, P. Kondratiuk, G. P., and P. Szymczak, Microfluidic observation of the onset of reactive in infiltration instability in an analog fracture, Geophys. Res. Lett. **43**, 6907 (2016).

[2] J. Colombani, Measurement of the pure dissolution rate constant of a mineral in water, Geochim. Cosmochim. Acta **72**, 5634 (2008).

[3] L. N. Plummer, T. L. M. Wigley, and D. L. Parkhurst, The kinetics of calcite dissolution in CO2-water systems at 5 °C to 60 °C and 0.0 to 1.0 atm of CO2, Am. J. Sci. **278**, 537 (1978).

[4] F. Dutka, V. Starchenko, F. Osselin, S. Magni, P. Szymczak, and A. J. C. Ladd, Time-dependent shapes of a dissolving mineral grain: comparisons of simulations with microfluidic experiments, Chem. Geol. **540**, 119459 (2020).

[5] A. J. C. Ladd and P. Szymczak, Use and misuse of large-density asymptotics in the reaction-infiltration instability, Water Resour. Res. **53**, 2419 (2017).

[6] V. Balakotaiah, Hyperbolic averaged models for describing dispersion effects in chromatographs and reactors, Korean J. Chem. Eng. **21**, 318 (2004).
[7] P. Szymczak and A. J. C. Ladd, The initial stages of cave formation: Beyond the one-dimensional paradigm, Earth Planet. Sci. Lett. **301**, 424 (2011).
[8] P. Szymczak and A. J. C. Ladd, Reactive-infiltration instabilities in rocks. Fracture dissolution, J. Fluid Mech. **702**, 239 (2012).

Chapter 3

Paper II: "Through history to growth dynamics: deciphering the evolution of spatial networks"

Author contributions

In this study, the author: implemented numerical tools to model network growth and performed network simulations, developed the backward evolution algorithm to extract growth laws from network geometry, validated it on simulated networks and applied it to real river network, analyzed and interpreted data, prepared figures, wrote the first draft, and co-edited all subsequent versions of the paper.

scientific reports

Check for updates

OPEN

Through history to growth dynamics: deciphering the evolution of spatial networks

Stanisław Żukowski[1,2], Piotr Morawiecki[3], Hansjörg Seybold[4] & Piotr Szymczak[1]✉

Many ramified, network-like patterns in nature, such as river networks or blood vessels, form as a result of unstable growth of moving boundaries in an external diffusive field. Here, we pose the inverse problem for the network growth—can the growth dynamics be inferred from the analysis of the final pattern? We show that by evolving the network backward in time one can not only reconstruct the growth rules but also get an insight into the conditions under which branch splitting occurs. Determining the growth rules from a single snapshot in time is particularly important for growth processes so slow that they cannot be directly observed, such as growth of river networks and deltas or cave passages. We apply this approach to analyze the growth of a real river network in Vermont, USA. We determine its growth rule and argue that branch splitting events are triggered by an increase in the tip growth velocity.

Many of the natural patterns are in the form of branched networks: from river networks or cave conduits, mineral dendrites, and viscous fingering patterns to biological systems such as blood vessels or leaf venation[1,2] (Fig. 1). The physical forces driving their growth vary from system to system: erosion, diffusion, and thermal conduction, to name just a few[3]. Despite these differences, there are many features which these networks share, which suggests a common underlying growth mechanism[4–6].

A prominent feature of network growth is the close coupling between geometry and dynamics. The field driving the growth and the network co-evolve in time, as the evolving network changes the boundary conditions for the field. Evolving the network in response to the surrounding field involves two major processes: (i) extension of the branches and (ii) bifurcation of a tip into two (or more) branches. To understand the co-evolution of the network and the field, it is important to understand how the extension and bifurcation processes are linked to the characteristics of the driving fields such as the gradient of the field in the vicinity of the tip. Once the *growth rules* are known, we can predict the evolution of the network geometry based on its configuration at an earlier time.

Such procedure has been applied to river networks[9–13], river deltas[14], viscous fingers[15], discharge trees[16] or coral growth[17], leading to network geometries qualitatively and quantitatively similar to those observed in nature. However, in many practical cases, the details of the growth rules are unknown. If, in addition, the temporal evolution of the pattern is exceedingly slow and can only be observed at a single instance of time, determining growth rules from a single snapshot in time becomes a necessity. This gives rise to the following question: can we deduce the growth rules from an instantaneous snapshot of the network geometry? In fact, even a single snapshot of a network configuration contains information about its growth history, which is inherently linked to growth dynamics.

For example, streets in cities are historically built in succession—the oldest being the longest and going through the whole city, and the younger extending from the first ones. To extract historical information from city maps, Lagesse et al.[18] used a multiscale approach exploiting local geometry and alignment at road crossings.

Geological systems, such as river networks, evolve over even longer time scales. They extend through erosion at the channel heads at a rate of less than a few millimeters per year[19]. One idea for deciphering the growth law in these systems is through a backward-forward approach. First, the network is grown backward in time using a parameterization of the growth rule with an initial set of parameters, and then it is grown forward in time again. Analyzing the correlation of the flux coming to the tips and the orientation of the branches after the backward-forward step, one can determine the optimal set of parameters that best replicates the initial network geometry[11].

[1]Institute of Theoretical Physics, Faculty of Physics, University of Warsaw, Warsaw, Poland. [2]Laboratoire Matière et Systèmes Complexes (MSC), UMR 7057, CNRS & Université Paris Cité, Paris, France. [3]Department of Mathematical Sciences, University of Bath, Bath, UK. [4]Department of Environmental System Science, ETH Zürich, Zürich, Switzerland. ✉email: piotr.szymczak@fuw.edu.pl

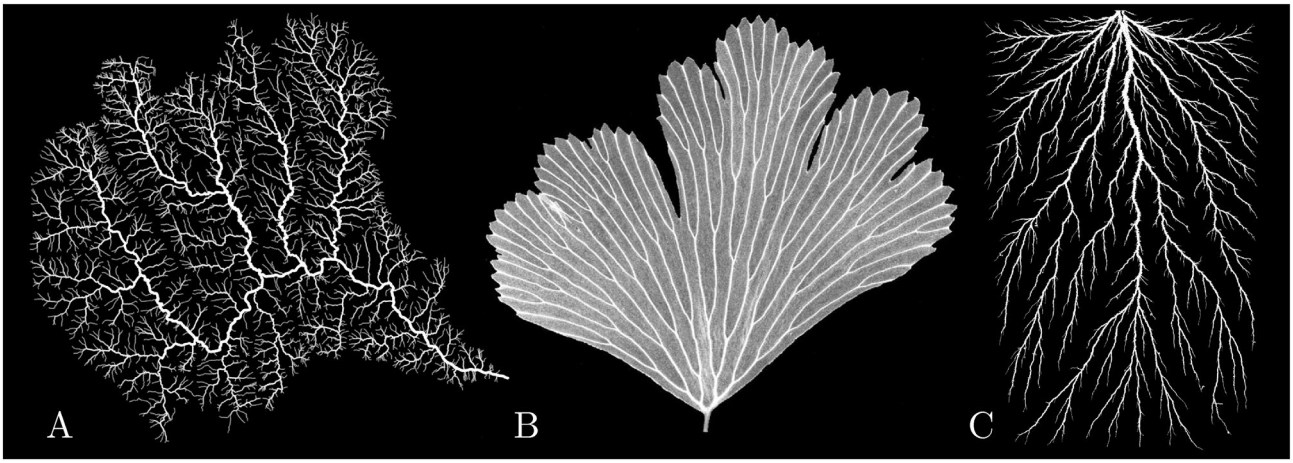

Figure 1. Examples of branched spatial networks in nature: (**A**) White River basin in Vermont, USA[7] (**B**) Adiantum leaf (photo: Jim Mattsson, Simon Fraser University, by permission) (**C**) Lichtenberg figure[8].

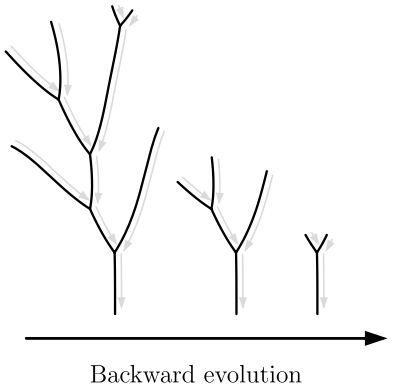

Figure 2. The backward evolution of a network. Consider a network of unknown growth dynamics. We postulate a certain growth rule and use it to evolve the network backward in time. During backtracking, we collect metrics to estimate the fitness of different growth rules and select the best.

In this paper, we present a comprehensive method to extract growth rules from a single snapshot of the network geometry—the Backward Evolution Algorithm (BEA) (Fig. 2). Within the BEA approach, we probe the space of possible growth rules linking the extension of the network with the gradient of the driving field. We then apply these growth rules backward in time, backtracking the evolution of the network completely down to its seeds. While backtracking, we collect multiple metrics to quantitatively estimate the fitness of a given growth rule and select the best. We validate this approach on synthetic data for networks grown in a diffusive field, demonstrating that we can not only successfully determine the growth rules of the branches but also assess the conditions under which branch splitting occurs. The method thus allows for a thorough analysis of the patterns and provides a glimpse into a previously inaccessible growth history.

The model

We begin by introducing a specific family of growth processes, namely, growth driven by a diffusive field. Here, the field is coupled to the network through the boundary conditions, as the branches absorb the field fluxes. Many natural growth processes can be described by such a system, for example, the formation of blood vasculature[20], dissolution patterns in porous media[21], river networks[10,22] or electric breakdowns[23].

If the internal dynamics of the field is fast compared to the evolution of the network, the field can be assumed to be quasi-static. This considerably simplifies modeling of the growth process as the diffusion equation reduces to the Poisson or Laplace equation for the driving field. Essentially, the equation governing the field can be derived from Fick's law, linking the flux ($\vec{J}$) to the gradient of the field ($\nabla\phi$):

$$\vec{J} = -\kappa \nabla \phi \tag{1}$$

with a respective transport coefficient κ. Combining (1) with the conservation of flux ($\nabla \cdot \vec{J} = P$) results in the Poisson equation:

$$\Delta\phi = -\frac{P}{\kappa}, \tag{2}$$

where P is a source term. For the special case $P = 0$ we recover the celebrated problem of Laplacian growth[3,24], in which an interface between two immiscible phases moves with a velocity proportional to the gradient of the harmonic field:

$$\vec{v} \propto \nabla\phi\,. \tag{3}$$

If the interface is an isoline of the field and the growth rate is proportional to the field gradient, small perturbations of the interface have a tendency to grow. At short wavelengths, the growth of the interface is stabilized by regularization mechanisms such as surface tension or kinetic undercooling[25]. Otherwise, the flux of the field concentrating on the tips favors very thin fingers and leads to their infinitely fast growth—the so-called ultraviolet catastrophe[26].

The longer wavelengths are generally unstable and have a tendency to grow and eventually transform into fingers[27–31]. There are two main processes responsible for the pattern formation in these systems: (i) screening between the nearby branches mediated by the harmonic field, which results in an increased growth rate of the longer branches and suppression of growth of the shorter ones, and (ii) tip splitting, when the branch bifurcates, giving rise to a pair of daughter branches. The interplay of these two processes leads to the appearance of a highly ramified hierarchical network-like structure.

Growth dynamics of a similar type underlies a wide range of different processes, including formation of the lungs[32–34], bacterial colony growth[35], cave formation[21,36], metallic dendrite formation in electrochemical deposition[37,38], dielectric breakdown[23], discharge trees[16], combustion fingers[39], tributary and distributary channel formation in river networks[9,14], dendritic patterns in superconducting films[40], leaf venation[41], or blood vasculature formation[20,42,43].

The thin finger model. Not every moving boundary problem leads to the emergence of a spatial network. Spatial transport networks have distinct branches, the widths of which are much smaller than the distances between them. They are also characterized by well-defined bifurcation points in which one branch splits into two. It is thus natural to describe the growth of the network in frames of the thin finger model (TFM), which approximates the growing fingers as lines that extend only in length[44–46]. As noted in Ref[44], such an approach provides also another method of regularizing the Laplacian growth at short wavelengths, without the need of introducing the surface tension. This model has been used for the analysis of fingered growth in both the Laplacian[45–48] and Poissonian fields[49,50].

Removing the ultraviolet catastrophe through the thin finger approximation comes at a cost. First, the field gradient at the tip becomes singular, diverging like $r^{-1/2}$ in the vicinity of the tip. In polar coordinates (where the direction of the tangent to the finger at the tip sets $\theta = 0$—see *Supplemental Information*, Fig. S1A) the field near the tip can be expanded[51,52]:

$$\phi(r,\theta) = a_1 r^{1/2}\cos\frac{\theta}{2} + a_2 r\sin\theta + a_3 r^{3/2}\cos\frac{3\theta}{2} + \mathcal{O}\left(r^2\right), \tag{4}$$

where the coefficients a_i depend on the boundary conditions far from the finger tip. Equation (4) holds also for the case of Poisson fields, as in a small area around the tip the flux contribution from the source term is negligible compared to the flux from the regions away from the tip. Each of the leading coefficients a_i in Eq. (4) has a clear physical interpretation[10] (*Supplemental Information*, Fig. S1).

First, the coefficient a_1 is linked to the total flux over a small circle of radius r_0 around the tip (*Supplemental Information*, Fig. S1E–F):

$$J|_{r_0} = \oint_{r_0} (-\kappa\nabla\phi)\cdot\hat{n}\,\mathrm{d}l = 2\kappa a_1 r_0^{1/2} + \mathcal{O}\left(r_0^{3/2}\right), \tag{5}$$

where r_0 is the typical width of the finger.

The coefficient a_2 is related to the field asymmetry with respect to the finger growth direction (*Supplemental Information*, Fig. S1G). With the positive a_2 flux of the field is larger on the right side of the tip and with the negative a_2 on the left. However, the finger grows in the direction of the largest flux and, as a result, it turns in such a way that a_2 always vanishes (principle of local symmetry[11]).

Finally, a_3 is related to the bimodality of the driving field in the neighborhood of the tip. If we consider a circle of radius r_B around the tip and study the field as a function of the angle θ, we notice that with a fixed $a_1 > 0$ and $a_2 = a_3 = 0$ the field has a single maximum at $\theta = 0$ (*Supplemental Information*, Fig. S1E–F). Now, if we take $a_3 < 0$, then the smaller it is, the flatter the maximum becomes. Eventually, when the second derivative of ϕ becomes negative, which corresponds to the negative value of a_3/a_1:

$$\frac{\partial^2\phi}{\partial\theta^2}\Big|_{\theta=0,r=r_B} < 0 \quad\Longrightarrow\quad a_3/a_1 < -\frac{1}{9r_B}, \tag{6}$$

the field becomes bimodal and there appear two maxima of the flux at $\pm\theta_0$ (*Supplemental Information*, Fig. S1H). Note that the threshold value of a_3/a_1 depends on the distance r_B from the tip at which the field is analyzed. For sufficiently small r_B the field profile is always symmetric with one maximum at $\theta = 0$[13].

Growth rules. The growth velocity in classical Laplacian growth is proportional to the field gradient. A widely used extension of this rule assumes a power-law relation between the flux into the tip and the growth velocity[23,53]:

$$v \propto J^{\eta} \propto |\nabla \phi|^{\eta}, \tag{7}$$

where η is a specific growth exponent. Recalling Eq. (5), we have:

$$v = \sigma a_1^{\eta}. \tag{8}$$

where σ is the proportionality constant linking flux with the growth rate of the tip. The value of the growth exponent, η, strongly affects the competition between the fingers[45,46,54] and hence, as shown later, results in qualitatively different network geometries (Fig. 4).

While the moving boundary problem in its continuous version has an inherent instability, which splits one finger into two daughter branches depending on the finger width and speed[55], in the TFM tip splitting is not an intrinsic part of the dynamics[56] and needs to be introduced by hand, based on certain criteria. Two different splitting criteria can be found in the literature—the velocity criterion[15,28] and the bimodality criterion[10,17].

The first is based on the observation that the instability wavelength (λ) decreases with increasing front propagation velocity[25,28]. As the finger accelerates at some point λ becomes smaller than its width, and the finger becomes destabilized. Such a criterion can be straightforwardly implemented in the TFM as a threshold on a_1: $a_1 > a_1^{\text{crit}}$.

The second criterion is linked to the appearance of two maxima of the flux in the neighborhood of the tip, which is related to the value of the a_3 coefficient. When for a given radius r_B the flux of the field has a single high maximum, the finger grows in the direction of this maximum. However, if the flux of the field from the sides of the tip becomes comparable to that from the front, or even higher (which corresponds to the bimodal field around the tip and the appearance of two maxima at $\pm\,\theta_0$—*Supplemental Information*, Fig. S1H), the finger attempts to grow in two directions at once, which results in a bifurcation. More precisely, we require the finger to split whenever a_3/a_1 becomes smaller than some critical value (which is negative if we consider the bimodal field around the tip or might be positive if we consider a single flat maximum[17]). This critical value depends on the value of r_B (Eq. 6), which introduces a new length scale in the system. For an insightful discussion on this length scale in the case of river networks we refer to Ref.[10].

Whenever a splitting criterion is fulfilled, two daughter branches are created at $\theta = \pm\,36°$ (measured in the coordinate system around the tip as before). As shown in Refs[45,46,57], the angle of $2\pi/5 = 72°$ between the two daughter branches is the stable opening angle in the TFM. This characteristic opening angle has also been found in natural stream networks formed by groundwater seepage[9] and has been used to characterize the climate dependence of river network patterns on Earth and Mars[58,59].

Results

Forward evolution. Given the growth rules described above, we can follow the growth of the network starting from the initial positions of the branches (seeds) to understand how the growth rules impact the final geometry of the structure. However, except for the simplest cases of one- and two-finger solutions[46], one needs to resort to numerical methods here.

First, we rescale the coordinates and the field in both the Laplace and the Poisson case (*Supplemental Information*, section 1), which results in the dimensionless equations:

$$\Delta \phi = 0 \quad \text{or} \quad \Delta \phi = -1 \tag{9}$$

respectively. In both cases, the dimensionless growth law becomes:

$$v = (a_1)^{\eta}. \tag{10}$$

Next, we construct a growth algorithm based on the finite element calculation of the driving field for a given geometry of the network and extension of the branches in streamline direction (*Supplemental Information*, section 2). The details of the growth algorithm are described in *Supplemental Information*, section 3.

We begin by considering a simple case of two fingers growing in a long channel with constant flux of the field coming from the top ($(\nabla \phi)_{\vec{n}} = 1$), absorbing boundary conditions ($\phi = 0$) on the fingers and the bottom wall, and reflective boundary conditions ($(\nabla \phi)_{\vec{n}} = 0$) on the side walls. The source term $P = 0$ implies that the Laplace equation ($\Delta \phi = 0$) needs to be solved to calculate the field, hence the name of the networks obtained in such a setup—*Laplacian*. The aspect ratio of the channel was set at 1:25, with Figs. 3 and 4 showing only the lower portion of the domain.

For a single finger, the parameter η would affect only the growth velocity, but not the network structure. The same holds for two identical fingers symmetrically placed left and right of the vertical symmetry line. Thus, we break the symmetry by starting from a configuration where the left finger is 50% shorter, and hence collects slightly less flux than the right one. For $\eta = 0$ the growth velocity of the fingers does not depend on the flux; thus, both fingers grow with the same velocity (Fig. 3A). For $\eta < 0$ the growth process is stable and the velocity is inversely proportional to the flux. Thus, the shorter tip which collects less flux is growing faster, catching up with its longer sibling at some point. For $\eta > 0$, however, we have a positive feedback between growth velocity and flux; thus, the right branch starts to outcompete the other. Eventually, it screens its sibling from the flux, just as the lightning rod screens the surrounding area. The larger the η, the stronger the effect, as shown in Fig. 3B,C.

Next, we present the evolution of branched networks, where we allow the splitting of the fingers according to the velocity criterion (Fig. 4). More specifically, a finger bifurcates if $a_1 > 0.8$. At low η, the competition between

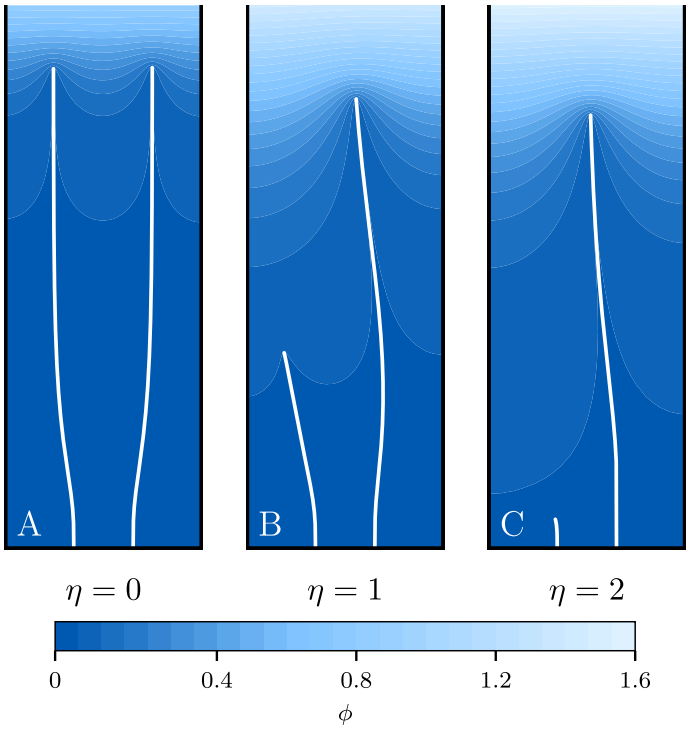

Figure 3. The evolution of two fingers for different growth exponents. Initially, the fingers are positioned symmetrically in the channel ($x_{\text{initial}} = \pm\ 0.3$), but their heights differ (0.01 vs. 0.02). The units here are chosen in such a way that the channel extends from $x = -1$ to $x = 1$. (**A**) For $\eta = 0$ the fingers grow with the same velocity. (**B**,**C**) At larger η the growth becomes unstable due to the competition between the fingers for an available flux. The colors in the figure correspond to the value of the field driving the growth.

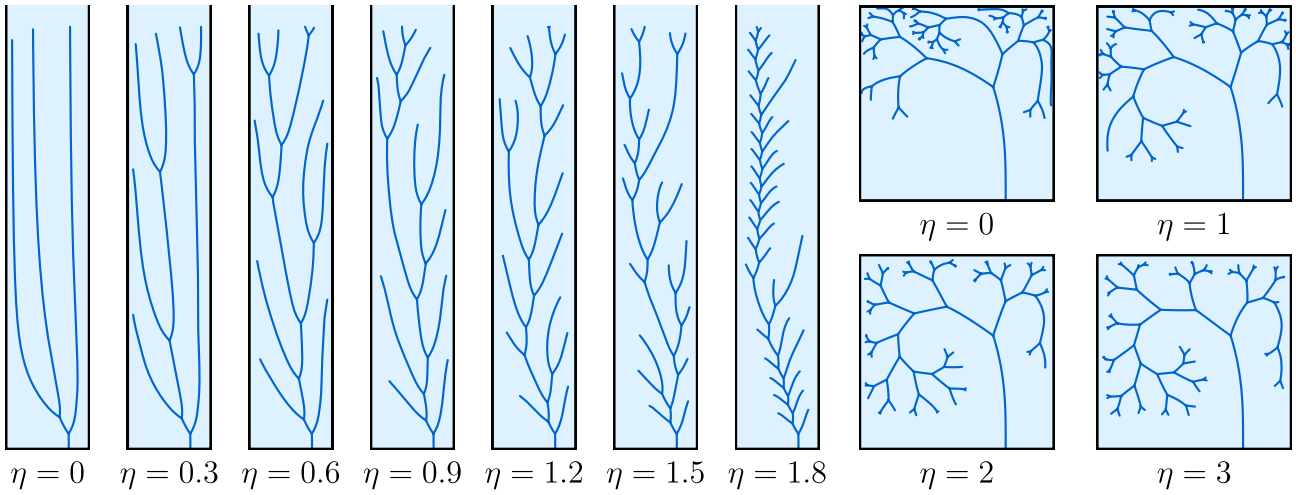

Figure 4. Comparison of the Laplacian and Poissonian networks for different η exponents. On the left, Laplacian networks in a channel with reflective side walls and flux of the field coming from the top. On the right, Poissonian networks in a square box with reflective side and top walls and non-zero source term. In the latter case, each of the networks has the same total sum of the lengths of the branches. The networks grow from a single seed initially placed at 3/4 of the channel width. Fingers can bifurcate with the velocity criterion $a_1 > 0.8$ in the Laplacian case and with the bimodality criterion $a_3/a_1 < -0.1$ in the Poissonian case.

the fingers is relatively weak. It takes then a long time for one finger to outgrow the other sufficiently to intercept enough extra flux in order to split again. The bigger the η, the more dynamic the evolution with a larger number of tip splittings. Laplacian structures, similar to those presented in Fig. 4 can be observed in natural systems, such as corals[17], dielectric breakdown patterns[23], combustion fingers[39], or leaf venation of evolutionary ancient plants[60].

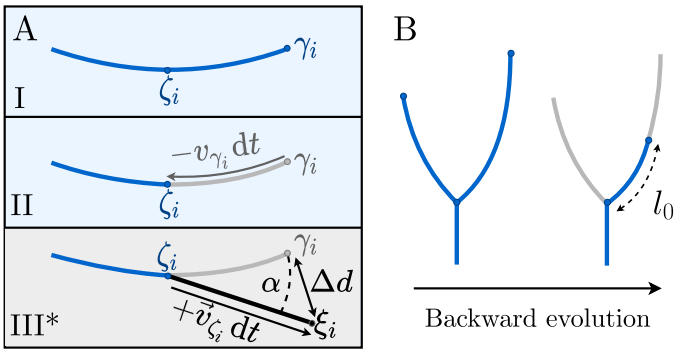

Figure 5. The Backward Evolution Algorithm. (**A**) I–II: The velocities of the tips (γ_i) are calculated, and each branch is trimmed by $v_{\gamma_i}\mathrm{d}t$. This gives the previous tip positions ζ_i, where we measure the local symmetry parameter (a_2/a_1^2). III*: Additionally, we can use the forward algorithm to obtain an extrapolated position ξ_i, and two additional metrics: the overshoot (Δd—distance between γ_i and ξ_i) and the angular deflection (α). (**B**) Definition of the length mismatch (l_0) at a bifurcation during the backward evolution.

In a second series of simulations, we consider a non-vanishing source term $P \neq 0$. Now, the Poisson equation ($\Delta\phi = -1$) is solved in the domain, hence the name of the networks—*Poissonian*. We grow the networks in a square box with reflective boundary conditions on the top, left, and right walls. As before, the absorbing boundary conditions are imposed on the bottom wall and the network itself. Because the flux is now produced uniformly across the domain, the system does not have a preferred growth direction, contrary to the Laplacian case. As a tip splitting criterion, we have chosen the bimodality bifurcation rule ($a_3/a_1 < -0.1$). The two elements: (i) weaker competition between the fingers connected to a uniform distribution of the field sources and (ii) the bifurcation criterion based on the field on the sides of the tip result in the creation of fractal-like structures, with progressively shorter branches splitting in a self-similar way. Consequently, the geometry of Poissonian networks does not depend as strongly on the η exponent as for Laplacian structures (compare the differences of trees in Fig. 4). Ramified, self-similar structures of this kind are encountered in river networks[10,22] or blood vasculature[20,42].

The backward evolution algorithm. Having analyzed the deterministic forward growth, we now focus on the question of whether it is possible to recover the value of the growth exponent and the bifurcation criteria given only the final geometries of the networks, such as those shown in Fig. 4. To this end, we construct the Backward Evolution Algorithm. The idea of the method is to start with a set of possible growth exponents η, and then evolve the system back in time while collecting geometric information on shrinking structures. These data then allow us to assess which growth rule reproduces the evolution of the system in the most accurate way.

To be more specific, we first assume some value of $\eta = \eta^*$, and then calculate the velocities at the current positions of the tips (v_{γ_i}—Fig. 5A, panels I–II), as well as the distance over which each tip will move over a timestep $\mathrm{d}t$: $\mathrm{d}s_i(t) = v_{\gamma_i}\mathrm{d}t = (a_1^i)^{\eta^*}\mathrm{d}t$. Using the reversed version of the growth algorithm (*Supplemental Information*, section 3) we then obtain the projected previous position of the tip (ζ_i) and trim each branch accordingly. This procedure can be repeated iteratively, trimming progressively more and more segments of the branches, and thus shrinking the whole network.

In each step of the BEA we collect the local symmetry measure—the a_2/a_1^2 value. As mentioned earlier, the a_2 coefficient should vanish along the real trajectory of a growing tip. Thus the value of a_2 (rescaled by a_1^2 to make it dimensionless) is a convenient measure of how far we are from the real trajectory of the finger. Additionally, we make a virtual forward step obtaining an extrapolated position of the tips (ξ_i in Fig. 5A, panel III*). Based on these data, the overshoot (Δd—distance between the points γ_i and ξ_i) and the angular deflection (α—angle between γ_i and ξ_i) are calculated. In this way, a backward-forward method is incorporated into the BEA, collecting the metrics throughout the whole backward evolution of the network, and not only in a single backward-forward step (as opposed to Ref[11]).

We evolve the network backward in time until it vanishes entirely. In this manner, in each step of the BEA we collect N values for each metric, where N is the number of tips. Next, we calculate the quartiles (Q_1, M, Q_3—quantiles of order 25%, 50% (median) and 75%, respectively) of the data collected over all time steps. This procedure is repeated for a range of η^* values. We expect that all metrics (local symmetry, overshoot and angular deflection) will be minimized at a particular value of η^*, which should correspond to the growth exponent of the original network (η_0).

To examine the effectiveness of the BEA, we first grow a test network with some specific value of $\eta = \eta_0$. Then we evolve it backward in time for a range of different η^* values and plot the resulting metrics as a function of η^*. Figure 6 shows the plots for a Laplacian network originally grown with $\eta_0 = 1.5$. Figure 6B–D presents the quartiles of the collected data. We observe that each median approaches zero exactly at the η_0 value that was initially imposed to produce the network (marked with the black dashed line).

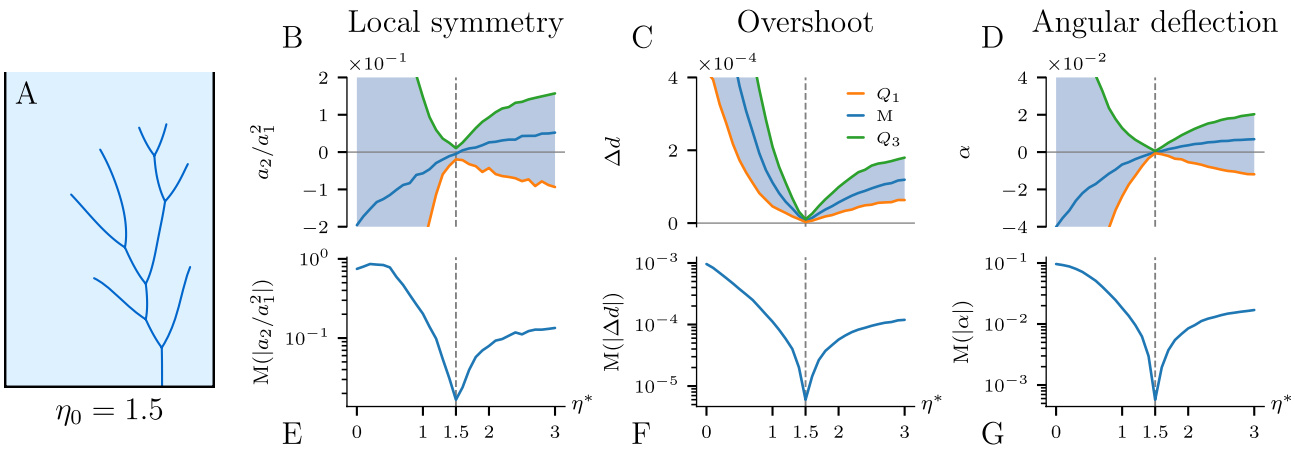

Figure 6. The Backward Evolution Algorithm applied to a synthetic Laplacian network. (**A**) Original network created with $\eta_0 = 1.5$ to which the algorithm was applied. (**B**–**D**) Quartiles of the collected values of the local symmetry, overshoot, and angular deflection. (**E**–**G**) Median of the absolute value of the corresponding metric plotted in a logarithmic scale. The pronounced minima allow us to estimate the correct η_0 (marked with the black dashed line on each plot). The results show that the BEA can precisely reconstruct the growth exponent of a given network.

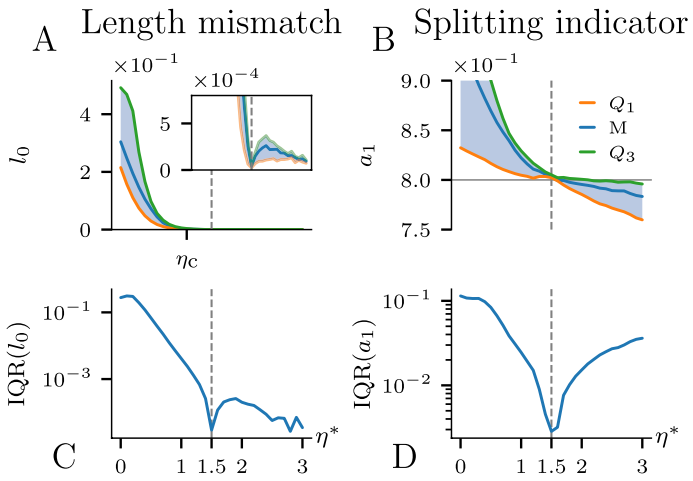

Figure 7. Analysis of the bifurcation points in the BEA: length mismatch (l_0) and a_1 coefficient at the splitting point as a function of the growth exponent (η^*). (**A**–**B**) Quartiles of the values of a corresponding metric. (**C**–**D**) Interquartile range of the distributions (distance between Q_1 and Q_3). The results confirm that the BEA is capable of reconstructing not only the growth exponent of a given network based on its bifurcation points but also the mechanism behind the tip splitting.

Note that at the correct value of the exponent ($\eta^\star = \eta_0$) the interquartile range (IQR—distance between Q_1 and Q_3 in 6B–D) of metrics collected during the backward evolution approaches zero. Conversely, for an incorrect η^*, the distribution of the collected data set has some spread due to the fact that we land in different places around the initial position after the backward-forward step. Consequently, the IQR dependence also exhibits a minimum at the correct $\eta^* = \eta_0$ value. In Fig. 6E-G we show the median of the absolute value of the collected data in a logarithmic scale. Pronounced minima observed at $\eta^* = \eta_0$ reflect both the fact that the value of a given metric is minimal for the correct η^* and the fact that the variance of the metric is minimal at $\eta^* = \eta_0$.

Let us consider the possibility of using the position of the bifurcation points in the solution of the inverse problem. Since the fingers split at a specific point, then—with the use of the correct growth rule—they should also converge to the same bifurcation point as the network is grown backward. If they do not converge simultaneously, then measuring the excess length of the longer branch (length mismatch l_0 in Fig. 5B) and minimizing it with respect to η^* should allow one to recover the correct growth exponent. Indeed, if we start with $\eta^* = 0$, the branches will be trimmed at the same rate and it will take less time for the shorter branch to reach the bifurcation point. In such a case, the length mismatch will be exactly equal to the initial length difference between the branches. With η^* approaching η_0, the length mismatch decreases monotonically to zero, since the longer branch—which was growing faster—will also be trimmed faster in the backward evolution. At the correct $\eta^* = \eta_0$ the branches converge to the bifurcation point simultaneously, which should result in the minimum of the length

mismatch, as well as its interquartile range. Throughout the backward evolution, we collect the mismatch value from all bifurcation points. The corresponding median and interquartile range exhibit minima at the correct $\eta^* = \eta_0$, as shown in Fig. 7A,C.

Interestingly, we observe a dramatic decrease of the length mismatch above $\eta^* \approx 1$ (Fig. 7A). This behavior is related to the stability of a single bifurcation in an unbounded domain, as studied analytically by Carleson and Makarov[45]. They have shown that for $\eta < \eta_c \approx 1.09382$ the growth of the daughter branches after splitting is stable and that the fingers move away from each other with equal velocities. For $\eta > \eta_c$, the competition between the branches makes their growth unstable, with one speeding up and the other slowing down. With a flipped time arrow, the stability of the system is also reversed. Thus, for $\eta > \eta_c$ both daughter branches should reach the bifurcation point at the same time, hence almost zero length mismatch for larger growth exponents. After zooming in we nevertheless observe a minimum at the correct η^*, which is related to the higher order effects such as the presence of other branches and the influence of the boundaries of the system. The above reasoning does not hold for bifurcations triggered by the bimodality criterion in the Poissonian case. Here, due to the presence of local sources, the competition between branches is weaker and, hence, a bifurcation can grow in a stable manner even for relatively high η. On the contrary, in the backward evolution there is no stabilizing effect, and we observe a pronounced minimum of the length mismatch (*Supplemental Information* Fig. S2E).

One can also analyze the expansion coefficients of the field indicating a splitting event at the bifurcation point (a_1 for the velocity bifurcation criterion or a_3/a_1 for the bimodality criterion). As can be seen in Fig. 7B, the values of a_1 at the bifurcation points are converging to one value for the correct $\eta^* = \eta_0$. Hence, minimizing the interquartile range of the bifurcation indicators is another way to estimate η_0 (Fig. 7D). Importantly, the values of a_1 or a_3/a_1 converge exactly to the values used as bifurcation criterion thresholds when the network was originally grown. Thus, the BEA analysis of bifurcations gives us not only the correct growth exponent but also allows us to recover the bifurcation criterion for a particular network.

The BEA can be applied as well to a Poissonian tree, giving similarly precise estimates of the growth exponent (*Supplemental Information*, Fig. S2). The precision of the predictions decreases somewhat with an increasing growth exponent, as shown in *Supplemental Information*, Fig. S3. This is connected to the increasing growth instability at high η—with increasing growth exponent the minima of the metrics become less pronounced, finally flattening totally, which makes the reconstruction of the growth rules and estimation of η_0 increasingly harder. This effect becomes pronounced around $\eta_0 = 4$ for the Laplace case and $\eta_0 = 6$ in the Poisson case. The wider range of precision in the Poissonian case might be the result of weaker screening and smaller differences of velocities between the fingers than in the corresponding Laplacian case.

Backward evolution of the river network. As a final application of our model, we use it to assess the growth laws of a real river network, namely the White River basin (HUC-01080105) in central Vermont, USA. This river network grows in a humid environment, where diffusive fluxes and groundwater flows may play a crucial role in its formation[58,61–63]. For our analysis, we used medium resolution channels in the White River basin, as mapped by the NHDPlus dataset[7] and preprocessed as described in *Supplemental Information*, section 4. We assume that the field driving the growth can then be described by the Poisson equation (Eq. 2), with precipitation being responsible for the source term. Using Eq. (7) for the rate of erosion, we can apply the BEA to extract the parameters of the underlying growth law.

The results of our analysis are presented in Fig. 8. As one could anticipate, the metrics are much more noisy than the ones based on the artificial network, with less pronounced minima of overshoot and angular deflection and only a local minimum of the local symmetry in the region where the rest of the metrics indicate η_0. The bifurcation length mismatch plot (Fig. 8B) is less revealing, with several shallow minima for $\eta > 1$.

To determine the growth exponent, we make use of the multiple metrics included in the BEA (local symmetry, overshoot, angular deflection Fig. 8A–C; their IQR *Supplemental Information*, Fig. S5; length mismatch and its IQR Fig. 8D–E; and IQR of the splitting indicator Fig. 8G). We normalize each metric so that its values, as a function of $\eta^\star$, range from 0 to 1 and average the resulting functions to produce a final measure of the fit of a particular η value (Fig. 8H). The resulting function has a single minimum at $\eta^* = 1.65 \pm 0.25$.

The appearance of the minimum in the splitting indicator plot (Fig. 8G) around $\eta^* = 1.65$ suggests that in this case the branch splitting events are triggered by an increase of the tip growth velocity. This is further confirmed by the analysis of the histogram of branch lengths in the White River, which shows an exponential distribution (*Supplemental Information*, section 5) similar to the analogous distributions for synthetic networks grown with the velocity bifurcation criterion. Additionally, we observe an abrupt decrease of the length mismatch for $\eta^* > \eta^c$ (8d), which is another indicator of the velocity bifurcation criterion, as already discussed (compare Fig. 7A and *Supplemental Information*, Fig. 2E).

Summary

We have shown that it is possible to use the final geometry of the spontaneously grown network to decipher its growth dynamics using the Backward Evolution Algorithm. We tested it on several synthetic networks and then analyzed the natural system—the White River basin. The BEA metrics consistently suggest that the growth exponent of this network is around $\eta = 1.65 \pm 0.25$. This indicates a nonlinear relation between the erosion rate and diffusive flux coming to springs, implying strong competition between different tributaries for groundwater flow. Additionally, we determined that the splitting events in this network were triggered by an increase of the growth velocity of the channel heads. The BEA method should be equally applicable to other systems, such as leaf venation, blood vessel networks, or dielectric breakdown patterns.

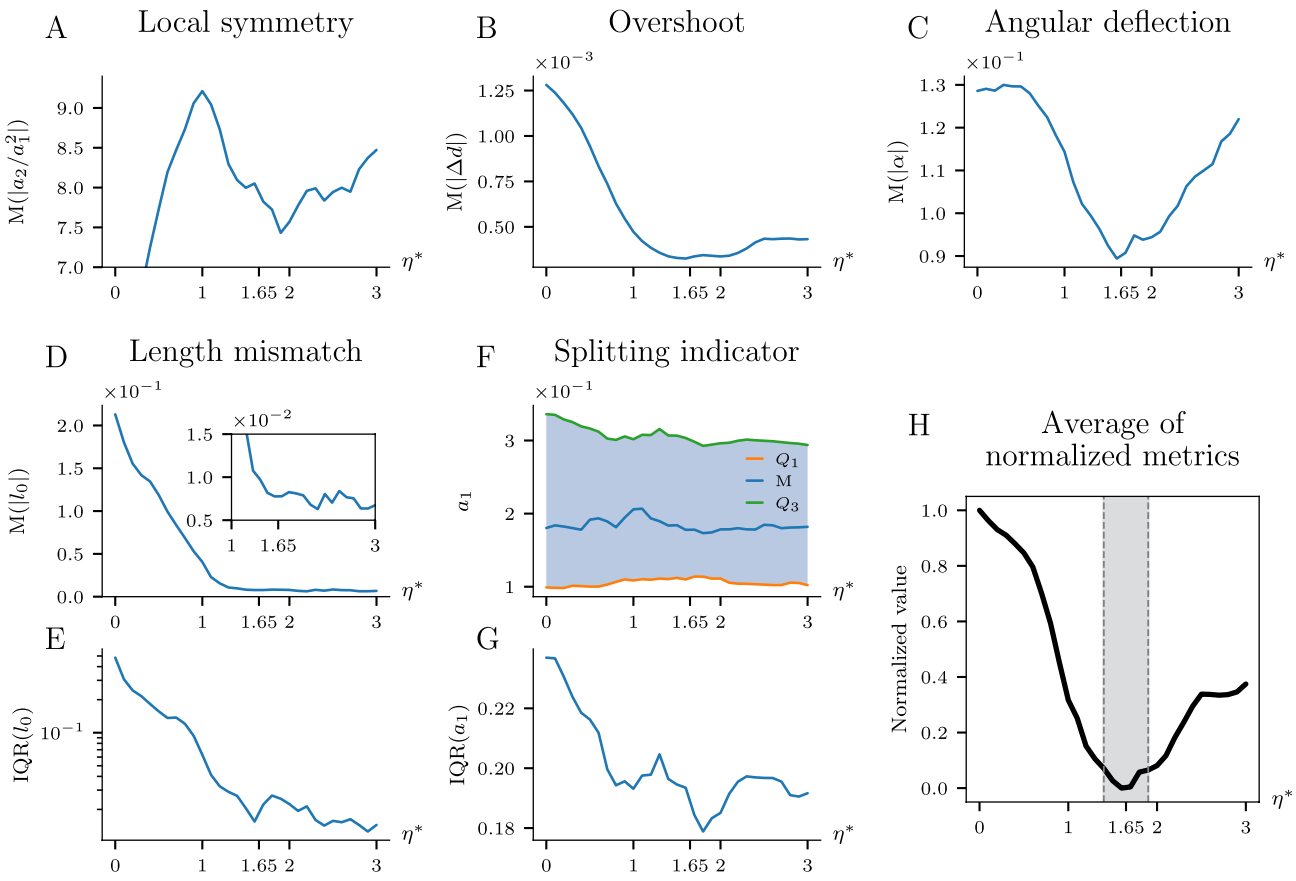

Figure 8. Results of the BEA on the White River network in Vermont, USA. (**A**–**C**) Median of the absolute value of the local symmetry, overshoot, angular deflection (**D**–**E**) Length mismatch (median of the absolute value and IQR) (**F**–**G**) Splitting indicator (quartiles and IQR) (**H**) Average of normalized metrics with a minimum around $\eta^* = 1.65 \pm 0.25$ (marked on each subplot).

Data availability

The datasets used and/or analyzed during the current study together with the source code are available on the GitHub repository (https://github.com/stzukowski/reticuler).

Received: 13 July 2022; Accepted: 18 November 2022
Published online: 27 November 2022

References

1. Ball, P. *Branches: Nature's Patterns: A Tapestry in Three Parts* (OUP, Oxford, 2009).
2. Gollub, J. P. & Langer, J. S. Pattern formation in nonequilibrium physics. *Rev. Mod. Phys.* **71**, S396 (1999).
3. Pelcé, P. New Visions on Form and Growth: Fingered Growth, Dendrites, and Flames (Oxford University Press on Demand, 2004).
4. Fleury, V., Gouyet, J.-F. & Leonetti, M. *Branching in Nature: Dynamics and Morphogenesis of Branching Structures, from Cell to River Networks* Vol. 14 (Springer Science & Business Media, Berlin, 2001).
5. Ronellenfitsch, H. & Katifori, E. Global optimization, local adaptation, and the role of growth in distribution networks. *Phys. Rev. Lett.* **117**, 138301 (2016).
6. Pelletier, J. D. & Turcotte, D. L. Shapes of river networks and leaves: Are they statistically similar?. *Philos. Trans. R. Soc. B* **355**, 307–311 (2000).
7. McKay, L. *et al.* NHDPlus version 2: User guide (2012).
8. Lichtenberg figure. https://paulslab.com/ (2017).
9. Devauchelle, O., Petroff, A. P., Seybold, H. J. & Rothman, D. H. Ramification of stream networks. *Proc. Natl. Acad. Sci.* **109**, 20832–6 (2012).
10. Petroff, A. P., Devauchelle, O., Seybold, H. J. & Rothman, D. H. Bifurcation dynamics of natural drainage networks. *Philos. Trans. R. Soc. A* **371**, 20120365 (2013).
11. Cohen, Y. *et al.* Path selection in the growth of rivers. *Proc. Natl. Acad. Sci.* **112**, 14132–14137 (2015).
12. Yi, R. S. *et al.* Symmetric rearrangement of groundwater-fed streams. *Proc. R. Soc. A* **473**, 20170539 (2017).
13. Devauchelle, O. *et al.* Laplacian networks: Growth, local symmetry, and shape optimization. *Phys. Rev. E* **95**, 033113 (2017).
14. Ke, W.-T., Shaw, J. B., Mahon, R. C. & Cathcart, C. A. Distributary channel networks as moving boundaries: Causes and morphodynamic effects. *J. Geophys. Res.* **124**, 1878–1898 (2019).
15. Pecelerowicz, M. & Szymczak, P. Stabilizing effect of tip splitting on the interface motion. *Phys. Rev. E* **94**, 062801 (2016).
16. Luque, A. & Ebert, U. Growing discharge trees with self-consistent charge transport: The collective dynamics of streamers. *New J. Phys.* **16**, 013039 (2014).
17. Kaandorp, J. A. & Kübler, J. E. Chapter 4.4 A Laplacian model of branching network. In *The Algorithmic Beauty of Seaweeds, Sponges and Corals* (Springer Science & Business Media, 2001).

18. Lagesse, C., Bordin, P. & Douady, S. A spatial multi-scale object to analyze road networks. *Netw. Sci.* **3**, 156–181 (2015).
19. Abrams, D. M. *et al.* Growth laws for channel networks incised by groundwater flow. *Nat. Geosci.* **2**, 193–196 (2009).
20. Nguyen, T.-H., Eichmann, A., Le Noble, F. & Fleury, V. Dynamics of vascular branching morphogenesis: The effect of blood and tissue flow. *Phys. Rev. E* **73**, 061907 (2006).
21. Szymczak, P. & Ladd, A. J. C. The initial stages of cave formation: Beyond the one-dimensional paradigm. *Earth Planet. Sci. Lett.* **301**, 424–432 (2011).
22. Petroff, A. P. *et al.* Geometry of valley growth. *J. Fluid Mech.* **673**, 245–254 (2011).
23. Niemeyer, L., Pietronero, L. & Wiesmann, H. J. Fractal dimension of dielectric breakdown. *Phys. Rev. Lett.* **52**, 1033 (1984).
24. Gustafsson, B., Teodorescu, R. & Vasil'ev, A. *Classical and Stochastic Laplacian Growth* (Springer, Berlin, 2014).
25. Meakin, P. *Fractals, Scaling and Growth Far from Equilibrium* Vol. 5 (Cambridge University Press, Cambridge, 1998).
26. Shraiman, B. & Bensimon, D. Singularities in nonlocal interface dynamics. In *Dynamics of Curved Fronts* 197–199 (1988).
27. Hill, S. Channeling in packed columns. *Chem. Eng. Sci.* **1**, 247–253 (1952).
28. Saffman, P. G. & Taylor, G. I. The penetration of a fluid into a porous medium or Hele-Shaw cell containing a more viscous liquid. *Proc. R. Soc. A* **245**, 312–329 (1958).
29. Langer, J. Instabilities and pattern formation in crystal growth. *Rev. Mod. Phys.* **52**, 1 (1980).
30. Kessler, D. A., Koplik, J. & Levine, H. Pattern selection in fingered growth phenomena. *Adv. Phys.* **37**, 255–339 (1988).
31. Zik, O., Olami, Z. & Moses, E. Fingering instability in combustion. *Phys. Rev. Lett.* **81**, 3868–3871 (1998).
32. Clément, R., Douady, S. & Mauroy, B. Branching geometry induced by lung self-regulated growth. *Phys. Biol.* **9**, 066006 (2012).
33. Lubkin, S. R. & Murray, J. A mechanism for early branching in lung morphogenesis. *J. Math. Biol.* **34**, 77–94 (1995).
34. Sapoval, B., Filoche, M. & Weibel, E. R. Smaller is better- but not too small: A physical scale for the design of the mammalian pulmonary acinus. *Proc. Natl. Acad. Sci.* **99**, 10411–10416 (2002).
35. Matsushita, M. & Fujikawa, H. Diffusion-limited growth in bacterial colony formation. *Phys. A* **168**, 498–506 (1990).
36. Cabeza, Y., Hidalgo, J. J. & Carrera, J. Competition is the underlying mechanism controlling viscous fingering and wormhole growth. *Geophys. Res. Lett.* **47**, e2019GL084795 (2020).
37. Brady, R. & Ball, R. Fractal growth of copper electrodeposits. *Nature* **309**, 225–229 (1984).
38. Kuhn, A. & Argoul, F. Spatiotemporal morphological transitions in thin-layer electrodeposition: The Hecker effect. *Phys. Rev. E* **49**, 4298 (1994).
39. Zik, O. & Moses, E. Fingering instability in combustion: An extended view. *Phys. Rev. E* **60**, 518 (1999).
40. Johansen, T. *et al.* Dendritic magnetic instability in superconducting MgB_2 films. *Europhys. Lett.* **59**, 599 (2002).
41. Sachs, T. The control of the patterned differentiation of vascular tissues. *Adv. Bot. Res.* **9**, 151–262 (1981).
42. Schneider, M., Reichold, J., Weber, B., Székely, G. & Hirsch, S. Tissue metabolism driven arterial tree generation. *Med. Image Anal.* **16**, 1397–1414 (2012).
43. Daub, J. T. & Merks, R. M. A cell-based model of extracellular-matrix-guided endothelial cell migration during angiogenesis. *Bull. Math. Biol.* **75**, 1377–1399 (2013).
44. Peterson, M. A. Singular Laplacian growth. *Phys. Rev. E* **57**, 3221–3226 (1998).
45. Carleson, L. & Makarov, N. Laplacian path models. *Journal d'Analyse Mathématique* **87**, 103–150 (2002).
46. Gubiec, T. & Szymczak, P. Fingered growth in channel geometry: A Loewner-equation approach. *Phys. Rev. E* **77**, 041602 (2008).
47. Pecelerowicz, M., Budek, A. & Szymczak, P. Effective description of the interaction between anisotropic viscous fingers. *Europhys. Lett.* **108**, 14001 (2014).
48. McDonald, R. Geodesic Loewner paths with varying boundary conditions. *Proc. R. Soc. A* **476**, 20200466 (2020).
49. Cohen, Y. & Rothman, D. H. Path selection in a Poisson field. *J. Stat. Phys.* **167**, 703–712 (2017).
50. McDonald, N. Finger growth and selection in a Poisson field. *J. Stat. Phys.* **178**, 763–774 (2020).
51. Derrida, B. & Hakim, V. Needle models of Laplacian growth. *Phys. Rev. A* **45**, 8759 (1992).
52. Brown, J. W. & Churchill, R. V. *Complex Variables and Applications* (McGraw-Hill, New York, 2009).
53. Hastings, M. B. & Levitov, L. S. Laplacian growth as one-dimensional turbulence. *Phys. D* **116**, 244–252 (1998).
54. Selander, G. Two Deterministic Growth Models Related to Diffusion-Limited Aggregation. Ph.D. thesis, Department of Mathematics, Royal Institute of Technology, Stockholm, Sweden (1999).
55. Lajeunesse, E. & Couder, Y. On the tip-splitting instability of viscous fingers. *J. Fluid Mech.* **419**, 125–149 (2000).
56. Peterson, M. A. Nonuniqueness in singular viscous fingering. *Phys. Rev. Lett.* **62**, 284 (1989).
57. Hastings, M. Growth exponents with 3.99 walkers. *Phys. Rev. E* **64**, 046104 (2001).
58. Seybold, H. J., Rothman, D. H. & Kirchner, J. W. Climate's watermark in the geometry of stream networks. *Geophys. Res. Lett.* **44**, 2272–2280 (2017).
59. Seybold, H. J., Kite, E. & Kirchner, J. W. Branching geometry of valley networks on Mars and Earth and its implications for early Martian climate. *Sci. Adv.* **4**, eaar6692 (2018).
60. Mitchison, G. A model for vein formation in higher plants. *Proc. R. Soc. B* **207**, 79–109 (1980).
61. Dunne, T. Formation and controls of channel networks. *Prog. Phys. Geogr.* **4**, 211–239 (1980).
62. Jerolmack, D. J. & Daniels, K. E. Viewing Earth's surface as a soft-matter landscape. *Nat. Rev. Phys.* **1**, 716–730 (2019).
63. Willgoose, G., Bras, R. L. & Rodriguez-Iturbe, I. Results from a new model of river basin evolution. *Earth Surf. Proc. Land.* **16**, 237–254 (1991).

Acknowledgements

This work was supported by the National Science Center (Poland) under research Grant No. 2016/21/B/ST3/01373. We would like to thank group of Daniel Rothman, MIT, and Olivier Devauchelle for the discussions and insightful remarks.

Author contributions

S.Ż., P.M., H.J.S., and P.S. designed and performed research; S.Ż, P.M., and P.S. analyzed data; and S.Ż, H.J.S., and P.S. wrote the paper.

Competing interests

The authors declare no competing interests.

Additional information

Supplementary Information The online version contains supplementary material available at https://doi.org/10.1038/s41598-022-24656-x.

Correspondence and requests for materials should be addressed to P.S.

Supplemental Material
Through history to growth dynamics: deciphering the evolution of spatial networks

Stanisław Żukowski[1,2], Piotr Morawiecki[3], Hansjörg Seybold[4], and Piotr Szymczak[1,*]

[1]Institute of Theoretical Physics, Faculty of Physics, University of Warsaw, Warsaw, Poland
[2]Laboratoire Matière et Systèmes Complexes (MSC), UMR 7057, CNRS & Université Paris Cité, Paris, France
[3]Department of Mathematical Sciences, University of Bath, Bath, United Kingdom
[4]Department of Environmental System Science, ETH Zürich, Zürich, Switzerland
[*]piotr.szymczak@fuw.edu.pl

1 Rescaling the Equations

First, we make the Poisson equation dimensionless by rescaling both the coordinates and the field as follows: $x' = \frac{x}{w}$ (with $2w$ being the width of the system) and $\phi' = \frac{\kappa}{w^2 P}\phi$. This leads to:

$$\Delta'\phi' = -1. \tag{1}$$

Next, we cast the growth rate equation (Eq. 8 in the main text) in the dimensionless form by scaling time by $t' = \sigma w^{\frac{3}{2}\eta-1}(\frac{P}{\kappa})^{\eta}t$ to obtain:

$$v' = (a_1')^{\eta}\,, \tag{2}$$

where $a_1' = \frac{\kappa}{w^{3/2}P}a_1$.

The rescaling in the Laplacian case ($P = 0$) is slightly different. Here, the system is usually fed by a flux of the field coming from the outside boundary of the system (J_0), so P in the Poissonian scalings is replaced by J_0/w. Now, $t'' = \sigma w^{\frac{1}{2}\eta-1}(\frac{J_0}{\kappa})^{\eta}t$, and the field: $\phi'' = \frac{\kappa}{wJ_0}\phi$, which leads to:

$$\Delta''\phi'' = 0\,, \tag{3}$$
$$v'' = (a_1'')^{\eta} \tag{4}$$

with $a_1'' = \frac{\kappa}{w^{1/2}J_0}a_1$.

2 Trajectory of the Tip

To construct a precise growth algorithm, we first derive the trajectory of the finger in the neighborhood of the tip. It can be obtained using the fact that the growth proceeds along a unique streamline going through the tip[1]. To simplify the analysis, let us move to the complex plane with $z = x + iy$ and analyze the solution of the Laplace equation ($\Delta\phi = 0$) in the vicinity of the tip. It is convenient to introduce the complex potential $\Phi(z)$ such that $\Phi = \phi + i\psi(z)$, with $\psi(z)$ being the corresponding stream function. Additionally, let us direct the finger along the negative imaginary axis with the tip at the origin. To find the complex potential near the finger tip, we first map the area outside the finger to the upper half plane by the mapping $\omega = \sqrt{iz}$. In the ω plane (mathematical plane), the complex potential vanishing at the real axis can be expanded in the Taylor series:

$$\tilde{\Phi}(\omega) = -i(a_1\omega + a_2\omega^2 + a_3\omega^3 + ...)\,. \tag{5}$$

This solution can then be mapped back to the z plane (physical plane) to yield:

$$\Phi(z) = \tilde{\Phi}(\omega(z)) = -i(a_1(iz)^{1/2} + a_2 iz + a_3(iz)^{3/2} + ...)\,, \tag{6}$$

which is equivalent to Eq. (4) in the main text.

To determine the streamlines in the mathematical plane, where $\omega = u + iv$, we calculate $\tilde{\psi}(u,v)$:

$$\tilde{\psi}(u,v) = \mathrm{Re}[\tilde{\Phi}(u+iv)] = -a_1 u - a_2 u^2 + a_2 v^2 + ...\,, \tag{7}$$

and equate it to a constant:

$$\tilde{\psi}(u,v) = A \implies -a_1 u - a_2 u^2 + a_2 v^2 = A\,. \tag{8}$$

The curves describing the streamlines, $\tilde{\gamma}(u,v)$, can thus be parameterized only with one parameter τ, with $u = \tau$ and $v = i(\tau - \tilde{\gamma}(u,v))$:

$$-a_1 u - a_2 \tau^2 + a_2 i^2 (\tau - \tilde{\gamma})^2 = A \implies \tilde{\gamma}(\tau) = \tau + i\sqrt{\beta\tau + \tau^2 + A/a_2}\,, \tag{9}$$

where $\beta = a_1/a_2$. As the tip is mapped to the point $\omega = 0$ in the mathematical plane, the streamline of interest is then given by $\tilde{\gamma}_0(0) = 0$, thus:

$$\tilde{\gamma}_0(\tau) = \tau + i\sqrt{\beta\tau + \tau^2}\,. \tag{10}$$

Moving back to the physical plane (with $z = -i\omega^2$) we obtain the formula describing the streamline entering the tip[2]:

$$\gamma_0(\tau) = -i\tilde{\gamma}_0(\tau)^2 = 2\tau\sqrt{\beta\tau + \tau^2} + i\beta\tau\,. \tag{11}$$

Using the fact that $x = \mathrm{Re}[\gamma_0(\tau)] = 2\tau\sqrt{\beta\tau + \tau^2}$ and $y = \mathrm{Im}[\gamma_0(\tau)] = \beta\tau$ we obtain:

$$x(y) = 2\sqrt{\frac{y^3}{\beta^2} + \frac{y^4}{\beta^4}} \approx \frac{2}{\beta} y^{3/2}\,. \tag{12}$$

We can also calculate the arclength as a function of y:

$$s(y) = \int_0^y \sqrt{1 + (\frac{\mathrm{d}x}{\mathrm{d}y'})^2}\mathrm{d}y' = \int_0^y \sqrt{1 + \frac{9}{\beta^2}y'}\mathrm{d}y' = \frac{2\beta^2}{27}\left[(\frac{9}{\beta^2}y + 1)^{3/2} - 1\right]\,. \tag{13}$$

Finally, we get the following set of equations for the streamline ($\beta = a_1/a_2$):

$$y(s) = \frac{\beta^2}{9}\left[\left(\frac{27s}{2\beta^2} + 1\right)^{2/3} - 1\right]\,, \tag{14}$$

$$x(y) = 2\sqrt{\frac{y(s)^3}{\beta^2} + \frac{y(s)^4}{\beta^4}}\,. \tag{15}$$

The above reasoning was carried out for the Laplacian case. However, as discussed in the main text, the Poissonian case will be fully equivalent, since we are interested in the small neighborhood of the tip here. In such a small area, the flux from the local sources is negligible compared to the flux from the regions far away from the tip, which brings the description of the system to the Laplacian case with flux entering through the boundaries only.

3 Growth Algorithm

Our growth algorithm is composed of a finite element solver[3] for the Laplace or Poisson equation, and an integration step extending the tips along the streamline γ_0 (Eq. (11)) by $\mathrm{d}s = v\mathrm{d}t$ via Eqs. (14)-(15). The second order method allows for an increased accuracy in the network growth simulations in comparison to the previous models[2,4].

The velocity of the tip is derived from the field through the expansion coefficients a_1, a_2 and a_3, which can be obtained by integration over a small circle of radius r:

$$a_1 = \frac{1}{\pi r_0^{1/2}} \int_{-\pi}^{\pi} \phi(r_0,\theta)\cos\frac{\theta}{2}\mathrm{d}\theta\,, \tag{16}$$

$$a_2 = \frac{1}{\pi r_0} \int_{-\pi}^{\pi} \phi(r_0,\theta)\sin\theta\mathrm{d}\theta\,, \tag{17}$$

$$a_3 = \frac{1}{\pi r_0^{3/2}} \int_{-\pi}^{\pi} \phi(r_0,\theta)\cos\frac{3\theta}{2}\mathrm{d}\theta\,. \tag{18}$$

Importantly, we require the numerical method used to construct the tip trajectory to be reversible. This ensures that after the backward-forward step in the Backward Evolution Algorithm, we end up in the same point, provided that a correct growth rule is used (except for the effects of numerical noise). Keeping this in mind, we use the implicit trapezoidal method[5]:

$$\vec{r}(t+\mathrm{d}t) = \vec{r}(t) + \frac{1}{2}\left[\mathrm{d}\vec{r}(t) + \mathrm{d}\vec{r}(t+\mathrm{d}t)\right], \tag{19}$$

which we solve iteratively. The reversed version of this algorithm can be expressed as follows:

$$s_i(t-\mathrm{d}t) = s_i(t) - \frac{1}{2}\left[\mathrm{d}s_i(t) + \mathrm{d}s_i(t-\mathrm{d}t)\right]. \tag{20}$$

Additionally, to limit the maximum displacement of the tip, we adjust the value of dt at each time step to keep ds of the fastest branch constant.

We tested our algorithm on a simple case of one finger growing in a semi-infinite channel with flux of the field coming from infinity. For this case, the analytical solution has been derived[6] which was compared with our numerical solutions to validate it.

4 Preprocessing of the river network

The data was extracted from the NHDPlus dataset[7]. Then, to limit the computational cost, we selected seven sub-trees of the whole network to apply the BEA algorithm on them (Fig. 4). The fragments were chosen to stem from the highest Strahler order streams[8], which was also treated as an absorbing boundary of their growth domain. The rest of the boundaries were marked out so that they lay between the neighboring sub-trees, following the watershed lines (see Fig. 4B). On these boundaries reflecting boundary conditions are imposed. The setup is thus similar to the box where the Poissonian simulations from Fig. 4 in the main text were conducted, but with more complicated geometry of the domain. Before applying the BEA algorithm, we also smoothed out the branches. We performed the sensitivity analysis introducing small changes in the shape of the selected sub-domain and smoothing procedure, changing the time step; and did not notice any significant difference in the results. The plots presented in Fig. 8 in main text and Fig. 5 are averaged results from the seven different areas of the White River basin.

5 Distribution of Segment Lengths

In Fig. 6 we present a comparison of histograms of segment lengths (distances between bifurcations) for: (i) the entire White River basin, (ii) simulations with the velocity-based splitting criterion and (iii) simulations with the bimodality splitting criterion. In the first two cases, we observe exponential distribution of segment lengths. However, there is a deficiency of very short branches (<500m for White River and <0.6 for the simulation). This is because the flux that was prior to bifurcation coming to a single mother branch is now divided between two daughter branches. It takes then some time for the new branches to move away from each other enough to get sufficient velocity and split again, which results in a lower number of very short segments. By contrast, simulations with the bimodality splitting criterion do not exhibit these features.

References

1. Devauchelle, O. *et al.* Laplacian networks: Growth, local symmetry, and shape optimization. *Phys. Rev. E* **95**, 033113 (2017).
2. Petroff, A. P., Devauchelle, O., Seybold, H. J. & Rothman, D. H. Bifurcation dynamics of natural drainage networks. *Philos. Transactions Royal Soc. A* **371**, 20120365 (2013).
3. Hecht, F. New development in FreeFem++. *J. Numer. Math.* **20**, 251–266 (2012).
4. Cohen, Y. *et al.* Path selection in the growth of rivers. *Proc. Natl. Acad. Sci.* **112**, 14132–14137 (2015).
5. Iserles, A. *A First Course in the Numerical Analysis of Differential Equations* (Cambridge University Press, 2009).
6. Gubiec, T. & Szymczak, P. Fingered growth in channel geometry: A Loewner-equation approach. *Phys. Rev. E* **77**, 041602 (2008).
7. McKay, L. *et al.* NHDPlus version 2: User guide (2012).
8. Horton, R. E. Erosional development of streams and their drainage basins; hydrophysical approach to quantitative morphology. *Geol. Soc. Am. Bull.* **56**, 275–370 (1945).

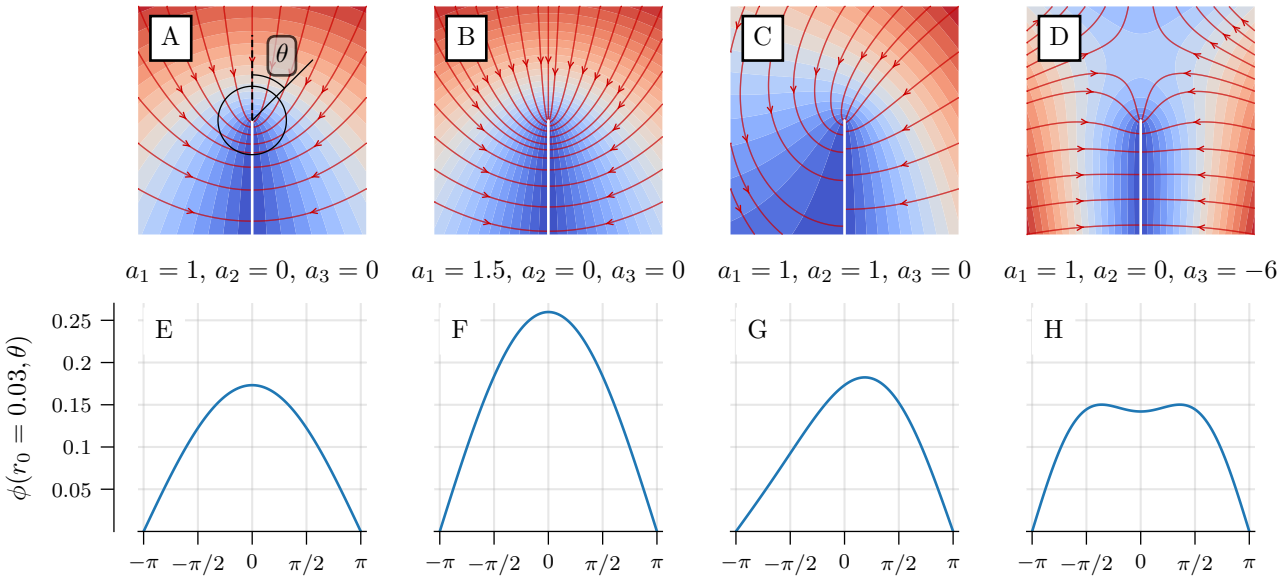

Figure 1. Impact of the a_1, a_2, a_3 coefficients on the field around the finger tip (after Ref.[2]). (A-D) Field around the finger tip (indicated by a white line). Colors from red to blue are related to the field magnitude, red arrows follow the field lines. (E-H) Profiles of the field along a small circle around the tip (black circle in A).

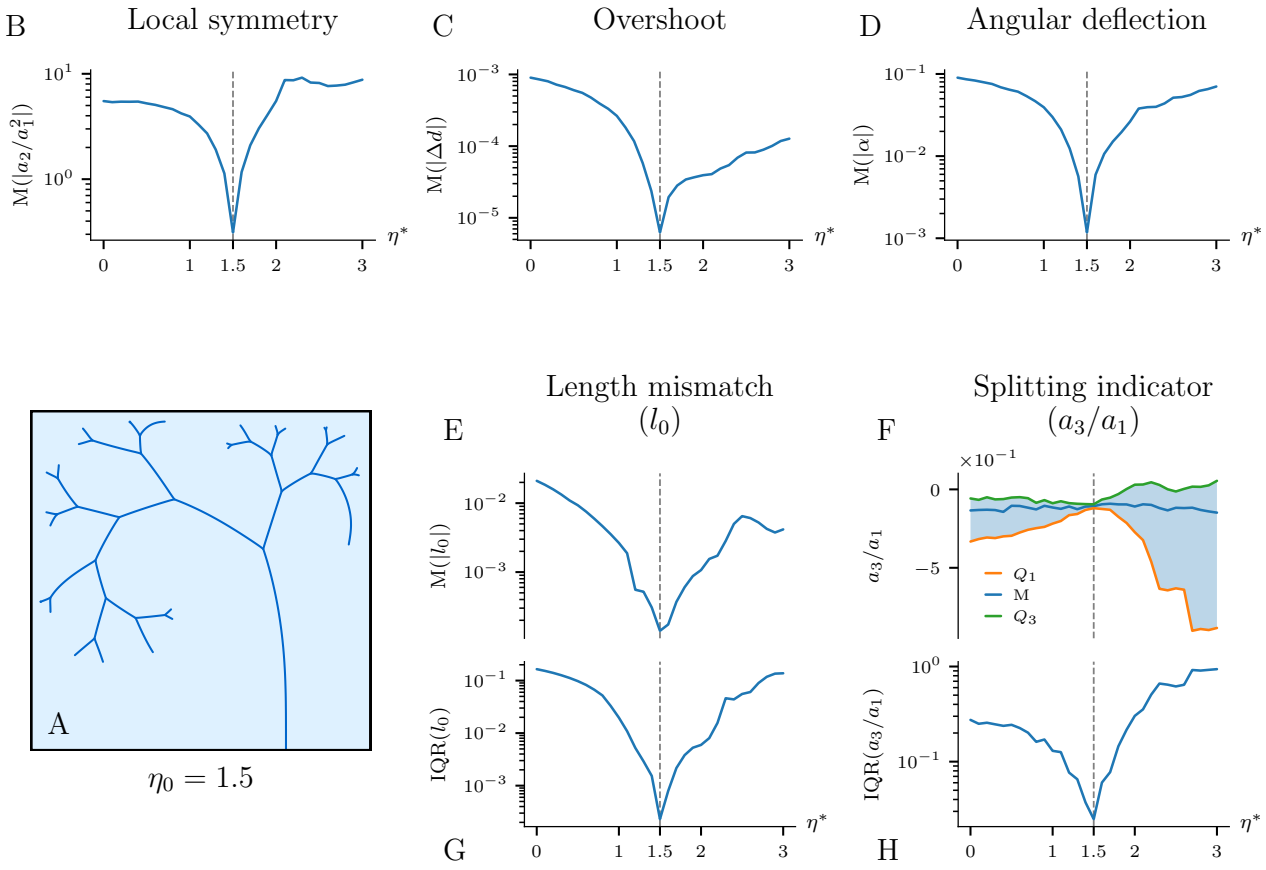

Figure 2. The Backward Evolution Algorithm on the synthetic Poissonian network. (A) A Poissonian network created with $\eta_0 = 1.5$, on which the algorithm was applied. (B-D) Median of the absolute value of local symmetry parameter, overshoot and angular deflection plotted in logarithmic scale. Pronounced minima allow us to estimate the correct η_0 (marked with the black dashed line on each plot). (E) Median of the absolute value of the length mismatch plotted in logarithmic scale. (F) Quartiles of the values of the bifurcation indicator a_3/a_1. (G-H) Interquartile range of the distributions (distance between Q_1 and Q_3) of the metrics from the bifurcation points.

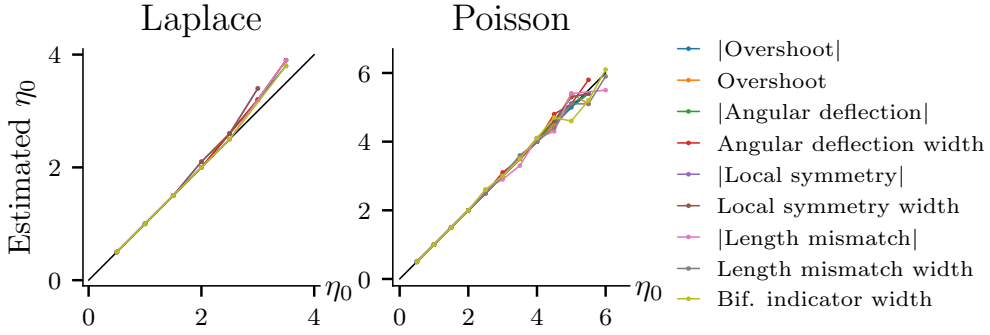

Figure 3. Reliability of the BEA in the Laplace and Poisson cases

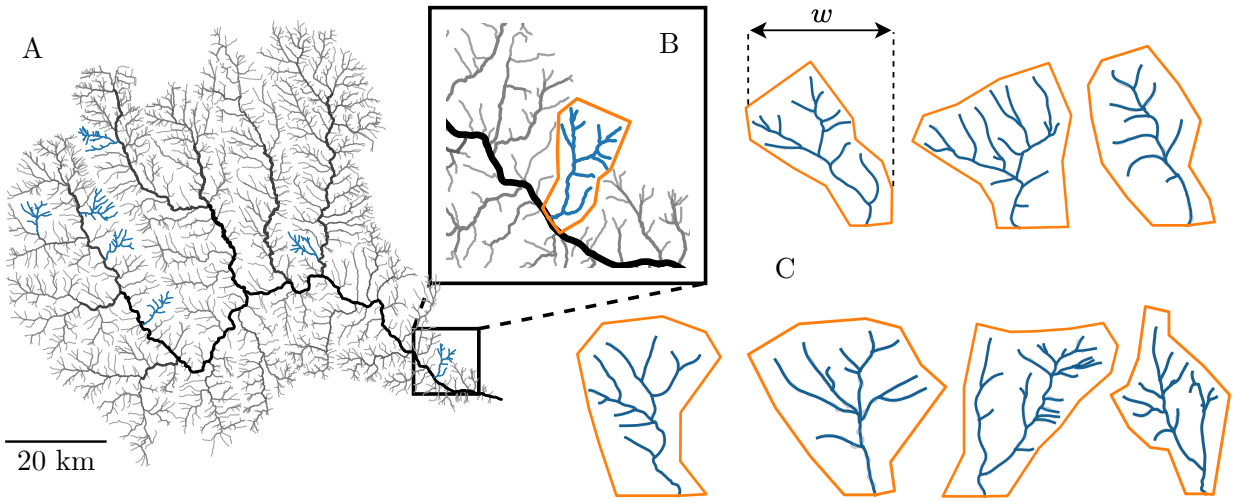

Figure 4. Preprocessing of the White River network before applying the BEA. (A) Whole White River basin with seven selected sub-trees marked in blue. (B) Zoom in on one of the selected sub-trees stemming from the highest Strahler order stream (black thick line). The rest of the boundaries (orange) were marked out so that they lay between the neighboring sub-trees. (C) Seven selected sub-trees with their domains after smoothing (blue). The original shapes are plotted in gray. For the numerical analysis, each of the sub-trees was rescaled to the same width $w = 2$.

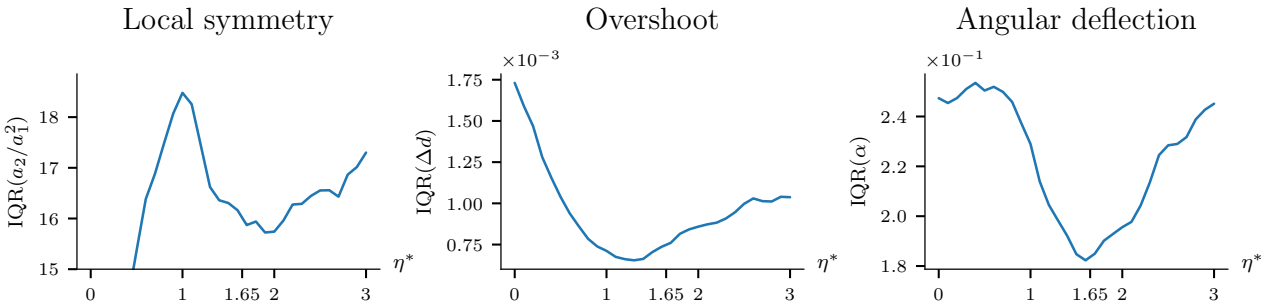

Figure 5. Interquartile range of the distributions of the local symmetry parameter, overshoot and angular deflection collected in the analysis of White River, Vermont, USA

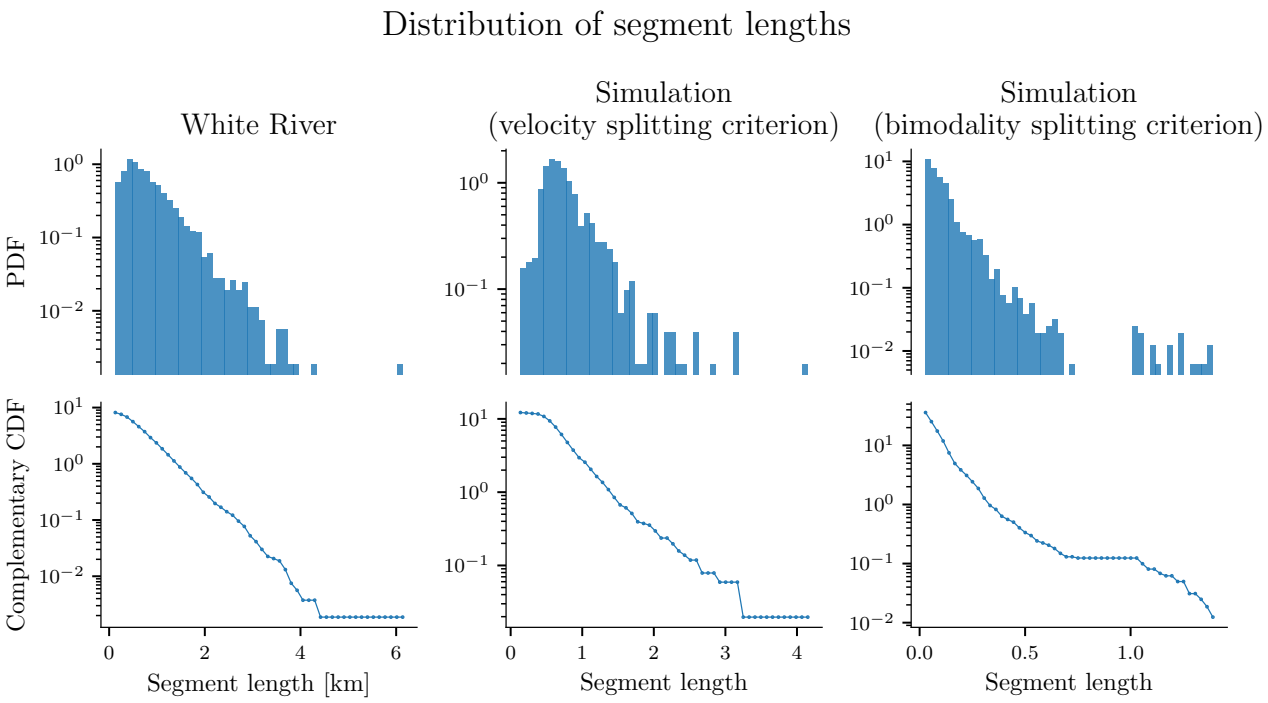

Figure 6. Comparison of the distributions of segment lengths in White River, Vermont, USA, a simulation with the Poissonian driving field and velocity-based splitting criterion, and a Poissonian simulation with the bimodality splitting criterion. The first row presents the probability density function of the segment lengths, whereas the second row shows complementary cumulative distribution functions.

Chapter 4

Paper III: "Breakthrough-induced loop formation in evolving transport networks"

Author contributions

In this study, the author: identified the characteristic loop formation event in various systems, provided theoretical description, developed numerical tools to study finger interactions and to model temporal evolution of the fingers, performed simulations of finger growth leading to loop formation, conducted the viscous fingering experiment, analyzed data from the experiments and compared them with theoretical results, prepared figures, wrote the first draft, and co-edited all subsequent versions of the paper.

PNAS RESEARCH ARTICLE | PHYSICS

Breakthrough-induced loop formation in evolving transport networks

Stanisław Żukowski[a,b,1], Annemiek Johanna Maria Cornelissen[b], Florian Osselin[c], Stéphane Douady[b], and Piotr Szymczak[a]

Affiliations are included on p. 7.

Edited by Daniel H. Rothman, Massachusetts Institute of Technology, Cambridge, MA; received January 30, 2024; accepted June 15, 2024, by Editorial Board Member Mehran Kardar

Transport networks, such as vasculature or river networks, provide key functions in organisms and the environment. They usually contain loops whose significance for the stability and robustness of the network is well documented. However, the dynamics of their formation is usually not considered. Such structures often grow in response to the gradient of an external field. During evolution, extending branches compete for the available flux of the field, which leads to effective repulsion between them and screening of the shorter ones. Yet, in remarkably diverse processes, from unstable fluid flows to the canal system of jellyfish, loops suddenly form near the breakthrough when the longest branch reaches the boundary of the system. We provide a physical explanation for this universal behavior. Using a 1D model, we explain that the appearance of effective attractive forces results from the field drop inside the leading finger as it approaches the outlet. Furthermore, we numerically study the interactions between two fingers, including screening in the system and its disappearance near the breakthrough. Finally, we perform simulations of the temporal evolution of the fingers to show how revival and attraction to the longest finger leads to dynamic loop formation. We compare the simulations to the experiments and find that the dynamics of the shorter finger are well reproduced. Our results demonstrate that reconnection is a prevalent phenomenon in systems driven by diffusive fluxes, occurring both when the ratio of the mobility inside the growing structure to the mobility outside is low and near the breakthrough.

nonlinear physics | unstable growth processes | transport networks

Significance

Loops are ubiquitous in animate and inanimate transport networks, from leaf venation to river deltas. Yet, current physical models fail to reproduce them accurately. We report a way of loop formation that manifests in remarkably diverse processes—from unstable fluid flows to the canal system of jellyfish. Near the breakthrough, when one of the branches reaches the outlet of the system, shorter branches revive and accelerate toward the longest one, ultimately leading to a reconnection event. This results in a hierarchical structure of interconnected fingers. Our explanation of the shared underlying mechanism behind the phenomenon significantly advances the understanding of how looping transport networks dynamically emerge.

Nature offers us a wide spectrum of spatial, transport networks, which provide key functions in living organisms and the surrounding environment. Examples span from leaf venation (1), blood vessels (2), jellyfish gastrovascular canal system (3), to river networks (4, 5), deltas (6, 7), or cave conduits (8, 9). Topologically, these networks can take the form of either branched, tree-like structures or looping patterns. The latter are more robust against damage (10), hence they are often favored by biological evolution. For example, it is thought that leaf venation is branched in ancestral plants, but highly reticulated in more evolutionary recent ones (11–13).

While the question of why looping networks might have been chosen by evolution and what quantity, if any, they optimize, was extensively studied (6, 10, 14–18), the question of how branches in the network interact to form a looping network remains unclear. A natural candidate for an underlying mechanism leading to reconnections is a tensorial stress field (19, 20). However, many networks in nature develop as a result of unstable growth processes in a scalar field (21, 22).

The growth in such a case is driven by the gradient of an external field, such as electric potential or concentration. Growing parts of the structure compete for the available flux of the field, effectively interacting with each other. The branches in the network try to go away from each other, to maximize the flux coming to their tips and avoid being shadowed (21–23). This mechanism, however, cannot explain the formation of loops, for which an effective attraction between the growing branches has to be present.

Surprisingly, loops suddenly appear across numerous systems as the longest branch reaches the outlet of the system. Here, we report that near the breakthrough, the shorter branch grows toward the longest one and reconnects to it (Fig. 1*A*). This results in a characteristic hierarchical pattern found in a large variety of systems (Fig. 1 *B*–*E*): dissolving fractures (24, 25), viscous fingering (26), discharge patterns (27), and even the growth of a gastrovascular canal network of the jellyfish *Aurelia* (3); see *Materials and Methods*, section 3.1 for a detailed description of the examples and experiments. The ubiquity of this process suggests the existence of a shared underlying mechanism, which we elucidate here.

Author contributions: S.Ż., A.J.M.C., F.O., S.D., and P.S. designed research; S.Ż., A.J.M.C., and F.O. performed research; S.Ż., A.J.M.C., S.D., and P.S. analyzed data; and S.Ż., A.J.M.C., S.D., and P.S. wrote the paper.

The authors declare no competing interest.

This article is a PNAS Direct Submission. D.H.R. is a guest editor invited by the Editorial Board.

[1]To whom correspondence may be addressed. Email: s.zukowski@uw.edu.pl.

This article contains supporting information online at https://www.pnas.org/lookup/suppl/doi:10.1073/pnas.2401200121/-/DCSupplemental.

Published July 10, 2024.

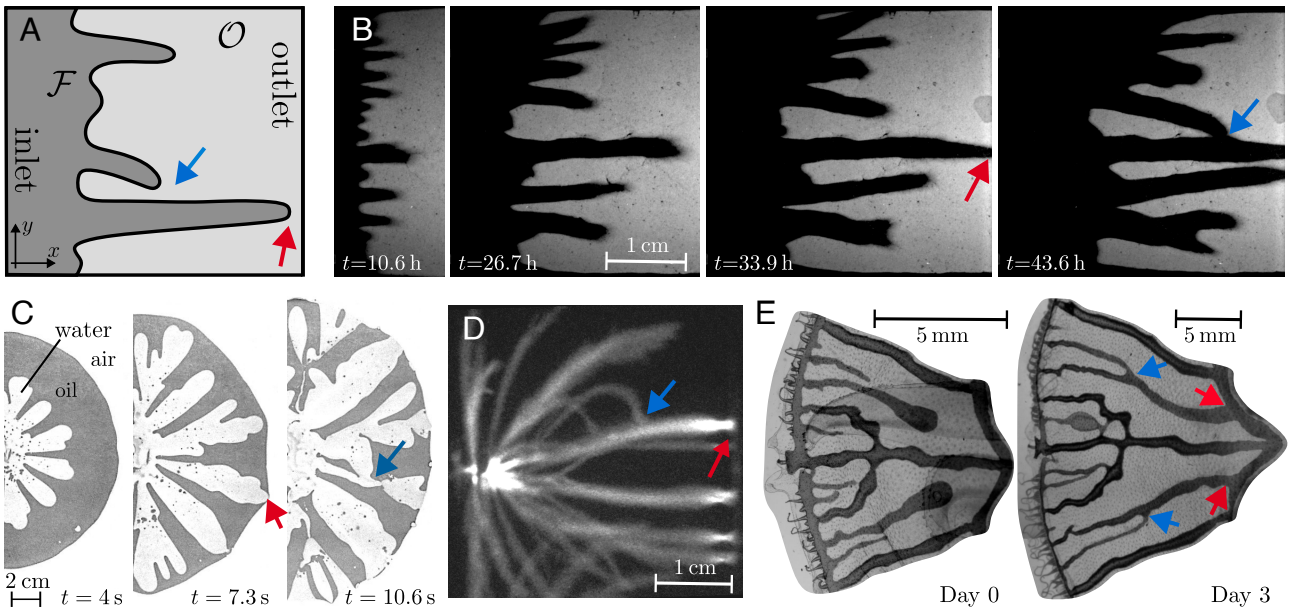

Fig. 1. Systems near breakthrough in nature. (*A*) Each system consists of two phases: an invading phase ($\mathcal{F}$) with mobility λ_1, and a displaced phase ($\mathcal{O}$) with mobility λ_2, separated by an interface. The growth direction is from left to right. Red arrows mark places where the fingers are near breakthrough or have already broken through, and blue arrows mark reconnections. (*B–E*) Examples of reconnection near breakthrough in various systems: (*B*) a fracture dissolution experiment in a Hele-Shaw cell, (*C*) viscous fingers in the Saffman–Taylor experiment, (*D*) streamer channels in air (photo: Sander Nijdam, Eindhoven University of Technology, by permission), (*E*) an octant of the jellyfish *Aurelia*, showing the gastrovascular canal network in dark gray (3).

Laplacian Growth. In many unstable growth processes, the boundary—the interface between two phases—moves due to the external forcing, such as pressure gradient between the inlet and outlet of the system (Fig. 1*A*). Important parameters in such models are the mobilities of the two phases, e.g., hydraulic permeabilities for pressure-driven growth. Whenever the mobility of the invading phase (λ_1) is larger than the mobility of the displaced phase (λ_2) the flux concentrates on small protrusions of the interface and the front can break into fingers (22, 28, 29). Because of the flux concentration, the fingers tend to grow more in length than in diameter. The width of the fingers is then set by surface tension, or other short-scale regularization mechanisms. Additional effects, such as tip splitting, can give rise to a highly ramified, hierarchical tree-like structure.

A paradigm for such growth processes is Laplacian growth, where the fingers extend with velocity proportional to the flux of a diffusive field (ϕ_i) given by: $\vec{J}_i = -\lambda_i \nabla \phi_i$, for $i = 1, 2$ depending on the phase. The conservation of the flux results in the Laplace equation for the field in both the invading ($\mathcal{F}$) and the displaced phase ($\mathcal{O}$):

$$\Delta\phi_1(\vec{x}) = 0, \quad \vec{x} \in \mathcal{F} \quad \text{and} \quad \Delta\phi_2(\vec{x}) = 0, \quad \vec{x} \in \mathcal{O}\,. \qquad [1]$$

These equations are supplemented with the continuity condition for the field and its flux at the interface ($\mathcal{T}$):

$$\begin{aligned} \phi_1(\vec{x}) &= \phi_2(\vec{x}) \qquad \vec{x} \in \mathcal{T}\,, \\ \lambda_1(\nabla\phi_1(\vec{x}))_n &= \lambda_2(\nabla\phi_2(\vec{x}))_n \quad \vec{x} \in \mathcal{T}\,, \end{aligned} \qquad [2]$$

where n denotes the normal to the interface. Additionally, the Dirichlet boundary condition is imposed on the inlet ($x = 0$) and outlet ($x = 1$) of the system:

$$\phi_1(x = 0) = 1 \quad \text{and} \quad \phi_2(x = 1) = 0\,. \qquad [3]$$

Note that the coordinates here are rescaled by the system length, and the field is rescaled by the value at the inlet.

Effect of Mobility Ratio. However, reticulated networks are usually not obtained in such models (21–23). This is due to the simplifying assumption that neglects the mobility of the invading phase, which is equivalent to taking the limit of mobility ratio going to infinity, $M = \lambda_1/\lambda_2 \to \infty$. This leads to the omission of the field drop within the fingers. The Laplace equation is then solved only in the displaced domain with a constant value of the field directly on the moving boundary. The Dirichlet boundary condition on the fingers results in i) long fingers screening the shorter ones and hindering their growth and ii) two parallel fingers growing away from each other as they get more flux from the sides.

If one takes into account a finite mobility ratio the effective repulsion and screening diminishes. The field inside the invading phase is then no longer constant and the resulting field gradients can make the fingers attract each other and create loops (30, 31). As shown by Budek et al. (31), this can occur only for a specific range of mobility and finger length ratios.

However, as presented in Fig. 1, the breakthrough reconnections are not limited to these specific scenarios. Notably, they can occur even in the general case of high mobility ratio, which was previously thought to be impossible due to screening effects. Nonetheless, near the breakthrough, screening diminishes, enabling the revival and growth of shorter branches toward the longest one, ultimately leading to a reconnection event. We demonstrate that contrary to previous studies reconnection is a prevalent phenomenon in Laplacian growth, occurring both in low mobility ratio cases and near the breakthrough.

1. Results and Discussion

1.1. Drop of Potential Along a Single Finger. To understand the generality of the breakthrough reconnections, we begin with a 1D case. Here, $\mathcal{F} = \{x \in [0, x_t]\}$, $\mathcal{O} = \{x \in [x_t, 1]\}$ and $\mathcal{T} = \{x_t\}$ is just the fingertip. The solution of the Eqs. **1–3** are then two piecewise linear functions stitched at the fingertip (Fig. 2*A*):

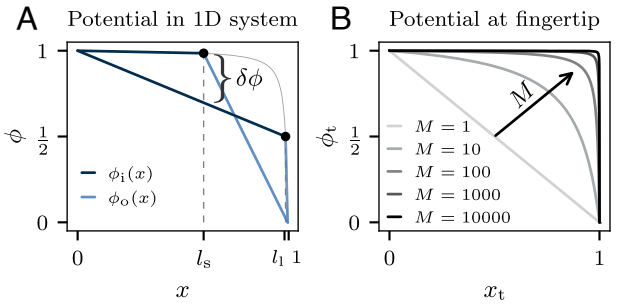

Fig. 2. Solutions of Eqs. **1**–**3** for a 1D system. (*A*) Potential in the system with mobility ratio $M = 100$ for a short finger of length l_s and a longer finger of length $l_l > l_s$. The dark line marks the field inside the finger (ϕ_i), the lighter line marks the field outside (ϕ_o), and the black dot marks the position of the fingertip. (*B*) A profile of the potential at the fingertip (ϕ_t) as a function of the tip position (x_t) for different mobility ratios. Such a profile for $M = 100$ is also plotted in (*A*) with a thin gray line.

$$\phi(x) = \begin{cases} 1 - \frac{x}{M - x_t(M-1)}, & \text{if } x \in [0, x_t] \\ \frac{1-x}{1-x_t(1-1/M)}, & \text{if } x \in [x_t, 1]. \end{cases} \quad [4]$$

A few remarks can be made based on this simple example.

First, for a finite mobility ratio ($M = 100$, Fig. 2*A*) when the fingertip is far from the outlet ($x_t = l_s \ll 1$), approximation of a constant field on the moving boundary works well, and the field inside the short finger can be treated as constant. However, if we take a longer finger ($x_t = l_l \approx 1$), there is a significant potential drop inside it. By comparing the field values at $x = l_s$ we see that there is a difference of potential between the two fingers:

$$\delta\phi \approx 1 - \phi(x = l_s, x_t = l_l) = \frac{l_s}{1 + d(M-1)}, \quad [5]$$

where $d = 1 - l_l$. If such fingers were placed at a distance δy next to each other, there would be a gradient of potential $\delta\phi/\delta y$, between the shorter finger tip and the longer finger, provided that the fingers do not influence each other. As a result, the shorter finger would be attracted toward the longer one.

Second, let us focus on the potential at the fingertip as a function of the tip position $\phi_t(x_t) = \phi(x = x_t)$ (Fig. 2*A*, light gray line and Fig. 2*B*), and analyze how it changes with the mobility ratio. The higher the M, the steeper the profile of the potential at the fingertip, and the longest finger must be closer to the outlet to feel its impact. As can be seen in Eq. **5**, $\delta\phi$ is inversely proportional to the product Md. This suggests that the critical distance, d_c, at which the pressure inside the longer finger begins to drop and the attraction between two fingers would appear, scales as $d_c \sim M^{-1}$.

In the limiting case $M \to \infty$ the functional dependence $\phi_t(x_t)$ becomes a step function (Fig. 2*B*). The fingers have a constant potential along their length, no matter how close they are to the outlet, and there is no difference in potential between them. However, when one of the fingers breaks through, the potential inside it takes the form $\phi(x) = 1 - x$. This instantaneous pressure drop inside the longer finger induces a pressure difference with respect to the shorter finger, $\delta\phi = l_s$. Consequently, at the moment of breakthrough, we observe a sudden transition from no interaction between the fingers to attraction of the shorter finger to the longer one.

1.2. Finger Interactions in Two Dimensions: Screening and Revival. Although insightful, the 1D model treats two fingers independently of each other and does not take into account effects of finger interactions such as screening. To investigate these effects we conduct numerical simulations in a 2D geometry. Two fingers are placed in a cell of length $L = 1$ and width $W = L/3$ with periodic boundary conditions on the bottom ($y = 0$) and top ($y = W$) wall. The long finger of length l_l is positioned at $y = 0$, and the short finger of length l_s is at $y = W/3$, as shown in Fig. 3 *A* and *B*. The fingers have a shape of thin rectangles of width $W/15$ with semicircular caps. We solve the equations for the field with the finite element method implemented in the FreeFEM++ software (32) (*Materials and Methods*, section 3.2).

Fig. 3 *A* and *B* represent isolines of the field (the same set of values) in two cases: $M = 10^6$ and $M = 10^2$. We observe that for high mobility ratio there is a negligible potential drop inside the fingers, and the longer finger attracts almost all of the flux. As a result, it screens the shorter one and would suppress its growth. For lower mobility ratio, due to the potential drop inside the longer finger, some flux can reach the shorter one, so it can still grow.

We consider the field values along the center line of the long and short fingers for the two mobility ratios (Fig. 3 *C* and *D*). The profiles along the longer finger are piecewise linear, similar to the 1D solutions presented in Fig. 2*A*. However, the field

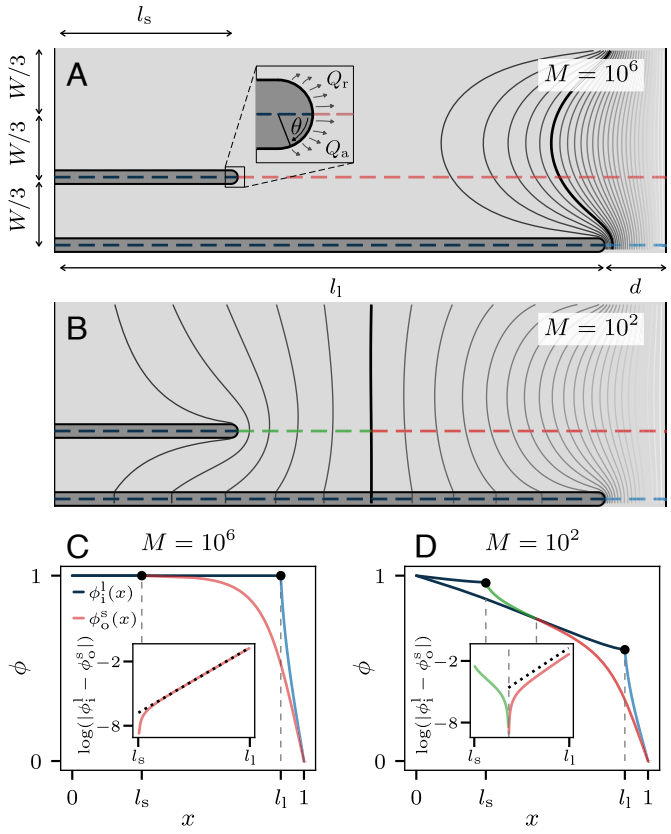

Fig. 3. Numerical solutions of Eqs. **1**–**3** for a 2D system. (*A* and *B*) A schematic of the 2D setup with two fingers (of lengths $l_s = 0.3$ and $l_l = 0.9$) in a periodic cell of length $L = 1$ and width $W = L/3$ with the isolines of the field for: (*A*) $M = 10^2$ and (*B*) $M = 10^6$. In the *Inset*, we mark the attractive (Q_a) and repulsive (Q_r) fluxes intercepted by the right and the left side of the fingertip, respectively. (*C* and *D*) Field values along the longer and shorter finger [cross-sections marked with dashed lines in (*A*) and (*B*)] for the two mobility ratios. *Insets* in (*C*) and (*D*): the difference between the field inside the longer finger and outside the shorter one: $\phi_i^l - \phi_o^s$. The black dashed line is a fit to the linear part of the plot in *Inset* (*C*), highlighting the exponential decay of $\phi_i^l - \phi_o^s$ (from the longer finger tip perspective).

values outside the shorter fingers (ϕ_o^s) are strongly influenced by the longer ones. In fact, the difference between the field inside the longer finger and the field outside the shorter one, $\phi_i^l - \phi_o^s$, decays exponentially from the perspective of the longer finger tip, as shown by the black dashed lines in *Insets* in Fig. 3 *C* and *D*. As a result, the shorter finger is strongly screened and almost no flux reaches its tip.

The situation changes drastically as the longer finger approaches the outlet. In Fig. 4*A*, we analyze the total flux Q through the tip of the shorter finger as a function of gap d—the distance from the longer finger tip to the outlet of the system. The length ratio is kept constant $l_s/l_l = 1/3$ and Q is calculated by integrating the flux at the shorter finger tip for $\theta \in [-\pi/2, \pi/2]$; see the *Inset* in Fig. 3*A*.

For relatively low mobility ratio, the shorter finger is weakly screened and receives some flux, even when the longer finger is far from the outlet (large d). The higher the M, the stronger the screening effect, hence for large d the total flux in the shorter finger is close to zero, and it only starts to increase as the gap gets smaller. Note that the critical distance from the outlet, at which the screening starts to diminish, decreases as M gets larger. This is a further manifestation of the fact that the critical gap at which screening vanishes scales as M^{-1}, as already described with the 1D model. The above confirms that for sufficiently small d, or after the breakthrough, short fingers that were strongly screened would revive and start growing again, as also noted in refs. 25 and 26.

Interestingly, for large M the $Q(d)$ dependence approaches a universal function that simply shifts in d as M increases. This suggests that the flow profiles should collapse onto a master curve when plotted as a function of Md, which is indeed the case (Fig. 4*B*). Moreover, if we define rescaled d: $d' = Md$, plug it into Eq. **5**, and take the limit of $M \to \infty$ we see that the master curve will be of the form $1/(1 + d')$. This can be adapted for a 2D system and written as

$$Q(d') = q_0 + (q_1 - q_0)/(1 + d'/d'_c). \qquad [6]$$

The three parameters q_0, q_1, d'_c can be easily extracted from the simulation results and have a clear physical interpretation: q_0 and q_1 are the flux reaching the shorter finger tip during screening phase and after revival, respectively; d'_c, the inflection point of the sigmoid, is the rescaled critical gap at which the shorter finger in the two-dimensional system revives. As can be seen in Fig. 4*B*, dashed line, Eq. **6** perfectly captures revival in our system.

1.3. Finger Interactions in Two Dimensions: Repulsion and Attraction. Having described the revival of the shorter finger, let us discuss the change in their growth direction near the breakthrough. To quantify this, we calculate the attractive, Q_a, and repulsive flux, Q_r, by integrating the flux on the shorter finger tip for $\theta \in [0, \pi/2]$ and $\theta \in [-\pi/2, 0]$, respectively (see *Inset* in Fig. 3*A*). We then take the difference of the two fluxes, $Q_a - Q_r$. The positive value of this quantity will be interpreted as an effective attraction and should result in the shorter finger growing toward the longer one. Conversely, if the value is negative the fingers repel. Fig. 4*C* represents repulsion-attraction maps as a function of two parameters: mobility ratio (M) and finger length ratio (l_s/l_l). The maps are shown for four gaps: $d = 1/2,\ 10^{-2},\ 10^{-4},\ 0$; the latter corresponds to the breakthrough.

For large gap (Fig. 4*C*, $d = 1/2$), we observe an island of attraction in the region of lower mobility ratio, $M \in (10^0 - 10^2)$, and the length ratio, $l_s/l_l \in (0, 0.6)$. This quantitatively agrees with the results of the resistor model presented by Budek et al. (31), where the interactions between the fingers distant from the outlet were analyzed. As described there and as can be seen in Fig. 4*C*, $d = 1/2$, for the systems of low mobility ratio the screening is weak and the fingers can attract each other to form loops. Note that in the other maps in Fig. 4*C*, regardless of the gap size d, the value of $Q_a - Q_r$ remains almost the same in the region of low mobility and length ratio. This suggests that in such systems the breakthrough will not drastically affect the dynamics and interactions between the fingers.

The impact of the gap size on the interactions is more apparent in the region of higher mobility ratio, $M \in (10^3 - 10^6)$, and length ratio, $l_s/l_l \in (0.6, 0.9)$. Here, the interactions change from slight to strong repulsion when the leading finger is distant from the outlet, $d = 1/2,\ 10^{-2}$, and finally, after the breakthrough, $d = 0$, we observe a transition from strong repulsion to strong attraction. Hence, for systems of higher mobility ratio, the impact of the breakthrough should be more striking in the dynamics of the fingers. In particular, even for very high mobility ratio, the longer finger will always attract the shorter ones after the breakthrough.

1.4. Temporal Evolution of the Fingers. Finally, we perform dynamic simulations of finger growth. During growth, we do not change the finger shape (constant width and semicircular tips) and extend it only in the direction from which the highest flux is coming (*Materials and Methods*, section 3.2). Here, we

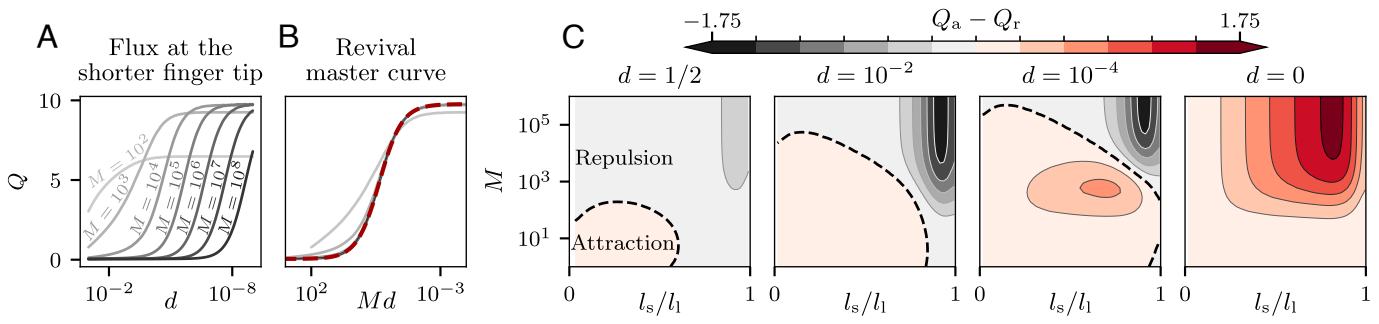

Fig. 4. Revival and interactions between the fingers when the gap changes. (*A*) Total flux intercepted by the shorter finger tip, $Q = Q_a + Q_r$ (as defined in *Inset* in Fig. 3*A*), as a function of d. The length ratio is kept constant, $l_s/l_l = 1/3$. (*B*) Total flux plotted as a function of Md. The master curve, red dashed line, corresponds to Eq. **6** plotted with $q_0 = 0.05, q_1 = 9.76, d'_c = 0.23$. (*C*) Maps of interactions between the fingers, $Q_a - Q_r$, as a function of two parameters: mobility ratio (M) and finger length ratio (l_s/l_l). Maps are plotted for four gaps: $d = 1/2,\ 10^{-2},\ 10^{-4},\ 0$. Red colors indicate attraction, gray repulsion, and the black dashed line separates the two.

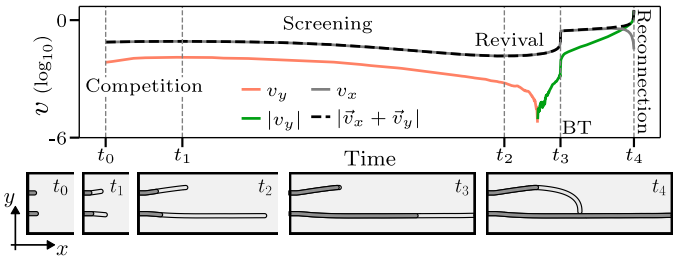

Fig. 5. Velocity of the shorter finger in the dynamical simulation of growth with mobility ratio $M = 1{,}000$. The black dashed line marks the total velocity of the finger, gray its x-component (pointing toward the outlet), red the y-component (repulsion from the longer finger), and green the absolute value of v_y (attraction to the longer finger). Gray vertical lines mark: initial time (t_0); start of screening (t_1), when the acceleration of the finger becomes negative; start of revival (t_2), when the acceleration changes its sign again; breakthrough (BT, t_3) and reconnection (t_4). Snapshots from the simulation were taken at the corresponding moments of the evolution (lighter color on the fingers marks the parts that grew between successive moments).

analyze the evolution of two fingers with slightly different initial lengths, $l_s = 0.04$ vs. $l_l = 0.05$, and mobility ratio in the system $M = 1{,}000$. With such initial conditions, we can observe all previously described interactions between the fingers: competition and repulsion, screening, revival, and attraction. The dynamics of the fingers are presented in Movie S1.

In Fig. 5, we show how the velocity of the shorter finger changes over time, along with the snapshots from the simulation. First, as the fingers start with similar lengths, we observe competition and repulsion between them—the fingers accelerate and grow with similar rate, until the longer finger wins and starts to screen the shorter one. At this moment ($t = t_1$), the shorter finger starts to slow down. As the longer finger approaches the outlet, the field inside it begins to decrease (as visible in Movie S1). Consequently, screening disappears and the overall flux within the shorter finger increases. The shorter finger revives and accelerates again ($t = t_2$).

Shortly after t_2 the attraction toward the longer finger appears: the positive v_y, away from the longer finger (depicted by the red line in Fig. 5) transitions to negative, toward the longer finger ($|v_y|$, marked with the green line in Fig. 5). This stage corresponds to the expansion of the attraction region on the interaction maps prior to the breakthrough (Fig. 4*A*). Then, just before the breakthrough ($t = t_3$), there is a sudden jump in velocity. This last boost significantly expedites the loop formation process. As the distance between the two fingers diminishes, the attraction intensifies. This cumulative, snowball-like effect, triggered by the breakthrough, culminates in the eventual reconnection at $t = t_4$.

1.5. Comparison of the Simulations to Experiments. We additionally present two simulations that qualitatively reproduce the behavior of the fingers in the fracture dissolution and Saffman–Taylor experiments seen in Fig. 1 *B* and *C*, with approximate mobility ratios of $M = 14$ and $M = 100$, respectively (see *Materials and Methods*, sections 3.1.1 and 3.1.2 for details on how the mobility ratio in the experiments is calculated). In these simulations, the fingers were initiated with lengths of $l_s = 0.002$ and $l_l = 0.18$. In *SI Appendix*, we include videos from the simulations (Movies S2 and S3) and videos from the experiments (Movies S4 and S5). In Fig. 6, we show the plots of the velocity of the shorter finger, both in the simulations and in the experiments, in the case of fracture dissolution ($M = 14$) and viscous fingering ($M = 100$).

As predicted in the previous section, in the case of the lower mobility ratio, the shorter finger is attracted toward the longer one almost from the very beginning of the evolution, both in the simulation (Fig. 6*A* and Movie S2) and the experiment (Fig. 6*B* and Movie S4). There is also no effect of screening, and flux is nonnegligible even when the longer finger is far away from the outlet. As a result, the finger grows with an almost constant total velocity, which remains unchanged even during the breakthrough.

In contrast, for higher mobility ratio, the shorter finger in the simulation (Fig. 6*C* and Movie S3) and in the experiment (Fig. 6*D* and Movie S5) is initially screened by the longer one and grows relatively slowly. Only after the breakthrough does it revive and eventually reconnect forming a loop.

2. Conclusions

As previously described in the literature, attractive interactions between the fingers can appear in the systems of low mobility ratio, leading to reconnections. For high mobility ratio, only screening and repulsion have been observed, resulting in branched loopless structures. However, when studying systems such as viscous fingering or fracture dissolution, experiments are often terminated when the invading phase reaches the border of the system. An unexpected behavior arises in a broad class of unstable growth processes when the proximity of the outlet is considered and the evolving structure breaks through.

We have shown that a striking transition in the system dynamics occurs when the breakthrough is reached, especially in the case of infinite mobility ratio, where a singular limit emerges. Prior to the breakthrough, the field along the longest finger remains constant regardless of its proximity to the outlet, and the finger screens the rest of the system. At the moment of breakthrough, however, the field in the longer finger drops dramatically, allowing the flux to reach the shorter neighboring fingers. This affects the dynamics of the shorter fingers, causing their revival and a strong attraction to the longer finger. The interplay of these two factors leads to reconnection and loop formation.

To explain breakthrough reconnections, we used a simplified model of growing Laplacian fingers: i) we neglected the jump in the field across the interface associated with the regularization mechanism; ii) we assumed that the change of mobility across the interface is discontinuous, rather than smooth as in, for instance, fracture dissolution; iii) we kept the shape of the fingers unchanged during their evolution, whereas in some systems, such as viscous fingering, when the fingers receive more flux, their tips begin to grow in width, which impacts their velocity (33, 34). Regardless, for high mobility ratio, boundary condition on the fingers transitions from a constant field in the initial state to a linear gradient near the breakthrough. This field change near the breakthrough is much larger than any jump in the field resulting from regularization mechanisms (*Materials and Methods*, section 3.1.2). The transition between the two boundary conditions might be more gradual due to ii) and iii), but it still significantly impacts the finger dynamics. This is evidenced by sudden loop formation observed in physical systems such as viscous fingering or discharge patterns, and also in living organisms such as the jellyfish *Aurelia* (Fig. 1 *B*–*E*).

The breakthrough reconnections are expected to occur in virtually any system driven by diffusive fluxes. Observing it in a system of a yet unknown growth mechanism, such as the gastrovascular canal network of the jellyfish (Fig. 1*E*), is a strong

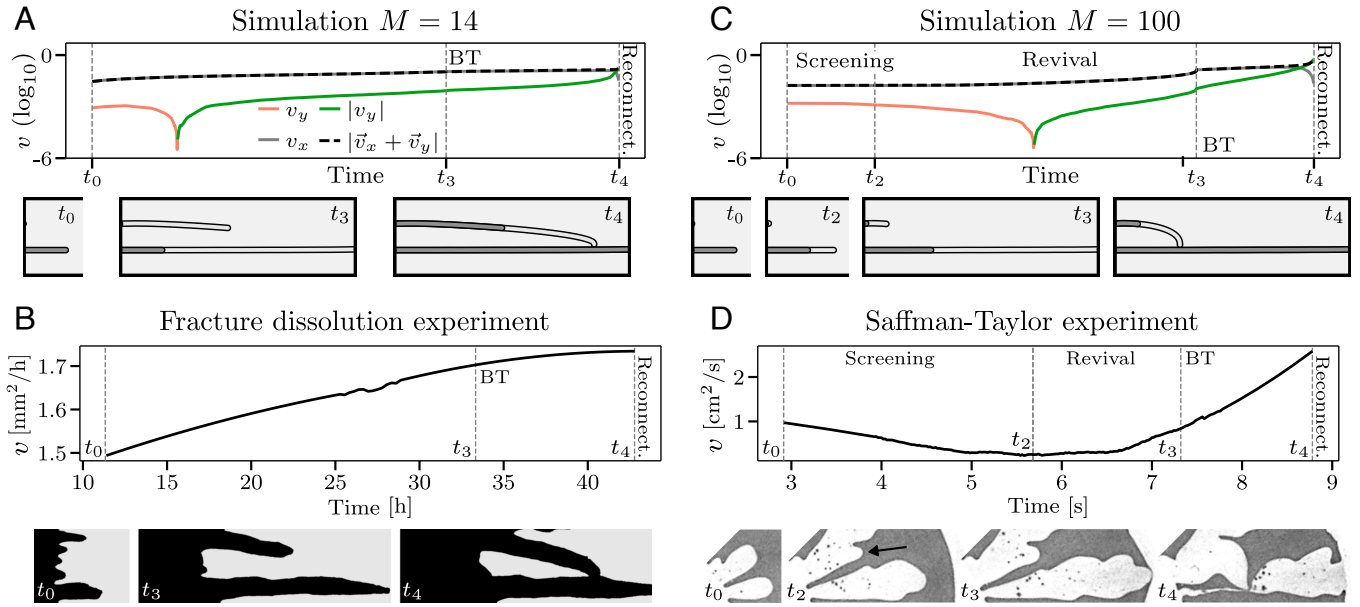

Fig. 6. Comparison of simulations to experiments. (*A* and *B*) Velocities of the shorter finger in the fracture dissolution simulation and experiment, respectively. The mobilities here are related to the aperture values in the dissolved and undissolved regions (*Materials and Methods*, section 3.1.1). The mobility ratio is $M = 14$. (*C* and *D*) Velocity of the shorter finger in the viscous fingering simulation and experiment. Here, the mobility ratio is the inverse of the viscosity ratio and is $M = 100$. The line colors and time points in the plots indicate the same as in Fig. 5. Snapshots were taken at the corresponding moments of the evolution. The lighter color on the fingers from the simulations marks the parts that grew between successive moments. The black arrow in (*D*) marks the shorter finger.

indication that the system dynamics are controlled by the effective diffusion of a morphogenic parameter. This sheds light on the possibility of dynamical loop formation in many systems.

3. Materials and Methods

3.1. Experiments.

3.1.1. Fracture dissolution. The fracture dissolution experiment presented in Fig. 1*B* was performed in a microfluidic setup described in detail in ref. 35. It consists of two polycarbonate disks. The bottom one contains a rectangular indentation (3.3 cm × 3.8 cm × 100 μm), which is initially filled with a soluble material, in our case plaster (Plaster of Paris, Blik Modelarski Alabastrowy). The top plate contains a hierarchical system of inlet and outlet channels connected to large inlet/outlet reservoirs (4.5 cm × 5 mm × 2 mm). Such a design helps to maintain uniform pressure across the width of the plaster. The aperture above the plaster is created by gluing the plates together with an ultrathin PET-based double-coated tape 70 μm thick with a rectangular hole the size of the plaster block. The cast was prepared with a 60% (w/w) ratio of water to plaster. This yields an average porosity of the block of $\phi = 50\%$ (measured porosity to water) and a permeability of 45 mD (measured by injection of isopropanol). Pure water is injected into the system with a syringe pump (Harvard Apparatus PHD2000) at a rate of $q = 0.5$ mL/h. We recorded the experiment with a UI 1550LE-C-HQ CCD camera (IOS, Germany), acquiring photographic images of the system every 100 s. In order to ensure homogeneous light intensity over the system, we used a circular fluorescent illuminator.

For experiments conducted in a Hele-Shaw cell, the mobility can be expressed as $\lambda = h^3/12\mu$, where h is the aperture of the Hele-Shaw cell available to the fluid and μ is the fluid viscosity. Thus, increasing the aperture in the dissolved part of the system (black area in Fig. 1*B*) effectively introduces two phases with different mobilities. The mobility ratio in this experiment was approximately $M = (h_1/h_2)^3 = (170/70)^3 \approx 14$.

3.1.2. Saffman–Taylor experiment. The Saffman–Taylor experiment presented in Fig. 1*C* was performed in a circular Hele-Shaw cell with a 1 mm separation between the bottom and top plates. The Hele-Shaw cell was initially filled with oil (dyed with paprika to increase contrast in the images). Water was injected into the system through an inlet located in the center of the top plate. The experiment was recorded with a Nikon D3000 camera. A LED panel was used below the Hele-Shaw cell to ensure uniform light intensity throughout the system. the mobility ratio is the inverse of the viscosity ratio and was of the order of $M = \mu_2/\mu_1 \approx 100$.

The pressure jump in a Hele-Shaw is estimated using the Young–Laplace equation: $\Delta p^{\text{cap}} = \gamma(2/b + 1/r)$, where $\gamma = 49$ mN/m is the surface tension between oil and water, $b = 1$ mm is the spacing between the plates, $r \sim 1$ cm is a typical radius of curvature for the fingers. This yields $\Delta p^{\text{cap}} \sim 10^{-3}$ Pa. When the breakthrough occurs, the pressure inside the longest finger drops from the inlet value to a linear gradient between the inlet and outlet. The typical pressure difference between inlet and outlet in our Saffman–Taylor experiment was of the order of 10^2 Pa. Thus, the change in ϕ induced by the breakthrough is 5 orders of magnitude larger than the pressure jump due to surface tension, and it can be neglected.

3.1.3. Jellyfish. The breakthrough reconnections can also be encountered in biological systems. The gastrovascular system of the jellyfish *Aurelia* is composed of canals in which seawater flows, carrying nutrients and oxygen to the surrounding tissues. New canals (sprouts) appear on the circulatory canal at the rim of the jellyfish subumbrella and grow toward four stomachs in the center of the jellyfish. We observed that the smaller sprouts reconnect to the long canal that just connected to the gastrocircular groove around the stomach (3) (Fig. 1*E*).

Jellyfish were reared at room temperature (22 °C) in artificial seawater prepared by diluting 28 g of synthetic sea salt (Instant Ocean; Spectrum Brands, Madison, WI) per liter of osmosis water (osmolarity 1100 mOsm). In the laboratory, polyps of the Roscoff strain (36) are used (obtained by courtesy of Konstantin Khalturin from the Marine Genomics Unit, Okinawa Institute of Science and Technology Graduate University, Onna, Okinawa, Japan). A more detailed description of jellyfish rearing can be found in ref. 3.

To observe the jellyfish gastrovascular system, the jellyfish are caught from the aquarium approximately 3 h after feeding them with artemia. In this way, the gastrovascular canals are colored orange by the digested artemia. They are anesthetized with magnesium chloride dissolved in seawater. Then, they are placed in a Petri dish in shallow seawater with the subumbrella facing up. The images are taken by transillumination using a Leica macro zoom (MACROFLUO LEICA Z16 APO S/No: 5763648) and a Photron Fastcam SA3 camera. The images were stitched using Adobe Photoshop. The canals in the images were highlighted with gray color.

3.1.4. Streamer discharge. Streamer discharges are fundamental building blocks of sparks and ligthnings. An experimental photo presented in Fig. 1*D*

was obtained by courtesy of Sander Nijdam (37). Here, the mobilities are the conductivities inside the discharge channel and the air. Breakthrough reconnections in this context have been observed in many experiments (38–40). In ref. 27 stereo photography was used to fully reconstruct the three-dimensional structure of the reconnection events.

3.1.5. Velocity of the fingers. To estimate the velocity of the fingers in the experiments, we binarized the images and prepared a mask that covered the area of the image in which the finger was growing. Next, we calculated the area of the shorter finger (within the mask) in successive frames. The approximate velocity of the finger was defined as the rate of change of this area. Finally, the velocity was smoothed using the Savitzky–Golay filter (function *savgol_filter* from the Scipy package).

3.2. Numerical Simulations. The numerical calculations and simulations were performed using the codes available on the GitHub repository (https://github.com/stzukowski/reticuler) (41, 42). In the temporal simulations, the fingers have a constant width and end with semicircular tips, as in the static numerical calculations. In each time step of the evolution we solve the equations for the field (Eqs. **1**–**3**) with the finite element method implemented in the FreeFEM++ software (32). To calculate the field in the system, we decompose it into two domains: the fingers and the outside. The mobility field is declared, $M(x, y)$, which is equal to λ_1 inside the fingers and λ_2 outside. Our script solves the equation for the field in the form: $\nabla \cdot (M(x, y)\nabla\phi(x, y)) = 0$.

To determine the velocity of the finger, we integrate the flux entering its tip. Following the principle of local symmetry (41, 43), we extend the finger in the direction from which the highest flux comes (while keeping its width constant). The dynamical simulation in Fig. 5 was initiated with branches of length $l_s = 0.04$ and $l_l = 0.05$, while the simulations in Fig. 6 started with branches of lengths: $l_s = 0.002$ and $l_l = 0.18$. The velocity in y direction in Figs. 5 and 6 was treated with the Savitzky–Golay filter (*savgol_filter* function from the Scipy package) to smooth the numerical noise caused by the small order of magnitude of this velocity.

Data, Materials, and Software Availability. All study data are included in the article and/or supporting information. The codes are available on the GitHub repository (https://github.com/stzukowski/reticuler) (42).

ACKNOWLEDGMENTS. This project was partially supported by the National Science Center (Poland) under research Grant 2020/02/Y/ST3/00121 and by the Mission for Transversal and Interdisciplinary Initiatives of the French National Center of Scientific Research in the program Auto-Organisation 2021 and 2022 under research Grants 212680, 284366, and 238661. We also acknowledge the funding from the Polish National Agency for Academic Exchange and Campus France under Grant BPN/BFR/2022/1/00033 in the program PHC Polonium. We also thank Sélène Jeammet for her help with the Saffman–Taylor experiment and Solène Song for the jellyfish timelapse images.

Author affiliations: [a]Institute of Theoretical Physics, Faculty of Physics, University of Warsaw, Warsaw 02-093, Poland; [b]Laboratoire Matière et Systèmes Complexes, UMR 7057, CNRS & Université Paris Cité, Paris 75013, France; and [c]Institut des Sciences de la Terre d'Orléans, UMR 7327, CNRS & BRGM & Université d'Orléans, Orléans 45100, France

1. G. J. Mitchison, A model for vein formation in higher plants. *Proc. R. Soc. B* **207**, 79–109 (1980).
2. T. H. Nguyen, A. Eichmann, F. Le Noble, V. Fleury, Dynamics of vascular branching morphogenesis: The effect of blood and tissue flow. *Phys. Rev. E* **73**, 061907 (2006).
3. S. Song *et al*., Morphogenesis of the gastrovascular canal network in Aurelia jellyfish: Variability and possible mechanisms. *Front. Phys.* **10** (2023).
4. A. P. Petroff *et al*., Geometry of valley growth. *J. Fluid Mech.* **673**, 245–254 (2011).
5. O. Devauchelle, A. P. Petroff, H. J. Seybold, D. H. Rothman, Ramification of stream networks. *Proc. Natl. Acad. Sci. U.S.A.* **109**, 20832–20836 (2012).
6. A. Konkol, J. Schwenk, E. Katifori, J. B. Shaw, Interplay of river and tidal forcings promotes loops in coastal channel networks. *Geophys. Res. Lett.* **49**, e2022GL098284 (2022).
7. W. T. Ke, J. B. Shaw, R. C. Mahon, C. A. Cathcart, Distributary channel networks as moving boundaries: Causes and morphodynamic effects. *J. Geophys. Res.* **124**, 1878–1898 (2019).
8. P. Szymczak, A. J. C. Ladd, The initial stages of cave formation: Beyond the one-dimensional paradigm. *Earth Planet. Sci. Lett.* **301**, 424–432 (2011).
9. I. Ghani, D. Koehn, R. Toussaint, C. W. Passchier, Dynamic development of hydrofracture. *Pure Appl. Geophys.* **170**, 1685–1703 (2013).
10. E. Katifori, G. J. Szöllősi, M. O. Magnasco, Damage and fluctuations induce loops in optimal transport networks. *Phys. Rev. Lett.* **104**, 048704 (2010).
11. C. K. Boyce, A. H. Knoll, Evolution of developmental potential and the multiple independent origins of leaves in Paleozoic vascular plants. *Paleobiology* **28**, 70–100 (2002).
12. C. K. Boyce, "The evolutionary history of roots and leaves" in *Vascular Transport in Plants*, N. M. Holbrook, M. A. Zwieniecki, Eds. (Elsevier, 2005), pp. 479–499.
13. S. Douady *et al*., A work on reticulated patterns. *C. R. Méc.* **348**, 659–678 (2020).
14. J. R. Banavar, F. Colaiori, A. Flammini, A. Maritan, A. Rinaldo, Topology of the fittest transportation network. *Phys. Rev. Lett.* **84**, 4745–4748 (2000).
15. S. Bohn, M. O. Magnasco, Structure, scaling, and phase transition in the optimal transport network. *Phys. Rev. Lett.* **98**, 088702 (2007).
16. M. Durand, Structure of optimal transport networks subject to a global constraint. *Phys. Rev. Lett.* **98**, 088701 (2007).
17. H. Ronellenfitsch, E. Katifori, Global optimization, local adaptation, and the role of growth in distribution networks. *Phys. Rev. Lett.* **117**, 138301 (2016).
18. F. Kaiser, H. Ronellenfitsch, D. Witthaut, Discontinuous transition to loop formation in optimal supply networks. *Nat. Commun.* **11**, 5796 (2020).
19. Y. Couder, L. Pauchard, C. Allain, M. Adda-Bedia, S. Douady, The leaf venation as formed in a tensorial field. *Eur. Phys. J. B* **28**, 135–138 (2002).
20. S. Bohn, L. Pauchard, Y. Couder, Hierarchical crack pattern as formed by successive domain divisions. *Phys. Rev. E* **71**, 046214 (2005).
21. V. Fleury, J. F. Gouyet, M. Leonetti, *Branching in Nature: Dynamics and Morphogenesis of Branching Structures, from Cell to River Networks* (Springer Science & Business Media, 2001), vol. 14.
22. P. Ball, *Branches: Nature's Patterns: A Tapestry in Three Parts* (OUP, Oxford, UK, 2009).
23. P. Meakin, *Fractals, Scaling and Growth Far from Equilibrium* (Cambridge University Press, 1998), vol. 5.
24. R. L. Detwiler, R. J. Glass, W. L. Bourcier, Experimental observations of fracture dissolution: The role of Peclet number on evolving aperture variability. *Geophys. Res. Lett.* **30**, 1648 (2003).
25. V. Starchenko, C. J. Marra, A. J. C. Ladd, Three-dimensional simulations of fracture dissolution. *J. Geophys. Res.* **121**, 6421–6444 (2016).
26. S. Yang, G. Kong, Z. Cao, Z. Wu, H. Li, Hydrodynamics of gas–liquid displacement in porous media: Fingering pattern evolution at the breakthrough moment and the stable state. *Adv. Water Res.* **170**, 104324 (2022).
27. S. Nijdam, C. G. C. Geurts, E. M. van Veldhuizen, U. Ebert, Reconnection and merging of positive streamers in air. *J. Phys. D* **42**, 045201 (2009).
28. M. Muskat, The flow of fluids through porous media. *J. Appl. Phys.* **8**, 274–282 (1937).
29. P. S. Stevens, *Patterns in Nature* (Little, Brown and Company, ed. 1, 1974).
30. A. Luque, U. Ebert, Growing discharge trees with self-consistent charge transport: The collective dynamics of streamers. *New J. Phys.* **16**, 013039 (2014).
31. A. Budek, K. Kwiatkowski, P. Szymczak, Effect of mobility ratio on interaction between the fingers in unstable growth processes. *Phys. Rev. E* **96**, 042218 (2017).
32. F. Hecht, New development in FreeFem++ *J. Numer. Math.* **20**, 251–266 (2012).
33. I. Bischofberger, R. Ramachandran, S. R. Nagel, An island of stability in a sea of fingers: Emergent global features of the viscous-flow instability. *Soft Matter* **11**, 7428–7432 (2015).
34. O. Zik, E. Moses, Fingering instability in combustion: An extended view. *Phys. Rev. E* **60**, 518 (1999).
35. F. Osselin *et al*., Microfluidic observation of the onset of reactive-infiltration instability in an analog fracture. *Geophys. Res. Lett.* **43**, 6907–6915 (2016).
36. K. Khalturin *et al*., Medusozoan genomes inform the evolution of the jellyfish body plan. *Nat. Ecol. Evol.* **3**, 811–822 (2019).
37. S. Nijdam, J. Teunissen, U. Ebert, The physics of streamer discharge phenomena. *Plasma Sources Sci. Technol.* **29**, 103001 (2020).
38. E. M. van Veldhuizen, W. R. Rutgers, Pulsed positive corona streamer propagation and branching. *J. Phys. D: Appl. Phys.* **35**, 2169–2179 (2002).
39. G. J. J. Winands *et al*., Temporal development and chemical efficiency of positive streamers in a large scale wire-plate reactor as a function of voltage waveform parameters. *J. Phys. D: Appl. Phys.* **39**, 3010–3017 (2006).
40. T. M. P. Briels, J. Kos, E. M. van Veldhuizen, U. Ebert, Circuit dependence of the diameter of pulsed positive streamers in air. *J. Phys. D: Appl. Phys.* **39**, 5201–5210 (2006).
41. S. Żukowski, P. Morawiecki, H. J. Seybold, P. Szymczak, Through history to growth dynamics: Deciphering the evolution of spatial networks. *Sci. Rep.* **12**, 20407 (2022).
42. S. Żukowski, Python package *reticuler*. GitHub. https://github.com/stzukowski/reticuler. Deposited 2 July 2024.
43. Y. Cohen *et al*., Path selection in the growth of rivers. *Proc. Natl. Acad. Sci. U.S.A.* **112**, 14132–14137 (2015).

Chapter 5

Paper IV: "Morphogenesis of the gastrovascular canal network in *Aurelia* jellyfish: Variability and possible mechanisms"

Author contributions

In this study, the author: performed part of the experiments, analyzed the growth dynamics – in particular identified the breakthrough-induced loop formation, participated in the analysis of results and co-wrote the paper.

frontiers | Frontiers in Physics

TYPE Original Research
PUBLISHED 09 January 2023
DOI 10.3389/fphy.2022.966327

OPEN ACCESS

EDITED BY
Pau Formosa-Jordan,
Max Planck Institute for Plant Breeding Research, Germany

REVIEWED BY
Florian Goirand,
Technical University of Munich, Germany
Raghunath Chelakkot,
Indian Institute of Technology Bombay, India
Luis Diambra,
National University of La Plata, Argentina

*CORRESPONDENCE
Annemiek J. M. Cornelissen,
annemiek.cornelissen@u-paris.fr

SPECIALTY SECTION
This article was submitted to Biophysics, a section of the journal Frontiers in Physics

RECEIVED 10 June 2022
ACCEPTED 30 November 2022
PUBLISHED 09 January 2023

CITATION
Song S, Żukowski S, Gambini C, Dantan P, Mauroy B, Douady S and Cornelissen AJ (2023), Morphogenesis of the gastrovascular canal network in *Aurelia* jellyfish: Variability and possible mechanisms.
Front. Phys. 10:966327.
doi: 10.3389/fphy.2022.966327

Morphogenesis of the gastrovascular canal network in *Aurelia* jellyfish: Variability and possible mechanisms

Solène Song[1], Stanisław Żukowski[1,2], Camille Gambini[1], Philippe Dantan[1], Benjamin Mauroy[3], Stéphane Douady[1] and Annemiek J. M. Cornelissen[1]*

[1]Laboratoire MSC, UMR 7057, Université Paris Cité—CNRS, Paris, France, [2]Faculty of Physics, Institute of Theoretical Physics, University of Warsaw, Warsaw, Poland, [3]Laboratoire J. A. Dieudonné, UMR 7351, Université Côte d'Azur—CNRS, Vader Center, Nice, France

Patterns in biology can be considered as predetermined or arising from a self-organizing instability. Variability in the pattern can, thus, be interpreted as a trace of instability, growing out from noise. Studying this variability can, thus, hint toward an underlying morphogenetic mechanism. Here, we present the variability of the gastrovascular system of the jellyfish *Aurelia*. In this variability emerges a typical biased reconnection between canals and time-correlated reconnections. Both phenomena can be interpreted as traces of mechanistic effects, the swimming contractions on the tissue surrounding the gastrovascular canals, and the mean fluid pressure inside them. This reveals the gastrovascular network as a model system to study the morphogenesis of circulation networks and the morphogenetic mechanisms at play.

KEYWORDS

morphogenesis, gastrovascular, network, jellyfish, instabilities, variability, mechanical constraints

1 Introduction

Morphogenesis remains an important question in biology. Independently of how the phenotype can be selected through natural selection, it remains essential to understand how it can appear, develop from its original fertilized egg, and get its own shape. Since humans observe nature, they classify similar shapes into species. Within one species, the shape is robustly perpetuated across generations. So, biological shapes are constrained enough within one species. Even with the discovery of many genes and produced molecules and their important role in morphogenesis, how these constraints are applied to guarantee a given result is not completely clarified. In particular, how a complex shape can appear while being constrained remains obscure [1]. A complex shape would need much information to be described, thus many regulations to achieve it. However, the unfolding in time of instability can lead to a regulated complex shape from a simple mechanism [2].

In his pioneering work, Alan Turing proposed that even if some morphogenesis can be implemented through the various concentrations of some chemical products, the pattern they present is created by a spatial instability [3]. This means that even if the original distribution of chemicals is homogeneous, this state will be unstable and spontaneously goes into patches of different concentrations. Also, the pattern is spontaneously created, not controlled: only its global characteristics, such as wavelength, which depends on the reactions and diffusion characteristics of the chemicals are set, not its particular position.

This view may seem contradictory with the constrained production of a stereotyped shape. However, many examples of fluctuating shapes can give the intuition of an underlying instability. In this study, this is the case we present for the formation of the gastrovascular network of the jellyfish *Aurelia*. Jellyfishes are very old life-forms that appeared before the "vertebrate" revolution but already present a complex vascular structure. This vascular structure is an open circuit, perfusing the whole body from the open mouth to the stomach pouches and back [4, 5]. The flow in this circuit is due both to the effect of the whole contraction of the body and to the action of many cilia on the internal epithelium. These canals, in a body plan which is basal in the animal tree, can be seen as an early simple model of a network of tubes with a transport function as the later evolved closed vascular networks such as the blood vascular network.

This gastrovascular canal network develops while the jellyfish grows from its first ephyra stage. This ephyra stage emerges from a sessile polyp [5, 6]. During the transformation of the polyp into jellyfish (a process called strobilation), this polyp is subjected to instability that creates many disks along its axial body, each disk being unstable in the radial direction and forming arms (lobes with two marginal lappets), of typical 8-fold symmetry. One after the other, the top disk further transforms and detaches, resulting in a free swimming jellyfish larva, the ephyra. This way of generation ensures that a series of jellyfish appears from a very same polyp, so they are clones. The development of the gastrovascular canal can be followed while the jellyfish goes from a star-like shape ephyra of a few mm diameters to a juvenile jellyfish of approximately 10 mm, which has just reached the circular shape of adult medusa to a mature jellyfish of about 100 mm.

We will focus on the growth of the pattern from juvenile, with few rather stereotyped canals, to adult, with many canals. The formation of the network before the juvenile stage has complex but more regular steps [5] and is not considered in this study. Subsequent growth happens with the sprouting of new canals and their reconnection with the rest of the system. There is a strong tendency for a sprouting canal to reconnect to the younger neighbor, leading in an ideal case to a particular fractal pattern. However, this bias is not absolute, and there are many variations. With the observation of these dynamics and their results of complex and varying shapes, we can get closer to the origin of the morphogenetic process. More precisely, the question of which phenomena can be responsible for the development of these shapes can be studied. In the following, we will present two possible phenomena with both some interests and limitations.

2 Canal network morphogenesis

2.1 Stereotypical morphology

The gastrovascular canal network in juvenile jellyfish can be presented with a stereotypical structure (see Figure 1A). In 1/8th of the jellyfish (an octant), there is radially one gastric pouch of the stomach (or the junction between two pouches) near the center, and a marginal ring canal, circling around the whole rim of the jellyfish. Radially, there are two canals, rather straight and unbranched, joining the side of the pouches to the marginal ring canal, the adradial canals. Between such two straight canals, there is a canal joining the gastric pouch (interradial canal) or directly in the mouth opening at the pouch junction (perradial canal) to the marginal ring canal and a rhopalium (a sensory organ that can be caricatured as an "eye"). These canals present, in the juvenile stage, two secondary side branches connecting the main inter or perradial canal with the ring canal, forming a trifurcation. There is no apparent difference between interradial and perradial morphologies. We will, thus, simply call them "trifurcate" canals (in contrast we can call the adradial canals the "straight" canals). In juveniles, new canals mainly sprout from the marginal ring canal and connect to one of the surrounding already existing radial canals.

After growth, for adult jellyfishes, it is tempting to present its shape as a regular, fractal one. Although a perfect one is rare, it can be sometimes observed in small jellyfish (we found occurrences in nature or in the Cherbourg Aquarium culture). The best way to understand it is, as for fractals, to describe its construction, step by step, with canals connecting to each other in a well-defined and precise order (Figure 1B). In the juvenile stage (Figure 1A) at the ring canal, the trifurcation cut the interval between the two straight canals in four. Roughly four new canals sprout from the ring canal, grow in these intervals, and connect either left or right to the two younger side canals of the fork. The next generation of eight canals would also connect to the last previous generation, leading to a distinctive tree shape (Figure 1B).

There is a strong tendency, around 80% of the cases (Figure 1C and Supplementary Material), for the new sprouting canals to connect to the younger radial canal at proximity. If we look at the distribution of "false" connections, that is, canals not connecting to the younger canal at proximity, per octant, we find the very asymmetric

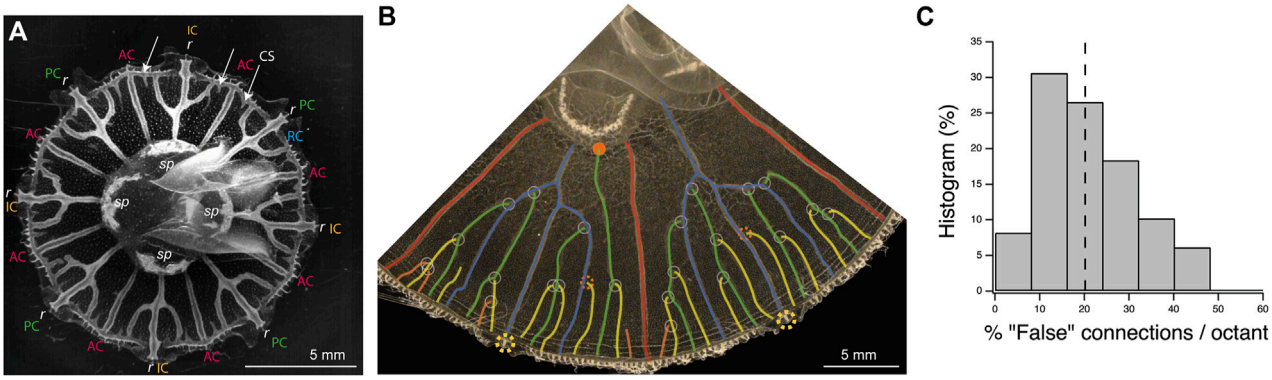

FIGURE 1
Structure and morphogenesis of the canal network of the gastrovascular system of the jellyfish *Aurelia*. **(A)** Picture of a juvenile jellyfish showing the structure of the gastrovascular system. There are typically four stomach pouches (*sp*), eight sensory organs, or rhopalium (*r*). At the periphery of the jellyfish there is a ring canal (RC in blue). Connecting this ring canal, from the sides of the stomach pouches, there are typically eight straight adradial canals (AC in red). Between these adradial canals, other canals connect either the stomach pouch, the perradial canal (PC in green), or the junction between two stomach pouches, the interradial canal (IC in orange), to the rhopalia. New canal sprouts (CS) sprout from the ring canal (arrows). **(B)** Picture of two octants of a later developmental stage (original in Supplementary Figure S2). The sprouting canals have reconnected to older ones, forming branched perradial and interradial canal systems (rhopalia, yellow dashed circles; adradial canals, and red; original trifurcate canals, blue). The sprouting canals have the tendency to reconnect to the youngest side canal (white circles), leading in theory to a specific fractal tree shape. The four (green) canals sprouting in the two intervals between the fork and the two intervals near the side straight canals (red) would connect to side branches of the original (blue) fork. The next eight canals (yellow) would connect to the previous one (green). Also, the next generation (orange) would connect to the previous one (yellow). Some connections do not follow this pattern and either reconnect to older ones (dashed red circles) or even directly to the stomach pouch (red disk). Some irregular growth is also visible on the left (perradial canals), leading to mixing of generations, as some fourth (orange) canals have already appeared, and even connected, while some third order (yellow) generations have not appeared yet or reconnected. **(C)** Histogram of the percentage of "false" connections (i.e., canal connections not made to the closest younger canal) in midsize jellyfish as in B, per octant (seven jellyfish with eight octants and one with nine octants $n = 65$ octants). There are, for instance, 10% of octants present between 32% and 40% of false connections. The median value (dashed line) is 20%.

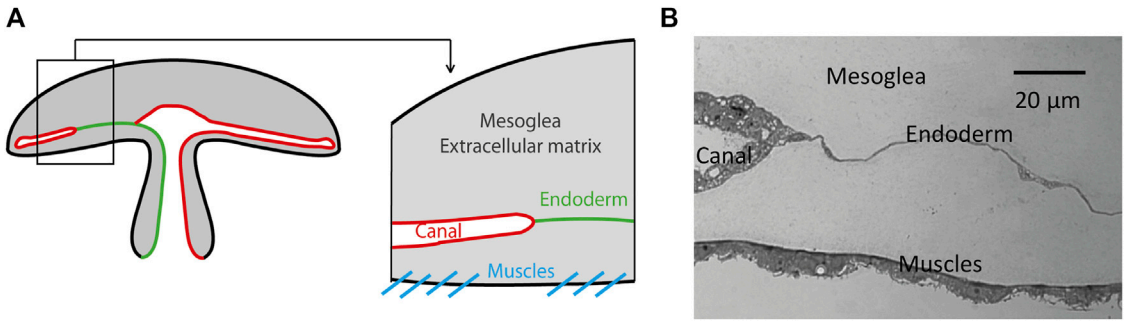

FIGURE 2
Anatomical position of the canals in the jellyfish *Aurelia*. The canals are surrounded by an endodermal layer positioned just above the lower *epidermis* with muscles. **(A)** Schematic representation. **(B)** Optical view of a histological 4 µm thick microtome slice of a fixed jellyfish.

distribution of Figure 1C. This indicates that it is a real bias and that the false connections accumulate independently, making it more probable to have only few false connections (but rare to have none) and rarer to have more false connections. The essential question arising from this structure and its development is to understand why new canals would connect to the younger previous ones.

2.2 Differential contraction

To understand this differential connection of the sprouting canal to the youngest close one, a first observation on the morphology and appearance of the canal itself is helpful. The canals, consisting of a canal wall with a monolayer of dense canal cells around a lumen, are situated inside a monolayer cell

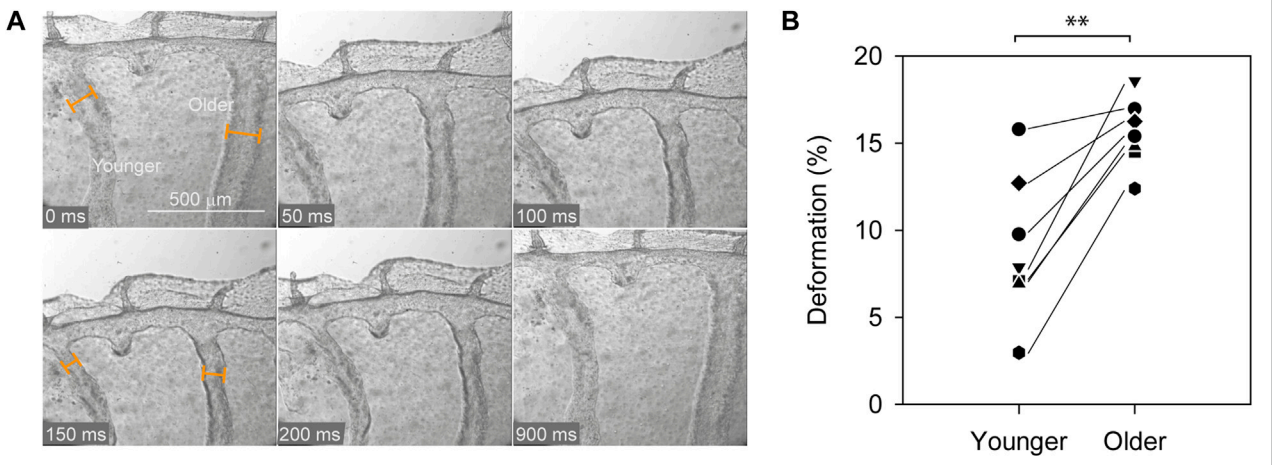

FIGURE 3
Relative contraction of canals during jellyfish swimming contraction. **(A)** A sequence of pictures showing a young and an older canal pictured during a contraction (with also a canal sprout in between). Canal width measurement during the resting phase and the maximum contraction allows measuring the relative contraction of the canals. **(B)** The pairwise measurement shows that the contraction of a young canal is significantly smaller than the one for older canals ($p < 0.01$, one-way repeated measures Anova, followed by a Student–Newman–Keuls test for a pairwise multiple comparison).

sheet with largely spread endodermal cells (see Figure 2). We have observed that the canal sprouts are growing in the endodermal sheet with cell proliferation around the tip of the canal [7].

The second important point for a possible morphogenetic mechanism is that these canals are growing while the jellyfish is growing, and it is growing while being, since the beginning, actively contracting, to swim and gather food. These contractions from a nearly flat state to a bell shape are done by a muscle sheet contracting and reducing the periphery perimeter. These movements then induce a considerable mechanical deformation to the endodermal layer, containing the canals, which is just above this muscle layer (Figure 2).

A proposed mechanism for the bias in connections is that the mechanical response to the contraction during swimming is different for different parts of the tissues. We propose that the endodermal cells which are not part of canals are submitted to a high mechanical stress as they are nearly incompressible, being held by the incompressible, but soft, upper and lower mesoglea [8]. On the contrary, canals are not flat; they enclose a lumen which protrudes out from the endodermal sheet (Figure 2B). Measurements during contractions show that the older the canal, the more deformable it is (Figures 3A,B). We propose this property as the cause of the bias leading growing canals to connect more frequently to younger canals than to older ones.

2.3 Simulating contraction

To see the effect of the differential contractibility of the canals, we analyzed the distribution of the stress in the jellyfish during muscle contractions. To do so, we build a mechanical model of the endoderm and of the canals of the jellyfish. The effects of the mesoglea elasticity and muscle contractions are injected through the boundary conditions.

The model geometry is limited to a slice of the endoderm near the ring canal. The endoderm slice is represented by a ring at the edge of a circular disk (Figure 4A), extending 1/5 of the jellyfish radius. We neglect the local convexity of the endoderm, approximating it with a plane surface. During swimming, the umbrella reduces its radius, increasing the convexity, but we assume it remains flat. The geometry of the canals and sprout were chosen to be coherent with our observations in a juvenile jellyfish of 1 cm diameter (see Supplementary Figure S7A).

The model follows the law of mechanics: $\rho \frac{\partial^2 u}{\partial t^2} - div(\sigma(\epsilon)) = 0$, where ρ is the density of the endoderm (assumed to be similar to that of water), u is the displacement of the material, $\varepsilon = \nabla u$ is the relative displacements of the material (strain), and $\sigma(\varepsilon)$ is its stress–strain relationship. To close the model, we further use the Hooke's law of elasticity to express the stress as a function of the strain. Since we are not interested in the global bell shape of the jellyfish and its change during the muscle contractions and spring back mediated by the mesoglea elasticity [8], we neglect the stress components in the direction normal to the (flat) endoderm surface, that is, $\sigma_z = 0$, $\sigma_{xz} = 0$, and $\sigma_{yz} = 0$. As a consequence, our model is a 2D model and Hooke's law reduces to

$$\sigma_x = \frac{E}{1-\nu^2}\left(\epsilon_{xx} + \nu\epsilon_{yy}\right),$$
$$\sigma_y = \frac{E}{1-\nu^2}\left(\epsilon_{yy} + \nu\epsilon_{xx}\right),$$

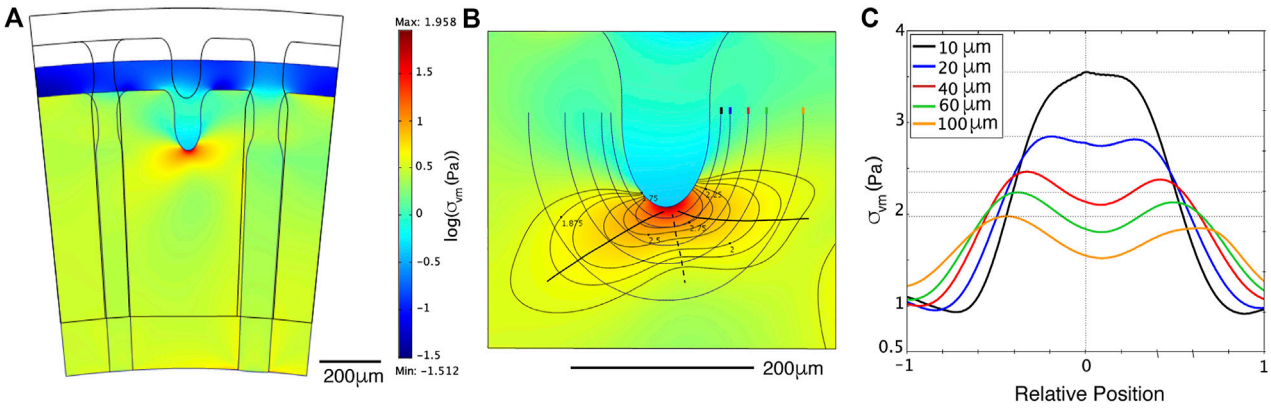

FIGURE 4
Stress distribution predicted by numerical simulations **(A)**: Finite element simulation with stiffer young canal (left) and softer old canal (right). The contraction is reproduced by reducing the radial distance with a constant angle, thus reducing the orthoradial one. The log of the mechanical stress (colored scale) is smaller (blue-green) in the soft right canal, and reduced around the sprouting canal (light blue), but concentrated at its tip (red spot). **(B)**: A zoom of the stress around the tip. Level lines, circling away the red spot reveal two lobes, one forward left to the young canal, one right to the old canal. Lines drawn at fixed distances are drawn with each its color code, to measure the stress along them. The two stress maximums and minimum along these successive lines are indicated by black full and dotted lines, respectively. **(C)**: The stress measured along these lines, centered on the axial position of the tip and rescaled from beginning to end, with their colors, and the distance to the finger indicated. Horizontal dotted lines show that the left maximum toward the young canal is always higher. This will turn the propagation of the new canal sprout toward the younger, stiffer one.

$$\sigma_z = 0,$$
$$\sigma_{xy} = \frac{E}{1+\nu}\epsilon_{xy},$$
$$\sigma_{xz} = 0,$$
$$\sigma_{xz} = 0,$$

with E being Young's modulus and ν Poisson's ratio. The observed difference of deformability (Figure 3) was translated into plausible elastic Young's moduli and Poisson ratio. We assume the endoderm as a flat rigid nearly incompressible elastic sheet. The near incompressibility in the plane is given by Poisson's ratio $\nu_{en} = 0.49$ and the rigidity by Young's modulus $E_{en} = 100\ Pa$. We modeled the canals in 2D by a compressible elastic membrane, with a lower Young's moduli than the endoderm. The chosen Poisson's ratio of the canals of 0.3 ($\nu_{yc} = \nu_{oc} = 0.3$; ν_{yc} being the Poisson's ratio for the young canal and ν_{oc} the Poisson's ratio for the old canal), allows for compression in the plane, translating the vertical expansion of the canals. The Young's modulus of the young canal is assumed to be stiffer with $E_{yc} = 30\ Pa$ than the old canal, for which $E_{oc} = 10\ Pa$.

The muscular orthoradial contraction is mimicked *via* the boundary conditions as shown in the Supplementary Figure S7B. To simplify, instead of compressing the whole two radial borders of the slice, we only reduce the radial position of the outer circular boundary. Following our observations, we typically reduce it by 200 µm in one second. The sides of the ring slice can only slip along the radial axis, and the inner circular boundary is free to move ($\sigma(\epsilon).n = 0$, with n the outer normal of the boundary). As a result, the whole slice compresses after one second. At the end of the contraction, the circular deformation is 4% at the outer edge (top of ring canal) and 5% at the inner edge. With these characteristics, the simulation can be performed quasi-statically. The model of contraction was studied with a numerical simulation based on finite elements.

The results show an accumulation of stress at the tip of a new canal (the stress is partly released at the sprouting canal, and all the residual stress around focuses on the tip), and the stress is slightly different in the two surrounding canals of different age/stiffness (Figure 4A). At the tip, the stress shows two lobes, toward both side canals, the one toward the younger canal being larger and more intense (Figure 4B). The quantitative result is that the maximum of stress is shifting toward the younger stiffer canal (Figure 4C). Based on these observations, we propose that high stress will guide the canal sprout to grow toward the younger stiffer radial side canal.

3 Variability

Since the connection of the sprouting canal to a younger close one is only a strong bias, there are many variations of patterns and only rarely a perfect one. Looking more generally at *Aurelia* jellyfish from different origins and growth conditions (see Section 6) also reveals variable patterns. The observed patterns display more variability than what we would expect from the previously described process based on successive sprouting of new canals from the rim and connection to the youngest neighboring canal.

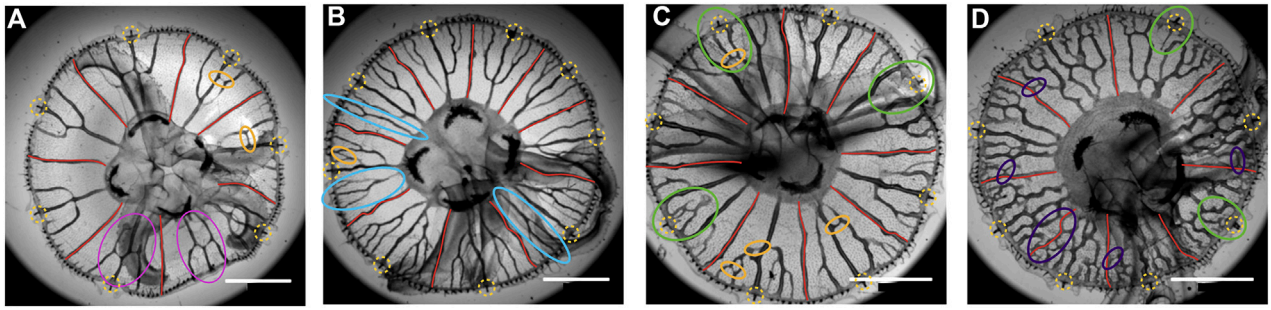

FIGURE 5
Four *Aurelia* specimens of around the same size, from Cherbourg. The rhopalia are surrounded by yellow-dashed circles, and the adradial canals are drawn in red. In **A**, the continuation of canals after connecting to the central one is indicated by pink ellipses. In **(A–C),** some interconnection between canals, forming loops, is indicated (orange ellipses). In **B**, some side canals never reconnect to the central one and connect directly to the stomach pouch (light blue ellipses). In **(C**,**D)**, some rhopalia are not connected to canals (green ellipses). In **D**, there are many meandering canals and reconnections making many loops, in particular reconnections with straight adradial canals (violet ellipses). Scale bar 5 mm.

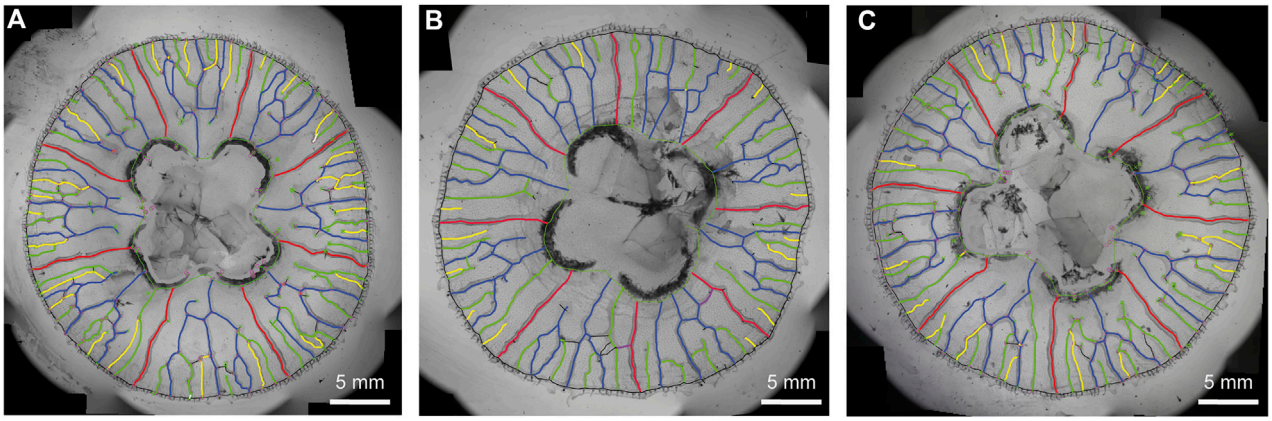

FIGURE 6
Three clones from the same polyp. **(A–C)** The pattern has been interpreted for easier comparison. As in Figure 1B, the adradial canals are drawn in red; the central canal, and the first side canals forming the trifurcation are drawn in blue; the second generation in green; the third in yellow. One can observe many irregularities as in Figure 5: side canals not reconnecting to the central one, reaching (or going to reach) the stomach pouch, interconnections to straight canals [violet, in **(B)**] and to other radial canals (black) making loops. All these irregularities, although similar in the three clones, are in detail different.

Figure 5 shows four cases giving an indication of the large variety of patterns. As a source of variability, one can observe that, even after reconnecting, the side canals would keep growing toward the stomach (pink ovals in Figure 5A). Another variation is the presence of meandering canals that are potential sites for the growth of new canals. Both modes of growth induce the formation of loops on large (old) jellyfish, transforming the gastrovascular network into a foam-like pattern (Figure 5D). This creates patterns much more difficult to analyze.

An interesting point is that since there is a variability in these patterns, one can study where these variations originate from. In the case of ephyrae coming from a single polyp, which means they are clones and grown together, thus in identical conditions, one can look at resulting patterns. Here, we present three such clones grown together (Figure 6). One can observe a similar type of pattern but still differences. This shows that, even for genetically identical jellyfish and an identical environment, there is no strict control of the pattern. This suggests a self-organized pattern formation, relying on instability, amplifying the noise.

4 Canal breakthrough

A particular type of deviation from the stereotypical development is interesting to see dynamically. During development, one can observe that some canal sprouts do not

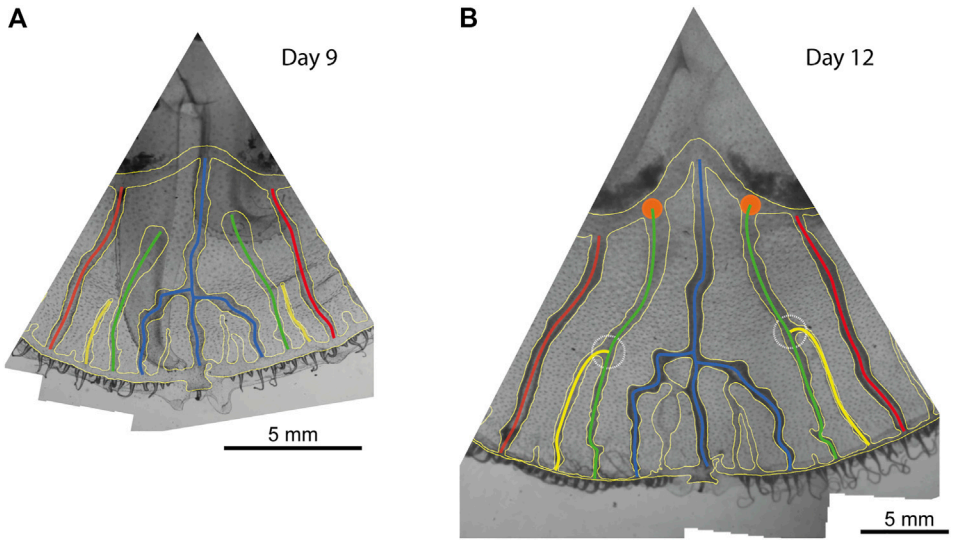

FIGURE 7
Two successive images of a jellyfish octant. **(A)** At day 9 of observation, secondary (green) side canals did not connect to the central ones and are reaching toward the stomach pouches. Similarly, there are two younger (yellow) canals growing aside of them without connecting either. **(B)** 3 days after, the side canals have reached the stomach pouch and connected (orange disks), and in the same period, the younger canals have also connected to these side canals (dashed white circles).

reconnect with the more central canals. Instead, they grow straight toward the stomach, independently from the other canals. It happens for the first-generation canals that sprout between the fork and the side adradial canals (see Figure 1B, Figure 5B), around 17% of the time (see Supplementary Material). Interestingly, in such a case, the next generation of side canals keeps growing independently too as long as the longest canal sprout did not reach the stomach pouch (see Figure 7A). However, as soon as the longest canal sprout reaches the stomach, it is observed that the smaller sprouts connect to the long canal that just got connected to the stomach (Figure 7B).

5 Discussion

When a pattern is constant, it is difficult to describe its origin and what controls it. On the contrary, variability helps get closer to the mechanisms producing these patterns. Here, we see that the pattern can be very variable, even in clonal jellyfish. That points to instabilities being at the origin of the pattern. Since Turing, we understand that instabilities mean that a homogeneous state is unstable, so that tiny inhomogeneities will grow to create a pattern. In this sense, instability starts with the amplification of noise. This first step results in a noisy pattern, which is a source of variability.

The further growth of the instability is often regulated by long-range interactions and global constraints (such as gradient of pressure). This leads to the growth of a regular pattern with a fixed wavelength for instance. This is how regular and reproducible patterns can appear, even if originating from an initial noise. In practice, this noise origin is often overlooked, and only regular patterns are studied theoretically. The most unstable regular pattern will be searched for, as it is the one most growing. Then, after a further restabilization, it will be the one finally observed. However, in some cases, the system keeps growing and being unstable, with no means of reorganization. This happens in physical systems, as in the Saffman–Taylor instability in circular geometry [9] or in biological growth, as in the lungs [10]. In such cases, the noise keeps being amplified, and variability can persist. This seems to be the case with the gastrovascular network of jellyfish.

There is still some regularity: the gastrovascular network can, under some growth conditions, follow a typical asymmetry (bias) and sometimes converge toward a stereotypical pattern. This comes from the interactions between canals, allowing regularization. However, we could guess that not following the bias comes from the presence of more noise, for instance, on the distance between canals, canal growth, and canal stiffness or resistivity. Such noise is well visible on Figure 1B, left, where successive generations of canals appear irregularly. This noise could blur the asymmetry and sometimes allows the sprouting canal to follow the second stress lobe (Figure 4), leading to a non-stereotypical connection. The fact that noise is the origin of these connections escaping the bias can be seen in the asymmetry of the distribution of Figure 1C. Noise leads to independent

misconnections, resulting into stereotypical octants with few mistakes but rarer octants with more numerous ones.

The sprouting of new canals from the circular ring canal also reveals instability of this ring that would be similar to the curving in the meandering canals, leading to local sprouting and later to other reconnections, forming small loops shunting the canals.

The fact that canals reconnect to each other is a particularly interesting phenomenon. The gastrovascular network is a tree structure connected to a ring canal. One would first imagine that it forms as a tree expanding with successive dichotomies of tips or side branching, and finally connecting to the ring canal. Here, we see a reverse growth: the branches appear from the ring canal, separated from each other, and reconnect only later. The reconnection between the canals leads to the formation of loops. The sprouting from other canals than the ring canal that further connect forms even more loops. This is interesting since the usual branching formation of trees, as in Laplacian growth [2], often forbids reconnection, hence the formation of loops [11]. Such reconnection is thus a particular phenomenon that deserves exploration.

This formation of loops by the reconnection of branches has to be differentiated from the case of stabilization and coarsening of loops. As for vascular remodeling from a capillary plexus [12], these systems start from homogeneously connected foam and particular dynamical evolution leads to the stabilization of large hierarchical loops [13–15]. Here, for the formation of loops by reconnection, the first mechanism proposed relates to cracks, which are known to reconnect [16], being related to two-dimensional stress [17], and leading to 2D-reticulated patterns [18, 19]. In this way, canals can be seen as the propagation of cracks in the endoderm. Stress accumulates at the tip of a new crack, and it is guided by the stress around it [16]. Here, too high stress at the tip of a sprout could induce the proliferation of cells [20, 21] and/or their transformation in canals cells, open the canals, and release the stress. The global stress field guides the movement of the tip of a new canal/crack. This relation to stress also explains the observed bias, that the crack is attracted to the larger stress, thus to the still stiff younger canal.

The second mechanism, even if related to Saffman–Taylor and Laplacian growth, would happen in the special case of resistive fingers [22]. This resistance creates gradients of pressure within the fingers. It allows connection of side fingers to a longer one when its pressure is locally lower. This particularly happens when the pressure in the longer one globally drops because of a connection to an outlet (breakthrough). This could explain the coincidence of a canal breaking through the stomach pouch and the reconnection of a side canal to it.

For the jellyfish canals, this would happen with the liquid pressure inside the growing canal sprouts during the muscle contractions in the orthoradial direction. However, when one canal sprout, in analogy with the Saffman–Taylor finger, reconnects directly to the stomach, then this transient high pressure at its tip drops to reach the pressure at the outlet, the stomach pouch. This dropping of pressure happens all along the canal, so that the lateral canal sprout can now perceive a place on the side with low pressure and be attracted to it.

These two mechanisms could be happening in the jellyfish or just be mechanical analogies of other phenomena. However, even from a mechanical point of view, they are not incompatible, being driven by the stress in the endodermal layer and the pressure in the canals, which are complementary parts of the mechanics of the network.

The source of large variability of the patterns, as shown in Figure 5, should also be investigated. Is it due to different growth conditions, growth histories, or also to different strains, revealing a different sensibility to mechanical constraints for instance?

Globally, these first observations show that the gastrovascular network results from a spontaneous organization, or, in other words, that it appears from instabilities, enhancing noise, so that two growths never produce the same result even with settings as close as possible (clones from a single polyp grown together in the same conditions). We consider that blood vascular networks in vertebrates [23–25] and venation in plant leaves [17] could result from similar spontaneous organization, however, with different detailed processes. Here, we show that there are clues that the morphogenesis of the gastrovascular pattern in the jellyfish could be related to mechanical processes, since it grows while the jellyfish is swimming with repetitive contractions. These contractions have clearly a mechanical effect on the tissue either by direct contraction or by a secondary effect on the flow inside the already existing canals.

6 Materials and methods

6.1 Jellyfish culture

Jellyfish *Aurelia aurita* were reared in the laboratory, at room temperature, in artificial seawater, produced by diluting 35 g or 28 g of synthetic sea salt (Instant Ocean; Spectrum Brands, Madison, WI) per liter of osmosis water (osmolarity 1,100 mOsm). Polyps of the Roscoff strain [26] were obtained by courtesy of Konstantin Khalturin from the Marine Genomics Unit, Okinawa Institute of Science and Technology Graduate University, Onna, Okinawa, Japan. Strobilation in polyps was induced by a lowering the temperature down to 10°C [27]. The newborn ephyrae were bred to adult stage. The measurements were performed on jellyfish at different sizes of juvenile jellyfish. Juvenile jellyfish had just reached the circular shape of adult medusas with a diameter of ~1 cm. Juveniles grow out into adult jellyfishes with fully developed stomach pouches.

Juvenile jellyfish (~1 cm in diameter) were obtained from the "Jellyfish Concept" in Cherbourg from their culture. The original polyps are extracted from the North Sea around Cherbourg. Juvenile jellyfish were bred to adults while growing. In the manuscript, we refer to these jellyfish as 'Cherbourg jellyfish'

when they originate from the Roscoff strain, we do not specify it in the manuscript.

6.2 Imaging of the gastrovascular canal network

The gastrovascular network of the jellyfish was observed using a Leica macro zoom (MACROFLUO LEICA Z16 APO S/No: 5763648) and a Photron Fastcam SA3 camera or directly using a Nikon D3300 camera with macro lens AF-S DX Micro NIKKOR 40 mm f/2.8G. Jellyfish were caught from the aquarium approximately 3 h after feeding with artemia when the gastrovascular canals were colored orange from the digested artemia. When they reach about 2.5 cm in diameter, jellyfish were anesthetized with magnesium chloride dissolved in water having the same salinity as the artificial seawater in which they are swimming. To anesthetize the jellyfish, the volume of the jellyfish with seawater was doubled with the magnesium chloride solution. Then, they are placed in a Petri dish in shallow seawater with the sub umbrella facing up. The images are taken by transillumination.

6.3 Histology

The histological section shown in Figure 2B was made for a preparation of observations with transmission electron microscopy. In short, whole juvenile jellyfish are fixed with a 5% glutaraldehyde solution in a 0.1 mol/L cacodylate solution overnight at 4°C [28]. After rinsing with 0.5 mol/L cacodylate solution (overnight at 4°C), the solution is replaced gradually by ethanol 95% after which it is transferred to 95% ethanol containing eosin, in order to stain the jellyfish. Then, the samples are placed in 100% ethanol which is subsequently gradually replaced by a pure molten wax solution. These samples are then cut by a microtome into thin lamellae of about 4 µm thickness. Longitudinal sections of juvenile jellyfish were sliced, starting the sections from the edge of the umbrella, and advancing towards the center of the jellyfish. Figure 2B shows a longitudinal section through a canal and the endoderm of a juvenile jellyfish of approximately 1 cm diameter. The section was visualized under a light microscope (Leica DMI-3000 B), a ×20 magnification objective, and a CCD camera (Andor, iXon3 885).

6.4 Canal diameter deformation measurements

Juvenile jellyfish (n = 7) of about 1 cm in diameter were filmed (30 frames per second) using a Leica inverse microscope (LEICA DMI-3000 B) with a ×20 objective (HCX PL Fluotar L ×20/0.40). The jellyfish were lying flat with the subumbrella facing down. In this position, jellyfish slightly contract occasionally. Two canals were filmed simultaneously. The older and younger canals were identified by looking at the canal network pattern. Off line, diameters were measured before and during contraction at three different positions along the canal and were averaged. Deformation of the canal was calculated by the ratio of the difference in diameter before and during contraction and the diameter before contraction, multiplied by 100. We used one-way repeated measures Anova, followed by a Student–Newman–Keuls test for pairwise multiple comparison to show the statistical difference between the deformation of the older canals versus the younger canals (SigmaPlot 12.5).

6.5 Numerical simulation

Numerical simulations were performed with finite elements toolbox COMSOL Multiphysics 3.5a [29]. We approximated the endoderm and the canals as 2D surface elements with different stiffness.

The simulations were performed on a small piece of a ring at the edge of a circular disk with a radius of 5 mm, with a radial length of 1 mm and with a 12° angle. The geometry of the canals and sprout were chosen to be coherent with our observations in a juvenile jellyfish of 1 cm diameter. The geometry with the simulation mesh is shown in the Supplementary Figure S7A.

We assume the endoderm as a flat rigid incompressible elastic sheet with Young's modulus $E_{en} = 100\,Pa$. The incompressibility of a material corresponds to a Poisson's ratio of 0.5. However, Hooke's law is only valid for Poisson's ratio <0.5. Hence, in our model, we approximate the incompressibility of the endoderm by setting its Poisson's ratio $\nu_{en} = 0.49$. The simulations in 2D imply the absence of out of plane buckling. This assumption is justified for small juveniles at the onset of contraction since the endoderm is held in plane by the mesoglea located above and below.

We modeled the canals in 2D by a slightly compressible elastic membrane, with lower Young's moduli than the endoderm. The young's modulus of the young canal is assumed to be stiffer with $E_{yc} = 30\,Pa$ than the old canal, $E_{oc} = 10\,Pa$. The Poisson's ratio of the canals equals 0.3 ($\nu_{yc} = \nu_{oc} = 0.3$), which allows for compression. It should be noted that the distribution of these stresses does not depend on the values of the Young modulus of the endoderm and the canals but only on the ratio of these values.

We observed that by choosing the elastic modulus of the canals 10 times lower than the endoderm, we obtained rates of reduction of the diameter of the ducts close to those observed *in vivo* (Figure 2B).

To simulate the muscular orthoradial contraction, we impose a reduction of the radial position of the outer circular boundary (at the ring canal). The sides of the ring slice can slip along the radial axis only, and the inner circular boundary is free to move ($\sigma(\epsilon).n = 0$, with n being the outer normal of the boundary).

The simulation was performed quasi-statically, meaning that each simulation step is in a dynamic equilibrium. The relative influence of inertia and elasticity on the system can be determined by computing the Cauchy dimensionless number $C = \frac{\rho V^2}{E}$, with ρ the density of the tissues and V local flow velocity. In our model, $V \approx 200$ µm/s, $\rho = 1{,}000$ kg/m^3 and E ranges from 10 to 100 Pa. Thus, $C<<1$ and the acceleration term $\rho\frac{\partial^2 u}{\partial t^2}$ is always negligible relatively to the elasticity term $div(\sigma(\epsilon))$. As a consequence, we can perform a quasi-static analysis: we solve the static equation $div(\sigma(\epsilon)) = 0$ with a maximal displacement of 200 µm of the outer circular boundary. Then, we reconstruct the time dynamics, thanks to the linearity of the equation relatively to the condition at this boundary.

We selected the mesh size so that a refinement of the mesh did not improve significantly the quality of the results. The mesh consisted in 7,563 triangular elements. The computation time was less than 1 s on an 3.7 GHz 2 Ghz Intel Xeon Gold 6,138.

The different values of the Young's and Poisson's moduli of the different elements under compression results in a distribution of stresses (σ_x, σ_y, σ_{xy}) which are accumulated at the tip of the sprout. The von Mises stresses (σ_{vm}), obtained by combining these different stresses [29], give a satisfactory scalar representation of the stress distribution in the endoderm:

$$\sigma_{vm} = \sqrt{\sigma_x{}^2 - \sigma_x\sigma_y + \sigma_y{}^2 + 3\sigma_{xy}{}^2}.$$

Data availability statement

The original contributions presented in the study are included in the article/Supplementary Material; further inquiries can be directed to the corresponding author.

Author contributions

SS performed the experiments, analyses of the network, in particular for the clones, and wrote the manuscript. SŻ performed the experiments, analyzed the growth dynamics, in particular for the breakthrough event, and wrote the manuscript. CG performed the experiments, in particular for the anatomy, analyses, in particular the contractions, and mechanical modeling and performed mechanical numerical simulations. PD performed mechanical numerical simulations. BM defined the numerical simulations and wrote the manuscript. SD analyzed the patterns and wrote the manuscript. AC directed the work, performed experiments, analyses, and modeling, and wrote the manuscript.

Funding

This work was supported by The LABEX "WHO AM I?" (No. ANR-11-LABX-0071) with a PhD fellowship for SS (doctorants 2015) and a collaborative grant (Projets collaboratifs 2013-II) and by the Mission for Transversal and Interdisciplinary Initiatives (MITI) of the French National Centre of Scientific Research (CNRS), AAP Auto-organisation 2021 and 2022.

Acknowledgments

The authors thank Carine Vias and Léna Zig for their excellent care for the jellyfish. They thank Vincent Fleury for pointing to them this biological system.

Conflict of interest

The authors declare that the research was conducted in the absence of any commercial or financial relationships that could be construed as a potential conflict of interest.

Publisher's note

Supplementary material

The Supplementary Material for this article can be found online at: https://www.frontiersin.org/articles/10.3389/fphy.2022.966327/full#supplementary-material

References

1. Collinet C, Lecuit T. Programmed and self-organized flow of information during morphogenesis. *Nat Rev Mol Cel Biol* (2021) 22(4):245–65. doi:10.1038/s41580-020-00318-6

2. Clément R, Blanc P, Mauroy B, Sapin V, Douady S. Shape self-regulation in early lung morphogenesis. *PLoS ONE* (2012) 7(5):e36925. doi:10.1371/journal.pone.0036925

3. Turing AM. The chemical basis of morphogenesis. *Philos Trans R Soc Lond Ser B, Biol Sci* (1952) 237(641):37–72. doi:10.1098/rstb.1952.0012

4. Southward AJ. Observations on the ciliary currents of the jelly-fish aurelia-aurita L. *J Mar Biol Assoc U K* (1955) 34(2):201–16. doi:10.1017/s0025315400027570

5. Russell FS. *The medusae of the British isles. Vol.Ii - pelagic scyphozoa with a supplement to the firts volume on hydromedusae*. Cambridge: Cambridge University Press (1970).

6. Fuchs B, Wang W, Graspeuntner S, Li Y, Insua S, Herbst E-M, et al. Regulation of polyp-to-jellyfish transition in Aurelia aurita. *Curr Biol* (2014) 24(3):263–73. doi:10.1016/j.cub.2013.12.003

7. Gambini C. *La morphogenaise gastrovasculaire de La méduse Aurelia aurita*. Paris: Université Paris Diderot (2012).

8. Gambini C, Abou B, Ponton A, Cornelissen AJ. Micro- and macrorheology of jellyfish extracellular matrix. *Biophysical J* (2012) 102(1):1–9. doi:10.1016/j.bpj.2011.11.4004

9. Thomé H, Rabaud M, Hakim V, Couder Y. The saffman–taylor instability: From the linear to the circular geometry. *Phys Fluids A: Fluid Dyn* (1989) 1(2):224–40. doi:10.1063/1.857493

10. Clément R, Douady S, Mauroy B. Branching geometry induced by lung self-regulated growth. *Phys Biol* (2012) 9(6):066006. doi:10.1088/1478-3975/9/6/066006

11. Douady S, Lagesse C, Atashinbar M, Bonnin P, Pousse R, Valcke P. A work on reticulated patterns. *Comptes rendus de l'Académie des Sci Série IIb, Mécanique, physique, astronomie* (2020) 348(6-7):659–78. doi:10.5802/crmeca.47

12. Risau W. Mechanisms of angiogenesis. *Nature* (1997) 386(6626):671–4. doi:10.1038/386671a0

13. Katifori E, Szöllősi GJ, Magnasco MO. Damage and fluctuations induce loops in optimal transport networks. *Phys Rev Lett* (2010) 104(4):048704. doi:10.1103/PhysRevLett.104.048704

14. Konkol A, Schwenk J, Katifori E, Shaw JB. Interplay of river and tidal forcings promotes loops in coastal channel networks. *Geophys Res Lett* (2022) 49(10):49. doi:10.1029/2022GL098284

15. Ronellenfitsch H, Katifori E. Phenotypes of vascular flow networks. *Phys Rev Lett* (2019) 123(24):248101. doi:10.1103/PhysRevLett.123.248101

16. Fender ML, Lechenault F, Daniels KE. Universal shapes formed by two interacting cracks. *Phys Rev Lett* (2010) 105(12):125505. doi:10.1103/PhysRevLett.105.125505

17. Couder Y, Pauchard L, Allain C, Adda-Bedia M, Douady S. The leaf venation as formed in a tensorial field. *Eur Phys J B* (2002) 28(2):135–8. doi:10.1140/epjb/e2002-00211-1

18. Bohn S, Pauchard L, Couder Y. Hierarchical crack pattern as formed by successive domain divisions. *Phys Rev E* (2005) 71(4):046214. doi:10.1103/PhysRevE.71.046214

19. Milinkovitch MC, Manukyan L, Debry A, Di-Poï N, Martin S, Singh D, et al. Crocodile head scales are not developmental units but emerge from physical cracking. *Science* (2013) 339(6115):78–81. doi:10.1126/science.1226265

20. Li B, Li F, Puskar KM, Wang JH. Spatial patterning of cell proliferation and differentiation depends on mechanical stress magnitude. *J Biomech* (2009) 42(11):1622–7. Epub 20090530. doi:10.1016/j.jbiomech.2009.04.033

21. Shraiman BI. Mechanical feedback as a possible regulator of tissue growth. *Proc Natl Acad Sci U S A* (2005) 102(9):3318–23. doi:10.1073/pnas.0404782102

22. Budek A, Kwiatkowski K, Szymczak P. Effect of mobility ratio on interaction between the fingers in unstable growth processes. *Phys Rev E* (2017) 96(4):042218. doi:10.1103/PhysRevE.96.042218

23. Al-Kilani A, Lorthois S, Nguyen TH, Le NF, Cornelissen A, Unbekandt M, et al. During vertebrate development, arteries exert a morphological control over the venous pattern through physical factors. *Phys Rev E* (2008) 77(5):051912. doi:10.1103/PhysRevE.77.051912

24. le Noble F, Fleury V, Pries A, Corvol P, Eichmann A, Reneman RS. Control of arterial branching morphogenesis in embryogenesis: Go with the flow. *Cardiovasc Res* (2005) 65(3):619–28. doi:10.1016/j.cardiores.2004.09.018

25. Nguyen TH, Eichmann A, Le NF, Fleury V. Dynamics of vascular branching morphogenesis: The effect of blood and tissue flow. *Phys Rev E* (2006) 73(6):061907. doi:10.1103/PhysRevE.73.061907

26. Khalturin K, Shinzato C, Khalturina M, Hamada M, Fujie M, Koyanagi R, et al. Medusozoan genomes inform the evolution of the jellyfish body plan. *Nat Ecol Evol* (2019) 3(5):811–22. doi:10.1038/s41559-019-0853-y

27. Kroiher M, Siefker B, Berking S. Induction of segmentation in polyps of Aurelia aurita (scyphozoa, Cnidaria) into medusae and formation of mirror-image medusa anlagen. *Int J Dev Biol* (2003) 44(5):485–90. doi:10.2108/zs160161

28. Chapman DM. Microanatomy of the bell rim of Aurelia aurita (Cnidaria: Scyphozoa). *Can J Zool* (1999) 77:34–46. doi:10.1139/z98-193

29. COMSOL. *Comsol Multiphysics®*. 3.5a ed. Stockholm, Sweden: Comsol A.B (2019).

Morphogenesis of Gastrovascular Canal Network in Aurelia Jellyfish: Variability and Possible Mechanisms

Supplementary Materials

1 Canals Connections statistics

We analyzed the connections between canals for 6 Jellyfish from the Roscoff strain, grown in the same conditions (28% salinity, 22°C), and roughly the same size (for the same number of canals/connections). It presents a reasonable dispersion of more or less regular jellyfishes, with more or less regular octants, and fluctuating number of direct stomach connections, with no clear correlations.

The labelling number correspond to the number of pictured jellyfish from the same batch.

The first column counts the number of "True" connections following the bias to the younger canal at proximity, per "octant", "Nb conn T".

The second column counts the number of "False" connections not following the bias to the younger canal at proximity (being older canal or stomach pouch), per "octant", "Nb conn F".

The third column shows the percentage of "False" connections (over all connections) not following the bias to the younger canal at proximity, "F%".

The fourth column count the number of "octant" per jellyfish (the first one has nine). There are two possible first generation canals after the fork, near the straight adradial canals, that can escape the fork and connect directly to the stomach pouch, so the number of possible connection is twice the number of octants.

The fifth column count the number of first generation canals outside the fork connecting directly to the stomach pouch, per "octant", "Nb stom conn".

The sixth column shows the percentage of direct stomach connection (over the number of all possible connections the number of first generation canals outside the fork connecting directly to the stomach pouch, per jellyfish, "stom conn %"

The numbers are summed per jellyfish, to see the variations of more or less regular jellyfish, and for the sixth jellyfish at the bottom, giving the overall percentages.

Gastrovascular Network Morphogenesis Supplementary

n°70	Nb con T	Nb con F	F %	Nb "octant"	Nb stom con	stom con %
	9	3	25			
	11	0	0			
	8	2	20			
	11	1	8			
	7	1	13			
	6	3	33			
	8	1	11			
	8	2	20			
	7	3	30		1	
total	75	16	18	9	1	6
n°83						
	9	4	25			
	8	3	27			
	11	2	15			
	14	1	7		1	
	10	3	23			
	11	4	21			
	11	1	8		1	
	12	1	8			
total	86	19	17	8	2	13
n°85						
	11	3	21		1	
	8	6	43			
	11	2	15			
	7	3	30		1	
	7	6	46			
	8	4	33			
	8	4	33			
	9	3	25			
total	69	31	31	8	2	13
n°86						
	10	2	17			
	10	1	9			
	10	3	23			
	11	1	8		1	
	9	2	18			
	8	1	11			
	10	1	9			
	9	1	10			
total	77	12	13	8	1	6
n°87						
	11	3	21		1	
	9	3	25			
	13	2	13		2	
	8	4	33			
	10	4	29		1	
	10	2	17			
	10	3	23		1	
	8	6	43			
total	79	27	25	8	5	31

n°101						
	14	1	7			
	11	4	27			
	10	3	23		1	
	10	3	23		2	
	12	2	14		1	
	13	2	13			
	10	5	33		2	
	12	0	0			
total	92	20	18	8	6	38
Total	478	125	21	49	17	17

2 Canal connection statistics pictures

Pictures of the sixth jellyfish with true connection indicated with white circle, false connections in red circles and in particular connection to the stomach pouch with circle filled with red.

The lower part of n°83 (Fig. S2) corresponds to the part drawn in Figure 1B.

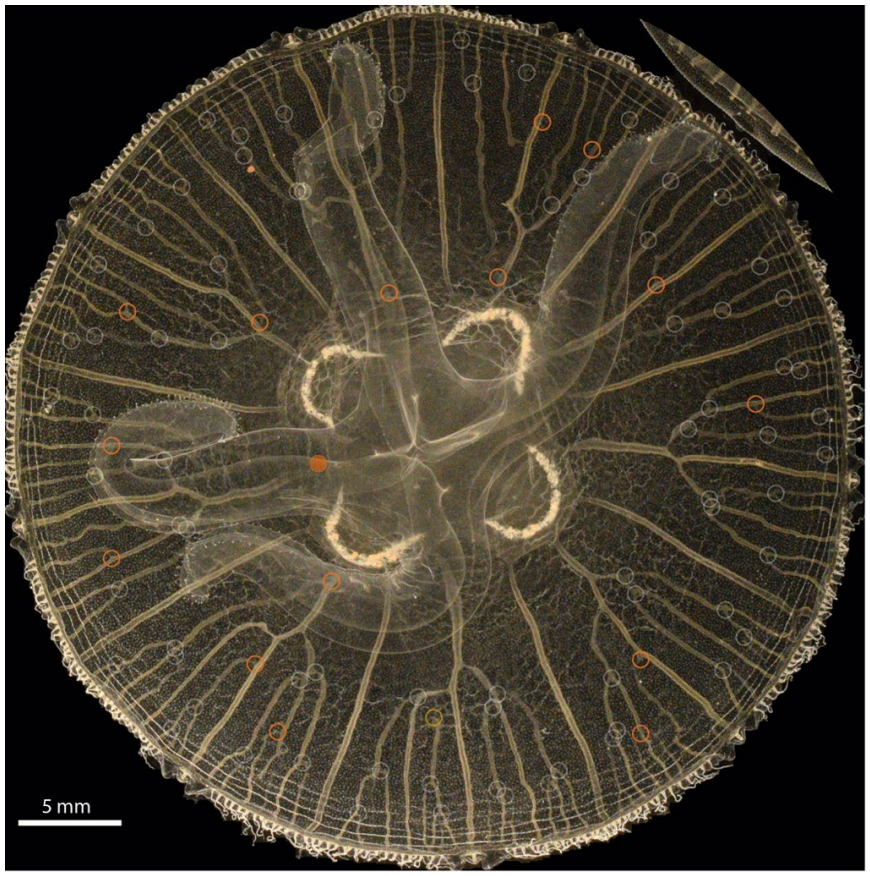

Fig. S1, n°70

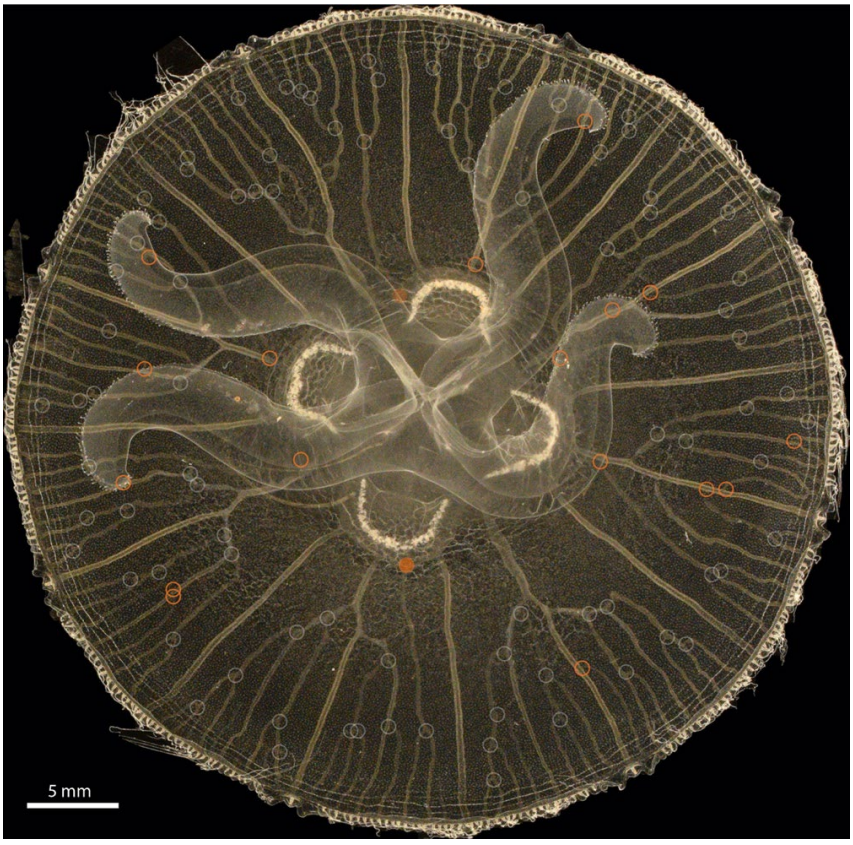

Fig. S2, n°83

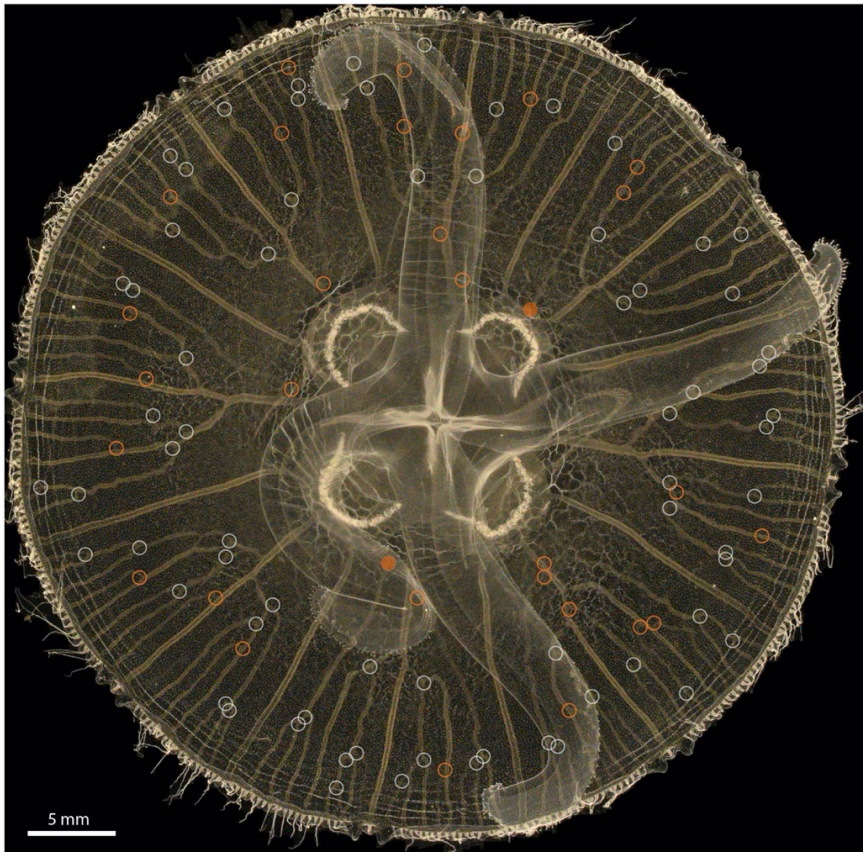

Fig. S3, n°85

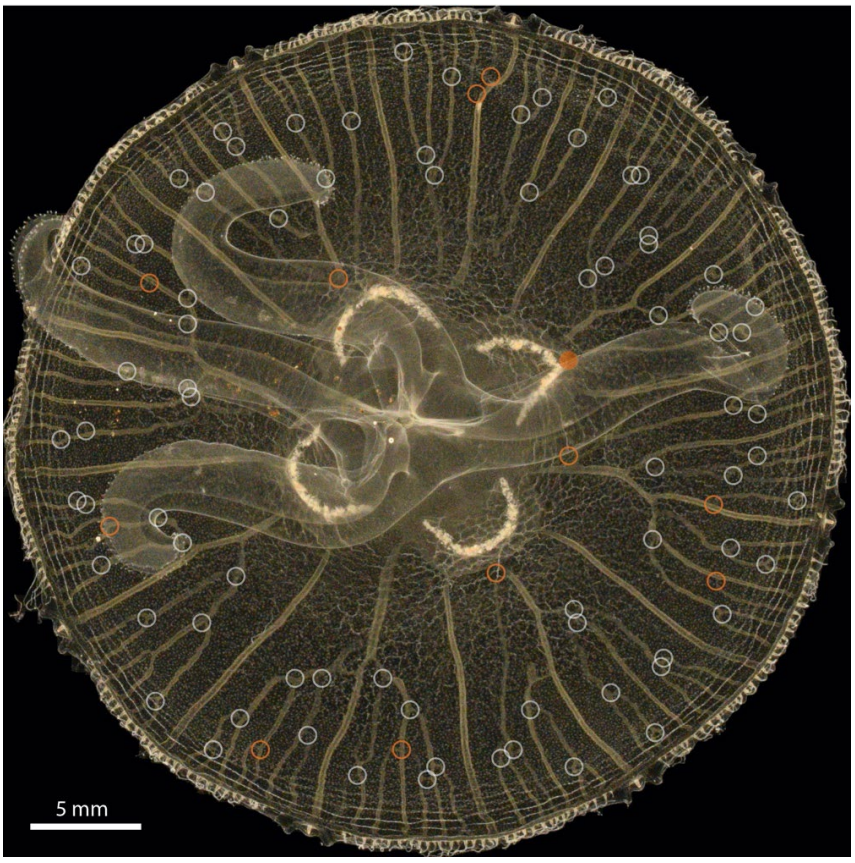

Fig. S4, n°86

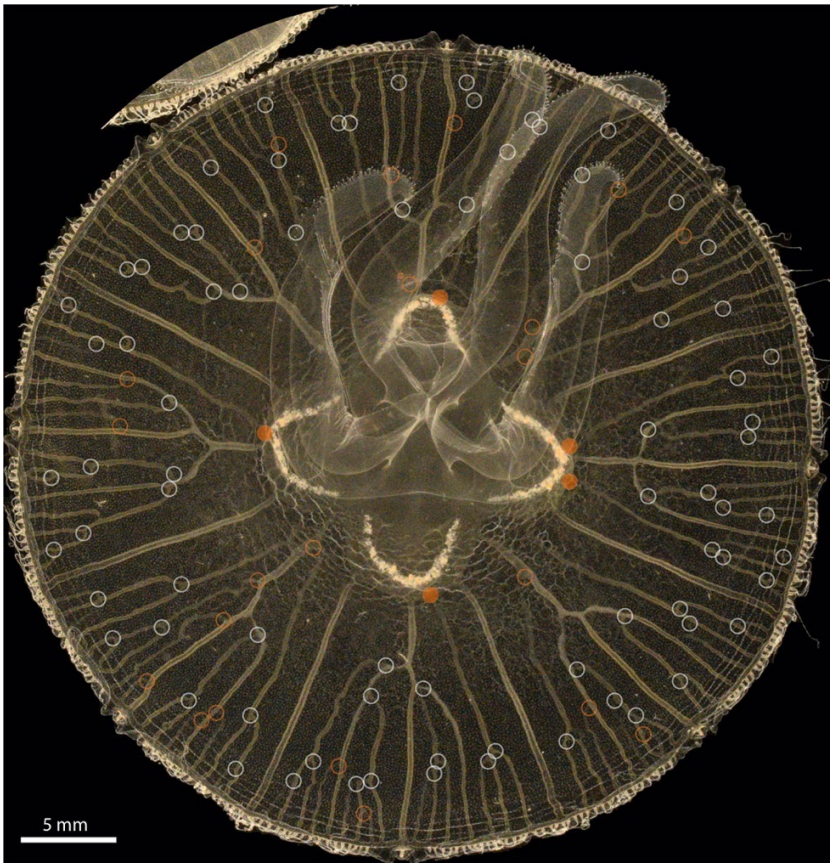

Fig S5, n°87

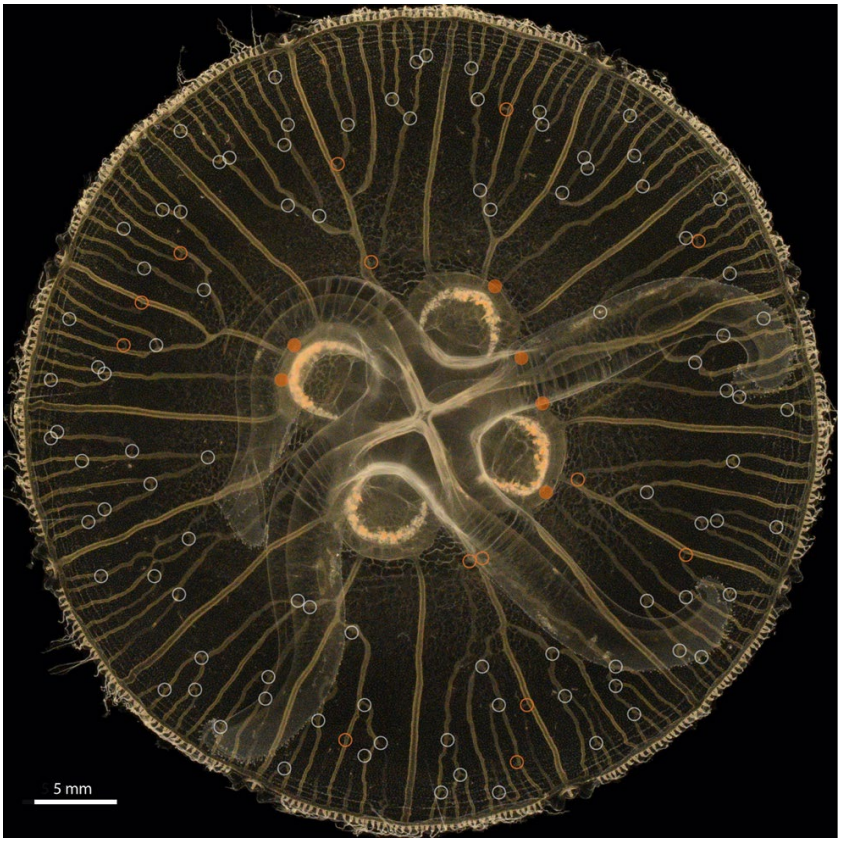

Fig S6, n°101

3 Numerical simulations frames

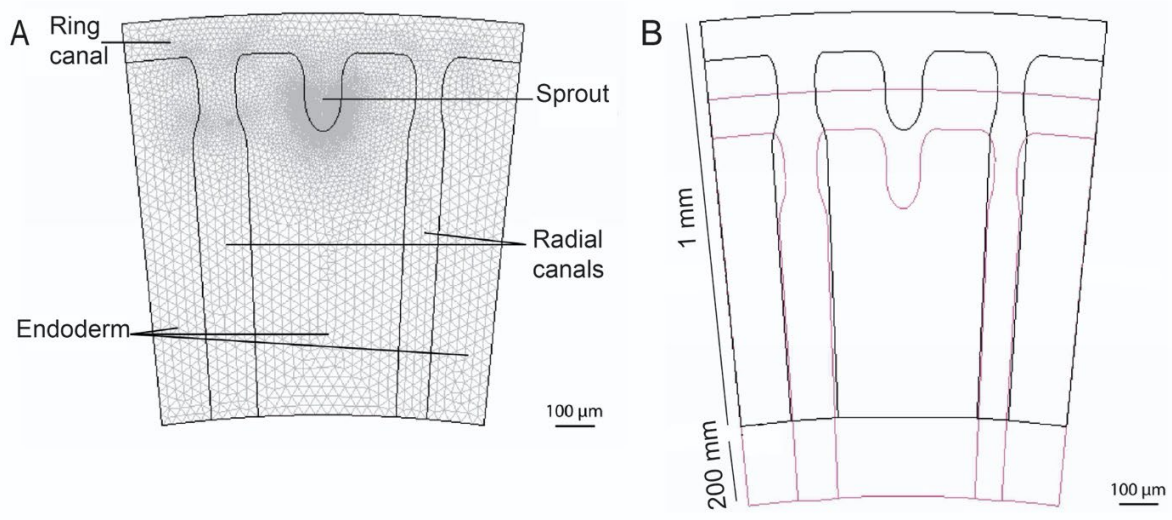

Fig. S7, A) detail of the mesh used, and the different zones with their names. B) detail and scales of the deformation imposed on the outer boundaries: angular contraction resulting in a smaller octant but with the same angular opening (black is original frame, pink is compressed frame).

Chapter 6

Morphogenesis of the gastrovascular canal network in *Aurelia* jellyfish: growth dynamics

In Chapter 5, we described the structure and variability of the jellyfish canal network. We suggested that the elongation of canals can be treated as a moving boundary problem, where the invading phase are the canal cells, and the receding phase are the endodermal cells. We proposed two hypothesis relating the canal growth to physical fields in the jellyfish. First, we analyzed the stress induced by swimming contractions of the jellyfish and how it concentrates at the tips of the growing sprouts. We proposed that this repeated mechanical effect can increase the tip cell proliferation and guide the sprouts to elongate in the highest stress direction preferably to the youngest canal in the neighborhood. Second, we noted a particular loop formation event in the morphogenesis of the canal network – a breakthrough-induced reconnection. As described in Chapter 4, this is an indication that the system dynamics may be controlled by diffusive fluxes.

In the following chapter, we examine the growth dynamics of the gastrovascular canal network in *Aurelia* jellyfish in order to validate the two hypotheses. We first approach the problem experimentally. Our goal is to induce phenotypic changes to the stereotypical network architecture of jellyfish by controlling their growth rate. This is achieved by modifying the environmental conditions in which they grow. In each experiment, we collect images of the jellyfish over a period of several dozen days and acquire time-lapses of *in vivo* canal network growth. We analyze the data to extract key information to reproduce the growth dynamics *in silico*. We then proceed with numerical modeling of the sprouts. We simulate the elongation of canals in response to the stress or pressure field.

6.1 Experiments

6.1.1 Methods

Specimen culture and image acquisition

The experiments were conducted at the Laboratoire Matière et Systèmes Complexes, Paris, France in the group of Dr Annemiek Cornelissen. Analogously to previous methods [151,152,155], the specimens were cultured in artificial seawater produced by diluting 28 g of synthetic sea salt (Instant Ocean; Spectrum Brands, Madison, WI) per liter of osmosis water (osmolarity 1100 mOsm). Polyps of the Roscoff strain were used, obtained by courtesy of Konstantin Khalturin from the Marine Genomics Unit, Okinawa Institute of Science and Technology Graduate University, Onna, Okinawa, Japan. The strobilation of polyps was induced by lowering the temperature to 10°C.

To ensure that the experiments are performed on ephyrae from a single polyp, the polyps were isolated and placed in separate Petri dishes. A strobilating polyp releases approximately ten ephyrae over the course of one or two days. Immediately after being released, the ephyrae were placed in an aquarium. From this point forward, the developmental age was defined as days post strobilation (dps).

The newborn ephyrae are reared in a standalone aquarium. To prevent them from settling, a continuous flow is created by aerating the water. Interestingly, after around two weeks of cultivation in this type of aquarium, the canals of the small jellyfish can dilate (Fig. 6.1). To avoid this, the jellyfish are transferred to larger aquariums after a week. In these aquariums, the flow is induced by a constant inflow of water from a water tower. Mature specimens demonstrate higher tolerance to the hydrodynamic conditions in the standalone aquarium, as verified by transferring them back to the standalone aquarium after several days of cultivation in a larger one.

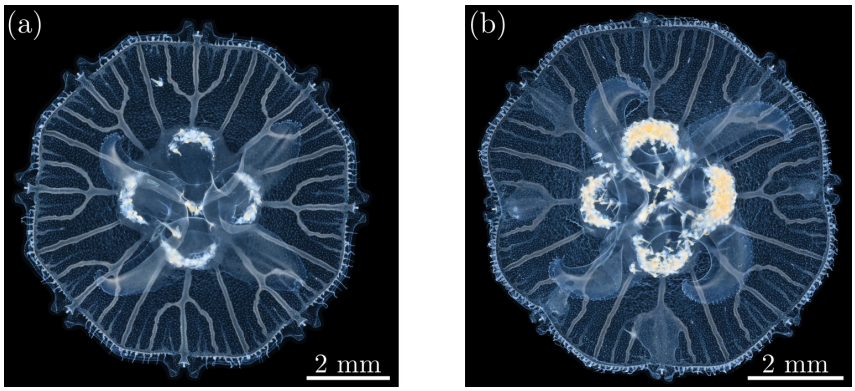

Figure 6.1 A jellyfish from Polyp 3 in Table 6.1 reared in a standalone aquarium. (a) At 15 days post strobilation (dps) the canal network has a healthy shape. (b) At 17 dps multiple canals are dilated.

In a typical experiment, the jellyfish are fed twice a day, except on weekends, when they are fed once a day. Due to variations in food intake, the number of jellyfish and offset of growth, we select feeding rations for each batch of jellyfish individually. We dose food between the maintenance threshold necessary for healthy development and the limit of maximum nutrient assimilation to prevent the accumulation of organic waste in the aquarium. The water in larger aquariums is kept at a constant room temperature of 22°C using a temperature control system.

After about a week, the ephyrae reach a circular shape with a radius of approximately 5 mm. We then divide a set of jellyfish clones from a polyp into subgroups. We culture the jellyfish under different conditions to control their growth rate. We manipulate the following factors: feeding frequency and ration, aquarium size, flow rate, and water temperature. In the Results section, we describe the different growth conditions and the resulting growth rates.

To image the jellyfish, they are caught from the aquarium approximately 3 hours after being fed artemia. This increases the contrast of the canals, turning them orange from the digested food. The jellyfish are placed in a Petri dish with shallow seawater facing up with their subumbrella. Images are taken using transillumination with a Nikon D3300 camera and an AF-S DX Micro NIKKOR 40 mm f/2.8G macro lens. After collecting the data, the jellyfish are returned to the aquarium.

Image analysis

To facilitate quantitative analysis, the experimental images had to be first segmented. The image analysis was conducted in two stages. First, the entire jellyfish was binarized, which allowed us to estimate jellyfish size. Second, the canals in the network were detected to analyze network architecture.

In the first part, the image segmentation was performed using the Segment Anything Model (SAM) [156] (sam2.1_hiera_tiny variant). This is a general-purpose object segmentation neural network model, pretrained on a dataset that includes 35 million segmentation masks. This vast scale provides flexibility for the model to accurately segment novel objects not represented in the pretraining dataset. We used bounding boxes (green in Fig. 6.2a) as inputs to isolate the jellyfish body from the background. We additionally fill potential holes and smooth the output of the model to obtain the final binary mask. It has 1 assigned to pixels corresponding to the jellyfish and 0 to the background (Fig. 6.2b). The jellyfish size, A, is then simply the sum of the pixels composing its binary mask (multiplied by the pixel size estimated in a calibration process). The jellyfish radius

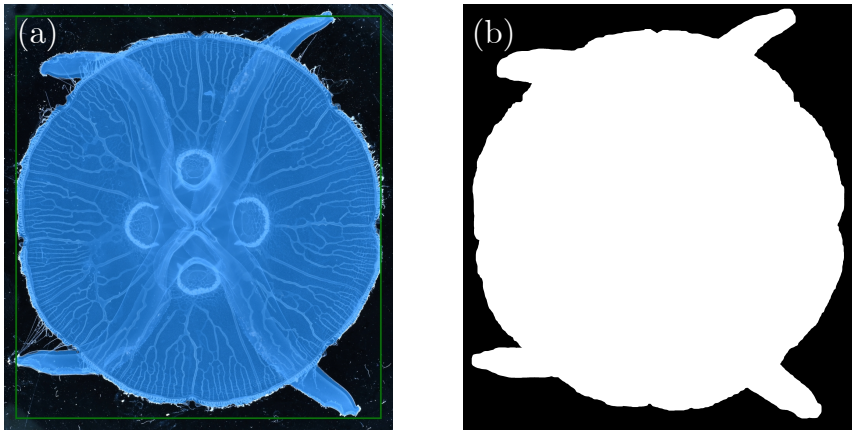

Figure 6.2 Segmenting the entire jellyfish body with with the Segment Anything Model. (a) The experimental image with the green bounding box used to prompt the model. The mask determined by the model is highlighted in blue. (b) The final binary mask resulting from filling potential holes in the SAM mask and smoothing it.

is determined by assuming a circular shape of the jellyfish body plan: $R_{\text{jellyfish}} = \sqrt{A/\pi}$.

The second part of the image analysis process, canal detection, was more technically challenging. The contrast between the canals and their surroundings depends on how much food the canals transport and digest. Canals that have just sprouted from the marginal canal and have not yet reconnected appear dim in the experimental images. Their luminosity increases as they mature and form a lumen, and reaches its maximum when the canal reconnects to the stomach or other canals and begins fully transporting nutrients. Due to the non-uniform luminosity and noise in the images, basic image analysis methods, such as thresholding, are insufficient.

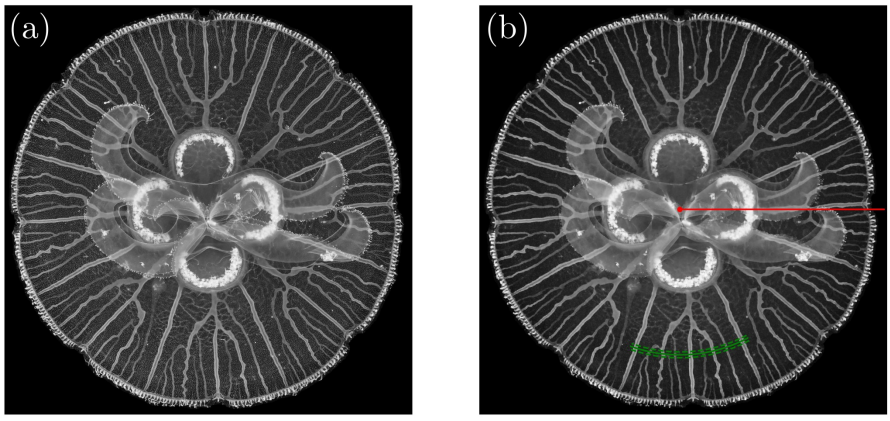

Figure 6.3 Image analysis to detect canals. (a) The grayscaled experimental image.(b) The image after top-hat noise removal. The red dot indicates the center of the jellyfish and the origin of the cylindrical coordinate system. The angle is measured from the red solid line. The green line shows the azimuthal cut, from which signal in Fig. 6.4 is plotted.

In our image analysis pipeline we exploit the predominantly radial orientation of the

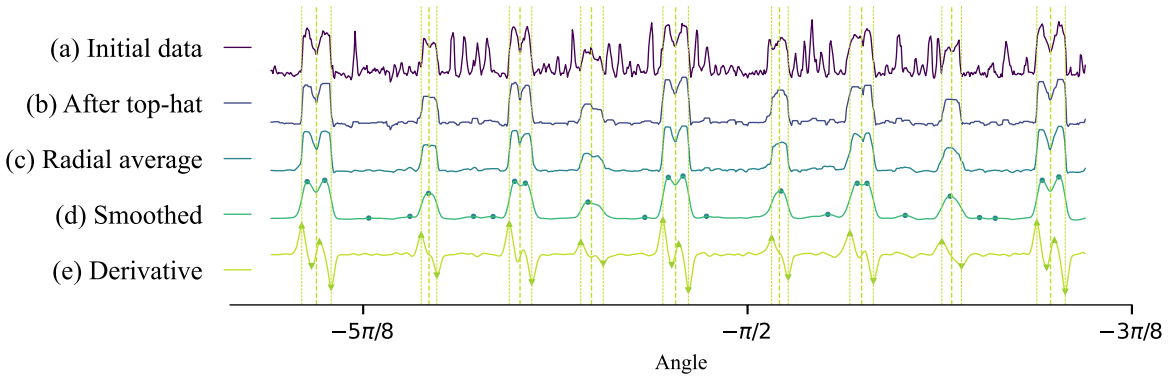

Figure 6.4 Signal from the azimuthal cut indicated in Fig. 6.3b. (a) The signal from the original image. (b) The signal from the image after the top-hat transform. (c) The radially averaged signal between the two green dashed lines in Fig. 6.3b. (d) The smoothed signal with a Gaussian filter. For some canals, the intensity inside is lower than on the edges. Therefore, the detected peaks (marked with dots) are not useful for determining the positions of the canals. (e) The maxima and minima in the intensity derivative are used to detect the edges of the canals.

canals. First, we remove the small-scale structures from the image by applying the top-hat transform (Fig. 6.3). This suppresses background noise, leaving the canal structures. Next, we establish a polar coordinate system centered at the jellyfish center (red dot in Fig. 6.3b). We select an azimuthal cut (the green solid line in Fig. 6.3b) and plot the image intensity as a function of angle. Fig. 6.4a shows the intensity signal directly from the experimental image, while Fig. 6.4b shows the signal from the image after top-hat transform. We further refine the signal by performing a radial average within an annulus bounded by the green dashed lines in Fig. 6.3b, and applying a Gaussian filter. The corresponding plots are presented in Fig. 6.4c-d.

Finally, we note that the intensity of the canal cross-sections is sometimes higher on the sides and lower in the center. This results in a bimodal intensity profile with peaks at the canal sides. Consequently, the peaks detected in the intensity plot (dots in Fig. 6.4d) do not correctly indicate the position of the canals. Instead, we compute the derivative of the intensity profile and detect its maxima and minima (triangles in Fig. 6.4e). Then, we can localize the canal sides by identifying pairs of successive extrema with similar magnitudes (vertical dashed lines in Fig. 6.4). This also allows us to estimate the canal width.

The above procedure can be applied to azimuthal cuts of different radii to detect canals in the entire jellyfish (Fig. 6.5). The algorithm has several limitations. Small, non-connected canals often have insufficient contrast and are overlooked. Reliance on a radial orientation of the canals limits the detection of orthoradial segments near junctions. Additionally, the jellyfish morphology deviates from perfect radial symmetry. Consequently,

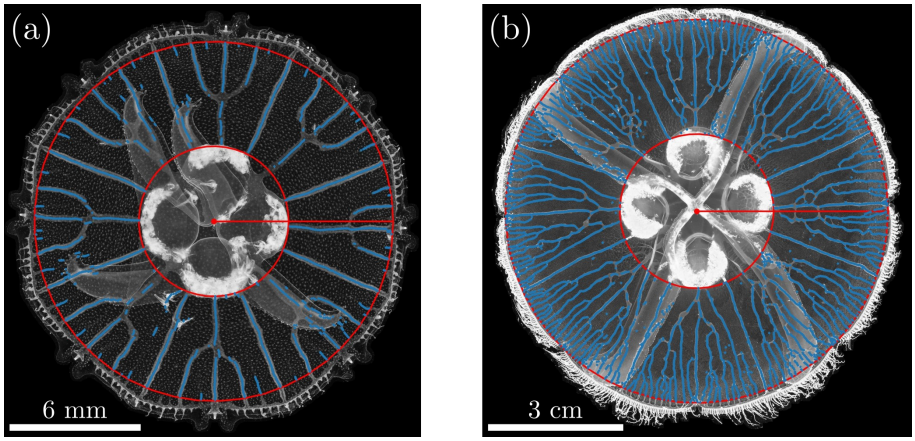

Figure 6.5 Detected canals in the entire jellyfish from Polyp 7 in Table 6.1. (a) A young (18 dpf) and (b) an older (26 dpf) jellyfish. The red circles of radi R_{rim} and R_{stomachs} border the area of detection, blue dots correspond to detected canals. The algorithm works better for older jellyfish, as the contrast of the canals increases with their age.

we cannot detect canals directly at the marginal canal, and the measured number of canals at $R = R_{\text{rim}}$ underestimates the number directly at the rim. Nevertheless, most canals are detected correctly, particularly for older jellyfish with a well established network, allowing us to analyze the radial distribution of canal number and typical canal spacing.

6.1.2 Results

Jellyfish size

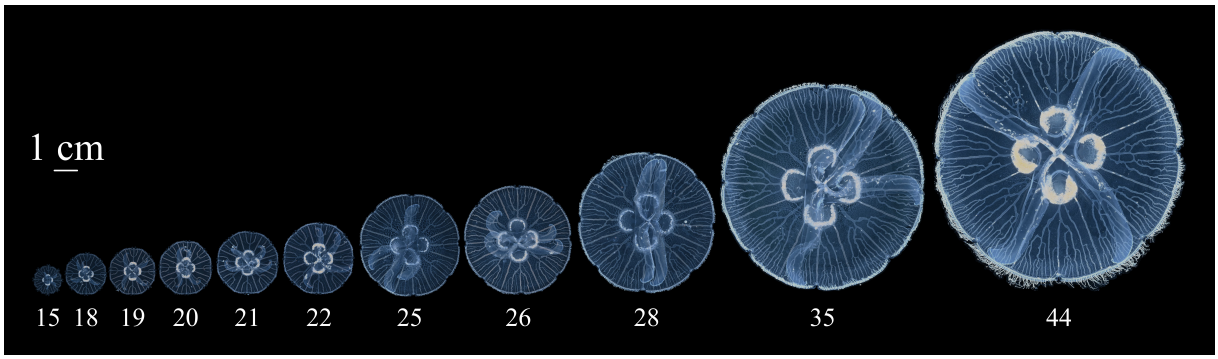

Figure 6.6 Timelapse of growth of jellyfish from Polyp 7. The numbers at the bottom indicate dps.

First, we analyze how the radius of the jellyfish changes over time (Figs. 6.7 and 6.8). We observe a linear growth of the jellyfish and study the impact of environmental conditions on the growth rate. In each experiment, we divide jellyfish from a single polyp into two groups and place them in separate aquariums. We conduct experiments in which

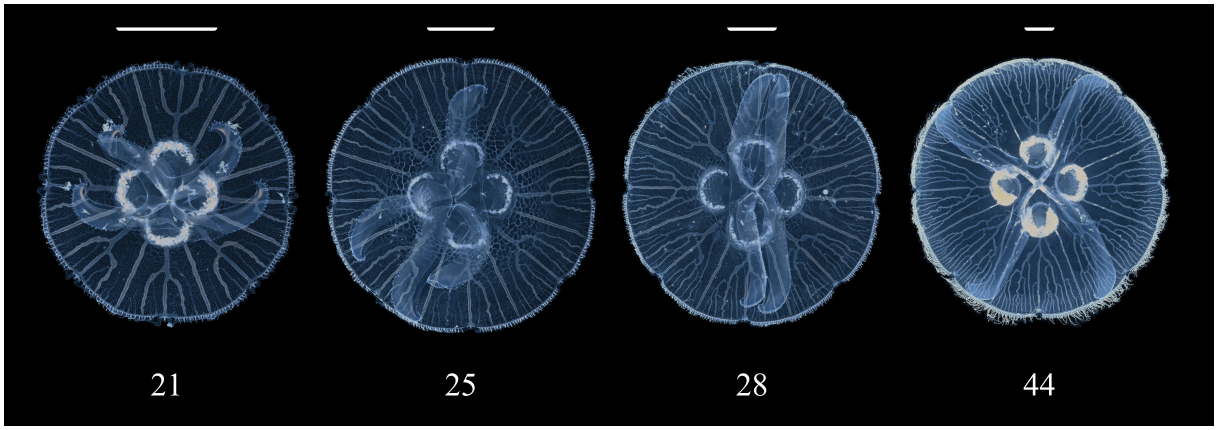

Figure 6.7 Canal network development in detail. Rescaled images of the jellyfish from Fig. 6.7 (Polyp 7). The numbers at the bottom indicate dps. The scalebar (white line) is always 1 cm.

we vary the growth conditions in the two aquariums. We observe that the jellyfish grow faster when the flow rate in the aquarium is higher (Polyps 1, 2). Higher feeding rations increase the growth rate (Polyp 2). Additionally, we observe that feeding the jellyfish more frequently also increases their growth rate (Polyp 7).

In the experiment from Polyp 3, we demonstrate that small jellyfish develop dilated canals when kept in a standalone aquarium for too long (Fig 6.1). Interestingly, transferring the jellyfish to a larger aquarium without aeration-induced flow for several days and then back to the aerated standalone aquarium does not induce canal dilation, as demonstrated in the experiments from Polyps 5 and 6. However, the volume of the aquarium influences their growth rate; larger tanks allow the jellyfish to grow faster. In the experiment from Polyp 4 we see that two groups kept in the separate aquariums follow the same growth trajectory if the other conditions are the same. In the experiment from Polyp 8, we observe spontaneous divergence in growth rate among the jellyfish in the same aquarium – one jellyfish started to outgrow the others. Finally, we find that jellyfish grow more slowly at higher temperatures (24.5°C).

In Fig. 6.8, growth rates were calculated for individual jellyfish via linear regression of radius over time, and then averaged within subgroups. Errors represent the Standard Error of the Mean (SEM). The growth rates in our experiments range from 0.65 to 2.04 mm/day and its mean is 1.41 ± 0.05 mm/day. The above information is summarized in Table 6.1 and in Fig 6.9. The latter also presents the statistical comparisons between groups. We note here that growth rates should be compared within pairs from a single polyp to control for potential confounding factors. These include technical challenges in standardizing flow velocity in all aquariums or the necessity of individually adjusting feeding regimes based on the jellyfish's condition.

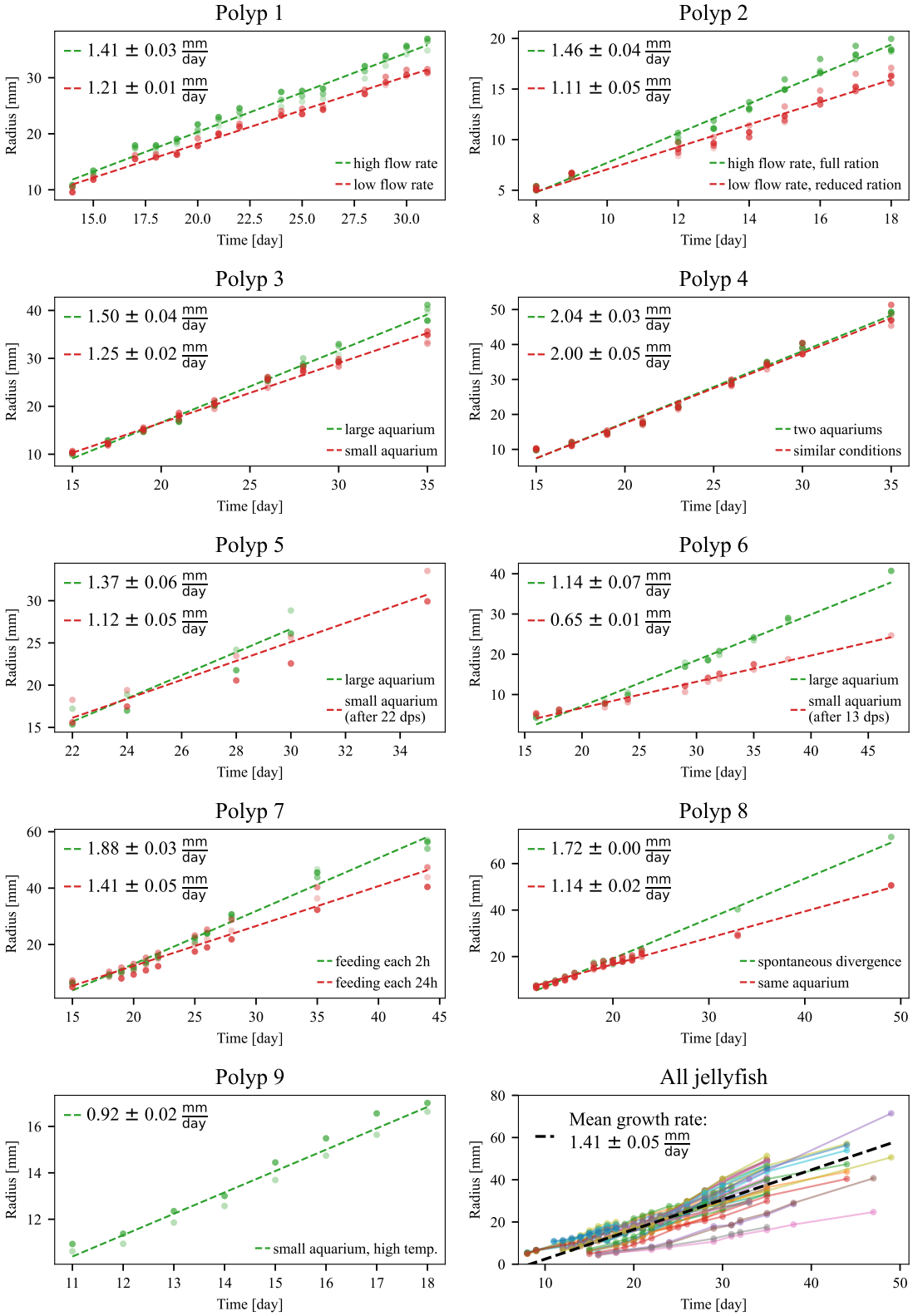

Figure 6.8 **Jellyfish radius in time.** Each red or green dot represents a jellyfish. The dashed lines represent the mean linear growth trajectory for each group, calculated by averaging the individual slopes of all polyps within that condition. Legend values indicate the Mean Growth Rate ± Standard Error of the Mean (SEM) and experimental conditions. The last panel presents all experiments on one plot (different colors), with the black dashed line representing the mean growth rate which is 1.41 ± 0.05 mm/day.

Table 6.1 **Experiments summary:** experimental conditions, growth rates (G), and number of specimens (n).

Experiment	Description	G [mm/day]	n
Polyp 1	High flow rate	1.41 ± 0.03	3
	Low flow rate	1.21 ± 0.01	3
Polyp 2	High flow rate, full feeding ration	1.46 ± 0.04	4
	Low flow rate, reduced feeding ration	1.11 ± 0.05	4
Polyp 3	Large aquarium	1.50 ± 0.04	4
	Small aquarium	1.25 ± 0.02	4
Polyp 4	Two aquariums, similar conditions	2.04 ± 0.03	4
		2.00 ± 0.05	4
Polyp 5	Large aquarium	1.37 ± 0.06	2
	Small aquarium (after 22 dps)	1.12 ± 0.05	2
Polyp 6	Large aquarium	1.14 ± 0.07	2
	Small aquarium (after 13 dps)	0.65 ± 0.01	2
Polyp 7	Feeding each 2h	1.88 ± 0.03	3
	Feeding each 24h	1.41 ± 0.05	3
Polyp 8	Spontaneous divergence	1.72	1
	(same aqaurium)	1.14 ± 0.02	4
Polyp 9	Small aquarium, high temp. (24.5°C)	0.92 ± 0.02	2

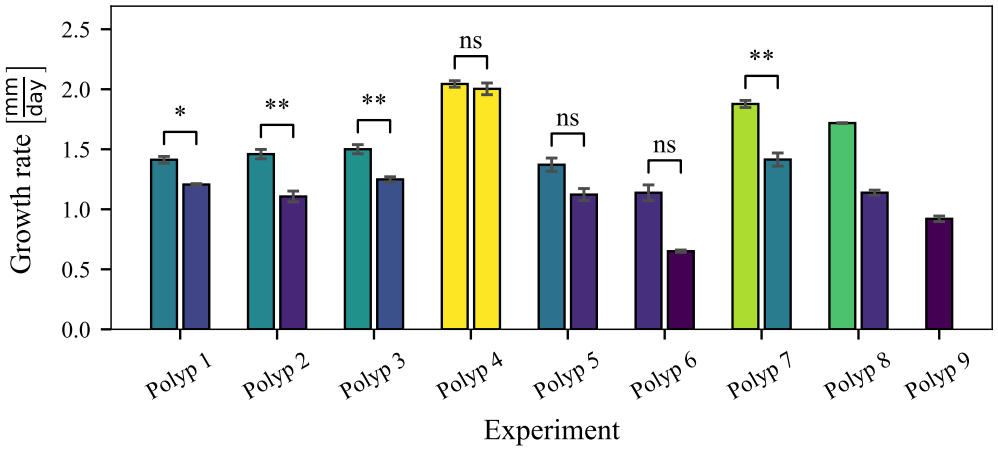

Figure 6.9 **Variation in jellyfish growth rates across environmental conditions.** Growth rates were calculated for individual jellyfish via linear regression of radius over time. Bar heights represent the mean growth rate of the population for each condition, and error bars represent the Standard Error of the Mean (SEM). Statistical significance between groups was assessed using Welch's t-test, which accounts for unequal variances ($*p < 0.05$, $**p < 0.01$, ns: not significant). Experimental conditions for jellyfish from Polyps 1–9 are presented in Table 6.1.

Radial distribution of canals

Next, we focus on the canal network. We begin by analyzing a single jelllyfish over time. We plot the number of canals, N, as a function of the distance from the rim, $R_{\text{rim}} - R$ (Fig. 6.10a). As the sprouts always initiate at the rim, the number of canals is the highest there. It then decreases monotonically as we approach the gastric pouches and we stop counting the sprouts that are still growing and terminate with a free-ending tip or have reconnected. In fact, the derivative of the number of canals, $\mathrm{d}N/\mathrm{d}R$, represents the number of free-ending tips and reconnections per unit length.

We plot the radial distribution of canals for a growing jellyfish (the lines from blue to yellow in Fig. 6.10a indicate its size). For larger jellyfish, we observe an increase in the number of canals at the rim, and the sprouts extending farther from the rim. Otherwise, the distributions have a similar shape, as if they were rescaled. To further investigate the self-similarity of the radial distribution of canals, we normalize the number of canals by the perimeter at a given radial position, $N/2\pi R$. We plot this quantity as a function of the relative radial position from the rim, $1 - R/R_{\text{rim}}$. The canal spatial frequency plots come closer to each other. For larger jellyfish, the canals appear to be less frequent (Fig. 6.10b). In other words, the typical spacing between centerlines of the canals, $2\pi R/N$, increases when we move from rim to stomachs and is in general greater for larger jellyfish (Fig. 6.10c). Analogously, the width of the canals, w, changes with radial position and the jellyfish size. We define canal separation as $d = (2\pi R - \sum_{i=0}^{N} w_i)/N$, where i indicates individual canals. This corresponds to the distance between the sidewalls of the canals. Canal density is then $1/d$.

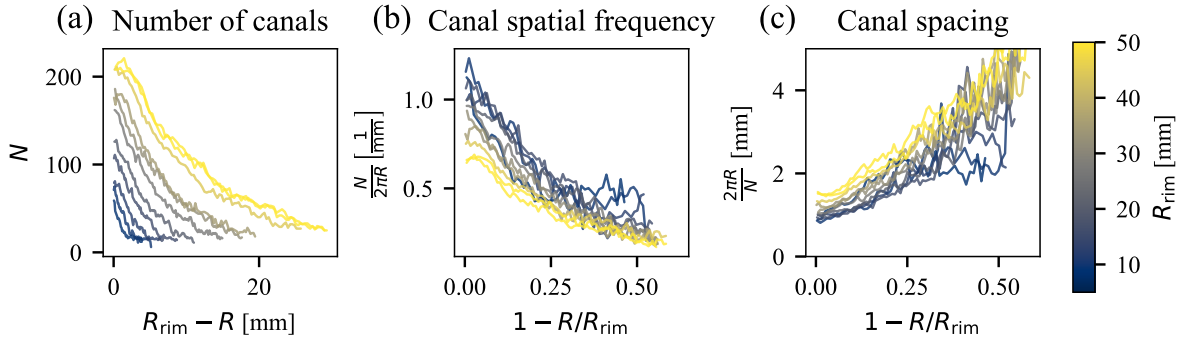

Figure 6.10 Radial distribution of canals in a single jellyfish over time. (a) The number of canals as a function of radial distance from the rim. (b) Canal spatial frequency – the number of canals divided by the perimeter at a certain radius – as a function of relative radial position. (c) Canal spacing – the inverse of canal spatial frequency. Colors are related to the jellyfish size, R_{rim}.

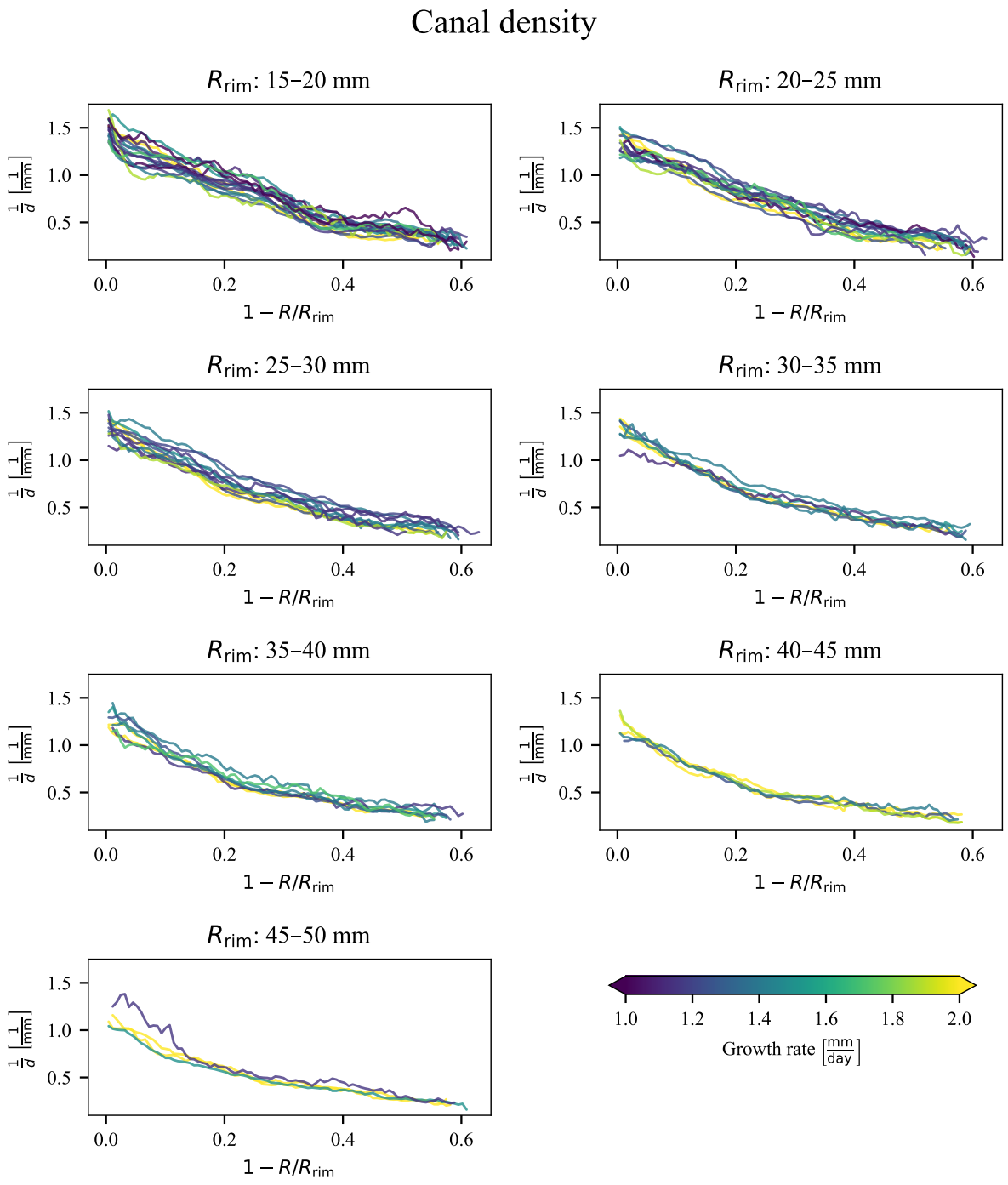

Figure 6.11 **The effect of growth rate on radial distribution of canals.** The panels include jellyfish within a specific size ranges. The lines correspond to experiments with different growth rates, indicated by the color of the line. The lines represent an average over multiple jellyfish within a group and over several time points.

We then verify whether the jellyfish growth rate affects the radial distribution of canals. We analyze groups of jellyfish growing at different rates, and average canal density profiles over all jellyfish within a group. As previously noted, canal separation increases in larger individuals. To mitigate this size-dependent effect, we categorize the jellyfish by size and additionally average canal density over time for periods when individuals fall within a specific radius range. The results are presented in Fig. 6.11. In each subplot, we analyze jellyfish within a specific size range. Each line represents an experiment with a different growth rate, indicated by the color of the line. The canal density profiles are an average of multiple jellyfish within a group at several time points.

We do not observe any particular impact of the growth rate on canal density profiles. The averaged canal densities collapse onto a single curve, particularly for larger jellyfish. For smaller individuals, the dispersion between curves is more pronounced, which may be attributed to limitations in the canal detection algorithm. At early stages, sprouts are smaller and exhibit lower contrast, making them less visible in experimental images.

To obtain a clearer representation of the influence of jellyfish size, we average all jellyfish within a specific R_{rim} range. We see a clear increase of canal separation (and a corresponding decrease in canal density) as the jellyfish size increases (Fig. 6.12). Interestingly, the vertical offset between the curves is most pronounced near the rim, $1 - R/R_{\text{rim}} < 0.3$ (see Fig. 6.12b). This corresponds to the radial position of the junction of the canals that compose the initial tri-fork structure.

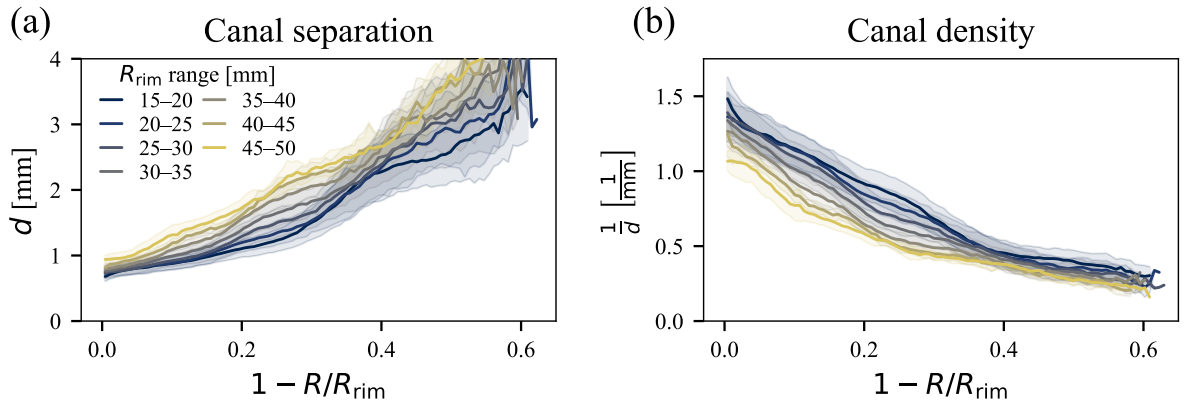

Figure 6.12 The effect of jellyfish size on radial distribution of canals. (a) Canal separation. (b) Canal density.

Finally, we analyze canal width, spacing and separation at the rim as a function of jellyfish size (Fig. 6.13). These measurements are essential for the numerical model because the observed canal spacing provides empirical constraints for the sprout initiation rules at the rim. Interestingly, as the jellyfish grows, the expansion of canal width compensates

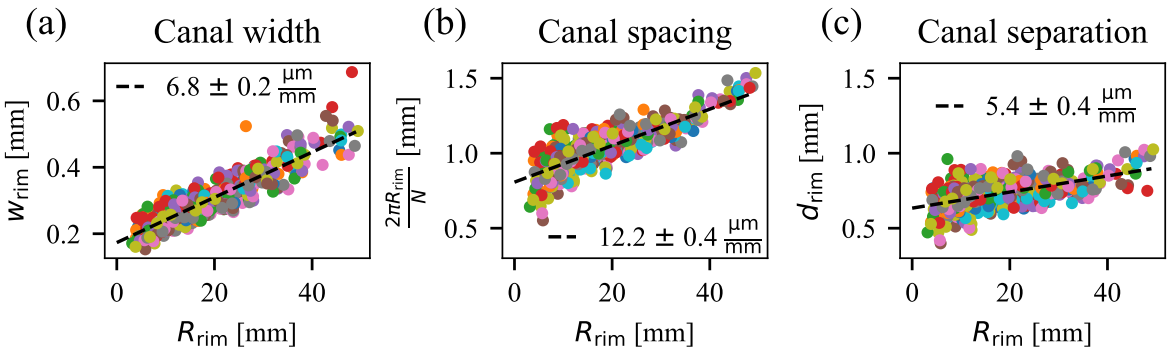

Figure 6.13 **Canal width, spacing, and separation at the rim.** Each dot represents the average value for one jellyfish. The black dashed line is a linear fit. The slope and standard error are indicated in the figure legends.

for the increased canal spacing, resulting in canal separation that depends only weakly on organism size. This may be related to the characteristic reaction-diffusion length in the system – the effective range of nutrient delivery from a canal.

6.2 Simulations

6.2.1 Model

Stress-driven growth

The stress-driven growth model is an extension of the analysis of stress concentration at the tip of a growing sprout, as described in Chapter 5 and Ref. [151]. In summary, we consider a plane stress problem for an octant. The area occupied by canals with lumens is approximated as a compressible elastic membrane with Young's modulus lower than that of the endoderm, $E_1 < E_2$. The chosen Poisson's ratio of 0.3 translates the vertical expansion of the canals into compression in the plane. Note that, unlike in Chapter 4, for simplicity we do not account for the softening of the canals with age and we assign the same Young's modulus value to all canals. We assume that the endoderm is a flat, rigid, nearly incompressible elastic sheet with Poisson's ratio $\nu_2 = 0.49$ and Young's modulus E_2. In the simulations, we investigate the effect of Young's modulus ratio, $E = E_2/E_1$, on the emerging canal network.

The model follows the quasistatic Cauchy momentum equation:

$$\nabla \cdot \sigma(\epsilon) = 0\,, \tag{6.1}$$

where ρ is the density of the endoderm (assumed to be similar to that of water), u is the displacement of the material, $\epsilon = \nabla u$ is the strain, and $\sigma(\epsilon)$ is the stress–strain relationship. We neglect the stress component in the z direction (normal to the endoderm surface) and the reduced 2D Hooke's law is expressed as:

$$\begin{aligned}
\sigma_x &= \frac{E_i}{1-\nu_i^2}(\epsilon_{xx} + \nu_i \epsilon_{yy})\,,\\
\sigma_y &= \frac{E_i}{1-\nu_i^2}(\epsilon_{yy} + \nu_i \epsilon_{xx})\,,\\
\sigma_z &= 0\,,\\
\sigma_{xy} &= \frac{E_i}{1+\nu_i}\epsilon_{xy}\,,\\
\sigma_{yz} &= 0\,,\\
\sigma_{xz} &= 0\,.
\end{aligned}$$

The orthoradial muscle contraction is mimicked by reducing the radial position of the rim by 4%. The following radial displacement is imposed on the rim: $u_r = -0.04 R_{\text{rim}}$.

Due to the radial symmetry of the jellyfish, the sides (the adradial canals) can only slip along the radial axis. The angular deformation vanishes there: $u_\theta = 0$. The gastric pouch is free to move: $\sigma(\epsilon) \cdot \mathbf{n} = 0$.

Local mechanical stresses acting on cells in a growing organism has been shown to modify gene expression patterns and control processes such as embryonic development [157, 158] and tumor progression [159]. Following these ideas, in Chapter 5, we proposed that the tip cells may also respond to mechanical stresses and increase proliferation when compressed. Consequently, the stress field effectively determines the growth velocity and guides the sprouts to elongate in the highest stress direction.

To determine the velocity and direction of growth we first reduce the stress tensor to a scalar representation – the von Mises stress:

$$\sigma_{\text{vm}} = \sqrt{\sigma_x^2 - \sigma_x\sigma_y + \sigma_y^2 + 3\sigma_{xy}^2}\,. \tag{6.2}$$

This simplifies the problem and gives a satisfactory scalar representation of the stress distribution in the endoderm, as discussed in Chapter 5.

The canals grow in the direction of maximum von Misses stress, σ_{vm}. As all tip cells take part in the elongation of the canal the velocity is proportional to the stress integrated at the tip:

$$v = \beta(\int_{\text{tip}} \sigma_{\text{vm}})\,, \tag{6.3}$$

where β is a phenomenological biological factor representing the responsiveness of canal cells to mechanical stimuli. The parameter β sets the timescale of canal growth and is calibrated such that the first generation of canals reaches the gastric pouches within approximately 10 days, consistent with our experimental observations.

Pressure-driven growth

At short timescales, in the order of minutes, live tissues behave elastically. However, on timescales exceeding cellular relaxation, in the order of hours, they begin to exhibit liquid-like properties [160]. The fluidization of tissues can be driven by several effects. For instance, decreased cortical tension or increased intercellular adhesion enables cells to move past one another and exchange neighbors [161], which allows the tissue to dissipate internal mechanical stress. Cell division and apoptosis also contribute to this process [162]. Modeling tissues as highly viscous fluids has proven useful in contexts such as embryonic development [160, 163], wound healing [164, 165], and cancerous tumor invasion [166, 167].

In the case of the jellyfish, the timescale of canal growth is much longer than the

typical timescale of cellular relaxation. This justifies treating the canal and endodermal cells as highly viscous fluids. Thus, canal growth is a moving boundary problem in which canal cells displace endodermal cells. We begin by treating it as a Laplacian growth problem, where cells are pushed by the pressure at the margin, exerted by the time-averaged contractions. Although biologically simplified, this model allows us to draw on intuitions of Laplacian growth, and it provides a baseline for understanding canal patterning. We leave extensions of the current framework for future investigation.

To derive the model, we first assume that cell flow velocity is described by Darcy's law:

$$\boldsymbol{v} = -\alpha \boldsymbol{\nabla} p \,, \tag{6.4}$$

where p is pressure and α is the mobility of cells that describes the magnitude of the effective friction in the system and is inversely proportional to the fluid viscosity, μ. We assume that a drag force, necessary to reduce Stokes flow to Darcy's law, originates from the mesoglea, which encapsulates the endoderm sheet from above and below. We treat the canal cells as a fluid of lower viscosity μ_1 that invades the endodermal cells, a more viscous fluid of viscosity μ_2. In the simulations we vary the viscosity ratio, $M = \mu_2/\mu_1$, and study its impact on the canal network geometry.

We assume that the cell proliferation is responsible mainly for the global growth of the jellyfish and not for internal pressure distribution that is dominated by time-averaged contractions. Consequently, we neglect the proliferation and impose the linear growth of jellyfish independently, at the growth rate measured in experiments. We additionally assume that the tissue is incompressible which leads to:

$$\boldsymbol{\nabla} \cdot \boldsymbol{v} = 0 \,. \tag{6.5}$$

A more biologically relevant model could incorporate a non vanishing right hand side of Eq. 6.5 that would account for the jellyfish growth or the intensified proliferation at the canal tips. The mass conservation equation could be also adapted to account for the in-plane compressibility of the canals.

The Eq. (6.5) leads us to the Laplace equation for pressure:

$$\Delta p = 0 \,. \tag{6.6}$$

The boundary conditions for an octant are chosen as follows. Given the radial symmetry of the problem, Neumann reflecting boundary conditions are applied on the adradial canals (the left and right boundaries of the octant): $\frac{\partial p}{\partial n} = 0$, where n is normal to the walls. The pressure field is defined relative to the gastric pouches, rendering them pressure-free

surfaces ($p = 0$). We assume that time-averaged contractions exert high pressure at the margin. Consequently, Dirichlet boundary condition is imposed on the bottom boundaries ($p = p_0$).

We take advantage of the fact that the growing canals maintain a well specified width. As in Chapter 4, we focus primarily on finger interactions, approximating the moving boundary problem with the evolution of fingers of constant width. In this model, the canal growth velocity is determined by integrating the pressure gradient at the tip:

$$v = \beta(\int_{\text{tip}} \nabla p)^{\eta}\,, \tag{6.7}$$

where β again sets a timescale of canal growth, and η is an exponent characterizing the scaling of the growth response to pressure.

Stochastic sprouting

As the jellyfish grows, the distance between neighboring canals increases, creating space for new sprouts. We initiate them with a probability that depends on the separation between neighboring canals, $d_{\text{rim},i}$. We use a sigmoidal function to calculate the probability of sprouting (Fig 6.14a):

$$h(d) = \frac{h_{\max}}{1 + e^{-(d-d_0)/k}}\,, \tag{6.8}$$

where $h_{\max}$ is the maximum limit of the function, d_0 is the position of the inflection point, and k is related to the sigmoid width and derivative at $d = d_0$: $h'(d_0) = \frac{h_{\max}}{4k}$.

This function assigns a small probability of sprouting when neighboring canals are close together, and a larger probability, that plateaus at $h_{\max}$, when the distance between them increases. The width of the transition zone depends on k. In the limit of $k \to 0$ and $h_{\max} \to \infty$ we recover deterministic sprouting whenever the threshold, d_0, is reached. Finite values of $h_{\max}$ result in an exponential decay of distribution of d at which new sprouts appeared. Increasing k allows new sprout initiation for $d < d_0$ and results in a wider distribution of d at which new sprouts appeared. We fine tune the parameters to reproduce distributions and the typical average spacing observed in experiments (Fig 6.14b). The following values of the parameters were used in the simulations: $k = 0.4$, $h_{\max} = 200$, and $d_0 = 2.9 + 0.03R_{\text{rim}}$. The increase in d_0 accounts for the slow growth of d_{rim}.

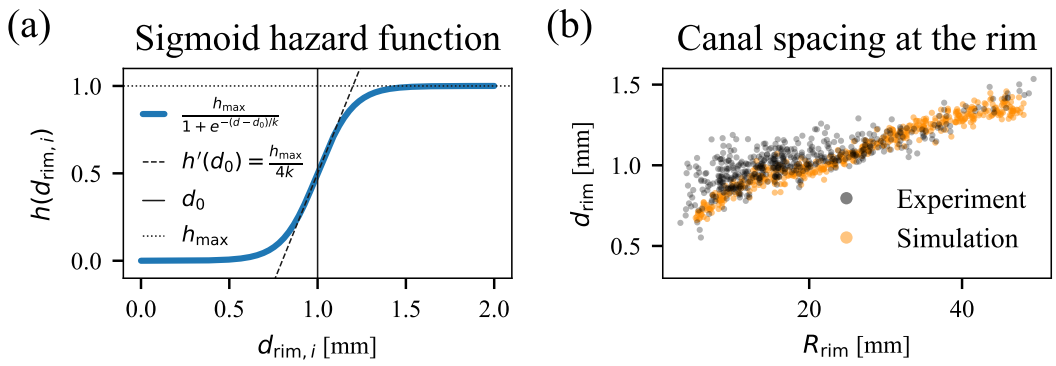

Figure 6.14 Stochastic sprouting at the rim. (a) A sigmoid function (Eq. (6.8)) used to determine the probability of sprouting depending on the distance between neighboring canals. (b) Comparison of the average canal spacing at the rim in experiments and simulations.

Network growth simulations

We base our simulations of canal network dynamics on the network evolution Python package developed in Chapter 4, and available on the GitHub repository (`https://github.com/stzukowski/reticuler`). We adapt it to the jellyfish case based on our experimental observations. We employ tetraradial symmetry and consider a single octant – one-eighth of an annulus between the marginal canal and the gastric pouches. We begin the simulations with a tri-fork structure in the middle and short sprouts on the rim – a typical setup for juvenile jellyfish. We impose linear growth on the jellyfish radius at the mean growth rate measured in experiments. In each timestep of the simulation, we use the finite element method to solve the elastic or diffusive problem. To calculate the field in the system, we decompose it into two domains: the canals and the endoderm. Each domain has different mechanical properties. We investigate the effect on the canal network structure of the canal-to-endoderm properties ratio – specifically, the Young's modulus ratio in the elastic case and the mobility ratio in the diffusive case.

To determine the velocity and growth direction of canals we integrate the corresponding field at the tips. The sprouts are subsequently elongated, and the entire jellyfish is radially scaled to maintain a constant growth rate. New sprouts are initiated at the rim, always at the midpoint between two neighboring canals. The moment of initiation is chosen stochastically, based on a sigmoid function. The sprouts grow until they reconnect to stomachs or other canals. Below we describe stochastic sprouting and stress- and pressure-driven growth in detail.

6.2.2 Results

We begin by analyzing the stress-driven growth. In Fig. 6.15, we present the dynamics of canal network formation *in silico* with the Young's modulus ratio set to $E = 9$. The simulated dynamics reproduce the dynamics observed on real jellyfish fairly well. The canals start growing at the rim and propagate toward the gastric pouch. They are generally attracted to each other, leading to reconnections over time. Interestingly, the first generation of sprouts can either reconnect to the tri-fork structure, like the sprout on the right in Fig. 6.15, or 'escape' and propagate further toward the gastric pouch, like the sprout on the left. This behavior of the first-generation sprouts is also observed in experiments, as seen in Fig. 6.7.

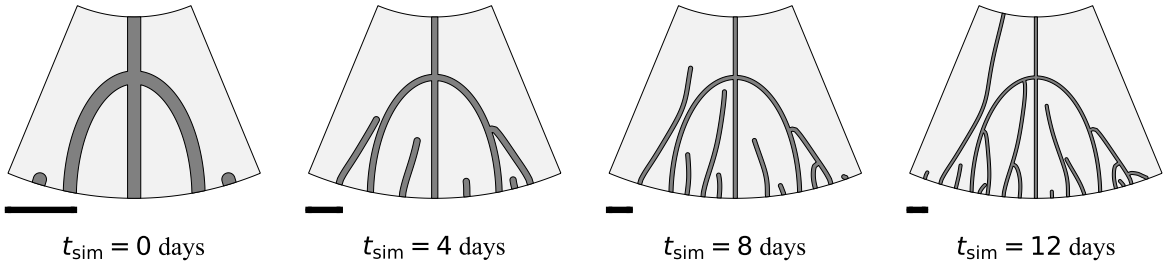

Figure 6.15 Time evolution of a canal network grown in response to the stress field with the Young's modulus ratio $E = 9$. The black line indicates a scalebar of length 1 cm.

In Fig. 6.16, we investigate the effect of the Young's modulus ratio, E, on the canal network structure. When the canals and the endoderm have the same Young's modulus value (corresponding to $E = 1$), the canals do not interact and grow straight. Increasing E leads to stronger attraction and consequently faster reconnection closer to the rim. This affects the canal spatial frequency profiles (Fig. 6.17). For low E, the normalized number of canals gradually decreases, wheras for higher E, it drastically drops close to the rim. Moderate values of E best reproduce the experimental data, especially for $1 - R/R_{\text{rim}} < 0.35$. At this radial position, the simulation results exhibit a sharp decrease in the normalized number of canals. This corresponds to the fixed position of the tri-fork junction in the simulations. All canals growing inside the tri-fork structure must reconnect before reaching this radial position, which explains the sudden jump in the curves. In real jellyfish, the radial position of this junction is not fixed, resulting in a much smoother canal spatial frequency profile after averaging.

Next, we analyze pressure-driven growth. In this case, the sprouts velocity is significantly affected by longer neighboring canals. Consequently, short sprouts grow much more slowly than long ones. This is contrary to experimental observations, in which sprout velocity does not vary greatly from canal to canal. To mitigate this effect in the simulations,

we set $\eta = 0$ in Eq. (6.7); thereby making all sprouts grow at the same velocity.

Apart from the need to dampen competition between the canals, the results are remarkably similar to those of stress-driven growth. As before, we observe that the canals do not interact and grow straight for the same viscosity of endodermal and canal cells (corresponding to $M = 1$). They are attracted to each other and reconnect faster at a high viscosity ratio (Fig. 6.18). Moderate values of the viscosity ratio visually reproduce canal network patterns observed in experiments and most closely reproduce the canal spatial frequency profile measured in experiments (Fig. 6.19).

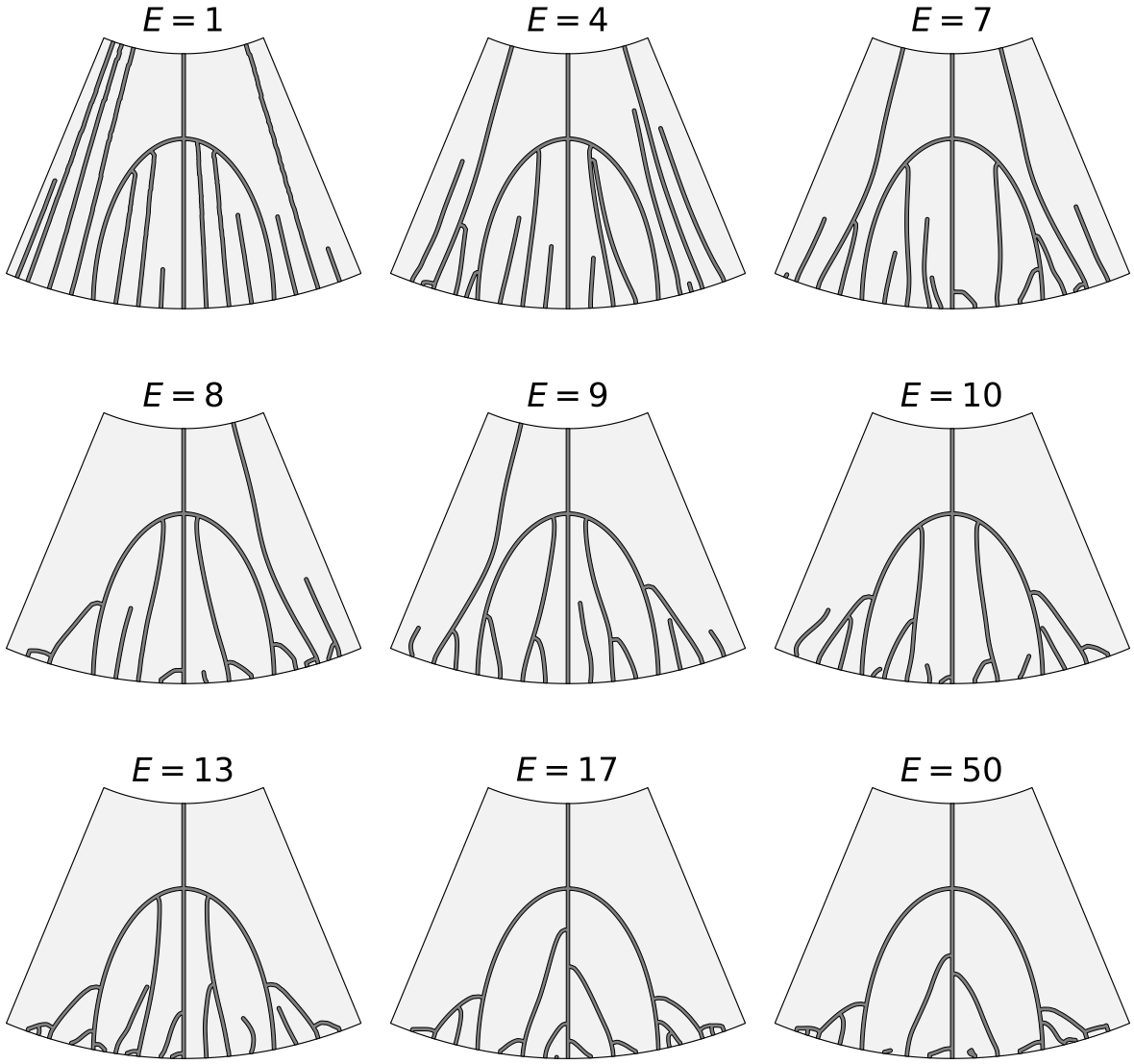

Figure 6.16 **The effect of the Young's modulus ratio on the canal network grown in response to the stress field.**

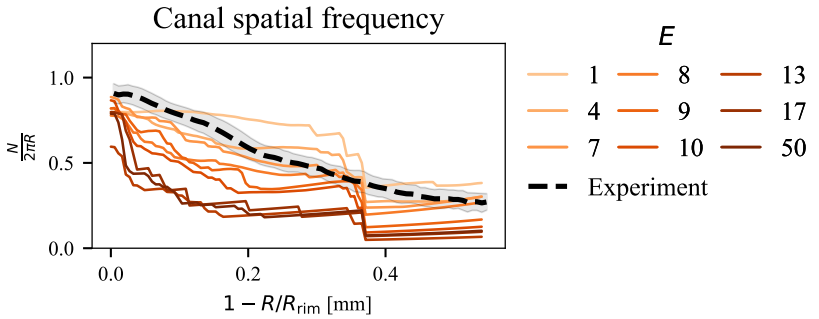

Figure 6.17 **The canal spatial frequency for different Young's modulus ratios.** As with the experimental data, the results were averaged over multiple individuals (simulation runs) and over time points at which the jellyfish size was between 2.5 and 3 cm. The black dashed line corresponds to the experiment.

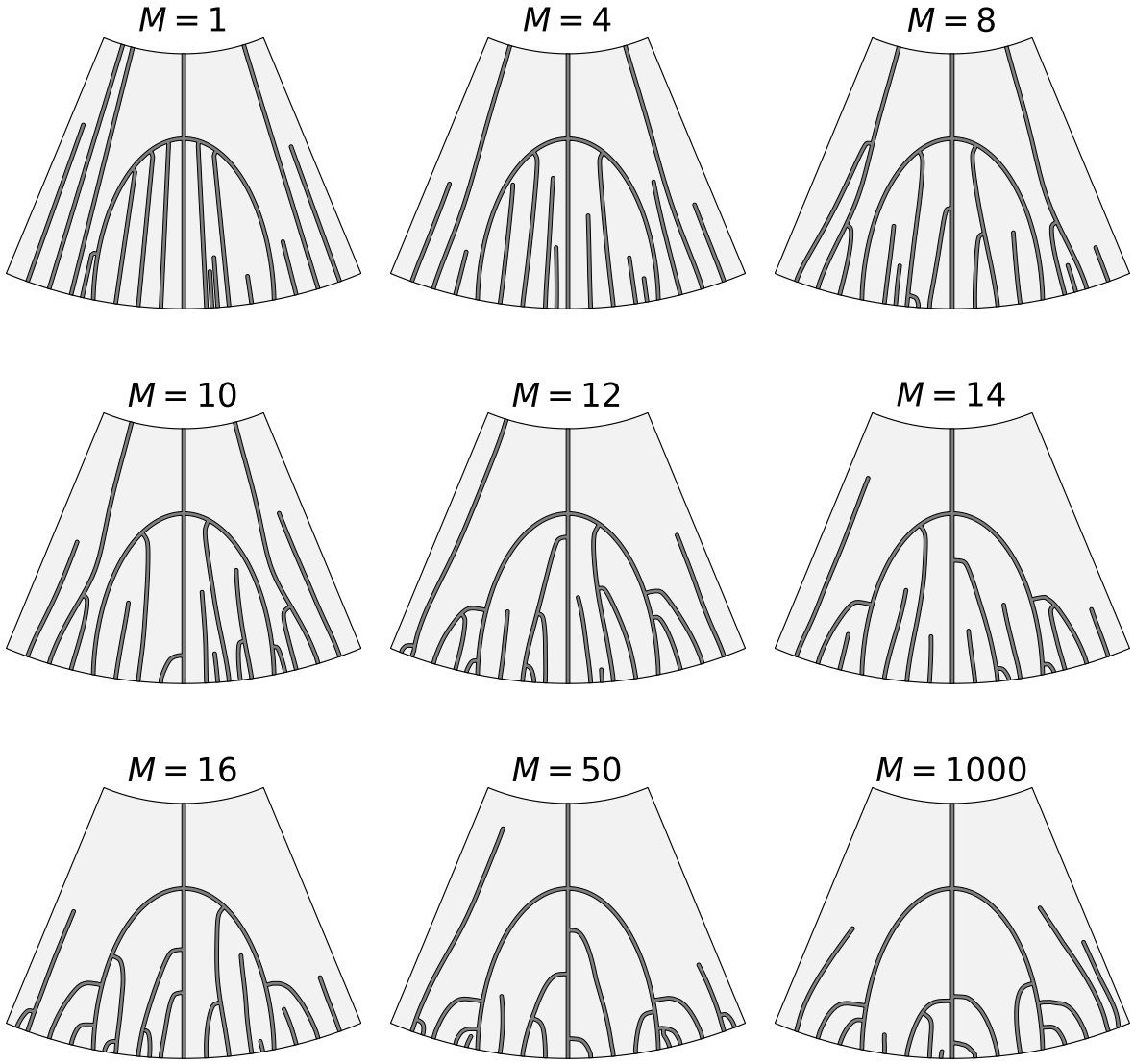

Figure 6.18 The effect of the viscosity ratio on the canal network grown in response to the pressure field.

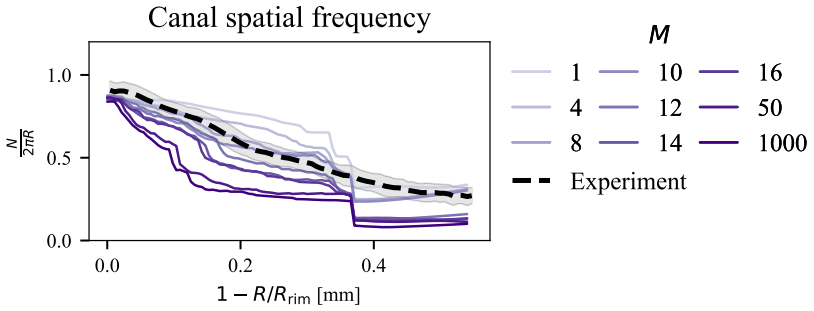

Figure 6.19 The canal spatial frequency for different viscosity ratios. As with the experimental data, the results were averaged over multiple individuals (simulation runs) and over time points at which the jellyfish size was between 2.5 and 3 cm. The black dashed line corresponds to the experiment.

6.3 Summary

In this chapter, we investigated the dynamics of jellyfish canal network formation through *in vivo* and *in silico* methods. We collected jellyfish images over a period of several dozen days, as they grew from ~5 mm to ~5 cm. The jellyfish radius grows linearly at a rate of 0.6 to 2 millimeters per day, depending on the growth conditions, such as food regime, flow rate, and aquarium size. We analyzed images to detect the canals in the network and plotted their azimuthally averaged density and spacing profiles as a function of relative radial position. These profiles do not depend on the growth rate, but slightly shift with the size of the jellyfish. In particular, we demonstrated that the typical canal spacing at the rim increases when the jellyfish grows. Interestingly, the spacing between the canals, adjusted for their changing width, remained nearly constant over time. This may be related to the characteristic reaction-diffusion length in the system – the effective range of nutrient delivery from a canal.

Next, we built a numerical model of the growing jellyfish canal network. We initiated the simulations with the stereotypical geometry of an octant – one-eighth of an annulus between the marginal canal and the stomachs. We imposed linear growth on the jellyfish radius at the mean growth rate measured in the experiments. New sprouts were initiated at the rim with a probability that depended on the separation between neighboring canals, reproducing the typical spacing observed in the experiments. In each timestep of the simulation, we solved the elastic or diffusive problem. The sprouts grew with a velocity proportional to the von Mises stress or pressure gradient value at the tip and in the maximum stress or gradient direction. We ran the simulations for different ratios of mechanical properties (Young's modulus or viscosity) of the endoderm to that of the canals. For low ratio, the canals do not interact and grow straight. For higher ratio, the canals attract each other strongly, leading to reconnections almost instantly after sprouting from the rim. Moderate ratio visually reproduced the patterns observed in *Aurelia* and produced canal spatial frequency profiles closest to the the ones measured from experiments. However, we did not notice preferential reconnections to the youngest neighboring canal.

In the future, the model could be expanded to account for variability in the position of the tri-fork junction. This would help to smooth out the canal spatial frequency profiles in the simulations, making them more consistent with our experimental observations. Another possible model extension could incorporate canal maturation and changes in its stifness or viscosity over time. This would account for the tendency to reconnect to the youngest canal in the neighborhood, as discussed in Chapter 5.

Bibliography

[1] M. Brizzi. Lyrella hennedyi (diatom). https://www.nikonsmallworld.com/galleries/2012-photomicrography-competition/lyrella-hennedyi-diatom, 2012.

[2] K. Libbrecht and R. Wing. *The Snowflake: Winter's Frozen Artistry*. Voyageur Press, Stillwater, 2015.

[3] NASA and ESA. The Crab Nebula (Hubble space telescope image). https://commons.wikimedia.org/wiki/File:Crab_Nebula.jpg, 2005. Public domain image taken by the Hubble Space Telescope.

[4] The root system of a black locust (Robinia pseudoacacia). https://commons.wikimedia.org/wiki/File:Robinia_pseudoacacia_root_system.JPG. Image by Ninjatacoshell. Licensed under Creative Commons Attribution-ShareAlike 3.0 Unported (CC BY-SA 3.0).

[5] Otrow. Photograph of lightning. https://commons.wikimedia.org/wiki/File:Lighting_barrage.jpg, 2020. Licensed under Creative Commons Attribution-ShareAlike 4.0 International (CC BY-SA 4.0).

[6] E. Ben-Jacob. From snowflake formation to growth of bacterial colonies II: Cooperative formation of complex colonial patterns. *Contemporary Physics*, 38(3):205–241, May 1997.

[7] M. A. Wilson. Photograph of manganese oxide dendrites on limestone. https://commons.wikimedia.org/wiki/File:Dendrites01.jpg, 2008. Released into the public domain by the author (PD).

[8] L. Wright and B. Thom. Coastal depositional landforms: a morphodynamic approach. *Progress in Physical Geography: Earth and Environment*, 1(3):412–459, October 1977.

[9] J. P. M. Syvitski, R. L. Slingerland, P. Burgess, E. Meiburg, A. B. Murray, P. L. Wiberg, G. E. Tucker, and A. Voinov. *Morphodynamic models: An overview*, volume 1. CRC Press, London, 1 edition, 2009.

[10] M. C. Cross and P. C. Hohenberg. Pattern formation outside of equilibrium. *Reviews of Modern Physics*, 65(3):851–1112, July 1993.

[11] P. S. Stevens. *Patterns in Nature*. Little, Brown and Company, 1st edition, 1974.

[12] J. P. Gollub and J. S. Langer. Pattern formation in nonequilibrium physics. *Reviews of Modern Physics*, 71(2):S396, 1999.

[13] D. W. Thompson. *On growth and form*. Cambridge University Press, 1917.

[14] P. Meakin. *Fractals, scaling and growth far from equilibrium*, volume 5. Cambridge University Press, 1998.

[15] P. Ball. *Flow: Nature's patterns: a tapestry in three parts*. OUP Oxford, 2009.

[16] P. Ball. *Shapes: Nature's patterns: a tapestry in three parts*. OUP Oxford, 2009.

[17] P. Ball. *Branches: Nature's patterns: a tapestry in three parts*. OUP Oxford, 2009.

[18] A. M. Turing. The chemical basis of morphogenesis. *Philosophical Transactions of the Royal Society of London. Series B, Biological Sciences*, 237(641):37–72, August 1952.

[19] P. Bourgine and A. Lesne. *Morphogenesis: origins of patterns and shapes*. Springer Science & Business Media, 2010.

[20] J. Davies. *Mechanisms of morphogenesis*. Academic Press, 2013.

[21] M. Leeder. On the interactions between turbulent flow, sediment transport and bedform mechanics in channelized flow. In J. Collinson and J. Lewin, editors, *Modern and Ancient Fluvial Systems*, volume 6, pages 5–18. The International Association of Sedimentologists, 1983.

[22] M. M. Perillo, J. L. Best, and M. H. Garcia. A new phase diagram for combined-flow bedforms. *Journal of Sedimentary Research*, 84(4):301–313, April 2014.

[23] P. Ortoleva, J. Chadam, E. Merino, and A. Sen. Geochemical self-organization II; the reactive-infiltration instability. *American Journal of Science*, 287(10), December 1987.

[24] G. Lamé and B. P. Clapeyron. Mémoire sur la solidification par refroidissement d'un globe liquide. *Annales de chimie et de physique*, 47:250–256, 1831.

[25] J. Stefan. {\"{U}}ber die Theorie der Eisbildung, insbesondere über die Eisbildung im Polarmeere. *Sitzungsberichte der Kaiserlichen Akademie der Wissenschaften. Mathematisch-Naturwissenschaftliche Classe*, 98(2):965–983, 1889.

[26] J. Stefan. {\"{U}}ber die Theorie der Eisbildung, insbesondere über die Eisbildung im Polarmeere. *Annalen der Physik und Chemie*, 42(2):269–286, 1891.

[27] Rayleigh. Investigation of the character of the equilibrium of an incompressible heavy fluid of variable density. *Proceedings of the London Mathematical Society*, s1-14(1):170–177, April 1883.

[28] G. I. Taylor. The instability of liquid surfaces when accelerated in a direction perpendicular to their planes. I. *Proceedings of the Royal Society of London. A. Mathematical and Physical Sciences*, 201(1065):192–196, March 1950.

[29] H. S. Hele-Shaw. The flow of water. *Nature*, 58(1489):34–36, 1898.

[30] G. G. Stokes. Mathematical proof of the identity of the stream lines obtained by means of a viscous film with those of a perfect fluid moving in two dimensions. *Report of the British Association*, 143, 1898.

[31] H. Darcy. *Les fontaines publiques de la ville de Dijon*, volume 2. Victor Dalmont, 1856.

[32] M. Muskat. The flow of fluids through porous media. *Journal of Applied Physics*, 8(4):274–282, 1937.

[33] S. Hill. Channeling in packed columns. *Chemical Engineering Science*, 1(6):247–253, 1952.

[34] S. Li and H. Li. Hydrodynamic simulation of the Rayleigh–Taylor instability. https://commons.wikimedia.org/wiki/File:HD-Rayleigh-Taylor.gif, 2006. Provided by Los Alamos National Laboratory under contract with the U.S. Department of Energy; free for use with proper attribution. See source page for licensing details.

[35] P. G. Saffman and G. I. Taylor. The penetration of a fluid into a porous medium or Hele-Shaw cell containing a more viscous liquid. *Proceedings of the Royal Society A*, 245(1242):312–329, 1958.

[36] W. Losert, B. Q. Shi, and H. Z. Cummins. Evolution of dendritic patterns during alloy solidification: Onset of the initial instability. *Proceedings of the National Academy of Sciences*, 95(2):431–438, January 1998.

[37] R. P. Sharma. *Self organization of flow in dissolving rocks*. PhD thesis, University of Warsaw, 2025.

[38] M. P. Cooper, R. P. Sharma, S. Magni, T. P. Blach, A. P. Radlinski, K. Drabik, A. Tengattini, and P. Szymczak. 4D tomography reveals a complex relationship between wormhole advancement and permeability variation in dissolving rocks. *Advances in Water Resources*, 175:104407, May 2023.

[39] W. W. Mullins and R. F. Sekerka. Morphological stability of a particle growing by diffusion or heat flow. *Journal of Applied Physics*, 34(2):323–329, 1963.

[40] W. W. Mullins and R. F. Sekerka. Stability of a planar interface during solidification of a dilute binary alloy. *Journal of Applied Physics*, 35(2):444–451, 1964.

[41] G. Rowan. Theory of acid treatment of limestone formations. *Journal of the Institute of Petroleum*, 45(431):321, 1959.

[42] P. J. Ortoleva. *Geochemical self-organization*. Oxford University Press, 1994.

[43] J. Chadam, D. Hoff, E. Merino, P. Ortoleva, and A. Sen. Reactive infiltration instabilities. *IMA Journal of Applied Mathematics*, 36(3):207–221, January 1986.

[44] G. Daccord and R. Lenormand. Fractal patterns from chemical dissolution. *Nature*, 325(6099):41–43, January 1987.

[45] P. Szymczak and A. J. C. Ladd. The initial stages of cave formation: Beyond the one-dimensional paradigm. *Earth and Planetary Science Letters*, 301:424–432, 2011.

[46] M. Lipar, P. Szymczak, S. Q. White, and J. A. Webb. Solution pipes and focused vertical water flow: Geomorphology and modelling. *Earth-Science Reviews*, 218:103635, July 2021.

[47] A. Gierer and H. Meinhardt. A theory of biological pattern formation. *Kybernetik*, 12(1):30–39, December 1972.

[48] H. Johnston. *Marvels of the universe: a popular work on the marvels of the heavens, the earth, plant life, animal life, the mighty deep*. Hutchinson & Co. (Publishers) Ltd., London, 1913.

[49] Photograph of woodruff. https://pixabay.com/photos/waldmeister-leaf-stalk-green-54164/. Image by Hans from Pixabay. See source page for licensing details.

[50] J. D. Murray. How the leopard gets its spots. *Scientific American*, 258(3):80–87, March 1988.

[51] C. Chap. Elaborate skin pattern of Giant Freshwater Puffer fish, Tetraodon mbu. Aquarium of Kew Gardens, London. https://commons.wikimedia.org/wiki/File:Giant_Puffer_fish_skin_pattern.JPG, February 2012. Licensed under Creative Commons Attribution-Share Alike 3.0 Unported (CC BY-SA 3.0).

[52] P. Gray and S. K. Scott. Sustained oscillations and other exotic patterns of behavior in isothermal reactions. *The Journal of Physical Chemistry*, 89(1):22–32, January 1985.

[53] N. Goldenfeld, P. Y. Chan, and J. Veysey. Dynamics of precipitation pattern formation at geothermal hot springs. *Physical Review Letters*, 96(25):254501, 2006.

[54] P. Szymczak. Shape of dissolution finger. Technical report, University of Warsaw, 2022.

[55] M. B. Short, J. C. Baygents, J. W. Beck, D. A. Stone, R. S. Toomey III, and R. E. Goldstein. Stalactite growth as a free-boundary problem: a geometric law and its platonic ideal. *Physical Review Letters*, 94(1):018501, 2005.

[56] M. B. Short, J. C. Baygents, and R. E. Goldstein. A free-boundary theory for the shape of the ideal dripping icicle. *Physics of Fluids*, 18(8), 2006.

[57] G. Ivantsov. The temperature field around a spherical, cylindrical, or pointed crystal growing in a cooling solution. *Dokl. Akad. Nauk SSSR*, 58:567–569, 1947.

[58] Y. B. Zeldovich, A. G. Istrtov, N. I. Kidin, and V. B. Librovich. Flame propagation in tubes: Hydrodynamics and stability. *Journal of Crystal Growth*, 24:1–13, 1980.

[59] P. Pelcé and A. Pumir. Cell shape in directional solidification in the small Péclet number limit. *Journal of Crystal Growth*, 73(2):337–342, 1985.

[60] J. Mac Huang and N. J. Moore. Morphological attractors in natural convective dissolution. *Physical Review Letters*, 128(2):024501, January 2022.

[61] A. S.-H. Chen and S. W. Morris. Experiments on the morphology of icicles. *Physical Review E*, 83(2):026307, 2011.

[62] G. H. Meyer. Test solutions for a one phase problem through conformal transformations. In J. Albrecht, L. Collatz, and K.-H. Hoffmann, editors, *Numerical treatment of free boundary value problems*, pages 202–210. Birkhäuser, Basel, 1982.

[63] B. Shraiman and D. Bensimon. Singularities in nonlocal interface dynamics. *Physical Review A*, 1984.

[64] P. Szymczak and A. J. C. Ladd. Reactive-infiltration instabilities in rocks. Fracture dissolution. *Journal of Fluid Mechanics*, 702:239–264, July 2012.

[65] R. Clément, S. Douady, and B. Mauroy. Branching geometry induced by lung self-regulated growth. *Physical Biology*, 9(6):066006, November 2012.

[66] S. R. Lubkin and J. D. Murray. A mechanism for early branching in lung morphogenesis. *Journal of Mathematical Biology*, 34(1):77–94, January 1995.

[67] B. Sapoval, M. Filoche, and E. R. Weibel. Smaller is better—but not too small: A physical scale for the design of the mammalian pulmonary acinus. *Proceedings of the National Academy of Sciences*, 99(16):10411–10416, August 2002.

[68] M. Matsushita and H. Fujikawa. Diffusion-limited growth in bacterial colony formation. *Physica A*, 168(1):498–506, 1990.

[69] Y. Cabeza, J. J. Hidalgo, and J. Carrera. Competition is the underlying mechanism controlling viscous fingering and wormhole growth. *Geophysical Research Letters*, 47(3), 2020.

[70] R. M. Brady and R. C. Ball. Fractal growth of copper electrodeposits. *Nature*, 309(5965):225–229, 1984.

[71] A. Kuhn and F. Argoul. Spatiotemporal morphological transitions in thin-layer electrodeposition: The Hecker effect. *Physical Review E*, 49(5):4298, 1994.

[72] L. Niemeyer, L. Pietronero, and H. J. Wiesmann. Fractal dimension of dielectric breakdown. *Physical Review Letters*, 52(12):1033, 1984.

[73] A. Luque and U. Ebert. Growing discharge trees with self-consistent charge transport: the collective dynamics of streamers. *New Journal of Physics*, 16(1):013039, 2014.

[74] O. Zik and E. Moses. Fingering instability in combustion: an extended view. *Physical Review E*, 60(1):518, 1999.

[75] O. Devauchelle, A. P. Petroff, H. J. Seybold, and D. H. Rothman. Ramification of stream networks. *Proceedings of the National Academy of Sciences*, 109(51):20832–6, December 2012.

[76] W.-T. Ke, J. B. Shaw, R. C. Mahon, and C. A. Cathcart. Distributary channel networks as moving boundaries: causes and morphodynamic effects. *Journal of Geophysical Research*, 124(7):1878–1898, 2019.

[77] S. Żukowski, P. Morawiecki, H. J. Seybold, and P. Szymczak. Through history to growth dynamics: deciphering the evolution of spatial networks. *Scientific Reports*, 12(1):20407, November 2022.

[78] T. H. Johansen, M. Baziljevich, D. V. Shantsev, P. E. Goa, W. N. Kang, H. J. Kim, E. M. Choi, M.-S. Kim, and S. I. Lee. Dendritic magnetic instability in superconducting MgB2 films. *Europhysics Letters*, 59(4):599, 2002.

[79] T. Sachs. The control of the patterned differentiation of vascular tissues. *Advances in Botanical Research*, 9:151–262, 1981.

[80] V. Fleury and L. Schwartz. Diffusion limited aggregation from shear stress as a simple model of vasculogenesis. *Fractals*, November 2011.

[81] M. Schneider, J. Reichold, B. Weber, G. Székely, and S. Hirsch. Tissue metabolism driven arterial tree generation. *Medical Image Analysis*, 16(7):1397–1414, 2012.

[82] J. T. Daub and R. M. H. Merks. A cell-based model of extracellular-matrix-guided endothelial cell migration during angiogenesis. *Bulletin of Mathematical Biology*, 75(8):1377–1399, 2013.

[83] D. J. Watts and S. H. Strogatz. Collective dynamics of 'small-world' networks. *Nature*, 393(6684):440–442, June 1998.

[84] A.-L. Barabási and R. Albert. Emergence of Scaling in Random Networks. *Science*, 286(5439):509–512, October 1999.

[85] F. Kaiser, H. Ronellenfitsch, and D. Witthaut. Discontinuous transition to loop formation in optimal supply networks. *Nature Communications*, 11(1):5796, November 2020.

[86] W. Risau. Mechanisms of angiogenesis. *Nature*, 386(6626):671–674, April 1997.

[87] A. Budek and P. Szymczak. Network models of dissolution of porous media. *Physical Review E*, 86(5):056318, November 2012.

[88] A. Konkol, J. Schwenk, E. Katifori, and J. B. Shaw. Interplay of river and tidal forcings promotes loops in coastal channel networks. *Geophysical Research Letters*, 49(10):e2022GL098284, 2022.

[89] A. Tero, S. Takagi, T. Saigusa, K. Ito, D. P. Bebber, M. D. Fricker, K. Yumiki, R. Kobayashi, and T. Nakagaki. Rules for biologically inspired adaptive network design. *Science*, 327(5964):439–442, January 2010.

[90] J. R. Banavar, F. Colaiori, A. Flammini, A. Maritan, and A. Rinaldo. Topology of the fittest transportation network. *Physical Review Letters*, 84(20):4745–4748, May 2000.

[91] S. Bohn and M. O. Magnasco. Structure, Scaling, and Phase Transition in the Optimal Transport Network. *Physical Review Letters*, 98(8):088702, February 2007.

[92] M. Durand. Structure of optimal transport networks subject to a global constraint. *Physical Review Letters*, 98(8):088701, February 2007.

[93] E. Katifori, G. J. Szöllősi, and M. O. Magnasco. Damage and fluctuations induce loops in optimal transport networks. *Physical Review Letters*, 104(4):048704, 2010.

[94] H. Ronellenfitsch and E. Katifori. Global optimization, local adaptation, and the role of growth in distribution networks. *Physical Review Letters*, 117(13):138301, 2016.

[95] M. Bramson and L. Gray. The survival of branching annihilating random walk. *Zeitschrift für Wahrscheinlichkeitstheorie und Verwandte Gebiete*, 68(4):447–460, December 1985.

[96] E. Hannezo, C. L. G. J. Scheele, M. Moad, N. Drogo, R. Heer, R. V. Sampogna, J. van Rheenen, and B. D. Simons. A unifying theory of branching morphogenesis. *Cell*, 171(1):242–255.e27, September 2017.

[97] M. C. Uçar, D. Kamenev, K. Sunadome, D. Fachet, F. Lallemend, I. Adameyko, S. Hadjab, and E. Hannezo. Theory of branching morphogenesis by local interactions and global guidance. *Nature Communications*, 12(1):6830, November 2021.

[98] S. V. Paramore, K. Goodwin, and C. M. Nelson. How to build an epithelial tree. *Physical Biology*, 19(6):061002, November 2022.

[99] H. Memelli, B. Torben-Nielsen, and J. Kozloski. Self-referential forces are sufficient to explain different dendritic morphologies. *Frontiers in Neuroinformatics*, 7, 2013.

[100] A. P. Petroff, O. Devauchelle, H. J. Seybold, and D. H. Rothman. Bifurcation dynamics of natural drainage networks. *Philosophical Transactions of the Royal Society A*, 371(2004):20120365, 2013.

[101] Y. Cohen, O. Devauchelle, H. J. Seybold, R. S. Yi, P. Szymczak, and D. H. Rothman. Path selection in the growth of rivers. *Proceedings of the National Academy of Sciences*, 112(46):14132–14137, 2015.

[102] R. S. Yi, Y. Cohen, O. Devauchelle, G. Gibbins, H. J. Seybold, and D. H. Rothman. Symmetric rearrangement of groundwater-fed streams. *Proceedings of the Royal Society A*, 473(2207):20170539, 2017.

[103] O. Devauchelle, P. Szymczak, M. Pecelerowicz, Y. Cohen, H. J. Seybold, and D. H. Rothman. Laplacian networks: Growth, local symmetry, and shape optimization. *Physical Review E*, 95(3):033113, 2017.

[104] M. Pecelerowicz and P. Szymczak. Stabilizing effect of tip splitting on the interface motion. *Physical Review E*, 94(6):062801, 2016.

[105] J. A. Kaandorp and J. E. Kübler. Chapter 4.4: A Laplacian model of branching network. In *The algorithmic beauty of seaweeds, sponges and corals*. Springer Science & Business Media, 2001.

[106] L. Mander and H. T. P. Williams. The robustness of some Carboniferous fossil leaf venation networks to simulated damage. *Royal Society Open Science*, 11(5):240086, May 2024.

[107] C. K. Boyce and A. H. Knoll. Evolution of developmental potential and the multiple independent origins of leaves in Paleozoic vascular plants. *Paleobiology*, pages 70–100, 2002.

[108] C. K. Boyce. The evolutionary history of roots and leaves. In N. M. Holbrook and M. A. Zwieniecki, editors, *Vascular transport in plants*, Physiological ecology, pages 479–499. Academic Press, Burlington, 2005.

[109] S. Douady, C. Lagesse, M. Atashinbar, P. Bonnin, R. Pousse, and P. Valcke. A work on reticulated patterns. *Comptes Rendus. Mécanique*, 348(6-7):659–678, 2020.

[110] Y. Couder, L. Pauchard, C. Allain, M. Adda-Bedia, and S. Douady. The leaf venation as formed in a tensorial field. *The European Physical Journal B*, 28(2):135–138, 2002.

[111] S. Bohn, L. Pauchard, and Y. Couder. Hierarchical crack pattern as formed by successive domain divisions. *Physical Review E*, 71(4):046214, April 2005.

[112] M. B. Hastings and L. S. Levitov. Laplacian growth as one-dimensional turbulence. *Physica D*, 116(1-2):244–252, 1998.

[113] R. V. Gol'dstein and R. L. Salganik. Brittle fracture of solids with arbitrary cracks. *International Journal of Fracture*, 10(4):507–523, December 1974.

[114] Y. Cohen and I. Procaccia. Dynamics of cracks in torn thin sheets. *Physical Review E*, 81(6 Pt 2):066103, June 2010.

[115] M. A. Peterson. Nonuniqueness in singular viscous fingering. *Physical Review Letters*, 62(3):284, 1989.

[116] V. Fleury, J.-F. Gouyet, and M. Leonetti. *Branching in nature: dynamics and morphogenesis of branching structures, from cell to river networks*, volume 14. Springer Science & Business Media, 2001.

[117] W. H. Preece. On the space protected by a lightning-conductor. *The London, Edinburgh, and Dublin Philosophical Magazine and Journal of Science*, 10(64):427–430, December 1880.

[118] M. B. Hastings. Growth exponents with 3.99 walkers. *Physical Review E*, 64(4):046104, 2001.

[119] L. Carleson and N. Makarov. Laplacian path models. *Journal d'Analyse Mathématique*, 87(1):103–150, 2002.

[120] T. Gubiec and P. Szymczak. Fingered growth in channel geometry: A Loewner-equation approach. *Physical Review E*, 77(4):041602, 2008.

[121] M. Pecelerowicz, A. Budek, and P. Szymczak. Competition between anisotropic viscous fingers. *The European Physical Journal Special Topics*, 223(9):1895–1906, September 2014.

[122] Y. Huang, G. Ouillon, H. Saleur, and D. Sornette. Spontaneous generation of discrete scale invariance in growth models. *Physical Review E*, 55(6):6433–6447, June 1997.

[123] A. Budek, K. Kwiatkowski, and P. Szymczak. Effect of mobility ratio on interaction between the fingers in unstable growth processes. *Physical Review E*, 96(4):042218, 2017.

[124] M. A. Peterson. Singular Laplacian growth. *Physical Review E*, 57(3):3221–3226, March 1998.

[125] M. Pecelerowicz, A. Budek, and P. Szymczak. Effective description of the interaction between anisotropic viscous fingers. *Europhysics Letters*, 108(1):14001, 2014.

[126] R. McDonald. Geodesic Loewner paths with varying boundary conditions. *Proceedings of the Royal Society A*, 476(2242):20200466, 2020.

[127] Y. Cohen and D. H. Rothman. Path selection in a Poisson field. *Journal of Statistical Physics*, 167(3):703–712, 2017.

[128] N. R. McDonald. Finger growth and selection in a Poisson field. *Journal of Statistical Physics*, 178(3):763–774, 2020.

[129] B. Derrida and V. Hakim. Needle models of Laplacian growth. *Physical Review A*, 45(12):8759, 1992.

[130] J. W. Brown and R. V. Churchill. *Complex variables and applications*. McGraw-Hill, 2009.

[131] F. Hecht. New development in FreeFem++. *Journal of Numerical Mathematics*, 20(3-4):251–266, 2012.

[132] R. Combescot, T. Dombre, V. Hakim, Y. Pomeau, and A. Pumir. Shape selection of Saffman-Taylor fingers. *Physical Review Letters*, 56(19):2036–2039, May 1986.

[133] F. Osselin, P. Kondratiuk, A. Budek, O. Cybulski, P. Garstecki, and P. Szymczak. Microfluidic observation of the onset of reactive-infitration instability in an analog fracture. *Geophysical Research Letters*, 43(13):6907–6915, 2016.

[134] N. Nakanishi, V. Hartenstein, and D. K. Jacobs. Development of the rhopalial nervous system in Aurelia sp.1 (Cnidaria, Scyphozoa). *Development Genes and Evolution*, 219(6):301–317, June 2009.

[135] T. Katsuki and R. J. Greenspan. Jellyfish nervous systems. *Current Biology*, 23(14):R592–R594, July 2013.

[136] A. P. Hoover, N. W. Xu, B. J. Gemmell, S. P. Colin, J. H. Costello, J. O. Dabiri, and L. A. Miller. Neuromechanical wave resonance in jellyfish swimming. *Proceedings of the National Academy of Sciences*, 118(11):e2020025118, March 2021.

[137] B. J. Gemmell, J. H. Costello, S. P. Colin, C. J. Stewart, J. O. Dabiri, D. Tafti, and S. Priya. Passive energy recapture in jellyfish contributes to propulsive advantage over other metazoans. *Proceedings of the National Academy of Sciences*, 110(44):17904–17909, October 2013.

[138] N. W. Xu and J. O. Dabiri. Low-power microelectronics embedded in live jellyfish enhance propulsion. *Science Advances*, 6(5):eaaz3194, January 2020.

[139] S. R. Anuszczyk and J. O. Dabiri. Electromechanical enhancement of live jellyfish for ocean exploration. *Bioinspiration & Biomimetics*, 19(2):026018, March 2024.

[140] S. Piraino, F. Boero, B. Aeschbach, and V. Schmid. Reversing the life cycle: Medusae transforming into polyps and cell transdifferentiation in Turritopsis nutricula (Cnidaria, Hydrozoa). *The Biological Bulletin*, 190(3):302–312, June 1996.

[141] C. Sinigaglia, S. Peron, J. Eichelbrenner, S. Chevalier, J. Steger, C. Barreau, E. Houliston, and L. Leclère. Pattern regulation in a regenerating jellyfish. *eLife*, 9:e54868, September 2020.

[142] M. J. Abrams, T. Basinger, W. Yuan, C.-L. Guo, and L. Goentoro. Self-repairing symmetry in jellyfish through mechanically driven reorganization. *Proceedings of the National Academy of Sciences*, 112(26):E3365–E3373, June 2015.

[143] R. Monahan-Earley, A. M. Dvorak, and W. C. Aird. Evolutionary origins of the blood vascular system and endothelium. *Journal of Thrombosis and Haemostasis*, 11(s1):46–66, 2013.

[144] D. A. Gold, T. Katsuki, Y. Li, X. Yan, M. Regulski, D. Ibberson, T. Holstein, R. E. Steele, D. K. Jacobs, and R. J. Greenspan. The genome of the jellyfish Aurelia and the evolution of animal complexity. *Nature Ecology & Evolution*, 3(1):96–104, January 2019.

[145] P. Cartwright, S. L. Halgedahl, J. R. Hendricks, R. D. Jarrard, A. C. Marques, A. G. Collins, and B. S. Lieberman. Exceptionally preserved jellyfishes from the middle Cambrian. *PLOS ONE*, 2(10):e1121, October 2007.

[146] F. S. Russell. *The Medusae of the British Isles II: Pelagic Scyphozoa*, volume II of *The Medusae of the British Isles*. Cambridge University Press, 1970.

[147] G. D. Kolbasova, A. O. Zalevsky, A. R. Gafurov, P. O. Gusev, M. A. Ezhova, A. A. Zheludkevich, O. P. Konovalova, K. N. Kosobokova, N. U. Kotlov, N. O. Lanina, A. S. Lapashina, D. O. Medvedev, K. S. Nosikova, E. O. Nuzhdina, G. A. Bazykin,

and T. V. Neretina. A new species of Cyanea jellyfish sympatric to C. capillata in the White Sea. *Polar Biology*, 38(9):1439–1451, September 2015.

[148] W. Zhao, S. Wang, Y. Zhou, M. Wang, L. Yang, J. Liu, L. Wang, and P. Zhu. Viscous fingering instability in one-end-lifted Hele-Shaw cells for producing three-dimensional hierarchical structures. *Journal of Colloid and Interface Science*, 699:138202, December 2025.

[149] M. Avian, L. Mancini, M. Voltolini, D. Bonnet, D. Dreossi, V. Macaluso, N. Pillepich, L. Prieto, A. Ramšak, A. Terlizzi, and G. Motta. A novel endocast technique providing a 3D quantitative analysis of the gastrovascular system in Rhizostoma pulmo: An unexpected through-gut in cnidaria. *PLOS ONE*, 17(8):e0272023, August 2022.

[150] S. Jeammet. *Ruptures Enlacées. Morphogénèse de Réseaux dans l'Argile*. PhD thesis, Université Paris Cité, 2023.

[151] C. Gambini. *La morphogenèse gastrovasulaire de la méduse aurelia aurita*. PhD thesis, Université Sorbonne Paris Cité, 2012.

[152] S. Song. *The evolution and development of vascular systems*. PhD thesis, Université Sorbonne Paris Cité, 2019.

[153] A. J. Southward. Observations on the ciliary currents of the jellyfish Aurelia aurita L. *Journal of the Marine Biological Association of the United Kingdom*, 34(2):201–216, 1955.

[154] A. V. Chernyshev and V. V. Isaeva. Formation of chaotic patterns of the gastrovascular system in the ontogenesis of the medusa Aurelia aurita. *Russian Journal of Marine Biology*, 28(5):347–351, 2002.

[155] S. Song, S. Żukowski, C. Gambini, P. Dantan, B. Mauroy, S. Douady, and A. J. M. Cornelissen. Morphogenesis of the gastrovascular canal network in Aurelia jellyfish: Variability and possible mechanisms. *Frontiers in Physics*, 10:966327, 2023.

[156] N. Ravi, V. Gabeur, Y.-T. Hu, R. Hu, C. Ryali, T. Ma, H. Khedr, R. Rädle, C. Rolland, L. Gustafson, E. Mintun, J. Pan, K. V. Alwala, N. Carion, C.-Y. Wu, R. Girshick, P. Dollár, and C. Feichtenhofer. SAM 2: Segment Anything in images and videos, October 2024.

[157] E. Farge. Mechanical Induction of Twist in the Drosophila Foregut/Stomodeal Primordium. *Current Biology*, 13(16):1365–1377, August 2003.

[158] T. Mammoto and D. E. Ingber. Mechanical control of tissue and organ development. *Development*, 137(9):1407–1420, May 2010.

[159] D. T. Butcher, T. Alliston, and V. M. Weaver. A tense situation: forcing tumour progression. *Nature Reviews Cancer*, 9(2):108–122, February 2009.

[160] G. Forgacs, R. A. Foty, Y. Shafrir, and M. S. Steinberg. Viscoelastic properties of living embryonic tissues: a quantitative study. *Biophysical Journal*, 74(5):2227–2234, May 1998.

[161] D. Bi, J. H. Lopez, J. M. Schwarz, and M. L. Manning. A density-independent rigidity transition in biological tissues. *Nature Physics*, 11(12):1074–1079, December 2015.

[162] J. Ranft, M. Basan, J. Elgeti, J.-F. Joanny, J. Prost, and F. Jülicher. Fluidization of tissues by cell division and apoptosis. *Proceedings of the National Academy of Sciences*, 107(49):20863–20868, December 2010.

[163] G. Serrano Nájera, A. M. Plum, B. Steventon, C. J. Weijer, and M. Serra. Control of tissue flows and embryo geometry in avian gastrulation. *Nature Communications*, 16(1):5174, June 2025.

[164] J. C. Arciero, Q. Mi, M. F. Branca, D. J. Hackam, and D. Swigon. Continuum model of collective cell migration in wound healing and colony expansion. *Biophysical Journal*, 100(3):535–543, February 2011.

[165] A. Ravasio, I. Cheddadi, T. Chen, T. Pereira, H. T. Ong, C. Bertocchi, A. Brugues, A. Jacinto, A. J. Kabla, Y. Toyama, X. Trepat, N. Gov, L. Neves De Almeida, and B. Ladoux. Gap geometry dictates epithelial closure efficiency. *Nature Communications*, 6(1):7683, July 2015.

[166] P. Tracqui. Biophysical models of tumour growth. *Reports on Progress in Physics*, 72(5):056701, April 2009.

[167] M. J. Bogdan and T. Savin. Fingering instabilities in tissue invasion: an active fluid model. *Royal Society Open Science*, 5(12):181579, December 2018.

Podsumowanie pracy po polsku

Kształty naturalne są często postrzegane jako wynik procesu optymalizacji lub jako z góry określone, na przykład przez program genetyczny. Podejście to pomija jednak kwestię mechanizmu ich powstawania. Aby to zrozumieć, musimy zbadać leżącą u ich podstaw dynamikę wzrostu. Badamy związek między kształtami końcowymi a procesami wzrostu, aby rozwiązać problem odwrotny: biorąc pod uwagę kształt, jak możemy określić szczegóły jego procesu wzrostu lub, szerzej, zidentyfikować fundamentalny mechanizm jego powstawania? Odpowiedź na to pytanie jest przydatna w wielu kontekstach, na przykład do rekonstrukcji warunków środowiskowych na podstawie form geologicznych lub do zrozumienia, jak powstrzymać procesy patologiczne w systemach biologicznych.

Koncentrujemy się na formach, które powstają jako niestabilność na ruchomym froncie. Małe wypustki rozwijają się później w palczaste kształty, które oddziałują ze sobą i mogą tworzyć strukturę sieciową. Przykłady obejmują kanały rozpuszczania (ang. solution pipes), sieci rzeczne, a nawet układ kanałów meduz Aurelia.

Najpierw analizujemy systemy, w których mechanizm wzrostu został wcześniej zidentyfikowany lub można go wyprowadzić teoretycznie. Pokazujemy, jak wyodrębnić prawa rządzące wzrostem lub warunkami podczas powstawania struktury, badając jedynie jej ostateczną geometrię. Jest to szczególnie ważne w przypadku form geologicznych, które ewoluują w skalach czasowych wykraczających poza ludzkie możliwości pomiarowe. Pokazujemy, że pojedynczy obraz geometrii wystarcza do rekonstrukcji historycznych wartości natężenia przepływu w powstającym rurociągu lub do zidentyfikowania praw wzrostu sieci rzecznej.

W długim okresie czasu niektóre formy naturalne osiągają kształt niezmienniczy (idealny), niezależny od warunków początkowych i charakteryzowany przez niewielką liczbę parametrów. Daje to unikatowy wgląd w warunki fizyczne, w których powstała struktura. W Rozdziale 2 badamy idealne formy palców powstałych w procesie rozpuszczania. Struktury te tworzą się w wyniku niestabilności reaktywno-infiltracyjnej – dodatniego sprzężenia zwrotnego między przepływem płynu a transportem reagentów, które występuje podczas rozpuszczania ośrodków spękanych lub porowatych. Badamy powstawanie

tych kanałów przypominających palce, wykorzystując komórkę Hele-Shawa z rozpuszczalnym dnem.

Obserwujemy silną rywalizację między palcami w tym systemie. Najdłuższy palec, który stanowi ścieżkę najmniejszego oporu, przechwytuje coraz większą część przepływu kosztem krótszych palców. W konsekwencji krótsze palce zwalniają i rozszerzają się. Co ciekawe, najdłuższy palec nie przyspiesza ani nie zmienia kształtu. Nałożenie migawek najdłuższego palca w trakcie jego ewolucji ujawnia, że od początku kreślił on ten sam kształt. Z czasem zachowująca stały kształt część palca po prostu przesuwa się w kierunku przepływu. Wyłania się coraz dłuższy, niezmienniczy palec.

Aby dokładniej zbadać powstawanie niezmienniczego kształtu, przeprowadziliśmy eksperymenty z pojedynczym palcem w wąskiej komórce mikroprzepływowej. Palce mają regularny kształt, ze stałym nachyleniem ścianek daleko od wierzchołka i parabolicznymi końcami. Są bardziej wydłużone przy wyższych prędkościach przepływu. Wykorzystując połączenie teorii transportu reaktywnego i technik odwzorowania konforemnego, można uzyskać kształt idealnego palca, który odpowiada kształtom obserwowanym w eksperymentach.

Analizę można rozszerzyć na trzy wymiary i wykorzystać do interpretacji form naturalnych, takich jak kanały rozpuszczania – pionowe struktury utworzone przez kwaśne deszcze infiltrujące wapień. Krytycznym parametrem kontrolującym idealny kształt jest liczba Pécleta, $\mathrm{Pe} = Q/Da$, gdzie Q to natężenie przepływu w systemie, D to stała dyfuzji, a a to promień kanału. Mierząc średnicę rury i jej profil boczny, możemy odtworzyć historyczne natężenie przepływu w powstającej rurze. Może to dostarczyć informacji o warunkach środowiskowych, w których się rozwijała.

Nawet jeśli struktura nie osiągnie idealnego kształtu, jej geometria kryje w sobie bogactwo informacji o prawach jej wzrostu i środowisku, w którym powstała. W Rozdziale 3 opisujemy ramy rekonstrukcji tych informacji z pojedynczego obrazu sieci morfodynamicznej. Rozważamy sieci rosnące wyłącznie na czubkach, których gałęzie wydłużają się i bifurkują w odpowiedzi na pole zewnętrzne. Pole i sieć współewoluują w czasie, ponieważ rosnąca sieć zmienia warunki brzegowe pola. Dynamikę sieci definiują prawa wzrostu – zbiór reguł, które łączą procesy rozszerzania i bifurkacji z charakterystyką pola sterującego, takiego jak jego gradient w pobliżu wierzchołka. Znając prawa wzrostu, możemy przewidzieć kształt sieci zarówno w przyszłości, jak i w przeszłości.

Aby rozszyfrować prawa wzrostu, opracowaliśmy algorytm wstecznej ewolucji. Najpierw parametryzuje się prawa wzrostu i wybiera początkowy zestaw parametrów. Wykorzystując te specyficzne reguły, sieć jest ewoluowana wstecz w czasie o mały krok dt, a następnie ewoluowana w przód w tym samym kroku czasowym. Jeśli wybrane prawo

wzrostu jest niepoprawne, odwracalność problemu w czasie zostaje zerwana i nie powracamy do stanu początkowego. I odwrotnie, z poprawnym prawem wzrostu replikujemy początkową geometrię po sekwencji kroku wstecz i w przód.

Następnie pomijamy krok naprzód, a procedura jest powtarzana, cofając ewolucję sieci aż do jej stanu początkowego. Mierząc odchylenia od stanu pierwotnego i inne wskaźniki po każdym kroku wstecz, takie jak symetria pola wokół każdego wierzchołka, możemy oszacować dopasowanie wybranej reguły wzrostu. Powtarzamy tę samą procedurę dla różnych zestawów parametrów i wybieramy optymalny.

Walidujemy to podejście, wykorzystując dane syntetyczne z symulacji sieci rozwijających się w polu dyfuzyjnym. Z powodzeniem określamy reguły wzrostu gałęzi oraz warunki, w których następuje ich rozgałęzienie. Następnie stosujemy to podejście do analizy wzrostu rzeczywistej sieci rzecznej w Vermont w USA. Nasze wyniki pokazują, że formujące się dopływy tej sieci silnie konkurowały o przepływ wód gruntowych. Argumentujemy również, że rozgałęzienia były wywoływane zwiększeniem prędkości wzrostu czubków rzek. To narzędzie otwiera nowe perspektywy dla analizy sieci przestrzennych w przyrodzie. Kompleksowa analiza sieci rzecznych na Ziemi mogłaby skorelować prawa wzrostu z lokalnymi warunkami klimatycznymi, takimi jak intensywność opadów. Mogłoby to posłużyć do rekonstrukcji dawnych warunków na innych planetach z reliktowymi sieciami rzecznymi. Podobna analiza oparta wyłącznie na kątach bifurkacji przyniosła obiecujące wyniki dotyczące niegdyś panującego klimatu na Marsie.

Następnie badamy pętle w sieciach fizycznych. Wykazano, że sieci pętlowe są bardziej odporne na uszkodzenia i podlegają selekcji w ewolucji biologicznej. Jednak niewiele wiadomo na temat ich rozwoju, szczególnie w procesie zwanym wzrostem wzrostem na czubku, w którym sieci wydłużają się się na końcach gałęzi w odpowiedzi na gradient pola zewnętrznego. Klasyczne modele tego procesu wyjaśniają konkurencję, ekranowanie i odpychanie między gałęziami i prowadzą do powstania sieci drzewiastych (bez pętli), takich jak te przedstawione w Rozdziale 3. Pozostaje pytanie: w jaki sposób gałęzie przyciągają się i łączą ponownie, tworząc pętle?

W Rozdziale 4 identyfikujemy nagłe formowanie się pętli w pobliżu zjawiska przebicia (ang. breakthrough). Gdy najdłuższy palec dociera do granicy układu, krótsze palce reaktywują się i są do niego przyciągane. Połączenia (rekoneksje) związane z przebiciem pojawiają się w niezwykle zróżnicowanych procesach, w tym wyładowaniach elektrycznych, kanałach w jaskiniach krasowych, rozpuszczaniu i lepkich palcach w komórce Hele-Shawa, czy kanałach w układzie trawiennym meduzy Aurelia. Wzrost tych struktur jest regulowany przez strumienie dyfuzyjne. Ważnym parametrem jest tutaj stosunek ruchliwości M – stosunek ruchliwości wewnątrz rosnących palców do ruchliwości na zewnątrz.

Poprzednie badania wykazały, że skończony stosunek ruchliwości osłabia ekranowanie i efektywne odpychanie w układzie. Może to prowadzić do formowania się pętli w określonych zakresach stosunków ruchliwości i długości palców. Jednak rekoneksje przebicia nie ograniczają się do tych konkretnych scenariuszy. W pobliżu przebicia gałęzie łączą się ponownie nawet przy wysokim stosunku ruchliwości, co wcześniej uważano za niemożliwe ze względu na efekty ekranowania.

Aby przedstawić fizyczne wyjaśnienie rekoneksji związanych z przebiciem, najpierw rozważamy jednowymiarowy model palcowania laplasowskiego. Zauważamy, że pole w obrębie krótkiego palca, znajdującego się z dala od ujścia układu, jest niemal stałe. Sugeruje to, że traktowanie palców jako izolinii pola (izopotencjałów), jak w Rozdziale 3, jest w tym przypadku uzasadnione. Jednakże pole maleje wzdłuż dłuższych palców bliżej ujścia. Przejście od palców izopotencjalnych do palców wykazujących gradient pola występuje w odległości od ujścia, która jest odwrotnie proporcjonalna do stosunku ruchliwości. Gdyby umieścić krótki i długi palec obok siebie, między wierzchołkiem krótkiego palca a długim palcem powstałaby różnica potencjałów. W konsekwencji, krótki palec byłby przyciągany przez dłuższy.

W modelu jednowymiarowym każdy palec jest traktowany niezależnie. W rzeczywistości jednak palce oddziałują na siebie; dłuższy palec osłania krótszy. Aby zbadać ten efekt, przeprowadziliśmy symulacje numeryczne układu dwuwymiarowego. Przy niskim stosunku ruchliwości krótszy palec jest słabo ekranowany i otrzymuje pewien strumień, nawet gdy dłuższy palec znajduje się daleko od ujścia. Im wyższy stosunek ruchliwości, tym silniejszy efekt ekranowania. W tym przypadku, gdy odstęp (odległość od najdłuższego palca do ujścia) jest duży, całkowity strumień w krótszym palcu jest bliski zeru. Wraz ze zmniejszaniem się odstępu, pole w najdłuższym palcu zaczyna spadać, a krótszy palec otrzymuje większy strumień.

Krótszy palec nie tylko reaktywuje się i zaczyna ponownie rosnąć, ale jego kierunek wzrostu również zmienia się w pobliżu punktu przebicia. Gdy odstęp jest duży, większy strumień pochodzi z zewnątrz, a krótszy palec odchyla się od dłuższego. W przypadku mniejszego odstępu, większy strumień pochodzi z dłuższego palca. Powoduje to skuteczne przyciąganie w kierunku dłuższego palca.

Na koniec adaptujemy model z rozdziału 2, uwzględniając skończony stosunek ruchliwości. Zamiast cienkich palców traktowanych jako izolinie pola, rozważamy palce o skończonej szerokości, wzdłuż których pole maleje. Przeprowadzamy symulacje ewolucji palców w czasie, aby pokazać, jak reaktywacja i przyciąganie do najdłuższego palca prowadzi do powstania dynamicznej pętli. Dla dwóch palców o nieznacznie różniących się długościach początkowych obserwujemy wszystkie opisane wcześniej interakcje między

nimi: rywalizację i odpychanie, osłanianie, reaktywację i przyciąganie.

Następnie przeprowadzamy eksperymenty w komórce Hele-Shawa: rozpuszczanie pęknięcia (jak opisano w Rozdziale 2) przy niskim stosunku ruchliwości i palcowanie lepkie przy wysokim stosunku ruchliwości. Porównujemy symulacje z eksperymentami i stwierdzamy, że dynamika krótszego palca została wiernie odwzorowana. Zarówno w eksperymentach, jak i symulacjach obserwujemy, że przy niskim stosunku ruchliwości krótszy palec nie jest ekranowany i od początku jest przyciągany do dłuższego. I odwrotnie, przy wysokim stosunku ruchliwości, krótszy palec jest początkowo ekranowany. Następnie reaktywuje się i nagle ponownie łączy się z dłuższym palcem. Nasze wyniki pokazują, że ponowne połączenie jest powszechnym zjawiskiem w systemach napędzanych strumieniami dyfuzyjnymi. Występuje zarówno wtedy, gdy ruchomość wewnątrz rosnącej struktury jest podobna do ruchomości na zewnątrz, jak i w pobliżu momentu przebicia.

W ostatniej części pracy skupiamy się na konkretnej biologicznej sieci pętli: systemie kanałów gastro-waskularnych meduzy Aurelia. Meduza ta jest cennym modelem do badania rozwoju biologicznych sieci transportowych ze względu na swoje położenie na drzewie filogenetycznym, prostą anatomię i łatwość obrazowania in vivo. Układ gastro-waskularny ma cztery żołądki w centrum meduzy. Pod koniec stadium efyry szesnaście prostych kanałów rozciąga się od środka meduzy do kanału obręczowego. Osiem kanałów adradialnych graniczy z ośmioma odcinkami, zwanymi oktantami, z prostym kanałem inter- lub perradialnym pośrodku każdego z nich. Zazwyczaj dwa krótsze kanały łączą się z kanałem środkowym, tworząc rozwidlenie przypominające trójząb. W miarę wzrostu meduzy z kanału obręczowego wyrastają nowe kanały, które rosną w kierunku środka. Niektóre kanały łączą się ponownie z innymi kanałami, podczas gdy inne biegną bezpośrednio do żołądków.

W Rozdziale 5 opisujemy strukturę sieci kanałów i jej zmienność. Koncentrujemy się na stadium od osobnika młodocianego do dorosłego meduzy. Idealną konstrukcję geometryczną wzoru kanału można opisać następująco: w każdym oktancie struktura rozwidlona dzieliłaby kanał brzeżny na cztery równe segmenty. Nowy kanał pojawiałby się w środku każdego segmentu. Te młode kanały rosłyby i łączyły się z najmłodszym kanałem w sąsiedztwie (z poprzedniej generacji), a zatem z kanałami bocznymi struktury rozwidlonej. Teraz kanał brzeżny miałby osiem segmentów, w których pojawiałaby się kolejna generacja kanałów. Te wypustki ponownie rosłyby i łączyłyby się z lewej lub prawej strony z najmłodszym kanałem w sąsiedztwie. Prowadziłoby to do charakterystycznego fraktalnego kształtu drzewa sieci kanałów.

Gdyby struktura kanału była z góry określona, konstrukcja geometryczna byłaby precyzyjnie zachowana, a kanały zawsze łączyłyby się z ostatnim, poprzednim pokoleniem. Określamy ilościowo odstępstwo od tej reguły i zliczamy liczbę „fałszywych” połączeń u

meduz wyhodowanych w naszym laboratorium. Chociaż kanały preferencyjnie łączą się z najmłodszym kanałem w okolicy, nie jest to ścisła reguła. Analiza wzorów kanałów meduz hodowanych w różnych warunkach dodatkowo ilustruje dużą zmienność systemu. Można to interpretować jako ślad niestabilności wynikający z zakłóceń stochastycznych, sugerujący, że wzór pojawia się w sposób samoorganizujący się.

Odnosimy ten samoorganizujący się proces do mechaniki meduz. Skurcze meduzy podczas pływania wywołują znaczne odkształcenia mechaniczne jej ciała. Wywiera to naprężenia mechaniczne na jednokomórkową błonę endodermalną, na której rosną kanały, i zwiększa ciśnienie w ich wnętrzu. Aby wykazać, że naprężenie koncentruje się na końcach rosnących kanałów, rozwiązujemy numerycznie równania równowagi, aby określić rozkład naprężeń w tkance meduzy. Rozważamy płaski stan naprężenia dla części oktantu w pobliżu kanału pierścieniowego. Zakładamy, że endoderma jest płaską, sztywną i prawie nieściśliwą błoną sprężystą. Obszar normalnie zajmowany przez kanały (światło kanału) jest aproksymowany jako ściśliwa błona sprężysta o module Younga niższym niż moduł endodermy. Wybrany współczynnik Poissona równy 0,3 przekłada pionowe rozszerzenie kanałów na ściskanie w płaszczyźnie.

Analizujemy kanał rosnącą między młodszym a starszym kanałem. Na podstawie obserwacji eksperymentalnych przypisujemy większą sztywność młodszemu kanałowi. Obserwujemy, że naprężenia kumulują się na końcu kanału. Starszy, bardziej miękki kanał relaksuje naprężenia; dlatego w pobliżu rosnącego końca maksymalne naprężenia występują po stronie młodszego, sztywniejszego kanału. Stawiamy hipotezę, że wysokie naprężenia prowadzą kanały, wyjaśniając jej preferencyjne łączenie się z młodszymi kanałami. Identyfikujemy również powstawanie pętli indukowanych przebiciem, szczegółowo opisane w Rozdziale 4. Sugeruje to, że przepływy dyfuzyjne mogą również odgrywać rolę w morfogenezie tego systemu.

W rozdziale 6 badamy dynamikę powstawania sieci kanałów meduzowych, aby zweryfikować dwie hipotezy. Problem ten analizujemy najpierw eksperymentalnie. Gromadzimy obrazy meduz przez okres kilkudziesięciu dni, w miarę jak rosną one od 5 mm do 5 cm. Promień meduzy rośnie liniowo w tempie od 0,6 do 2 milimetrów dziennie, w zależności od warunków wzrostu, takich jak dieta, natężenie przepływu i rozmiar akwarium. Analizujemy obrazy, aby wykryć kanały w sieci i nanosimy na wykres ich uśrednioną azymutalnie gęstość i profile odstępów jako funkcję względnego położenia radialnego. Profile te nie zależą od tempa wzrostu, ale zmieniają się wraz z rozmiarem meduzy. W szczególności wykazujemy, że typowy odstęp między kanałami na krawędzi zwiększa się wraz ze wzrostem meduzy. Co ciekawe, odstępy między kanałami, dostosowane do ich zmieniającej się szerokości, pozostają niemal stałe w czasie. Może to być związane z charakterystyczną

długością reakcji-dyfuzji w systemie – efektywnym zasięgiem dostarczania składników odżywczych z kanału.

Na koniec dostosowujemy model numeryczny z Rozdziałów 3 i 4, aby symulować rosnącą sieć kanałów meduz. Rozpoczynamy symulacje od typowej geometrii – jednej ósmej pierścienia między kanałem brzeżnym a żołądkami. Wymuszamy liniowy wzrost promienia meduzy ze średnią szybkością wzrostu mierzoną w eksperymentach. Nowe kanały są umieszczane na krawędzi z prawdopodobieństwem zależnym od odległości między sąsiednimi kanałami, odtwarzając typowe odstępy obserwowane w eksperymentach. W każdym kroku czasowym symulacji rozwiązujemy problem sprężysty lub dyfuzyjny. Kanałyę rosną z prędkością proporcjonalną do wartości naprężenia zredukowanego (von Misesa) lub gradientu ciśnienia na czubku i w kierunku maksymalnego naprężenia lub gradientu. Przeprowadzamy symulacje dla różnych stosunków właściwości mechanicznych (moduł Younga lub lepkość) endodermy do kanałów. Przy niskim stosunku kanały nie oddziałują na siebie i rosną prosto. Przy wyższym współczynniku kanały silnie się przyciągają, co prowadzi do ponownego połączenia niemal natychmiast po wyjściu z krawędzi. Umiarkowany współczynnik odtwarza wzorce obserwowane w eksperymentach i zmierzone profile gęstości przestrzennej kanałów. Omawiamy ograniczenia modelu i nakreślamy przyszłe kierunki badań.

Résumé substantiel en français

Les formes naturelles sont souvent considérées comme le résultat d'un processus d'optimisation ou comme étant prédéterminées, par exemple par un programme génétique. Cela néglige toutefois la question de savoir *comment* ces formes apparaissent initialement. Pour comprendre cela, nous devons examiner la dynamique de croissance sous-jacente. Nous étudions la relation entre les formes finales et les processus de croissance afin de traiter le problème inverse : étant donné une forme, comment déterminer les détails de son processus de croissance ou, plus largement, identifier le mécanisme fondamental à l'origine de son émergence ? La réponse à cette question est utile dans de nombreux contextes, par exemple pour reconstruire des informations environnementales à partir de formes géologiques ou pour comprendre comment arrêter des processus pathologiques dans les systèmes biologiques. Nous nous concentrons sur des formes qui débutent par une instabilité sur un front en mouvement. Les petites protubérances se développent ensuite en formes digitées qui interagissent entre elles et peuvent former une structure en réseau. Les exemples vont des conduits de dissolution aux réseaux fluviaux, en passant par le réseau de canaux des méduses *Aurelia*.

Dans un premier temps, nous analysons des systèmes dont le mécanisme de croissance a déjà été identifié ou peut être dérivé théoriquement. Nous démontrons comment extraire des détails sur les lois de croissance ou les conditions régissant l'émergence d'une structure simplement en examinant sa géométrie finale. Ceci est particulièrement important pour les formes géologiques qui évoluent sur des échelles de temps dépassant les capacités de mesure humaines. Nous montrons qu'un simple cliché de la géométrie suffit pour reconstruire les débits historiques dans un conduit de dissolution en formation ou pour identifier les lois de croissance d'un réseau fluvial. À la limite des temps longs, certaines formes naturelles atteignent une forme idéale, indépendante des conditions initiales et caractérisée par un petit nombre de paramètres. Cela offre un aperçu unique des conditions physiques dans lesquelles la structure a émergé.

Dans le Chapitre 2, nous étudions les formes idéales de doigts de dissolution. Ces structures résultent de l'instabilité d'infiltration réactive — une rétroaction positive entre

l'écoulement du fluide et le transport de réactifs qui se produit lors de la dissolution de milieux fracturés ou poreux. Nous examinons la formation de ces canaux digitiformes en utilisant une cellule de Hele-Shaw microfluidique à fond soluble. Nous observons une forte compétition entre les doigts dans ce système. Le doigt le plus long, qui offre le chemin de moindre résistance, capture une quantité croissante du flux au détriment des doigts plus courts. Par conséquent, les doigts plus courts ralentissent et s'élargissent. Il est intéressant de noter que le doigt le plus long n'accélère pas et ne change pas de forme. La superposition des clichés du doigt le plus long tout au long de son évolution révèle qu'il trace la même forme depuis le début. Au fil du temps, la partie invariante du doigt se décale simplement dans la direction de l'écoulement, faisant émerger un doigt invariant de plus en plus long.

Pour étudier plus en détail l'émergence de la forme invariante, nous avons réalisé des expériences sur un doigt unique dans une cellule microfluidique étroite. Les doigts présentent une forme régulière, avec une pente constante au niveau des parois loin de la pointe et des pointes paraboliques. Ils sont plus allongés à des débits plus élevés. En combinant la théorie du transport réactif et des techniques de transformation conforme, il est possible de dériver la forme du doigt idéal correspondant aux formes observées expérimentalement. L'analyse peut être étendue à trois dimensions et utilisée pour interpréter des formes naturelles, telles que les conduits de dissolution — des canaux verticaux formés par l'infiltration d'eau de pluie acide dans le calcaire. Le paramètre critique contrôlant la forme idéale est le nombre de Péclet, $\mathrm{Pe} = Q/Da$, où Q est le débit dans le système, D est la constante de diffusion et a est le rayon du canal. En mesurant le diamètre du conduit et sa pente sur les côtés, nous pouvons reconstruire le débit historique dans un conduit de dissolution en formation. Cela peut fournir des informations sur les conditions environnementales dans lesquelles ils se sont développés.

Même si une structure n'atteint pas une forme idéale, sa géométrie recèle une multitude d'informations sur ses lois de croissance et l'environnement dans lequel elle s'est formée. Dans le Chapitre 3, nous décrivons un cadre permettant de reconstruire ces informations à partir d'un unique cliché d'un réseau morphodynamique. Nous considérons des réseaux à croissance apicale (« tip-growing ») dont les branches s'étendent et bifurquent en réponse à un champ externe. Le champ et le réseau co-évoluent dans le temps, car le réseau en croissance modifie les conditions aux limites du champ. La dynamique du réseau est définie par des lois de croissance — un ensemble de règles liant les processus d'extension et de bifurcation aux caractéristiques du champ moteur, telles que son gradient au voisinage de la pointe. Une fois les lois de croissance connues, nous pouvons prédire la forme du réseau dans le futur, mais aussi dans le passé.

Pour décrypter les lois de croissance, nous avons développé l'Algorithme d'Évolution

Rétrograde (Backward Evolution Algorithm). Tout d'abord, les lois de croissance sont paramétrées et un ensemble initial de paramètres est sélectionné. En utilisant ces règles de croissance spécifiques, le réseau évolue en arrière dans le temps sur un petit intervalle, dt, puis évolue vers l'avant sur le même pas de temps. Si la loi de croissance sélectionnée est incorrecte, la réversibilité temporelle du problème est brisée et nous ne revenons pas à l'état d'origine. Inversement, avec une loi de croissance correcte, nous reproduisons la géométrie initiale après l'étape arrière-avant. L'étape avant est ensuite négligée et la procédure est répétée, remontant l'évolution du réseau jusqu'à ses germes. En mesurant les écarts par rapport à l'état d'origine et d'autres métriques après chaque étape arrière, comme la symétrie du champ autour de chaque pointe, nous pouvons estimer la pertinence de la règle de croissance sélectionnée. Nous répétons la même procédure pour différents ensembles de paramètres et sélectionnons le plus optimal. Nous validons cette approche à l'aide de données synthétiques issues de simulations de réseaux cultivés dans un champ diffusif. Les règles de croissance des branches et les conditions d'apparition des ramifications sont déterminées avec succès.

Nous appliquons ensuite cette approche pour analyser la croissance d'un véritable réseau fluvial dans le Vermont, aux États-Unis. Nos résultats montrent que les affluents en formation de ce réseau ont été en forte compétition pour le flux d'eau souterraine. Nous soutenons également que les événements de bifurcation ont été déclenchés par une augmentation de la vitesse de croissance des pointes. Cet outil ouvre de nouvelles perspectives pour l'analyse des réseaux spatiaux dans la nature. Une analyse complète des réseaux fluviaux sur Terre pourrait corréler les lois de croissance avec les conditions climatiques locales, telles que l'intensité des précipitations. Cela pourrait être utilisé pour reconstruire les conditions passées sur d'autres planètes dotées d'anciens réseaux fluviaux. Une analyse similaire basée uniquement sur les angles de bifurcation a donné des résultats prometteurs concernant le climat autrefois prédominant sur Mars.

Ensuite, nous étudions les boucles dans les réseaux physiques. Il a été démontré que les réseaux bouclés sont plus résilients aux dommages et sont sélectionnés par l'évolution biologique. Cependant, on sait peu de choses sur leur développement, en particulier dans un processus de croissance apicale, où les réseaux s'étendent à l'extrémité des branches en réponse au gradient d'un champ externe. Les modèles classiques de ce processus expliquent la compétition, l'écrantage et la répulsion entre les branches et produisent des réseaux purement ramifiés, tels que ceux présentés au Chapitre 3. La question demeure : comment les branches s'attirent-elles et se reconnectent-elles pour former des boucles ?

Dans le Chapitre 4, nous identifions la formation soudaine de boucles près de l'événement de perçage (« breakthrough »). Lorsque le doigt le plus long atteint la limite

du système, les doigts plus courts reprennent leur croissance et sont attirés vers lui. Les reconnexions lors du perçage apparaissent dans des processus remarquablement divers, incluant les décharges électriques, les conduits dans les grottes karstiques, la dissolution et les doigts visqueux dans une cellule de Hele-Shaw, ainsi que les canaux du système gastrovasculaire de la méduse *Aurelia*. La croissance de ces structures est régie par des flux diffusifs. Un paramètre important ici est le rapport de mobilité, M — le rapport entre la mobilité à l'intérieur des doigts en croissance et la mobilité à l'extérieur. Des études antérieures ont montré qu'un rapport de mobilité fini réduit l'écrantage et la répulsion effective dans le système. Cela peut conduire à la formation de boucles dans des plages spécifiques de rapports de mobilité et de longueurs de doigts. Cependant, les reconnexions lors du perçage ne se limitent pas à ces scénarios spécifiques. Près du perçage, les branches se reconnectent même pour un rapport de mobilité élevé, ce qui était auparavant jugé impossible en raison des effets d'écrantage.

Pour fournir une explication physique aux reconnexions lors du perçage, nous considérons d'abord un modèle unidimensionnel de doigts laplaciens. Nous notons que le champ à l'intérieur d'un doigt court loin de la sortie du système est presque constant. Cela suggère que traiter les doigts comme des isolignes du champ, comme dans le Chapitre 4, est justifié dans ce cas. Cependant, le champ diminue le long des doigts plus longs proches de la sortie. La transition de doigts isolignes à des doigts présentant un gradient de champ se produit à une distance de la sortie inversement proportionnelle au rapport de mobilité. Si un doigt court et un doigt long étaient placés l'un à côté de l'autre, il y aurait une différence de potentiel entre la pointe du doigt court et le doigt long. Par conséquent, le doigt court serait attiré par le plus long. Dans le modèle unidimensionnel, chaque doigt est traité indépendamment. En réalité, cependant, les doigts interagissent ; le doigt le plus long écrante le plus court. Pour étudier cet effet, nous menons des simulations numériques d'un système bidimensionnel. Pour un faible rapport de mobilité, le doigt le plus court est faiblement écranté et reçoit un certain flux, même lorsque le doigt le plus long est loin de la sortie. Plus le rapport de mobilité est élevé, plus l'effet d'écrantage est fort. Dans ce cas, lorsque l'écart — la distance entre le doigt le plus long et la sortie — est grand, le flux total dans le doigt le plus court est proche de zéro. À mesure que l'écart diminue, le champ dans le doigt le plus long commence à chuter et le doigt le plus court reçoit plus de flux. Le doigt le plus court non seulement reprend sa croissance, mais sa direction de croissance change également près de l'événement de perçage. Lorsque l'écart est grand, plus de flux provient de l'extérieur et le doigt le plus court s'éloigne du plus long. Pour un écart plus petit, plus de flux provient du doigt le plus long. Cela résulte en une attraction effective vers le doigt le plus long.

Enfin, nous adaptons le modèle du Chapitre 3 pour inclure un rapport de mobilité fini.

Au lieu de doigts fins traités comme des isolignes du champ, nous considérons des doigts de largeur finie avec un champ décroissant le long de ceux-ci. Nous effectuons des simulations de l'évolution temporelle des doigts pour démontrer comment la reprise de croissance et l'attraction vers le doigt le plus long conduisent à la formation dynamique de boucles. Pour deux doigts ayant des longueurs initiales légèrement différentes, nous observons toutes les interactions précédemment décrites entre eux : compétition et répulsion, écrantage, reprise de croissance et attraction. Nous menons ensuite des expériences dans une cellule de Hele-Shaw : dissolution de fractures (comme décrit au Chapitre 2) avec un faible rapport de mobilité et digitation visqueuse avec un rapport de mobilité élevé. Nous comparons les simulations aux expériences et constatons que la dynamique du doigt le plus court est reproduite avec précision. Tant dans les expériences que dans les simulations, nous observons que, pour un faible rapport de mobilité, le doigt le plus court n'est pas écranté et est attiré vers le plus long dès le début. À l'inverse, pour un rapport de mobilité élevé, le doigt le plus court est initialement écranté. Il reprend ensuite sa croissance et se reconnecte soudainement au doigt le plus long. Nos résultats démontrent que la reconnexion est un phénomène prévalent dans les systèmes régis par des flux diffusifs. Elle se produit aussi bien lorsque la mobilité à l'intérieur de la structure en croissance est similaire à la mobilité extérieure qu'à l'approche du perçage.

Dans la dernière partie de la thèse, nous nous concentrons sur un réseau biologique bouclé spécifique : le système de canaux gastrovasculaires de la méduse *Aurelia*. La méduse est un modèle précieux pour étudier le développement des réseaux de distribution biologiques en raison de sa position dans l'arbre phylogénétique, de son anatomie simple et de la facilité d'imagerie in vivo. Le système gastrovasculaire comporte quatre poches stomacales au centre de la méduse. À la fin du stade ephyra, seize canaux droits s'étendent du centre de la méduse vers le canal annulaire marginal. Huit canaux adradiaux bordent huit sections, appelées octants, avec un canal droit inter- ou perradial au milieu de chacune. Typiquement, deux canaux plus courts sont connectés au canal central, formant une fourche en trident. À mesure que les méduses grandissent, de nouveaux canaux bourgeonnent depuis le canal annulaire marginal et croissent vers le centre. Certains bourgeons se reconnectent à d'autres canaux, tandis que d'autres vont directement aux estomacs.

Dans le Chapitre 5, nous décrivons la structure du réseau de canaux et sa variabilité. Nous nous concentrons sur le stade allant de la méduse juvénile à l'adulte. La construction géométrique idéale du motif des canaux peut être décrite comme suit : dans chaque octant, la structure en fourche diviserait le canal marginal en quatre segments égaux. Un nouveau bourgeon apparaîtrait au milieu de chaque segment. Ces bourgeons croîtraient et se connecteraient au canal le plus jeune dans le voisinage (issu de la dernière génération précédente), donc aux canaux latéraux de la structure en fourche. Désormais, le canal

marginal aurait huit segments où la prochaine génération de bourgeons apparaîtrait. Ces bourgeons croîtraient à nouveau et se connecteraient à gauche ou à droite, au canal le plus jeune dans le voisinage. Cela conduirait à la forme d'arbre fractal distinctive du réseau de canaux. Si la structure des canaux était prédéterminée, la construction géométrique serait suivie précisément et les bourgeons se connecteraient toujours à la dernière génération précédente. Nous quantifions l'écart par rapport à cette règle et comptons le nombre de « fausses » connexions chez les méduses élevées dans notre laboratoire. Bien que les bourgeons se connectent préférentiellement au canal le plus jeune dans le voisinage, ce n'est pas une règle stricte. L'analyse des motifs de canaux de méduses élevées dans des conditions différentes illustre davantage la grande variabilité du système. Cela peut être interprété comme une trace d'instabilité résultant du bruit, suggérant que le motif émerge d'une manière auto-organisée.

Nous relions ce processus auto-organisé à la mécanique des méduses. Les contractions natatoires de la méduse induisent des déformations mécaniques considérables sur son corps. Cela exerce une contrainte mécanique sur le feuillet endodermique unicellulaire sur lequel les canaux croissent et augmente la pression à l'intérieur de ceux-ci. Pour démontrer que la contrainte se concentre aux pointes des bourgeons en croissance, nous résolvons numériquement l'équation de quantité de mouvement de Cauchy afin de déterminer la distribution des contraintes dans les tissus de la méduse. Nous considérons un problème de contrainte plane pour une portion d'octant proche du canal annulaire. Nous supposons que l'endoderme est un feuillet élastique plat, rigide et presque incompressible. La zone normalement occupée par les canaux avec lumens est approximée comme une membrane élastique compressible d'un module de Young inférieur à celui de l'endoderme. Le coefficient de Poisson choisi de 0.3 traduit l'expansion verticale des canaux en compression dans le plan. Nous analysons un petit bourgeon croissant entre des canaux plus jeunes et plus âgés. Sur la base d'observations expérimentales, nous attribuons une rigidité plus élevée au canal plus jeune. Nous observons que la contrainte s'accumule à la pointe du bourgeon. Le canal plus âgé et plus mou relâche la tension ; par conséquent, près de la pointe en croissance, la contrainte maximale se trouve du côté du canal plus jeune et plus rigide. Nous émettons l'hypothèse que la forte contrainte guide le bourgeon, expliquant son attachement préférentiel aux canaux plus jeunes. Nous identifions également la formation de boucles induite par le perçage, décrite en détail au Chapitre 4, dans le développement du réseau de canaux. Cela suggère que les flux diffusifs peuvent également jouer un rôle dans la morphogenèse de ce système.

Dans le Chapitre 6, nous étudions la dynamique de la formation du réseau de canaux de la méduse afin de valider les deux hypothèses. Nous abordons d'abord le problème expérimentalement. Nous collectons des images de méduses sur une période de plusieurs

douzaines de jours, alors qu'elles passent de ~5 mm à ~5 cm. Le rayon de la méduse croît linéairement à un taux de 0,6 à 2 millimètres par jour, selon les conditions de croissance, telles que le régime alimentaire, le débit et la taille de l'aquarium. Nous analysons les images pour détecter les canaux dans le réseau et tracer leurs profils de densité et d'espacement moyennés azimutalement en fonction de la position radiale relative. Ces profils ne dépendent pas du taux de croissance, mais changent avec la taille de la méduse. En particulier, nous démontrons que l'espacement typique des canaux au niveau du bord augmente lorsque la méduse grandit. Il est intéressant de noter que l'espacement entre les canaux, ajusté en fonction de leur largeur changeante, reste presque constant dans le temps. Cela peut être lié à la longueur caractéristique de réaction-diffusion dans le système — la portée effective de l'apport en nutriments depuis un canal.

Enfin, nous adaptons le modèle numérique des Chapitres 3 et 4 pour simuler la croissance du réseau de canaux de la méduse. Nous initions les simulations avec la géométrie stéréotypée d'un octant — un huitième d'anneau entre le canal marginal et les estomacs. Nous imposons une croissance linéaire sur le rayon de la méduse au taux de croissance moyen mesuré dans les expériences. De nouveaux bourgeons sont insérés au bord avec une probabilité qui dépend de la séparation entre les canaux voisins, reproduisant l'espacement typique observé dans les expériences. À chaque pas de temps de la simulation, nous résolvons le problème élastique ou diffusif. Les bourgeons croissent avec une vitesse proportionnelle à la contrainte de von Mises ou à la valeur du gradient de pression à la pointe et dans la direction de la contrainte ou du gradient maximal. Nous exécutons les simulations pour différents rapports de propriétés mécaniques (module de Young ou viscosité) de l'endoderme par rapport à celles des canaux. Pour un rapport faible, les canaux n'interagissent pas et poussent droit. Pour un rapport plus élevé, les canaux s'attirent fortement, conduisant à des reconnexions presque instantanément après le bourgeonnement depuis le bord. Un rapport modéré reproduit les motifs observés dans les expériences et les profils de fréquence spatiale des canaux mesurés. Nous discutons des limites du modèle et esquissons les futures directions de recherche.